National Technical University of Athens
School of Applied Mathematical and Physical Sciences
Department of Mathematics

The Radon transform, its generalization and their applications in PET and SPECT medical imaging

Nicholas Protonotarios

PhD thesis

2019

Στη Χρυσίνα μου, τον Μανώλη μου και τον Ηλία μου.

Contents

List of figures

List of tables

Acknowledgments

First and foremost I want to sincerely thank my mentor and friend Thanasis Fokas. His constant encouragement, his brilliant ideas, his genius and his wit have changed me inescapably. Words cannot describe how deeply I admire him. Thanasis has influenced me immensely; he is undoubtedly my role-model and my superhero!

I am forever grateful to my supervisor, George Kastis for always being there for me throughout my occasionally tough PhD years. George is one of the kindest people I've ever met. His sense of justice and equality have inspired me from day one. It seems that, apart from constant scientific guidance, in George I've gained an honest and true friend.

I am also immensely thankful to my supervisor, Antonis Charalambopoulos. Antonis is such a brilliant and entusiastic mathematician: he's opened up my mind and has taught me to never be afraid to ask all the questions that come to my mind, however silly they may seem. His sophisticated humor and inspiring eloquence have helped me immeasurably; he is a dear friend.

I would like to express my deepest gratitude to my friend and bright medical physicist, Marinos Metaxas, who urged me to email Thanasis in the first place! Without Marinos's initial suggestion, this PhD would not exist.

I am grateful for the financial support of the Research Committee of the Academy of Athens via "Inverse problems and medical imaging" (800/920).

Apart from my supervisors, I have been very fortunate to collaborate with world-class scientists like the fantastic basketballer Kostas Kostarelos of the University of Manchester, Krzysztof Kacperski of the Polish Centre for Nuclear Research, and George Spyrou of CING.

I would particularly like to thank my basketball mate Panagiotis Tsiamyrtzis of AUEB for helping me enormously in my sinogram masking paper with his wonderful CUSUM ideas. I also thank Nadia Nikita for her valuable suggestions and comments, as well as Nikos Demiris and Giannis Ntzoufras.

I thank Theodore Skouras of the University Hospital of Patras, as well as Miklos Kovacs, Gabor Nemeth and Andras Wirth of Mediso Medical Imaging Systems, for providing SPECT/CT data. Furthermore, I am grateful to Dr. Vangelis Marinakis of the Technological Educational Institute of Western Greece, whose earlier code provided the starting point of aSRT.

I would also like to thank the IIBEAA guys: Manolis Athanasiadis, Marilena Bourdakou, Tasos Gaitanis, Evi Gheka, Hari Leontiadou, Manos Oikonomakis, and especially the KEΘEM gang, Alexandros Vrachliotis and Evi Tzabazidou: thanks so much for your support and for the countless hours at the office!

I would like to show my greatest appreciation to Alexis Bacopoulos, who played a key role in my transition from engineering to applied mathematics. He's definitely the biggest Hub Science fan! I thank the ΣΕΜΦΕ and NTUA people: Kouli Kyriaki, especially for introducing me to Antonis, Efi Floraki, Eleftheria Skoursi, George Domazakis, Alekos Arvanitakis, Vanda Douka, Nikos Giannakakis, Dimitris Fouskakis, the late Panagiotis Tsekrekos, Dimitris Tzanettis, Themistocles Rassias, Konstantinos Laskaridis, George Matsopoulos, Nikos and Tasos Doulamis, as well as Giannis Stratis from NKUA.

I want to thank my hilarious friend Manolis Zoulias for always being there for me at my darkest hours at the office, my fantastic companion in our common quest to disseminate science, Konstantinos Politis, for our inspiring Hub Science collaboration, which led us to meet Thanasis. Furthermore, I also wish to thank my friends Eleni Grammatikopoulou, Lampros Antoniou, and Alexander Manolakis for helping with the layout of this thesis. I especially thank my friend HrG for helping me debug my code and, more importantly, for the infinite hours of psychotherapeutic Pro Evolution soccer! Many thanks to the wonderful Eden Baldos for her constant support and for taking excellent care of my boys for the last 5 years.

Last but not least, I thank my parents Manolis and Ersi, for supporting me for so long, i.e. for the last forty years, despite their occasional whining regarding the admittedly late start of my PhD, and my sisters Catherine and Thalia, for always believing in their little brother. Respect folks and sistaz!

I dedicate this work to the love of my life, my absolutely fantastic wife Chryssina, and to our two charming, wonderful and brilliant little devils, Manolis and Elias. These three have taught me how to love, how to live and how to laugh. Always in love and always in awe!

Abstract

In the present thesis, the following three different mathematical problems are solved: (a) the problem of edge detection in the Radon (ρ, θ)-space, (b) the problem of deblurring in the attenuated Radon (ρ, θ)-space, and (c) the problem of the inversion of the attenuated Radon transform via a new analytic formula, following the pioneering work of Novikov and Fokas, and the associated numerical implementation, referred to as the *attenuated spline reconstruction technique* (aSRT).

The above mathematical problems involve the inversion of the celebrated Radon transform of a function, defined as the set of all its line integrals, as well as the inversion of a certain generalization of the Radon transform of a function, the so-called *attenuated Radon transform*, defined as the set of all its *attenuated* line integrals. The non-attenuated and attenuated versions of the Radon transform provide the mathematical foundation of two of the most important available medical imaging techniques, namely positron emission tomography (PET), and single-photon emission computed tomography (SPECT).

Although Radon himself derived in 1917 the inversion of the transform bearing his name, seventy four years later Novikov and Fokas rederived this well-known formula by considering two classical problems in complex analysis known as the $\bar{d}$-problem and the scalar Riemann-Hilbert problem. Although the inversion can be obtained in a simpler manner by the use of the Fourier transform, the derivation of Novikov and Fokas allowed Novikov to invert the attenuated Radon transform in 2002. It took Fokas, Iserles and Marinakis four more years to establish a more straightforward derivation of this inversion. Following their work, one of the main results of the present thesis involves the formulation of an equivalent inversion for the attenuated Radon transform. It is not suprising that even today, more than a century after its seminal publication, Radon's work is still highly influential.

In Chapter 1, the Radon transform in $\mathbb{R}^2$ and its attenuated generalization are presented, whereas in Chapter 2 their inversions, especially in the context of non-Fourier analysis, are constructed. Chapter 3 deals with the problem of sinogram edge detection in the context of inverse problems. Furthermore, in Chapter 4, aSRT is analyzed, which provides a novel analytic inversion formula for the attenuated Radon transform. This new inversion formula involves the computation of the Hilbert transforms of the linear attenuation function and of two sinusoidal functions of the attenuated data. Finally, in Chapter 5, the problem of deblurring in the attenuated Radon (ρ, θ)-space is solved.

The mathematical problems solved in this thesis are quite different from one another, however they bear several intrinsic similarities. They are all key elements of a large class of mathematical problems, associated with the mathematical foundations of emission tomography. The inversion of the Radon transform and of its attenuated generalization constitute fundamental problems in the mathematical core of medical imaging.

Extended abstract in Greek

Ο περίφημος μετασχηματισμός Radon μιας δισδιάστατης συνάρτησης ορίζεται ως το σύνολο όλων των επικαμπυλίων ολοκληρωμάτων αυτής επί ευθειών. Υπάρχει ένα είδος γενικευμένου μετασχηματισμού Radon, ο επονομαζόμενος *εξασθενημένος μετασχηματισμός Radon,* ο οποίος ορίζεται ως το σύνολο όλων των επικαμπυλίων ολοκληρωμάτων μίας δισδιάστατης συνάρτησης επί ευθειών, εξασθενημένης ως προς μία συνάρτηση εξασθένισης. Τόσο η μη εξασθενημένη, όσο και η εξασθενημένη εκδοχή του μετασχηματισμού Radon παρέχουν το μαθηματικό υπόβαθρο σε δύο από τις σημαντικότερες τεχνικές ιατρικής απεικόνισης σήμερα, συγκεκριμένα το PET και το SPECT, αντίστοιχα.

Ο μη εξασθενημένος μετασχηματισμός Radon σχετίζεται με το αντίστροφο μαθηματικό πρόβλημα της ανακατασκευής μίας συνάρτησης από τα επικαμπύλια ολοκληρώματά της. Το κύριο μέλημα στην απεικόνιση PET είναι η αριθμητική εφαρμογή της αντιστροφής του μη εξασθενημένου μετασχηματισμού Radon. Ομοίως, στην περίπτωση του εξασθενημένου μετασχηματισμού Radon, το αντίστοιχο αντίστροφο μαθηματικό πρόβλημα περιλαμβάνει την ανακατασκευή μίας συνάρτησης από τα «εξασθενημένα» επικαμπύλια ολοκληρώματά της. Ο κύριος στόχος της απεικόνισης SPECT είναι η αντιστροφή του εξασθενημένου μετασχηματισμού Radon.

Το 1991, οι Novikov και Φωκάς επανεξέτασαν την ήδη γνωστή, τότε, αντιστροφή του μετασχηματισμού Radon πραγματοποιώντας *φασματική ανάλυση* στην ακόλουθη εξίσωση ιδιοτιμών

$$\left[\frac{1}{2}\left(k+\frac{1}{k}\right)\partial_{x_1}+\frac{1}{2\mathrm{i}}\left(k-\frac{1}{k}\right)\partial_{x_2}\right]u=f,\quad k\in\mathbb{C}, \tag{A.1}$$

όπου οι δείκτες υποδηλώνουν μερική παραγώγιση. Η ανάλυση αυτή εμπεριέχει δύο προβλήματα της σύγχρονης μιγαδικής ανάλυσης, συγκεκριμένα το πρόβλημα $\bar{d}$ (d-bar), και το βαθμωτό πρόβλημα Riemann-Hilbert (RH), αντίστοιχα.

Μολονότι η αντιστροφή του μετασχηματισμού Radon μπορεί να επιτευχθεί με σαφώς απλούστερο τρόπο, δηλαδή με χρήση του δισδιάστατου μετασχηματισμού Fourier, το πλεονέκτημα της αντιστροφής κατά Novikov και Φωκά κατέστη εμφανές έντεκα χρόνια αργότερα (2002) από τον Novikov. Ο Novikov απέδειξε ότι ο εξασθενημένος μετασχηματισμός Radon μπορεί, όπως ακριβώς και ο μη εξασθενημένος, να αντιστραφεί με τη βοήθεια φασματικής ανάλυσης. Στην εξασθενημένη περίπτωση, όμως, η ανάλυση αυτή δεν εφαρμόζεται στην εξίσωση ιδιοτιμών (A.1), αλλά σε μία γενίκευση αυτής:

$$\left[\frac{1}{2}\left(k+\frac{1}{k}\right)\partial_{x_1}+\frac{1}{2\mathrm{i}}\left(k-\frac{1}{k}\right)\partial_{x_2}-\mu\right]u=f,\quad k\in\mathbb{C}. \tag{A.2}$$

Τέσσερα χρόνια αργότερα, το 2006, οι Φωκάς, Iserles και Μαρινάκης αντέστρεψαν τον εξασθενημένο μετασχηματισμό Radon με ακόμη απλούστερο τρόπο, χρησιμοποιώντας τα αποτελέσματα της φασματικής ανάλυσης των εξισώσεων ιδιοτιμών (A.1) και (A.2). Λεπτομέρειες αυτής της νέας αντιστροφής παρατίθενται στο Ενότητα 2.2 του παρόντος κειμένου.

Ένα από τα κύρια αποτελέσματα της παρούσας διατριβής είναι η διατύπωση μιας ισοδύναμης αντιστροφής για τον εξασθενημένο μετασχηματισμό Radon, ακολουθώντας το πρωτοποριακό έργο των Novikov και Φωκά. Παρουσιάζουμε λεπτομερώς μία νέα εξίσωση αναλυτικής αντιστροφής εξασθενημένων ολοκληρωτικών μετασχηματισμών Radon, βλ. Θεώρημα A.10, καθώς και τον αντίστοιχο αλγόριθμο ανακατασκευής εικόνας, με την ονομασία *attenuated spline reconstruction technique* (aSRT).

Στην παρούσα διατριβή, με τίτλο «Ο μετασχηματισμός Radon, οι γενικεύσεις του και εφαρμογές αυτών στις ιατρικές απεικονίσεις PET και SPECT» επιλύουμε τρία διαφορετικά μαθηματικά προβλήματα:

1. το πρόβλημα της εύρεσης συνόρων στον κατά Radon (ρ,θ)-χώρο, δηλαδή στο ημιτονόγραμμα (sinogram), και της ανακατασκευής των δεδομένων μέσω στατιστικής σωρευμένων αθροισμάτων (CUSUM statistics), βλ. Κεφάλαιο 3,
2. το πρόβλημα της αναλυτικής αντιστροφής του εξασθενημένου μετασχηματισμού Radon μέσω μιας νέας εξίσωσης, βλ. Θεώρημα A.10, και της αντίστοιχης αριθμητικής υλοποίησης αυτής (aSRT), που παρουσιάζονται στο Κεφάλαιο 4, και
3. το πρόβλημα του «ξεθολώματος» (deblurring) του εξασθενημένου ημιτονογράμματος στον Radon (ρ,θ)-χώρο και της επακόλουθης ανακατασκευής των «ξεθολωμένων» (deblurred) δεδομένων, βλ. Κεφάλαιο 5.

Τα μαθηματικά προβλήματα που περιγράφονται παραπάνω παρότι είναι αρκετά διαφορετικά μεταξύ τους, ωστόσο διαθέτουν εγγενείς ομοιότητες. Τα προβλήματα αυτά ανήκουν σε μία ευρύτατη κατηγορία μαθηματικών προβλημάτων που σχετίζονται με την τομογραφία και την πυρηνική ιατρική. Η αντιστροφή του μετασχηματισμού Radon και της εξασθενημένης γενίκευσής του αποτελούν μαθηματικά προβλήματα που σχετίζονται, εν τέλει, με την ανακατασκευή ιατρικής εικόνας. Τέτοιου είδους προβλήματα διαμορφώνουν το θεμελιώδες μαθηματικό υπόβαθρο της τομογραφίας εκπομπής ποζιτρονίων PET και της τομογραφίας εκπομπής μονών φωτονίων SPECT.

Έχουν περάσει πάνω από εκατό χρόνια από την πρωτοποριακή δημοσίευση του Johann Radon το 1917. Η συγκεκριμένη δημοσίευση έμελλε να αποτελέσει το έναυσμα για τη δημιουργία ενός καινούριου κλάδου στην ιατρική, τον κλάδο της τομογραφίας. Το έργο του Radon εξακολουθεί να ασκεί μεγάλη επιρροή στην ερευνητική κοινότητα παγκοσμίως μέχρι σήμερα.

Μετασχηματισμός Radon στον $\mathbb{R}^2$

Τοπικές συντεταγμένες. Μία ευθεία L στο x_1x_2-επίπεδο δύναται να προσδιοριστεί από την προσημασμένη απόστασή της από την αρχή των αξόνων ρ, $(-\infty < \rho < \infty)$, και από τη γωνία την οποία σχηματίζει με τον άξονα x_1, θ $(0 \leq \theta < 2\pi)$, βλ. σχήμα 1.1. Συμβολίζοντας τα μοναδιαία διανύσματα επί της L με $\mathbf{e}^{\parallel}$ και $\mathbf{e}^{\perp}$, προκύπτει ότι:

$$\begin{aligned} \mathbf{e}^{\parallel} &= (\cos\theta, \sin\theta)\,, \\ \mathbf{e}^{\perp} &= (-\sin\theta, \cos\theta)\,. \end{aligned}$$

Επομένως, κάθε σημείο $\mathbf{x} = (x_1, x_2)$ επί της L σε καρτεσιανές συντεταγμένες εκφράζεται βάσει των τοπικών συντεταγμένων (ρ, τ) ως εξής:

$$\mathbf{x} = \rho\,\mathbf{e}^{\perp} + \tau\,\mathbf{e}^{\parallel},$$

όπου το τ υποδηλώνει το μήκος του ευθύγραμμου τμήματος που ανήκει στην ευθεία. Επομένως,

$$x_1 := x_1(\rho, \tau; \theta) = \tau\cos\theta - \rho\sin\theta, \tag{A.3a}$$

$$x_2 := x_1(\rho, \tau; \theta) = \tau\sin\theta + \rho\cos\theta. \tag{A.3b}$$

Αντιστρέφοντας τις εξισώσεις (A.3), προκύπτουν οι τοπικές συντεταγμένες συναρτήσει των τοπικών, δηλαδή

$$\rho := \rho(x_1, x_2; \theta) = x_2 \cos\theta - x_1 \sin\theta, \tag{A.4a}$$

$$\tau = \tau(x_1, x_2; \theta) = x_2 \sin\theta + x_1 \cos\theta. \tag{A.4b}$$

Χώρος συναρτήσεων Schwartz. Σε ό, τι ακολουθεί, θα αναφερόμαστε σε συναρτήσεις Schwartz.

Ορισμός A.1. *Ο χώρος συναρτήσεων Schwartz στον $\mathbb{R}^n$, ή ο χώρος των ταχέως μειούμενων συναρτήσεων (rapidly decreasing functions) συμβολίζεται με $\mathcal{S}(\mathbb{R}^n)$ και ορίζεται ως:*

$$\mathcal{S}(\mathbb{R}^n) = \{f \in C^\infty(\mathbb{R}^n) : ||f||_{\alpha,\beta} < \infty\} \subset C^\infty(\mathbb{R}^n), \tag{A.5}$$

όπου

$$||f||_{\alpha,\beta} = \sup_{x\in\mathbb{R}^n} \left|x^\alpha D^\beta f(x)\right|, \quad \forall \text{ πολυδείκτη } \alpha, \beta,$$
$$\left|x^\alpha D^\beta f(x)\right| \to 0, \quad \text{καθώς } |x| \to \infty. \tag{A.6}$$

Μετασχηματισμός Radon. Ο περίφημος μετασχηματισμός Radon μίας δισδιάστατης συνάρτησης ορίζεται ως το σύνολο όλων των επικαμπύλιων ολοκληρωμάτων αυτής επί ευθειών. Πιο συγκεκριμένα:

Ορισμός A.2. *Το επικαμπύλιο ολοκλήρωμα μίας δισδιάστατης συνάρτησης Schwartz $f \in \mathcal{S}(\mathbb{R}^2)$ επί ευθειών στο επίπεδο, βλ. Ορισμό A.1, αποτελεί τον επονομαζόμενο «μετασχηματισμό Radon», $\mathcal{R}$, της $f(x_1, x_2)$ και συμβολίζεται με $\widehat{f}(\rho, \theta)$. Ο μετασχηματισμός Radon αποθηκεύεται συνήθως στη μορφή ενός ημιτονογράμματος, το οποίο εκφράζεται ως εξής:*

$$\widehat{f}(\rho,\theta) = (\mathcal{R}f)(\rho,\theta) = \int_{-\infty}^{\infty} f(\tau\cos\theta - \rho\sin\theta, \tau\sin\theta + \rho\cos\theta)\mathrm{d}\tau,$$
$$0 \le \theta < 2\pi, \ -\infty < \rho < \infty, \tag{A.7}$$

Μέσω του συναρτησιακού Dirac, η εξίσωση (A.7) μπορεί να γραφεί ως:

$$\widehat{f}(\rho,\theta)=\int_{-\infty}^{\infty}\int_{-\infty}^{\infty}f(x_1,x_2)\delta(\rho+x_1\sin\theta-x_2\cos\theta)\mathrm{d}x_1\mathrm{d}x_2. \tag{A.8}$$

Ο μετασχηματισμός (A.7) αποτελεί ένα *αντίστροφο πρόβλημα*: Δεδομένης της συνάρτησης $\widehat{f}(\rho,\theta)$, $0\leq\theta<2\pi$, $-\infty<\rho<\infty$, επιθυμούμε να «ανακατασκευάσουμε» τη συνάρτηση $f(x_1,x_2)$. Πρόκειται για το μαθηματικό πρόβλημα της τομογραφίας εκπομπής ποζιτρονίων PET. Το πρόβλημα αυτό το έλυσε, κατ΄ αρχήν, ο ίδιος ο Radon το 1917. Η αντιστροφή του μετασχηματισμού Radon αναλύεται εκτενώς στα Κεφάλαια 2 και 4.

Εξασθενημένος μετασχηματισμός Radon στον $\mathbb{R}^2$

Το μαθηματικό πρόβλημα της τομογραφίας εκπομπής μονών φωτονίων SPECT εμπεριέχει τη γενίκευση του μετασχηματισμού Radon, και πιο συγκεκριμένα τον *εξασθενημένο μετασχηματισμό Radon ή εκθετικό μετασχηματισμό Radon*, τον οποίο συμβολίζουμε με $\mathcal{R}_\mu$. Η συνάρτηση του συντελεστή γραμμικής εξασθένισης, ή απλώς εξασθένιση, συμβολίζεται με $\mu(x_1,x_2)$.

Ορισμός A.3. *Ορίζουμε το επικαμπύλιο ολοκλήρωμα μίας δισδιάστατης συνάρτησης Schwartz $f\in\mathcal{S}(\mathbb{R}^2)$ επί ευθειών στο επίπεδο, εξασθενημένης ως προς τη συνάρτηση εξασθένισης μ, ως τον «εξασθενημένο μετασχηματισμό Radon», $\mathcal{R}_\mu$ της $f(x_1,x_2)$ και τον συμβολίζουμε με $\widehat{f}_\mu(\rho,\theta)$. Ο εξασθενημένος μετασχηματισμός Radon αποθηκεύεται συνήθως στη μορφή ενός εξασθενημένου ημιτονογράμματος, το οποίο εκφράζεται ως εξής:*

$$\widehat{f}_\mu(\rho,\theta)=\left(\mathcal{R}_\mu f\right)(\rho,\theta)=\int_{-\infty}^{\infty}e^{-\int_\tau^\infty\mu(s\cos\theta-\rho\sin\theta,s\sin\theta+\rho\cos\theta)\mathrm{d}s}\times$$
$$f(\tau\cos\theta-\rho\sin\theta,\tau\sin\theta+\rho\cos\theta)\mathrm{d}\tau,\ 0\leq\theta<2\pi,\ -\infty<\rho<\infty. \tag{A.9}$$

Ο μετασχηματισμός (A.9) αποτελεί,όπως ακριβώς και ο μετασχηματισμός (A.7), ένα *αντίστροφο πρόβλημα*: Δεδομένων των συναρτήσεων $\widehat{f}_\mu(\rho,\theta)$, $0\leq\theta<2\pi$, $-\infty<\rho<\infty$ και $\mu(x_1,x_2)$, επιθυμούμε να ανακατασκευάσουμε τη συνάρτηση $f(x_1,x_2)$. Πρόκειται για το μαθηματικό πρόβλημα της τομογραφίας εκπομπής μονών φωτονίων SPECT. Η αντιστροφή του εξασθενημένου μετασχηματισμού Radon αναλύεται εκτενώς στο Κεφάλαιο 4.

Παρατήρηση Α.4. *Στην οριακή κατάσταση μηδενικής εξασθένισης, δηλαδή*

$$\mu(x_1, x_2) \to 0,$$

ο εξασθενημένος μετασχηματισμός Radon $\mathcal{R}_\mu$ μετατρέπεται στον μη εξασθενημένο μετασχηματισμό Radon $\mathcal{R}$:

$$\lim_{\mu \to 0} \mathcal{R}_\mu(\cdot) =: \mathcal{R}_0(\cdot) = \mathcal{R}(\cdot).$$

Αντιστροφή μετασχηματισμού Radon στον $\mathbb{R}^2$

Μία από τις συνήθεις μαθηματικές τεχνικές στον τομέα της ιατρικής απεικόνισης βασίζεται στο *θεώρημα κεντρικής τομής* (central slice theorem). Το θεώρημα αυτό παρέχει ένα βασικό εργαλείο για την αντιστροφή του μετασχηματισμού Radon, η οποία βασίζεται στους μετασχηματισμούς Fourier.

Θεώρημα Α.5. *(Θεώρημα κεντρικής τομής). Ο δισδιάστατος μετασχηματισμός Fourier $\mathcal{F}_2$ μίας συνάρτησης $f(x_1, x_2)$ είναι ίσος με τον μονοδιάστατο μετασχηματισμό Fourier $\mathcal{F}_1$ του μετασχηματισμού Radon $\mathcal{R}$ της f. Σε αμιγή συμβολισμό τελεστών, το παραπάνω αποδίδεται ως*

$$\mathcal{F}_2 \{f\} = \mathcal{F}_1 \{\mathcal{R} \{f\}\}, \tag{A.10}$$

όπου ο μετασχηματισμός $\mathcal{F}_2$ είναι ίσος με

$$(\mathcal{F}_2 \{f\})(\xi_1, \xi_2) = \int_{-\infty}^{\infty} \int_{-\infty}^{\infty} f(x_1, x_2) e^{-2\pi \mathrm{i}(\xi_1 x_1 + \xi_2 x_2)} \mathrm{d}x_1 \mathrm{d}x_2, \tag{A.11}$$

ενώ ο μετασχηματισμός $\mathcal{F}_1$ δίνεται από τον τύπο

$$(\mathcal{F}_1 \{g\})(r) = \int_{-\infty}^{\infty} g(\rho) e^{-2\pi \mathrm{i} r \rho} \mathrm{d}\rho, \tag{A.12}$$

και ο μετασχηματισμός $\mathcal{R}$ ορίζεται στην εξίσωση (A.7)*.*

Πόρισμα Α.6. *Το θεώρημα κεντρικής τομής συνεπάγεται ότι η κατά Fourier αντιστροφή του μετασχηματισμού Radon είναι, σε γραφή τελεστών, η ακόλουθη:*

$$\mathcal{R}^{-1} = \mathcal{F}_2^{-1} \mathcal{F}_1. \tag{A.13}$$

Η αντιστροφή του μετασχηματισμού Radon μπορεί να επιτευχθεί και χωρίς τους μετασχηματισμούς Fourier. Μπορούμε να αντιστρέψουμε τον μετασχηματισμό Radon με έναν πιο περίπλοκο τρόπο, χρησιμοποιώντας εργαλεία της μιγαδικής ανάλυσης. Ωστόσο, τα υπολογιστικά πλεονεκτήματα της αντιστροφής χωρίς τους μετασχηματισμούς Fourier είναι ιδιαιτέρως σημαντικά, και θα γίνουν σαφή στο Κεφάλαιο 4. Στο κεφάλαιο αυτό παρουσιάζουμε ένα από τα κύρια αποτελέσματα της παρούσας διατριβής.

Όπως αναφέρθηκε προηγουμένως, το 1991, ο Roman Novikov και ο Θανάσης Φωκάς αντέστρεψαν τον μετασχηματισμό Radon εφαρμόζοντας φασματική ανάλυση στην εξίσωση (A.1). Στην ανάλυση που ακολουθεί, υιοθετούμε μία αλγοριθμική προσέγγιση για την αντιστροφή του μετασχηματισμού Radon. Συγκεκριμένα, τα βήματα του αλγορίθμου είναι δύο:

(α) **Ευθύ πρόβλημα.** Λύνουμε την εξίσωση ιδιοτιμών (A.1) ως προς την συνάρτηση f για όλες τις ιδιοτιμές $k \in \mathbb{C}$. Η λύση της εξίσωσης ιδιοτιμών πρέπει να είναι φραγμένη για κάθε $k \in \mathbb{C}$. Το ευθύ πρόβλημα αποτελεί χαρακτηριστική περίπτωση $\bar{d}$-προβλήματος (d-bar problem).

(β) **Αντίστροφο πρόβλημα.** Δεδομένου ότι η λύση της εξίσωσης ιδιοτιμών (A.1) είναι φραγμένη για όλες τις μιγαδικές ιδιοτιμές k, συμπεραίνουμε ότι υπάρχει ισοδύναμη αναπαράσταση για την u, η οποία, αντί να εξαρτάται από την f, εξαρτάται από τον μετασχηματισμό Radon της f ($\widehat{f}$), βλ. εξίσωση (A.7). Το αντίστροφο πρόβλημα αποτελεί χαρακτηριστική περίπτωση βαθμωτού προβλήματος Riemann-Hilbert (RH) ή scalar Riemann-Hilbert problem.

Ορισμός A.7. *Ο μετασχηματισμός Hilbert μίας συνάρτησης $u(t)$ ορίζεται ως το ακόλουθο ολοκλήρωμα:*

$$\mathcal{H}\left\{u(t)\right\} = \frac{1}{\pi}\left(PV\int_{-\infty}^{\infty}\frac{u(\tau)}{\tau - t}\mathrm{d}\tau\right), \tag{A.14}$$

όπου το PV συμβολίζει το κατά Cauchy ολοκλήρωμα κύριας τιμής

$$PV\int_{L} g(\tau)\mathrm{d}\tau = \lim_{\epsilon\to 0}\int_{L-L_\epsilon} g(\tau)\mathrm{d}\tau, \tag{A.15}$$

και το L_ε αναπαριστά το τμήμα της καμπύλης L με κέντρο το σημείο t, και μήκος ίσο με 2ϵ.

Πρόταση Α.8. *Ο αντίστροφος του μετασχηματισμού Radon* $\widehat{f}(\rho,\theta)$*, μίας συνάρτησης* $f(x_1,x_2)\in\mathcal{S}(\mathbb{R}^2)$*, όπως ορίζεται στην εξίσωση* (Α.7) *δίνεται από τον τύπο:*

$$f(x_1,x_2)=-\frac{1}{4\pi}\int_0^{2\pi}\left[\frac{\partial(\mathcal{H}\widehat{f})(\rho,\theta)}{\partial\rho}\right]_{\rho=x_2\cos\theta-x_1\sin\theta}\mathrm{d}\theta, \tag{Α.16}$$

με $-\infty<x_1,x_2<\infty$*, και το σύμβολο* $\mathcal{H}$ *να αναπαριστά τον μετασχηματισμό Hilbert ως προς τη μεταβλητή* ρ*, όπως στην εξίσωση* (Α.14)*, ήτοι*

$$(\mathcal{H}\widehat{f})(\rho,\theta)\equiv\frac{1}{\pi}\ PV\int_{-\infty}^{\infty}\frac{\widehat{f}(r,\theta)}{r-\rho}\mathrm{d}r,\quad -\infty<\rho<\infty,\quad 0\le\theta<2\pi. \tag{Α.17}$$

Αντιστροφή εξασθενημένου μετασχηματισμού Radon στον $\mathbb{R}^2$

Ο Novikov απέδειξε ότι η αντιστροφή του εξασθενημένου μετασχηματισμού Radon επιτυγχάνεται μέσω φασματικής ανάλυσης της εξίσωσης ιδιοτιμών (Α.2), η οποία αποτελεί γενίκευση της εξίσωσης (Α.1). Ωστόσο, η αντιστροφή αυτή δύναται να επιτευθεί με τη χρήση των αποτελεσμάτων της αντιστροφής του μη εξασθενημένου μετασχηματισμού Radon, βλ. Πόρισμα 2.9, σελ. 72.

Πρόταση Α.9. *Ο αντίστροφος του εξασθενημένου μετασχηματισμού Radon* $\widehat{f}_\mu(\rho,\theta)$ *μιας συνάρτησης* $f(x_1,x_2)$*, εξασθενημένης ως προς τη συνάρτηση εξασθένισης* $\mu(x_1,x_2)$*, με* $f,\mu\in S(\mathbb{R}^2)$*, βλ. εξίσωση* (Α.9)*, δίνεται από τον τύπο*

$$f(x_1,x_2)=\frac{1}{4\pi}(\partial_{x_1}-\mathrm{i}\partial_{x_2})\int_0^{2\pi}e^{\mathrm{i}\theta}J(x_1,x_2,\theta)\mathrm{d}\theta,\quad -\infty<x_1,x_2<\infty, \tag{Α.18}$$

όπου η συνάρτηση J *ορίζεται ως εξής:*

$$J(x_1,x_2,\theta)=e^{M(\tau,\rho,\theta)}L_\mu(\rho,\theta)\widehat{f}_\mu(\rho,\theta)\Big|_{\substack{\tau=x_2\sin\theta+x_1\cos\theta\\ \rho=x_2\cos\theta-x_1\sin\theta}}, \tag{Α.19}$$

και οι ποσότητες M *και* L_μ *ισούνται με*

$$M(\tau,\rho,\theta) = \int_\tau^\infty \mu\left(s\cos\theta - \rho\sin\theta, s\sin\theta + \rho\cos\theta\right) \mathrm{d}s, \tag{A.20}$$

$$L_\mu(\rho,\theta) = e^{P^-\widehat{\mu}(\rho,\theta)} P^- e^{P^-\widehat{\mu}(\rho,\theta)} + e^{-P^+\widehat{\mu}(\rho,\theta)} P^+ e^{P^+\widehat{\mu}(\rho,\theta)}. \tag{A.21}$$

Στην εξίσωση (A.21)*, το* $\widehat{\mu}$ *αναπαριστά τον μετασχηματισμό Radon της συνάρτησης εξασθένισης* μ*, δηλαδή*

$$\widehat{\mu}(\rho,\theta) = \int_{-\infty}^\infty \mu\left(\tau\cos\theta - \rho\sin\theta, \tau\sin\theta + \rho\cos\theta\right) \mathrm{d}\tau, \\ 0 \le \theta < 2\pi, \quad -\infty < \rho < \infty, \tag{A.22}$$

ενώ οι προβολικοί τελεστές $P^\pm$ *δίνονται από την ακόλουθη εξίσωση:*

$$(P^\mp g)(\rho) = \pm\frac{g(\rho)}{2} + \frac{1}{2\pi\mathrm{i}}\, PV \int_{-\infty}^\infty \frac{g(r)}{r-\rho}\mathrm{d}r = \pm\frac{g(\rho)}{2} + \frac{1}{2\mathrm{i}}(\mathcal{H}g)(\rho). \tag{A.23}$$

Εύρεση συνόρων στον Radon (ρ,θ)-χώρο δεδομένων με αθροίσματα CUSUM

Στο κεφάλαιο 3 καταπιανόμαστε με το πρόβλημα της ανίχνευσης των συνόρων του ημιτονογράμμου, στο πλαίσιο των αντίστροφων μαθηματικών προβλημάτων της πυρηνικής ιατρικής. Το πρόβλημα του προσδιορισμού των συνόρων (περιγραμμάτων) των αντικειμένων στις εικόνες πυρηνικής ιατρικής έχει μελετηθεί εκτενώς στο παρελθόν, ωστόσο το μεγαλύτερο μέρος της ανάλυσης έχει επικεντρωθεί στην απεικόνιση ενός μόνο αντικειμένου. Σκοπός της μελέτης μας είναι η ανάπτυξη μίας αυτοματοποιημένης μεθόδου για τον προσδιορισμό των συνόρων ενός ή πολλών αντικειμένων σε απεικονίσεις πυρηνικής ιατρικής, και ιδιαίτερα σε τομογραφικές εικόνες PET και SPECT, ανακατασκευασμένες με φιλτραρισμένη οπισθοπροβολή (*filtered back-projection*, FBP). Τα προαναφερθέντα σύνορα στον Radon (ρ,θ)-χώρο δεδομένων μπορούν να χρησιμοποιηθούν στην τομογραφία εκπομπής PET ή SPECT, για τον υπολογισμό των συνόρων του σώματος και για τη διόρθωση της εξασθένισης. Η ανίχνευση των συνόρων των προς απεικόνιση αντικειμένων επιτυγχάνεται εφαρμόζοντας μία τροποποιημένη τεχνική σωρευτικών αθροισμάτων (cumulative sums, CUSUM) στο ημι-

τονόγραμμα, δηλαδή τον (ρ, θ)-χώρο δεδομένων του μετασχηματισμού Radon των εν λόγω εικόνων. Με τη νέα προσέγγισή μας είμαστε σε θέση να ανιχνεύσουμε αυτόματα όλα τα αντικείμενα που απεικονίζονται στην ιατρική εικόνα, χωρίς να απαιτείται a priori γνώση του συνολικού αριθμού των αντικειμένων αυτών. Αξιολογήσαμε τη μέθοδό μας με προσομοιωμένα ομοιώματα, όπως το ομοίωμα ποιότητας εικόνας (image quality phantom IQ) και δύο ψηφιακά ομοιώματα πολλαπλών αντικειμένων, με το μη-προσομοιωμένο ομοίωμα NEMA, και με μία κλινική μελέτη θώρακα. Προς αυτή την κατεύθυνση, χρησιμοποιήσαμε τον PET τομογράφο GE Discovery. Τα περιγράμματα που ανιχνεύσαμε επιτυγχάνουν ακρίβεια ρίζας μέσου τετραγώνου (root mean square) ίση με 1.14 pixels, 1.69 pixels και 3.28 pixels, και απόσταση κατά Hausdorff (Hausdorff distance) ίση με 3.13, 3.12 και 4.50 pixels, για την προσομοίωση του ομοιώματος IQ, το πραγματικό ομοίωμα NEMA και την κλινική μελέτη, αντίστοιχα. Τα αποτελέσματα αντιστοιχούν σε σημαντική βελτίωση σε σχέση με πρόσφατα αποτελέσματα που ελήφθησαν σε παρόμοιες μελέτες. Αναφέρουμε επίσης ότι λάβαμε τοπικό σφάλμα εντοπισμού optimal sub-pattern assignment (OSPA) της τάξης των 0.94 και 1.48, για τα προσομοιωμένα ομοιώματα δύο και τριών αντικειμένων, αντίστοιχα. Η μέθοδος μας λειτουργεί αποτελεσματικά σε σύνολα κυρτών αντικειμένων, και ως εκ τούτου παρέχει ένα ισχυρό εργαλείο για τον αυτόματο προσδιορισμό συνόρων με ακριβή αποτελέσματα. Αξίζει να σημειωθεί ότι με την εφαρμογή της μεθόδου μας, μειώνεται σημαντικά ο χρόνος υπολογισμού κατά την ανακατασκευή των εικόνων.

Μέθοδος CUSUM

Για να αναδείξουμε την πινακοποιημένη του μορφή, συμβολίζουμε το ημιτονόγραμμο με $\widehat{f}_{ij},$, ανεξαρτήτως εξασθένισης. Πρόκειται για το μετασχηματισμό Radon της δισδιάστατης συνάρτησης κατανομής ραδιενέργειας $f(x_1, x_2)$. Το ημιτονόγραμμο αποτελεί έναν πίνακα με N_θ γραμμές και N_ρ στήλες, οι οποίες αντιστοιχούν στα ορίσματα ρ και θ, με στοιχεία

$$\widehat{f}_{ij} = \widehat{f}(\rho_i, \theta_j), \quad \text{για} \quad i = 1, \ldots, N_\rho, \quad \text{και} \quad j = 1, \ldots, N_\theta.$$

Στις ιατρικές απεικονίσεις PET και SPECT, υποθέτουμε ότι η συνάρτηση $(\widehat{f}_{ij})$ διαθέτει πεπερασμένο φορέα, βλ. σχήμα 3.1. Δεδομένου του πεπερασμένου φορέα της $\widehat{f}_{ij}$, είναι ασφαλές να υποθέσουμε ότι για κάθε γραμμή j του ημιτονόγραμμου υπάρχουν δύο «σχεδόν μηδενικά διαστήματα», ένα από τα αριστερά

και ένα από τα δεξιά. Συμβολίζουμε το μήκος των διαστημάτων αυτών με ℓ_L και ℓ_R pixels, αντίστοιχα. Χωρίς περιορισμό της γενικότητας υποθέτουμε ότι

$$\ell_L = \ell_R = \ell$$

και αντιμετωπίζουμε το ℓ ως ελεύθερη παράμετρο. Η παράμετρος ℓ παρέχει ακριβή εκτίμηση της κατανομής του θορύβου στα δύο άκρα του ημιτονογράμμου. Προκειμένου να βρεθεί η απότομη μεταβολή (άλμα) του ημιτονογράμμου σε κάθε γραμμή j, εισάγουμε τα ακόλουθα CUSUM αθροίσματα $L_n^{(j)}$ και $R_n^{(j)}$ από αριστερά και από δεξιά, αντίστοιχα:

$$L_0^{(j)} = 0, \tag{A.24a}$$

$$L_n^{(j)} = \max\left\{0, L_{n-1}^{(j)} + \widehat{f}_{n,j} - \left(\mu_L^{(j)} + \lambda\sigma_L^{(j)}\right)\right\}, \quad n = 1, \ldots, N_\rho, \tag{A.24b}$$

όπου με $\mu_L^{(j)}$ συμβολίζουμε τον μέσο και με $\sigma_L^{(j)}$ την τυπική απόκλιση του «σχεδόν μηδενικού διαστήματος» από αριστερά, για κάθε γραμμή j:

$$\mu_L^{(j)} = \frac{1}{\ell}\sum_{i=1}^{\ell}\widehat{f}_{ij} \quad \text{και} \quad \sigma_L^{(j)} = \sqrt{\frac{1}{\ell}\sum_{i=1}^{\ell}\left(\widehat{f}_{ij} - \mu_L^{(j)}\right)^2}, \tag{A.25}$$

ενώ με λ συμβολίζουμε τον πολλαπλασιαστή της τυπικής απόκλισης, στον οποίο συνήθως δίνουμε την τιμή $\lambda = 3$. Από τον ανωτέρω ορισμό γίνεται σαφές ότι το σωρευτικό άθροισμα από αριστερά είναι αυξάνον, δηλαδή:

$$L_m^{(j)} \geq L_n^{(j)} \quad \text{για κάθε} \quad m > n.$$

Ομοίως,

$$R_{N_\rho}^{(j)} = 0, \tag{A.26a}$$

$$R_{n-1}^{(j)} = \max\left\{0, R_n^{(j)} + \widehat{f}_{n-1,j} - \left(\mu_R^{(j)} + \lambda\sigma_R^{(j)}\right)\right\}, \quad n = N_\rho, N_{\rho-1}, \ldots, 2, 1, \tag{A.26b}$$

όπου με $\mu_R^{(j)}$ συμβολίζουμε τον μέσο και με $\sigma_R^{(j)}$ την τυπική απόκλιση του

«σχεδόν μηδενικού διαστήματος» από δεξιά, για κάθε γραμμή j:

$$\mu_R^{(j)} = \frac{1}{\ell} \sum_{i=N_\rho-\ell+1}^{N_\rho} \widehat{f}_{ij} \quad \text{και} \quad \sigma_R^{(j)} = \sqrt{\frac{1}{\ell} \sum_{i=N_\rho-\ell+1}^{N_\rho} \left(\widehat{f}_{ij} - \mu_R^{(j)}\right)^2}. \tag{A.27}$$

Από τον ανωτέρω ορισμό γίνεται σαφές ότι το σωρευτικό άθροισμα από δεξιά είναι φθίνον, δηλαδή:

$$R_m^{(j)} \leq R_n^{(j)} \quad \text{για κάθε} \quad m > n.$$

Εύρεση συνόρων: $N = 1$ (ένα αντικείμενο)

Για την εύρεση των δύο ακραίων, ή συνοριακών, pixels της j-ιοστής γραμμής του ημιτονόγραμμου

$$\rho_{L_0}^{(j)} \quad \text{και} \quad \rho_{R_0}^{(j)},$$

αντίστοιχα, βρίσκουμε πρωτίστως τους παρακάτω δείκτες:

$$i_{L_0}^{\prime(j)} = \max_{1<n<N_\rho} \ker L_n^{(j)} \quad \text{και} \quad i_{R_0}^{\prime(j)} = \min_{1<n<N_\rho} \ker R_n^{(j)}, \tag{A.28}$$

όπου $\ker \Lambda$ είναι το μηδενικό σύνολο του Λ, με

$$\ker \Lambda = \{\text{όλοι οι δείκτες } i \text{ τέτοιοι ώστε } \Lambda = 0\}, \quad \Lambda \in \left\{L_i^{(j)}, R_i^{(j)}\right\}.$$

Για κάθε γραμμή j, δημιουργούνται δύο «νέφη» δεικτών, και συγκεκριμένα

$$(i_{L_0}^{\prime(j)}, j) \quad \text{και} \quad (i_{R_0}^{\prime(j)}, j).$$

Έπειτα, εφαρμόζουμε πολυωνυμική προσέγγιση βαθμού $n \geq 3$ και λαμβάνουμε δύο καμπύλες δεικτών,

$$i_{L_0}^{\text{fit}} = i_{L_0}^{\text{fit}}(j) \quad \text{και} \quad i_{R_0}^{\text{fit}} = i_{R_0}^{\text{fit}}(j).$$

Επίσης, αν εισάγουμε μία παράμετρο padding p (σε pixels), με $p \in \mathbb{N}$ τότε:

$$i_{L_0}^{(j)} = i_{L_0}^{\text{fit}}(j) - p \quad \text{και} \quad i_{R_0}^{(j)} = i_{R_0}^{\text{fit}}(j) + p, \quad p = 0, 1, \ldots, \left\lfloor \frac{N_\rho}{2} \right\rfloor. \tag{A.29}$$

Με αυτό τον τρόπο, δημιουργούνται δύο καμπύλες, και συγκεκριμένα οι

$$\rho_{L_0} = \rho_{L_0}(\theta_j) \quad \text{και} \quad \rho_{R_0} = \rho_{R_0}(\theta_j),$$

οι οποίες αντιστοιχούν στους δείκτες

$$i_{L_0} = i_{L_0}(j) \quad \text{και} \quad i_{R_0} = i_{R_0}(j),$$

αντίστοιχα. Οι καμπύλες αυτές αποτελούν τα εξωτερικά σύνορα του ημιτονογράμμου. Αν το ημιτονόγραμμο αποτελείται από μία συμπαγή μη μηδενική περιοχή, τότε η προς ανακατασκευή εικόνα αναπαριστά ένα αντικείμενο με κλειστό σύνορο.

Εύρεση συνόρων: $N > 1$ (πολλά αντικείμενα)

Αν η εικόνα αναπαριστά N ξεχωριστά αντικείμενα με σύνορα κλειστές καμπύλες, τότε το ημιτονόγραμμο αποτελείται από πολλές, «σχεδόν μηδενικές» περιοχές. Σε αυτή την περίπτωση, πρέπει να ταξινομήσουμε κάθε γραμμή j σύμφωνα με τον αριθμό των κορυφών της: αν για μια σταθερή γραμμή j^* (και επομένως σταθερή γωνία θ_{j^*}) ο αριθμός των κορυφών είναι $N_{j^*} = 2$, τότε η συνάρτηση

$$g(\rho_i) = \widehat{f}_{ij^*} = \widehat{f}(\rho_i, \theta_{j^*})$$

διαθέτει δύο κορυφές στη μεταβλητή ρ_i. Ο αριθμός των διακριτών αντικειμένων στην εικόνα ακολουθεί τον αντίστοιχο αριθμό των κορυφών, σε κάθε γραμμή, υπό την έννοια

$$N = \max_{1 \le j \le N_\theta} N_j. \tag{A.30}$$

Όταν πρόκειται για πολυκόρυφα ημιτονόγραμμα αναζητούμε «σχεδόν μηδενικά» υποδιαστήματα εντός του ακόλουθου διαστήματος δεικτών

$$I_0^{(j)} = [i_{L_0}^{(j)}, i_{R_0}^{(j)}], \tag{A.31}$$

και πάλι μέσω σωρευμένων αθροισμάτων, για κάθε γωνία θ. Επομένως, προσπαθούμε να βρούμε αριστερά και δεξιά «εσωτερικά» συνοριακά pixels

$$i_{L_k}^{(j)} \quad \text{και} \quad i_{R_k}^{(j)}, \quad \text{για} \quad k = 1, \dots N_j - 1,$$

έξω από τα οποία η τιμή της συνάρτησης $\widehat{f}$ μηδενίζεται. Σημειώνουμε ότι η

οριακή τιμή $k = 0$ αναπαριστά την περίπτωση $N = 1$, όπως περιγράψαμε στην προηγούμενη ενότητα. Για απλούστευση, υιοθετούμε τον συμβολισμό

$$I_k^{(j)} = [i_{L_{k-1}}^{(j)}, i_{R_{N_j-k}}^{(j)}], \quad k = 1, \ldots, N_j, \quad N_j > 1. \tag{A.32}$$

Κατά τη διαδικασία εύρεσης των συνόρων πολλαπλών αντικειμένων, ανακύπτει μία εγγενής δυσκολία: ο αριθμός των διακριτών αντικειμένων (N) δεν είναι a priori γνωστός. Για να αντιμετωπίσουμε τη δυσκολία αυτή, διανέμουμε M τον αριθμό «αντιπροσώπους» CUSUM (A_m) εντός του διαστήματος $I_0^{(j)}$. Είναι σημαντικό να σημειώσουμε ότι ο σριθμός M είναι ένας προκαθορισμένος, αρκούντως μεγάλος θετικός ακέραιος. Οι προτεινόμενες τιμές για την παράμετρο M απαιτούν τουλάχιστον $M > N_\rho$, π.χ. $M = 1000$. Κάθε αντιπροσώπος είναι υπεύθυνος για τον εντοπισμό απότομων αλλαγών τόσο στα αριστερά, όσο και στα δεξιά. Η αναζήτηση για τον κάθε αντιπρόσωπο ξεκινά από τυχαίο, κάθε φορά, pixel εκκίνησης,

$$s_m \in I_0^{(j)}, \quad m = 1, \ldots, M.$$

Κάθε αντιπρόσωπος εφαρμόζει τον αλγόριθμο CUSUM μέσα στο διάστημα $I_0^{(j)}$. Χρησιμοποιούμε την ίδια ακριβώς μέθοδο, όπως και στο αρχικό διάστημα, μόνο που αυτή τη φορά εντάσσουμε στη θεώρησή μας ένα στοιχείο τυχαιότητας, διότι δεν γνωρίζουμε εκ των προτέρων αν ο εκάστοτε αντιπρόσωπος θα βρει ένα νέο υποδιάστημα. Δηλαδή, δεν γνωρίζουμε αν $N \geq 2$.

Ομοίως, ορίζουμε για κάθε γραμμή j τα σωρευτικά αθροίσματα $L_n^{(j)}(A_m)$, για την αριστερή πλευρά, και $R_n^{(j)}(A_m)$, για τη δεξιά πλευρά, αντίστοιχα:

$$L_{\rho_{L_0}}^{(j)}(A_m) = 0, \tag{A.33a}$$

$$L_n^{(j)}(A_m) = \max\left\{0, L_{n-1}^{(j)}(A_m) + \widehat{f}_{n,j} - \left(\mu_L^{(j)} + \lambda\sigma_L^{(j)}\right)\right\}, \tag{A.33b}$$

και

$$R_{N_\rho}^{(j)}(A_m) = 0, \tag{A.34a}$$

$$R_{n-1}^{(j)}(A_m) = \max\left\{0, R_n^{(j)}(A_m) + \widehat{f}_{n-1,j} - \left(\mu_R^{(j)} + \lambda\sigma_R^{(j)}\right)\right\}, \tag{A.34b}$$

όπου οι παρενθέσεις υποδηλώνουν την εξάρτηση του σωρευμένου αθροίσματος από τον m-ιοστό αντιπρόσωπο, ο οποίος ξεκίνησε την αναζήτηση εσωτερικών συνόρων από το s_m, $m = 1, \ldots, M$, ενώ οι ποσότητες $\mu_L^{(j)}$ και $\sigma_L^{(j)}$ δίνονται από

την εξίσωση (A.25), οι ποσότητες $\mu_R^{(j)}$ και $\sigma_R^{(j)}$ δίνονται από την εξίσωση (A.27), και το λ περιγράφεται παραπάνω. Επομένως, για να βρούμε το $i_{L_1}^{(j)}$, εφόσον υπάρχει (δηλαδή $N_j > 1$), λαμβάνουμε το ελάχιστο μεταξύ των αντιπροσώπων:

$$i_{L_1}^{(j)} = \min_{1\le m\le M} \left\{ \max_{1<n<N_\rho} \ker L_n^{(j)}(A_m) \right\} - p. \tag{A.35a}$$

Αντίστοιχα, για να βρούμε το $i_{R_1}^{(j)}$, εφόσον υπάρχει, λαμβάνουμε το μέγιστο μεταξύ των αντιπροσώπων:

$$i_{R_1}^{(j)} = \max_{1\le m\le M} \left\{ \min_{1<n<N_\rho} \ker R_n^{(j)}(A_m) \right\} + p, \tag{A.35b}$$

Ακολουθούμε την ίδια διαδικασία αναδρομικά, για να βρούμε τους δείκτες

$$i_{L_2}^{(j)} \quad \text{και} \quad i_{R_2}^{(j)} \quad \text{μέχρι} \quad i_{L_{N_j-1}}^{(j)} \quad \text{και} \quad i_{R_{N_j-1}}^{(j)}, \quad \text{για κάθε} \quad N_j > 1,$$

όπου αυτοί υπάρχουν. Σημειώνουμε ότι αν για κάποιο

$$k^* \le N_j - 1,$$

το συνοριακό pixel $i_{L_{k^*}}^{(j)}$ (ή αντίστοιχα το $i_{R_{k^*}}^{(j)}$) δεν υπάρχει, τότε εξ΄ ορισμού αναθέτουμε σε αυτόν το δείκτη την τιμή 0, δηλαδή αν

$$\text{το } k^* \text{ είναι τέτοιο ώστε } \nexists \; i_{L_{k^*}}^{(j)} \text{ ή } \nexists \quad i_{R_{k^*}}^{(j)},$$

τότε

$$i_{L_k}^{(j)} = 0 \quad \text{ή} \quad i_{R_k}^{(j)} = 0, \quad \forall \quad k > k^*. \tag{A.35c}$$

Χρησιμοποιώντας τον παραπάνω ορισμό, μπορούμε να ποσοτικοποιήσουμε την αδυναμία περαιτέρω ταξινόμησης των υποδιαστημάτων $I_k^{(j)}$, χωρίς την πρότερη γνώση του N_j.

Μάσκα Radon (ρ, θ)-δεδομένων: Μονοκόρυφα ημιτονόγραμμα

Η επικάλυψη του ημιτονογράμμου (sinogram masking) στην περίπτωση $N = 1$ επιτυγχάνεται, για κάθε γραμμή j, θέτοντας την μάσκα ίση με 1 εντός του $I_0^{(j)}$ και 0 οπουδήποτε αλλού. Η μάσκα του ημιτονογράμμου, $\mathbf{M}_S^1$, είναι ένας πίνακας ο οποίος περιέχει στοιχεία ίσα με 0 ή 1, ως εξής:

$$\mathbf{M}_S^1(\rho_i, \theta_j) = \begin{cases} 1, & \text{αν } i \in I_0^{(j)} \\ 0, & \text{αλλού} \end{cases}, \quad \text{για} \quad N = 1. \tag{A.36}$$

Μάσκα Radon (ρ, θ)-δεδομένων: Πολυκόρυφα ημιτονόγραμμα

Η δημιουργία της μάσκας του ημιτονογράμμου στην περίπτωση $N > 1$ είναι σαφώς δυσκολότερη. Επιτυγχάνεται, για κάθε γραμμή j, θέτοντας την τιμή της μάσκας ίση με 1 εντός των διαστημάτων $I_k^{(j)}$, $k = 1, \ldots, N$ και ίση με 0 οπουδήποτε αλλού. Η μάσκα του ημιτονογράμμου, $\mathbf{M}_S^N$, είναι ένας πίνακας ο οποίος περιέχει στοιχεία ίσα με 0 ή 1, και αποτελεί διαφοροποίηση της εξίσωσης (A.36) ως εξής:

$$\mathbf{M}_S^N(\rho_i, \theta_j) = \begin{cases} 1, & \text{αν } i \in \bigcup_{k=1}^{N} I_k^{(j)} \\ 0, & \text{αλλού} \end{cases}, \quad \text{για} \quad N > 1, \tag{A.37}$$

όπου τα N και $I_k^{(j)}$ δίνονται από τις εξισώσεις (A.30) και (A.32), αντίστοιχα. Σημειώνουμε ότι οι εξισώσεις (A.36) και (A.37) παρέχουν τις απαραίτητες πληροφορίες για τη δημιουργία της μάσκας του ημιτονόγραμμου για κάθε περίπτωση, χωρίς να απαιτείται ο πρότερος προσδιορισμός της τιμής του N.

Μάσκα ανακατασκεασμένης εικόνας

Η μάσκα της εικόνας, $\mathbf{M}_I$, κατασκευάζεται λαμβάνοντας υπόψη ότι ένα pixel το οποίο είναι εκτός συνόρου και συνεπώς έχει μηδενική τιμή, μπορεί να εξαιρεθεί από το ημιτονόγραμμο, αφού πρώτα εξακριβωθούν οι θέσεις των ανιχνευτών $\rho_k = \rho_k(\theta_l)$ για όλες τις γωνίες θ_l που λαμβάνουν συνεισφορά από το συγκεκριμένο pixel. Τότε, για κάθε (x_1, x_2), αν υπάρχει έστω και ένα θ_k, τέτοιο ώστε $\widehat{f}(\rho_k, \theta_l) = 0$, προκύπτει ότι η συναρτησή $f(x_1, x_2)$ να ισούται με 0. Η συνθήκη αυτή απορρέει από τη φύση του μετασχηματισμού Radon, ο οποίος είναι ένα άθροισμα μη αρνητικών όρων, και επομένως ισούται με μηδέν μόνο όταν όλοι οι όροι είναι μηδενικοί. Έπειτα, ανακατασκευάζουμε τη μάσκα του ημιτονογράμμου για να λάβουμε την μάσκα της εικόνας.

Σε αυτή την κατεύθυνση, συμβολίζουμε με Q_{x_1} και Q_{x_2} τον αριθμό των γραμμών (x_1 διεύθυνση) και των στηλών (x_2 διεύθυνση) της ανακατασκευασμένης εικόνας. Η συνήθης πρακτική στις ιατρικές απεικονίσεις υπαγορεύει τετραγωνικές εικόνες, δηλαδή $Q_{x_1} = Q_{x_2} = Q$, επομένως η μάσκα της εικόνας ($\mathbf{M}_I = \mathbf{M}_I(x_{1_i}, x_{2_j})$, με $i = 1, \ldots, Q$) είναι ένας τετραγωνικός πίνακας $Q \times Q$. Για κάθε $(x_{1_i}, x_{2_j})_{i,j=1}^{Q}$ βρίσκουμε τα $\rho = \rho(\theta_l)$ για όλες τις τιμές $(\theta_l)_{l=1}^{N_\theta}$.

Στη γενική περίπτωση, το υπολογισμένο ρ δεν συμπίπτει κατ΄ ανάγκη με την διαμέριση $\{\rho_k\}_{k=1}^{N_\rho}$ του ημιτονογράμμου $\widehat{f}_{kl}$. Επομένως, πρέπει να βρούμε

τον πλησιέστερο δείκτη k (και συνεπώς τη θέση ρ_k), δεδομένου ότι το ρ θα βρίσκεται πάντα σε ένα διάστημα της μορφής $[\rho_k, \rho_{k+1}]$ για κάποιο k. Με αυτό τον τρόπο, η υπολογισμένη καμπύλη $\rho = \rho(\theta)$ μετατρέπεται στην $\rho_k = \rho_k(\theta_l)$, ως αποτέλεσμα της μετατόπισής της προς τον πλησιέστερο δείκτη, για όλες τις γωνίες θ_l. Η τιμή της μάσκας του ημιτονογράμμου υπολογίζεται επί της καμπύλης, δηλαδή $\mathbf{M}_S(\rho_k(\theta_l), \theta_l)$. Αν υπάρχει έστω και μία γωνία $\theta_l = \tilde{\theta}$ τέτοια ώστε $\mathbf{M}_S(\rho_k, \tilde{\theta}) = 0$, τότε η μάσκα της εικόνας θα ισούται με 0, ειδάλλως θα ισούται με 1:

$$\mathbf{M}_I(x_i, y_j) = \begin{cases} 0, & \text{αν } \exists\ \theta_l \text{ τέτοιο ώστε } \mathbf{M}_S(\rho_k(\theta_l), \theta_l) = 0 \\ 1, & \text{αλλού} \end{cases}, \tag{A.38}$$

για $k = 1, \ldots, N_\rho$ και $l = 1, \ldots, N_\theta$.

Μία νέα, αναλυτική μέθοδος αντιστροφής του εξασθενημένου μετασχηματισμού Radon

Στο Κεφάλαιο 4 παρουσιάζουμε την «attenuated spline reconstruction technique» (aSRT). Η μέθοδος aSRT προσδίδει μία καινοτόμο προσέγγιση στον τομέα της ανακατασκευής ιατρικών εικόνων SPECT. Η νέα αυτή τεχνική βασίζεται σε έναν αναλυτικό τύπο που αποδίδει τον αντίστροφο εξασθενημένο μετασχηματισμό Radon. Συγκεκριμένα, περιλαμβάνει τον υπολογισμό των μετασχηματισμών Hilbert της γραμμικής συνάρτησης εξασθένισης και δύο ημιτονοειδών συναρτήσεων του εξασθενημένου ημιτονογράμμου, βλ. εξίσωση (A.9). Οι ανωτέρω υπολογισμοί εκτελούνται με χρήση δεδομένων εξασθένισης από αξονικούς τομογράφους (CT) καθώς και με χρήση τριτοβάθμιων συναρτήσεων spline. Στόχος μας είναι:

(α) να παρουσιάσουμε το μαθηματικό υπόβαθρο της νέας μεθόδου αντιστροφής του εξασθενημένου μετασχηματισμού Radon, ως ευρείας γενίκευσης της μεθόδου των Φωκά, Iserles και Μαρινάκη (2006),

(β) να ανακατασκευάσουμε προσομοιωμένα και κλινικά δεδομένα SPECT χρησιμοποιώντας τη νέα μας μέθοδο, και

(γ) να αξιολογήσουμε την μέθοδο ανακατασκευής aSRT, συγκρίνοντάς την με τις δύο βασικές μεθόδους ανακατασκευής, και συγκεκριμένα την αναλυτική μέθοδο FBP και την επαναληπτική μέθοδο OSEM.

Προς αυτή την κατεύθυνση, πραγματοποιήσαμε μελέτες προσομοίωσης χρησιμοποιώντας ένα ομοίωμα ποιότητας εικόνας (IQ phantom) και μία κατάλληλη συνάρτηση εξασθένισης. Οι ανακατασκευές δημιουργήθηκαν για 45, 90 και 180 γωνίες με 20 πραγματοποιήσεις και εμπεριείχαν θόρυβο κατά Poisson, σε τρία διαφορετικά επίπεδα (noise levels, NL), δηλαδή 100% (NL1), 50% (NL2) και 10% (NL3) των συνολικών κρούσεων, αντίστοιχα. Επίσης, ανακατεσκευάσαμε εξασθενημένα ημιτονόγραμμα SPECT από την μελέτη ενός ομοιώματος Jaszczak, καθώς και από μια κλινική SPECT/CT μελέτη μυοκαρδίου.

Συγκρίναμε τα αποτελέσματα ανακατασκευής aSRT, FBP και OSEM χρησιμοποιώντας μετρικές εικόνας, συμπεριλαμβάνομένης της αντίθεσης (contrast), του bias και της τραχύτητας (image roughness). Τα αποτελέσματα υποδεικνύουν ότι με τη μέθοδο aSRT παράγονται ακριβείς ανακατασκευές για προσομοιωμένα και πραγματικά ομοιώματα, καθώς και για κλινικά δεδομένα.

Συγκεκριμένα, στην περίπτωση της κλινικής μελέτης του μυοκαρδίου, η μέθοδος aSRT παρήγαγε ανακατασκευές εικόνας με υψηλότερη «ψυχρή αντίθεση» (cold contrast) απ΄ ότι οι μέθοδοι FBP και OSEM. Με την ενσωμάτωση της διόρθωσης εξασθένισης, η μέθοδος aSRT παρέχει βελτιωμένη εναλλακτική στην αναλυτική μέθοδο FBP. Αυτό είναι ιδιαίτερα ελπιδοφόρο, ειδικά στην απεικόνιση των λεγόμενων «κρύων» περιοχών, όπως αυτές μελετώνται σε ισχαιμικά επεισόδια του μυοκαρδίου με μερική ή πλήρη απόφραξη των στεφανιαίων αρτηριών.

Ένα θεώρημα για την αντιστροφή του εξασθενημένου μετασχηματισμού Radon

Θεωρούμε μία ευθεία L στο επίπεδο, η οποία χαρακτηρίζεται από τις τοπικές συντεταγμένες, βλ. εξισώσεις (A.3) και (A.4). Ο εξασθενημένος μετασχηματισμός Radon μίας δισδιάστατης Schwartz συνάρτησης f ορίζεται στην εξίσωση (A.9).

Το αντίστροφο πρόβλημα που αναδύεται από την εξίσωση (A.9) λύθηκε το 2006 από τους Φωκά, Iserles και Μαρινάκη. Η λύση δίνεται στην Πρόταση A.9 και συγκεκριμένα στις εξισώσεις (A.18)–(A.21) και περιλαμβάνει προβολικούς τελεστές και μετασχηματισμούς Hilbert.

Θεώρημα A.10. *Η εξίσωση αντιστροφής του εξασθενημένου μετασχηματισμού Radon* (A.18) *είναι ισοδύναμη με την αναπαράσταση*

$$f(x_1,x_2) = -\frac{1}{2\pi}\int_0^{2\pi} e^{M(\tau,\rho,\theta)}\left[M_\rho(\tau,\rho,\theta)G(\rho,\theta)+G_\rho(\rho,\theta)\right]\Big|_{\substack{\rho=x_2\cos\theta-x_1\sin\theta\\ \tau=x_2\sin\theta+x_1\cos\theta}} \mathrm{d}\theta, \tag{A.39}$$

όπου οι δείκτες υποδηλώνουν μερική παραγώγιση ως προς τη μεταβλητή ρ*, η συνάρτηση* M *ορίζεται στην εξίσωση* (A.20) *και η συνάρτηση* G *δίνεται από τον τύπο*

$$G(\rho,\theta) = e^{-\frac{1}{2}\widehat{\mu}(\rho,\theta)}\left[\cos(F(\rho,\theta))G^C(\rho,\theta)+\sin(F(\rho,\theta))G^S(\rho,\theta)\right]. \tag{A.40}$$

Οι συναρτήσεις G^C *και* G^S *ορίζονται ως εξής:*

$$G^C(\rho,\theta) = \frac{1}{2\pi}PV\int_{-\infty}^{\infty} e^{\frac{1}{2}\widehat{\mu}(r,\theta)}\cos F(r,\theta)\frac{\widehat{f}_\mu(r,\theta)\mathrm{d}r}{r-\rho}, \tag{A.41a}$$

$$G^S(\rho,\theta) = \frac{1}{2\pi}PV\int_{-\infty}^{\infty} e^{\frac{1}{2}\widehat{\mu}(r,\theta)}\sin F(r,\theta)\frac{\widehat{f}_\mu(r,\theta)\mathrm{d}r}{r-\rho}, \tag{A.41b}$$

ενώ συνάρτηση F *ως εξής:*

$$F(\rho,\theta) \equiv \frac{1}{2}\mathcal{H}\left\{\widehat{\mu}(\rho,\theta)\right\} = \frac{1}{2\pi}\left(PV\int_{-\infty}^{\infty}\frac{\widehat{\mu}(r,\theta)}{r-\rho}\mathrm{d}r\right), \tag{A.42}$$

όπου με $\mathcal{H}$ *συμβολίσαμε τον μετασχηματισμό Hilbert ως προς τη μεταβλητή* ρ*, όπως στην εξίσωση* (A.14)*. Οι συναρτήσεις* $\widehat{\mu}$ *και* $\widehat{f}_\mu$ *δίνονται στις εξισώσεις* (A.22) *και* (A.9)*, αντίστοιχα.*

Απόδειξη. Εφαρμόζουμε τον τελεστή L_μ, που ορίζεται στην εξίσωση (A.21), στον εξασθενημένο μετασχηματισμό Radon ($\widehat{f}_\mu$), βλ. εξίσωση (A.9), ως ακολούθως:

$$\begin{aligned}\left(L_\mu\widehat{f}_\mu\right)(\rho,\theta) = \Big\{&e^{P^-\widehat{\mu}(\rho,\theta)}P^-e^{P^-\widehat{\mu}(\rho,\theta)}\\ &+ e^{-P^+\widehat{\mu}(\rho,\theta)}P^+e^{P^+\widehat{\mu}(\rho,\theta)}\Big\}\,\widehat{f}_\mu(\rho,\theta).\end{aligned} \tag{A.43}$$

Από τις εξισώσεις (A.23) και (A.42) συνεπάγεται ότι

$$e^{P^\pm\widehat{\mu}} = e^{\pm\frac{\widehat{\mu}}{2}-\mathrm{i}F}. \tag{A.44}$$

Άρα,

$$e^{P^-\widehat{\mu}}P^-\left\{e^{-P^-\widehat{\mu}}\widehat{f}_\mu\right\} = e^{-\frac{\widehat{\mu}}{2}-\mathrm{i}F}\left[-\frac{1}{2}e^{\frac{\widehat{\mu}}{2}+\mathrm{i}F}\widehat{f}_\mu + \frac{1}{2\mathrm{i}}\mathcal{H}\left\{e^{\frac{\widehat{\mu}}{2}+\mathrm{i}F}\widehat{f}_\mu\right\}\right], \quad \text{(A.45a)}$$

και

$$e^{-P^+\widehat{\mu}}P^+\left\{e^{P^+\widehat{\mu}}\widehat{f}_\mu\right\} = e^{-\frac{\widehat{\mu}}{2}+\mathrm{i}F}\left[\frac{1}{2}e^{\frac{\widehat{\mu}}{2}-\mathrm{i}F}\widehat{f}_\mu + \frac{1}{2\mathrm{i}}\mathcal{H}\left\{e^{\frac{\widehat{\mu}}{2}-\mathrm{i}F}\widehat{f}_\mu\right\}\right]. \quad \text{(A.45b)}$$

Η περαιτέρω ανάλυση των εξισώσεων (A.45) μας οδηγεί στην αποκρυπτογράφηση της εξίσωσης (A.43). Συγκεκριμένα, για να απλουστεύσουμε την εξίσωση (A.43), πρωτίστως λαμβάνουμε υπόψη την εξίσωση (A.42), και έπειτα συνδυάζουμε τις εξισώσεις (A.44) και (A.45), ώστε να ξαναγράψουμε τον τελεστή L_μ στη μορφή

$$\left(L_\mu\widehat{f}_\mu\right)(\rho,\theta) = \frac{1}{2\mathrm{i}}e^{-\frac{\widehat{\mu}}{2}}\left[e^{-\mathrm{i}F}\mathcal{H}\left\{e^{\frac{\widehat{\mu}}{2}+\mathrm{i}F}\widehat{f}_\mu\right\} + e^{\mathrm{i}F}\mathcal{H}\left\{e^{\frac{\widehat{\mu}}{2}\mathrm{i}F}\widehat{f}_\mu\right\}\right]. \quad \text{(A.46)}$$

Χρησιμοποιώντας τον τύπο του Euler

$$e^{\iota F} = \cos F + \iota \sin F,$$

μπορούμε να γράψουμε την εξίσωση (A.46) ως εξής:

$$\left(L_\mu\widehat{f}_\mu\right)(\rho,\theta) = \frac{1}{2\mathrm{i}}e^{-\frac{\widehat{\mu}}{2}}\left[(\cos F - \mathrm{i}\sin F)\mathcal{H}\left\{e^{\frac{\widehat{\mu}}{2}+\mathrm{i}F}\widehat{f}_\mu\right\}\right.$$
$$\left.+(\cos F + \mathrm{i}\sin F)\mathcal{H}\left\{e^{\frac{\widehat{\mu}}{2}-\mathrm{i}F}\widehat{f}_\mu\right\}\right]. \quad \text{(A.47a)}$$

Αναπτύσσουμε περαιτέρω την εξίσωση (A.47a) για να λάβουμε

$$\left(L_\mu\widehat{f}_\mu\right)(\rho,\theta) = \frac{1}{2\mathrm{i}}e^{-\frac{\widehat{\mu}}{2}}\left[\cos F\left(\mathcal{H}\left\{e^{\frac{\widehat{\mu}}{2}+\mathrm{i}F}\widehat{f}_\mu\right\} + \mathcal{H}\left\{e^{\frac{\widehat{\mu}}{2}-\mathrm{i}F}\widehat{f}_\mu\right\}\right)\right.$$
$$\left.-\mathrm{i}\sin F\left(\mathcal{H}\left\{e^{\frac{\widehat{\mu}}{2}+\mathrm{i}F}\widehat{f}_\mu\right\} - \mathcal{H}\left\{e^{\frac{\widehat{\mu}}{2}-\mathrm{i}F}\widehat{f}_\mu\right\}\right)\right], \quad \text{(A.47b)}$$

η οποία συνεπάγεται

$$\left(L_\mu\widehat{f}_\mu\right)(\rho,\theta) = \frac{1}{2\pi\mathrm{i}}e^{-\frac{\widehat{\mu}}{2}}\left[\cos F\left(PV\int_{-\infty}^{\infty}\frac{e^{\frac{\widehat{\mu}}{2}+\mathrm{i}F}+e^{\frac{\widehat{\mu}}{2}-\mathrm{i}F}}{r-\rho}\widehat{f}_\mu\mathrm{d}r\right)\right.$$
$$\left.-\mathrm{i}\sin F\left(PV\int_{-\infty}^{\infty}\frac{e^{\frac{\widehat{\mu}}{2}+\mathrm{i}F}-e^{\frac{\widehat{\mu}}{2}-\mathrm{i}F}}{r-\rho}\widehat{f}_\mu\mathrm{d}r\right)\right]. \quad \text{(A.47c)}$$

Με αυτό τον τρόπο ξαναγράφουμε την παραπάνω εξίσωση

$$\left(L_\mu \widehat{f_\mu}\right)(\rho,\theta) = \frac{1}{2\pi \mathrm{i}} e^{-\frac{\widehat{\mu}}{2}} \left[\cos F \left(PV \int_{-\infty}^{\infty} \frac{e^{\frac{\widehat{\mu}}{2}}(e^{\mathrm{i}F} + e^{-\mathrm{i}F})}{r-\rho} \widehat{f_\mu} \mathrm{d}r\right) - \mathrm{i} \sin F \left(PV \int_{-\infty}^{\infty} \frac{e^{\frac{\widehat{\mu}}{2}}(e^{\mathrm{i}F} - e^{-\mathrm{i}F})}{r-\rho} \widehat{f_\mu} \mathrm{d}r\right)\right], \quad \text{(A.47d)}$$

και συνεχίζουμε

$$\left(L_\mu \widehat{f_\mu}\right)(\rho,\theta) = \frac{1}{2\pi \mathrm{i}} e^{-\frac{\widehat{\mu}}{2}} \left[\cos F \left(PV \int_{-\infty}^{\infty} \frac{e^{\frac{\widehat{\mu}}{2}}(2\cos F)}{r-\rho} \widehat{f_\mu} \mathrm{d}r\right) - \mathrm{i} \sin F \left(PV \int_{-\infty}^{\infty} \frac{e^{\frac{\widehat{\mu}}{2}}(2\mathrm{i} \sin F)}{r-\rho} \widehat{f_\mu} \mathrm{d}r\right)\right]. \quad \text{(A.47e)}$$

Το τελευταίο βήμα περιλαμβάνει τον ακόλουθο χειρισμό:

$$\left(L_\mu \widehat{f_\mu}\right)(\rho,\theta) = \frac{2}{\mathrm{i}} e^{-\frac{\widehat{\mu}}{2}} \left[\cos F \left(\frac{1}{2\pi}\left\{PV \int_{-\infty}^{\infty} \frac{e^{\frac{\widehat{\mu}}{2}} \cos F}{r-\rho} \widehat{f_\mu} \mathrm{d}r\right\}\right) + \sin F \left(\frac{1}{2\pi}\left\{PV \int_{-\infty}^{\infty} \frac{e^{\frac{\widehat{\mu}}{2}} \sin F}{r-\rho} \widehat{f_\mu} \mathrm{d}r\right\}\right)\right]. \quad \text{(A.47f)}$$

Αυτό μας οδηγεί στην τελική μορφή της απλούστευσης της εξίσωσης (A.46), ως εξής:

$$\left(L_\mu \widehat{f_\mu}\right)(\rho,\theta) = -2\mathrm{i} e^{-\frac{\widehat{\mu}}{2}} \left[\cos(F) G^C + \sin(F) G^S\right], \quad \text{(A.48)}$$

με τις συναρτήσεις $G^C(\rho,\theta)$ και $G^S(\rho,\theta)$ να ορίζονται στις εξισώσεις (A.41a) και (A.41b), αντίστοιχα. Στην εξίσωση (A.48), αν λάβουμε υπόψη τον ορισμό (A.40) της συνάρτησης $G(\rho,\theta)$, προκύπτει ότι

$$\left(L_\mu \widehat{f_\mu}\right)(\rho,\theta) = -2\mathrm{i} G(\rho,\theta). \quad \text{(A.49)}$$

Επομένως, η εξίσωση (A.43) μετατρέπεται στην εξίσωση (A.49). Σημειώνουμε ότι η εξίσωση (A.49) υποδηλώνει ότι η συνάρτηση

$$\left(L_\mu \widehat{f_\mu}\right)(\rho,\theta)$$

είναι αμιγώς φανταστική, δηλαδή

$$\mathrm{Re}\left\{\left(L_\mu \widehat{f_\mu}\right)(\rho,\theta)\right\} = 0.$$

Επομένως, από τις εξισώσεις (A.19) και (A.49) συνεπάγεται ότι

$$J(x_1,x_2,\theta) = -2\mathrm{i}\left[e^{M(\tau,\rho,\theta)}G(\rho,\theta)\right]_{\substack{\tau=x_2\sin\theta+x_1\cos\theta\\ \rho=x_2\cos\theta-x_1\sin\theta}}. \tag{A.50}$$

Άρα, χρησιμοποιώντας τον διαφορικό τελεστή

$$(\partial_{x_1} - \mathrm{i}\partial_{x_2}) = e^{-\mathrm{i}\theta}(\partial_\tau - \mathrm{i}\partial_\rho), \tag{A.51}$$

ο οποίος προκύπτει από την εφαρμογή του κανόνα της αλυσίδας στις τοπικές συντεταγμένες, βλ. εξισώσεις (A.3), μπορούμε να υπολογίσουμε τη δράση του τελεστή (A.51) στη συνάρτηση J:

$$\begin{aligned}(\partial_{x_1} - \mathrm{i}\partial_{x_2})J &= -2\mathrm{i}e^{-\mathrm{i}\theta}(\partial_\tau - \mathrm{i}\partial_\rho)\left\{e^M G\right\}_{\substack{\rho=x_2\cos\theta-x_1\sin\theta\\ \tau=x_2\sin\theta+x_1\cos\theta}}\\ &= -2\mathrm{i}e^{-i\theta}\left[e^M(M_\tau - \mathrm{i}M_\rho)G + e^M(G_\tau - \mathrm{i}G_\rho)\right]_{\substack{\rho=x_2\cos\theta-x_1\sin\theta\\ \tau=x_2\sin\theta+x_1\cos\theta}}\\ &= -2e^{-\mathrm{i}\theta}e^M\left[-\mathrm{i}\mu G + M_\rho G + G_\rho\right]_{\substack{\rho=x_2\cos\theta-x_1\sin\theta\\ \tau=x_2\sin\theta+x_1\cos\theta}},\end{aligned} \tag{A.52}$$

όπου χρησιμοποιήσαμε τις ιδιότητες

$$M_\tau(\tau,\rho,\theta)\Big|_{\substack{\rho=x_2\cos\theta-x_1\sin\theta\\ \tau=x_2\sin\theta+x_1\cos\theta}} = \mu(x_1,x_2) \quad \text{και} \quad G_\tau(\rho,\theta) = 0.$$

Εισάγουμε τον τελεστή $(\partial_{x_1} - \mathrm{i}\partial_{x_2})$ εντός του ολοκληρώματος στο δεξί μέλος της εξίσωσης (A.18) και συνδυάζουμε την εξίσωση (A.50) με την εξίσωση (A.52), για να λάβουμε

$$f(x_1,x_2) = -\frac{1}{2\pi}\int_0^{2\pi} e^M\left[-\mathrm{i}\mu G + M_\rho G + G_\rho\right]\Bigg|_{\substack{\rho=x_2\cos\theta-x_1\sin\theta\\ \tau=x_2\sin\theta+x_1\cos\theta}} \mathrm{d}\theta. \tag{A.53}$$

Ο πρώτος όρος του ολοκληρώματος στο δεξί μέλος της εξίσωσης (A.53) απλο-

ποιείται ως εξής:

$$-\mathrm{i}\int_0^{2\pi}\mu(x_1,x_2)\left[e^{M(\tau,\rho,\theta)}G(\rho,\theta)\right]_{\substack{\tau=x_2\sin\theta+x_1\cos\theta\\ \rho=x_2\cos\theta-x_1\sin\theta}}\mathrm{d}\theta = \frac{1}{2}\mu(x_1,x_2)\int_0^{2\pi}J(x_1,x_2,\theta)\mathrm{d}\theta. \quad \text{(A.54)}$$

Στην εξίσωση (2.9) του άρθρου των Φωκά, Iserles και Μαρινάκη [8], αντικαθιστούμε τη συνάρτηση μ με τη συνάρτηση u, και υπολογίζουμε την τιμή της για $\lambda = 0$. Επομένως,

$$u(x_1,x_2,0) = \frac{1}{2\pi}\int_0^{2\pi}J(x_1,x_2,\theta)\mathrm{d}\theta.$$

Επιπροσθέτως, το όριο $\lambda \to 0$ της εξίσωσης (2.2) του ίδιου άρθρου υποδηλώνει ότι

$$\frac{\partial u(x_1,x_2,0)}{\partial \bar{z}} = 0,$$

Ως εκ τούτου, η συνάρτηση u είναι αναλυτική παντού, συμπεριλαμβανομένου και του απείρου. Αν επικαλεστούμε την υπόθεση στην Πρόταση 2.1 του εν λόγω άρθρου, συγκεκριμένα ότι η συνάρτηση u ικανοποιεί τη συνοριακή συνθήκη

$$u = O\left(\frac{1}{z}\right), \quad z \to \infty,$$

έπεται από το θεώρημα του Liouville ότι η ακέραια συνάρτηση u θα πρέπει να είναι παντού μηδενική. Κατά συνέπεια

$$\int_0^{2\pi}J(x_1,x_2,\theta)\mathrm{d}\theta = 0. \quad \text{(A.55)}$$

Άρα, λαμβάνοντας υπόψη την εξίσωση (A.55), η εξίσωση (A.54) συνεπάγεται

$$\int_0^{2\pi}\mu(x_1,x_2)\left[e^{M(\tau,\rho,\theta)}G(\rho,\theta)\right]_{\substack{\tau=x_2\sin\theta+x_1\cos\theta\\ \rho=x_2\cos\theta-x_1\sin\theta}}\mathrm{d}\theta = 0.$$

Από τα παραπάνω γίνεται σαφές ότι η εξίσωση (A.53) λαμβάνει τη μορφή

$$f(x_1,x_2) = -\frac{1}{2\pi}\int_0^{2\pi}e^M\left(M_\rho G + G_\rho\right)\Big|_{\substack{\rho=x_2\cos\theta-x_1\sin\theta\\ \tau=x_2\sin\theta+x_1\cos\theta}}\mathrm{d}\theta. \quad \text{(A.56)}$$

Επομένως, η εξίσωση (A.18) μετατρέπεται στην εξίσωση (A.39). ■

Καθάρισμα θολών Radon δεδομένων

Στο Κεφάλαιο 5 παρουσιάζουμε μια νέα τεχνική για το «ξεθόλωμα» (deblurring) ανακατασκευασμένων με τη μέθοδο aSRT εικόνων από δεδομένα τομογράφων SPECT/CT, εφοδιασμένων με κατευθυντήρες παραλλήλων οπών (parallel-hole collimators). Η νέα μας μέθοδος βασίζεται στην ταξινόμηση του κατευθυντήρα με βάση το blurring προφίλ του, και όχι τη συνάρτηση σημειακής απόκρισης αυτού (point-response function, PSF). Με το ξεθόλωμα του αρχικού εξασθενημένου ημιτονόγραμμου, είμαστε σε θέση να ανακατασκευάσουμε λιγότερο θολές και περισσότερο ευκρινείς εικόνες.

Πραγματοποιήσαμε μελέτες προσομοίωσης σε ένα ομοίωμα ποιότητας εικόνας (IQ) με κατάλληλη συνάρτηση γραμμικής εξασθένισης. Οι ανακατασκευές δημιουργήθηκαν για 180 γωνίες. Μελετήσαμε 20 πραγματοποιήσεις οι οποίες εμπεριείχαν θόρυβο κατά Poisson, σε επίπεδο 50% των συνολικών κρούσεων. Για την προσομοίωση του ομοιώματος IQ, χρησιμοποιήσαμε έναν τυπικό κατευθυντήρα χαμηλής ενέργειας και υψηλής ανάλυσης (LEHR). Στη συνέχεια θολώσαμε τα Radon δεδομένα του εξασθενημένου ημιτονογράμμου χρησιμοποιώντας ένα Gaussian προφίλ με τυπική απόκλιση $\sigma = 0.019$. Πραγματοποιήσαμε συγκρίσεις μεταξύ των θολών και των «καθαρισμένων» ανακατασκευών, χρησιμοποιώντας δύο μετρικές: α) την τοπική μετρική της «θερμής αντίθεσης» (hot contrast), και β) την ολιστική μετρική «no-reference perceptual blur metric». Τα προκαταρκτικά μας αποτελέσματα υποδεικνύουν ότι ο αλγόριθμός μας είναι ικανός να αντισταθμίσει αποτελεσματικά το φαινόμενο θολώματος των Radon δεδομένων λόγω κατευθυντήρα, ειδικά στο πλαίσιο των εικόνων SPECT που ανακατασκευάστηκαν με τη μέθοδο aSRT. Οι μετρικές που επιστρατεύσαμε καθιστούν τον αλγόριθμό μας χρήσιμο στην κλινική απεικόνιση SPECT καθώς και στη βιοϊατρική επεξεργασία εικόνας. Επομένως, η προτεινόμενη τεχνική αντιστάθμισης του θολώματος των κατευθυντήρων με παράλληλες οπές, δύναται να βελτιώσει την ποιότητα εικόνας σε ανακατασκευές εξασθενημένων Radon δεδομένων από τομογράφους SPECT/CT.

Αριθμητική υλοποίηση με τριτοβάθμιες splines

Στόχος μας είναι να λύσουμε την εξίσωση

$$g_\mu(\rho,\theta) = \int_{-\frac{\pi}{2}}^{\frac{\pi}{2}} w(\delta)\ \widetilde{g}_\mu(r\delta+\rho,\theta+\delta)\ \mathrm{d}\delta, \tag{A.57}$$

για τα «ιδανικά» δεδομένα $\widetilde{g}_\mu$ συναρτήσει των «θολωμένων» δεδομένων g_μ, δεδομένης της συνάρτησης βάρους w και της ακτίνας περιστροφής r. Για την αριθμητική υλοποίηση, επιστρατεύουμε τριτοβάθμιες συναρτήσεις spline. Σε κάθε υποδιάστημα $[\rho_i, \rho_{i+1}]$ για όλα τα $i = 1, \ldots, n-1$, αναπτύσσουμε τις $g_\mu(\rho, \theta)$ και $\widetilde{g}_\mu(\rho, \theta)$ ως κυβικές splines στη μεταβλητή ρ, τις οποίες συμβολίζουμε με $S_i^{(3)}(\rho, \theta)$ και $\widetilde{S}_i^{(3)}(\rho, \theta)$, αντίστοιχα. Επομένως,

$$g_\mu(\rho, \theta) = S_i^{(3)}(\rho, \theta) = \sum_{j=0}^{3} c_i^{(j)}(\theta)\rho^j, \tag{A.58a}$$

και

$$\widetilde{g}_\mu(\rho, \theta) = \widetilde{S}_i^{(3)}(\rho, \theta) = \sum_{j=0}^{3} \widetilde{c}_i^{\,(j)}(\theta)\rho^j. \tag{A.58b}$$

Λαμβάνουμε υπόψη ότι η συνάρτηση $g_\mu(\rho, \theta)$, $-1 \leq \rho \leq 1$, $0 \leq \theta \leq 2\pi$, δίνεται για κάθε γωνία θ στα n σημεία $\{\rho_i\}_1^n$. Συμβολίζουμε την τιμή της g_μ στα ρ_i με g_i, ως εξής:

$$g_i := g_i(\theta) = g_\mu(\rho_i, \theta), \quad \rho_i \in [-1, 1], \quad \theta \in [0, 2\pi). \tag{A.59}$$

Η κυβική spline $S_i^{(3)}(\rho, \theta)$ που ορίζεται στην εξίσωση (A.58a) παρεμβάλλει τη συνάρτηση $g_\mu(\rho, \theta)$ στους κόμβους $\{\rho_i\}_{i=1}^n$ υπό την έννοια

$$S_i^{(3)}(\rho_i, \theta) = g_i, \quad i = 1, \ldots, n-1. \tag{A.60}$$

Επιπροσθέτως, υποθέτουμε ότι η συνάρτηση $g_\mu(\rho, \theta)$ και η μερική παράγωγός της ως προς ρ μηδενίζονται στα άκρα $\rho_1 = -1$ και $\rho_n = 1$:

$$g_\mu(-1, \theta) = g_\mu(1, \theta) = 0, \quad 0 \leq \theta < 2\pi, \tag{A.61a}$$

$$\frac{\partial g_\mu}{\partial \rho}(-1, \theta) = \frac{\partial g_\mu}{\partial \rho}(1, \theta) = 0, \quad 0 \leq \theta < 2\pi. \tag{A.61b}$$

Οι σταθερές $\{c_i^{(j)}\}_1^n$ του αναπτύγματος spline (A.58a) του εξασθενημένου ημιτονογράμμου $g_\mu(\rho, \theta)$ μπορούν να υπολογισθούν με βάση την spline δομή που παρουσιάζεται εκτενώς στην Ενότητας 4.3.2 της παρούσας διατριβής. Συγκεκριμένα, οι σταθερές αυτές δίνονται από τις ακόλουθες εξισώσεις:

$$c_i^{(0)}(\theta) = \frac{\rho_{i+1} g_i - \rho_i g_{i+1}}{\Delta_i} + \frac{g_i''}{6}\left(-\rho_{i+1}\Delta_i + \frac{\rho_{i+1}^3}{\Delta_i}\right) + \frac{g_{i+1}''}{6}\left(\rho_i \Delta_i - \frac{\rho_i^3}{\Delta_i}\right), \tag{A.62a}$$

$$c_i^{(1)}(\theta) = \frac{g_{i+1} - g_i}{\Delta_i} - \frac{g_i''}{6}\left(-\Delta_i + \frac{3\rho_{i+1}^2}{\Delta_i}\right) + \frac{g_{i+1}''}{6}\left(-\Delta_i + \frac{3\rho_i^2}{\Delta_i}\right), \quad \text{(A.62b)}$$

$$c_i^{(2)}(\theta) = \frac{1}{2\Delta_i}(\rho_{i+1} g_i'' - \rho_i g_{i+1}''), \quad \text{(A.62c)}$$

$$c_i^{(3)}(\theta) = \frac{g_{i+1}'' - g_i''}{6\Delta_i}, \quad \text{(A.62d)}$$

και

$$\Delta_i = \rho_{i+1} - \rho_i, \quad \text{(A.62e)}$$

όπου ο συμβολισμός g_i'' υποδηλώνει τη δεύτερη μερική παράγωγο της παρεμβάλλουσας συνάρτησης spline[1] $S_i^{(3)}(\rho, \theta)$ ως προς τη μεταβλητή ρ, υπολογισμένη στις θέσεις ρ_i, δηλαδή για κάθε $i = 1, \ldots, n$

$$g_i'' = \left.\frac{\partial^2 S_i^{(3)}(\rho, \theta)}{\partial \rho^2}\right|_{\rho=\rho_i} = S_i^{(1)}(\rho_i, \theta) = 2c_i^{(2)}(\theta) + 6c_i^{(3)}(\theta)\rho_i. \quad \text{(A.63)}$$

Οι εξισώσεις (A.62) περιλαμβάνουν τις γνωστές συναρτήσεις $\{g_i\}_1^n$ καθώς και τις άγνωστες συναρτήσεις $\{g_i''\}_1^n$. Συμβολίζουμε την πρώτη παράγωγο της συνάρτησης spline $S_i^{(3)}$ με $S_i^{(2)}$, όπου ο εκθέτης 2 υποδηλώνει ότι η συνάρτηση $S_i^{(2)}$ είναι δευτεροβάθμια, και την υπολογίζουμε όπως στην εξίσωση (A.63):

$$S_i^{(2)}(\rho, \theta) = \frac{\partial S_i^{(3)}(\rho, \theta)}{\partial \rho} = c_i^{(1)}(\theta) + 2c_i^{(2)}(\theta)\rho + 3c_i^{(3)}(\theta)\rho^2. \quad \text{(A.64)}$$

Για τον υπολογισμό των συναρτήσεων $\{g_i''\}_1^n$ ακολουθούμε τη μέθοδο του άρθρου [56]: επιλύουμε το σύστημα των ακόλουθων n εξισώσεων, δεδομένης της συνέχειας πρώτης (κατά ρ), παραγώγου της κυβικής spline:

$$S_i^{(2)}(\rho_{i+1}, \theta) = S_{i+1}^{(2)}(\rho_{i+1}, \theta), \quad \text{(A.65a)}$$

$$S_1^{(2)}(\rho_1, \theta) = S_{n-1}^{(2)}(\rho_n, \theta) = 0, \quad \text{(A.65b)}$$

για κάθε $i = 1, \ldots, n-2$ και $\theta \in [0, 2\pi)$. Η απαίτηση συνέχειας της spline, συγκεκριμένα ότι $S_i^{(3)}(\rho_{i+1}, \theta) = S_{i+1}^{(3)}(\rho_{i+1}, \theta)$ για $i = 1, \ldots, n-2$ και $S_1^{(3)}(\rho_1, \theta) = S_{n-1}^{(3)}(\rho_n, \theta) = 0$ (βλ. εξισώσεις (A.61)), ουσιαστικά υποδηλώνει ότι οι κόμβοι

[1] Η δεύτερη μερική παράγωγος της τριτοβάθμιας συνάρτησης spline $S_i^{(3)}(\rho, \theta)$ ως προς τη μεταβλητή ρ συμβολίζεται με $S_i^{(1)}(\rho, \theta)$, δεδομένου ότι είναι μία πρωτοβάθμια spline ως προς την ίδια μεταβλητή.

$\{\rho_i\}_1^n$ αποτελούν αιρόμενες λογαριθμικές ανωμαλίες (removable logarithmic singularities).

Για την αντιστροφή του ολοκληρώματος της εξίσωσης (A.57), χρησιμοποιούμε τις εξισώσεις (A.58)

$$\sum_{j=0}^{3} c_i^{(j)}(\theta)\rho^j = \int_{-\Delta}^{\Delta} w(\delta) \left(\sum_{j=0}^{3} \widetilde{c}_i^{\,(j)}(\theta)(r\delta+\rho)^j \right) \mathrm{d}\delta. \tag{A.66}$$

Αφού συμβολίσουμε το ολοκλήρωμα στο δεξί μέλος της εξίσωσης (A.66) με I, αναπτύσσουμε

$$\begin{aligned} I = \left(\sum_{j=0}^{3} \widetilde{c}_i^{\,(j)}(\theta)\rho^j \right) I_0 + \left[\widetilde{c}_i^{\,(1)}(\theta) + 2\widetilde{c}_i^{\,(2)}(\theta)\rho + 3\widetilde{c}_i^{\,(3)}(\theta)\rho^2 \right] r I_1 \\ + \left[\widetilde{c}_i^{\,(2)}(\theta) + 3\widetilde{c}_i^{\,(3)}(\theta)\rho \right] r^2 I_2 + \widetilde{c}_i^{\,(3)}(\theta) r^3 I_3, \end{aligned} \tag{A.67}$$

όπου

$$I_j = \int_{-\Delta}^{\Delta} w(\delta)\delta^j \delta\delta \quad j = 0, 1, 2, 3. \tag{A.68}$$

Για κάθε $j = 0, 1, 2, 3$, το ολοκλήρωμα I_j αναπαριστά την j-ιοστή ροπή της συνάρτησης βάρους w του κατευθυντήρα. Δεδομένου ότι η συνάρτηση w είναι κανονικοποιημένη, δηλαδή

$$\int_{-\infty}^{\infty} w(\delta)\mathrm{d}\delta = \int_{-\frac{\pi}{2}}^{\frac{\pi}{2}} w(\delta)\mathrm{d}\delta = 1, \tag{A.69}$$

η εξίσωση (A.68) συνεπάγεται

$$I_0 = 1, \quad I_1 = 0, \quad I_2 = \beta, \quad \text{ανδ} \quad I_3 = 0, \tag{A.70}$$

όπου η παράμετρος β συμβολίζει την απόκλιση της συνάρτησης w. Συγκεκριμένα, στην περίπτωση τριγωνικής συνάρτησης βάρους, όπου

$$w(\delta) = \begin{cases} \dfrac{1}{\Delta^2}\left(\delta + \Delta\right), & \delta \in [-\Delta, 0], \\ \dfrac{1}{\Delta^2}\left(\Delta - \delta\right), & \delta \in (0, \Delta], \\ 0, & \text{αλλού}, \end{cases} \tag{A.71}$$

η απόκλιση είναι

$$\beta = \frac{\Delta^2}{6},$$

ενώ στην περίπτωση Gaussian συνάρτησης βάρους, όπου

$$w(\delta) = \frac{1}{\sqrt{2\pi}\sigma} e^{-\frac{\delta^2}{2\sigma^2}}, \quad \sigma = \sigma(\Delta). \tag{A.72}$$

η απόκλιση είναι

$$\beta = \sigma^2.$$

Στην εξίσωση (A.67), εισάγουμε τις υπολογισμένες στις εξισώσεις (A.70) παραμέτρους και διαπιστώνουμε ότι η εξίσωση (A.66) μπορεί να γραφεί στην ακόλουθη μορφή:

$$\begin{aligned} c_i^{(0)}(\theta) + c_i^{(1)}(\theta)\rho + c_i^{(2)}(\theta)\rho^2 + c_i^{(0)}(\theta)\rho^3 = &\left[\widetilde{c}_i{}^{(0)}(\theta) + r^2\beta\widetilde{c}_i^{(2)}(\theta)\right] \\ &+ \left[\widetilde{c}_i^{(1)}(\theta) + 3r^2\beta\widetilde{c}_i^{(3)}(\theta)\right]\rho + \widetilde{c}_i^{(2)}(\theta)\rho^2 + \widetilde{c}_i^{(3)}(\theta)\rho^3. \end{aligned} \tag{A.73}$$

Επομένως,

$$\widetilde{c}_i{}^{(0)}(\theta) = c_i^{(0)}(\theta) + r^2\beta c_i^{(2)}(\theta), \tag{A.74a}$$

$$\widetilde{c}_i{}^{(1)}(\theta) = c_i^{(1)}(\theta) + 3r^2\beta c_i^{(3)}(\theta), \tag{A.74b}$$

$$\widetilde{c}_i{}^{(2)}(\theta) = c_i^{(2)}(\theta), \tag{A.74c}$$

$$\widetilde{c}_i{}^{(3)}(\theta) = c_i^{(3)}(\theta). \tag{A.74d}$$

Οι παραπάνω σταθερές αντιστοιχούν στη ζητούμενη κυβική spline, δηλαδή

$$\widetilde{S}_i^{(3)}(\rho,\theta) = \sum_{j=0}^{3} \widetilde{c}_i{}^{(j)}(\theta)\rho^j, \quad \rho_i \in [-1,1], \quad \theta \in [0,2\pi). \tag{A.75}$$

Introduction

The celebrated Radon transform [1, 2] of a two-dimensional function is defined as the set of all its line integrals [3]. There exists a certain generalization of the Radon transform, the so-called *attenuated Radon transform*, defined as the set of all line integrals of a two-dimensional function attenuated with respect to an attenuation function. The non-attenuated and attenuated versions of the Radon transform provide the mathematical foundation of two of the most important medical imaging techniques, referred to as positron emission tomography (PET) [4], and single-photon emission computed tomography (SPECT) [5], respectively.

The non-attenuated Radon transform gives rise to an associated inverse problem, namely to "reconstruct" a function from its line integrals. The main task in PET imaging is the numerical implementation of the inversion of the non-attenuated Radon transform. Similarly, in the case of the attenuated Radon transform, the corresponding inverse problem is to reconstruct a function from its attenuated line integrals. The main task in SPECT imaging is the inversion of the attenuated Radon transform.

In [6], Novikov and Fokas rederived the well-known inversion of the Radon transform by performing the so-called *spectral analysis* of the following eigenvalue equation:

$$\left[\frac{1}{2}\left(k+\frac{1}{k}\right)\partial_{x_1}+\frac{1}{2\mathrm{i}}\left(k-\frac{1}{k}\right)\partial_{x_2}\right]u=f,\quad k\in\mathbb{C},\tag{I.1}$$

where subscripts denote partial differentiation with respect to x_1 and x_2, respectively. This analysis encompasses two certain problems in modern complex analysis known as the $\bar{d}$-problem and the scalar Riemann-Hilbert (RH) problem, respectively.

Although the inversion of the Radon transform can be obtained in a less complicated manner, namely by employing the two-dimensional Fourier

transform, the advantage of the derivation of [6] was established eleven years later (2002) by Novikov [7]: Novikov demonstrated that the inverse attenuated Radon transform can be derived by applying an analysis similar to that performed in the eigenvalue equation (I.1). In this direction, he performed the spectral analysis of a slight generalization of equation (I.1), namely of the eigenvalue equation

$$\left[\frac{1}{2}\left(k+\frac{1}{k}\right)\partial_{x_1}+\frac{1}{2\mathrm{i}}\left(k-\frac{1}{k}\right)\partial_{x_2}-\mu\right]u=f,\quad k\in\mathbb{C}. \tag{I.2}$$

Four years later, in 2006, by employing the results of the analysis of equations (I.1) and (I.2), Fokas, Iserles and Marinakis derived the inverse attenuated Radon transform in a more straightforward manner [8]. Details of this derivation are presented in [9] and in Section 2.2 of this manuscript. One of the main results of the present thesis is the formulation of an equivalent inversion for the attenuated Radon transform, following the pioneering work of Novikov and Fokas. A new analytic inversion formula is presented in detail, as well as the corresponding image reconstruction algorithm.

In the present thesis, we solve three different mathematical problems, namely:

1. the problem of detection of edges and boundaries in the Radon (ρ,θ)-space and the subsequent reconstruction of the cleared data, which we solved via CUSUM statistics; this is presented in Chapter 3.
2. The problem of the inversion of the attenuated Radon transform via a new analytic formula, see theorem 4.1, and the corresponding numerical implementation (aSRT); this is presented in Chapter 4.
3. The problem of deblurring in the attenuated Radon (ρ,θ)-space and the subsequent reconstruction of the deblurred data, which we solved via spline interpolation; this is demonstrated in Chapter 5.

The mathematical problems described above are quite different from one another, however they bear several intrinsic similarities. They are all key elements of a large class of mathematical problems, associated with the mathematical foundations of emission tomography. The inversion of the Radon transform and of its attenuated generalization are problems playing a fundamental role in the mathematical formulation of medical image reconstruction. They form the fundamental mathematical setting of PET and SPECT tomography.

Figure I.1: Portrait of Johann Radon (undated photograph from the Austrian Academy of Sciences).

I.1 Historical remarks

Johann Radon

Johann Karl August Radon (1887-1956), depicted in figure I.1, was a distinguished Austrian mathematician. In 1917 he wrote a seminal article [1] entitled "Über die Bestimmung von Funktionen durch ihre Integralwerte längs gewisser Mannigfaltigkeiten"[2] for the *Berichte der Sächsischen Akademie der Wissenschaft zu Leipzig*[3]. In this article, Radon introduced an integral transform pair that was meant to give birth to the fields of computed tomography and mathematical image reconstruction. This transform would later be referred to as the *Radon transform*. Radon followed Hendrik Antoon

[2]"On the determination of functions from their integral values along certain manifolds", translated in English by P.C. Parks in 1986 [2].

[3]Reports of the Saxon Academy of Sciences and Humanities of Leipzig.

Lorentz's[4] unpublished work in 1905, where the initial Radon problem was described, and a three-dimensional function was recovered from its integrals over corresponding planes [11]. The inversion of the integral transform in three dimensions was introduced by Hermann Bockwinkel in [12], through his work on the propagation of light in biaxial crystals. In this work, Bockwinkel mentions the inversion equation as Lorentz's [13]. The Radon transform formulation provides the mathematical framework for a large number of inverse problems, not only in mathematics and medical imaging, but in physics, geology and certain other areas [14]. Nowadays, it is globally acknowledged that Radon pioneered the reconstruction of images from projections. In 2003, in order to honor his contributions to science, the Austrian Academy of Sciences named the "Institute for Computational and Applied Mathematics" after Johann Radon. Today, more than 100 years after his pioneering publication, Radon's work is still highly influential in the research community worldwide.

CT: Cormack and Hounsfield

Allan MacLeod Cormack (1924–1998) was a renowned South African physicist. Along with Godfrey Hounsfield, Cormack was awarded the Nobel Prize in Physiology or Medicine in 1979 for his work on X-ray computed tomography. Cormack's mathematical work [15, 16] extended Radon's ideas and essentially gave rise to computed tomography (CT). According to the Royal Swedish Academy of Sciences, Cormack developed the necessary mathematical methods of calculation for obtaining images of the body's interior [17]. Essentially, in 1963, Cormack implemented tomographic reconstructions for the X-ray scanner [3].

Sir Godfrey Newbold Hounsfield (1919–2004) was a pioneering English electrical engineer. Hounsfield invented the computed tomographic scanner, and hence made an unparalleled contribution to medicine. In his obituary [18], Caroline Richmond mentions that he actually conceived the idea of computed tomography during a weekend ramble in 1967. Hounsfield described a complete computed tomography system in his patent application in 1968. In 1969, he built an X-ray scanner, whereas in 1972, Hounsfield and

[4]Nobel Prize in Physics 1902 awarded jointly to Hendrik Antoon Lorentz and Pieter Zeeman "in recognition of the extraordinary service they rendered by their research into the influence of magnetism upon radiation phenomena" [10].

radiologist Jamie Ambrose built the first ever medical CT scanner. In the description of his work and achievements [19], the Royal Swedish Academy of Sciences reports that, surprisingly, by the time he conceived his tomographic scanner, Hounsfield was unaware of neither Radon's nor Cormack's contributions in the field of image reconstruction.

PET: Hoffman, Mullani, Phelps and Ter-Pogossian

In 1972, the Washington University School of Medicine research group of Michael Phelps, Edward Hoffman, Nizar Mullani and Michel Ter-Pogossian [20, 21] built PETT II, a device which used the detection of annihilation coincidence to generate reconstructed tomography images [22]. The same group developed the Positron Emission Tomography scanner in 1973, following the concept of the corresponding PET camera, built to investigate functional characteristics of human interior organs. Since then, PET scans have become a standard in nuclear medicine; they have saved and prolonged lives, and have made some operations unnecessary [23]. The number of PET scans has increased impressively, although at varying rates worldwide [24].

SPECT: Edwards and Kuhl

SPECT was introduced in 1963 by David Kuhl and Roy Edwards [25], remarkably, almost 60 years ago. In their groundbreaking experiments on emission tomography, Kuhl and Edwards developed a tomographic scanner, designed to image single-photon (γ-ray) emitters [26, 27]. It took 13 more years for Kuhl and his associates to reach "Mark IV", the final version of their scanning system [28].

Combinations: PET/CT and SPECT/CT

In the early 2000s, the combination of PET and CT (PET/CT) was introduced by electrical engineer Ronald Nutt and physicist David Townsend [29]. The PET/CT device, combining two triumphs of technology namely PET and CT, was characterized as a "winning combination" by Time magazine's "Inventions 2000" section [23]. As in the case of PET/CT, quite recently, integrated SPECT/CT scanners have been made available [30]. There is an increase in the demand of new hybrid SPECT/CT devices, since they offer the unique opportunity to provide accurate, attenuation-corrected reconstructed images [31]. SPECT/CT achieves increased specificity through precise localization and characterization of its functional findings [32].

I.2 A little bit of medical physics

Nuclear medicine provides powerful, non-invasive functional imaging tools in order to detect several human diseases [33]. These tools involve radioactive materials for the efficient imaging of several properties of a patient's physiology, such as morphology or function [34]. In nuclear medicine, the main goal of tomography is to determine the radioactivity distribution of a radiopharmaceutical injected in a patient's body [35, 36]. The choice of radiopharmaceutical is application-specific. The radiotracer will target the organ to be imaged and localize there by a chemical process. Once the organ becomes radioactive it emits either positrons (β^+ or e^+) or photons (γ-rays). The two main categories of emission tomography differ on whether the radioactive isotope of the radiopharmaceutical emits positrons (PET) or single photons (SPECT). The emitted radiation is detected by a system of detectors [37], which will in turn create, after reconstruction, an image of the radioisotope distribution within the organ of interest.

PET physics

PET makes use of the unique characteristics of decaying radionuclides inside radiopharmaceuticals, such as FDG (^{18}F-2-deoxy-2-fluoro-D-glucose). When a radionuclide is injected inside the patient, it is distributed in tissues in a manner determined by its biochemical properties [38], following bichemical modification [39]. Then, the radioisotope decays and emits a positron (anti-electron). Following β^+ decay, the ejected positron has a very short lifetime[5], and rapidly combines with an electron in the tissue. As a consequence, the electron and anti-electron annihilate and their masses, denoted by m_{e^+} and m_{e^-}, respectively, are converted into electromagnetic energy:

$$E = mc^2 = (m_{e^+} + m_{e^-})c^2 = 1.022 \text{ MeV} = 2 \times 511 \text{ keV}, \tag{I.3}$$

since

$$m_{e^+} = m_{e^-} = 9.109 \times 10^{-31} \text{ kg} = 2 \times 0.511 \ \frac{\text{MeV}}{c^2}. \tag{I.4}$$

The energy is then released as high energy photons. This process produces two 511 keV γ-particles propagating in opposite directions [36]. Then, PET detectors detect these annihilation photons, as coincidence γ-rays [4]. In PET, tumors with higher glucose metabolism usually appear as regions with higher radioactivity, hence visible in emission tomography images [36].

[5]The mean lifetime of the so-called *singlet* or *para-positronium* state, $^1S_0$ or p-Ps, is of the order of 10^{-10} sec.

SPECT physics

In SPECT, a patient is injected with a pharmaceutical labeled with a radionuclide, which emits photons [3]. SPECT utilizes the unique chemical characteristics of decaying radiopharmaceuticals, consisting of a targeting agent labeled with a certain radioisotope, such as technetium-99 (^{99}Tc) [40]. As in PET, the radioactivity of the radiopharmaceutical is distributed in the body in a fashion governed by its unique biochemical properties [38]. The injected radiotracers radiate single photons and the detectors count these individual photons, as *γ-ray events* [5]. SPECT images are generated using gamma cameras that record the photons emitted by the tracer inside the tissue of the patient [41].

I.3 Beer's law

In SPECT diagnostic imaging, let us denote the γ-ray by L and the linear attenuation coefficient of the patient's tissue at the point (x_1, x_2) by $\mu(x_1, x_2)$. Furthermore, we denote the corresponding γ-ray intensity at the same point by $I(x_1, x_2)$. Then, a photon traveling a very short distance δs undergoes a relative intensity loss

$$\frac{\delta I}{I} = -\mu \delta s. \tag{I.5}$$

If δs is zero, then the intensity is preserved, hence the intensity loss vanishes. However, in the limit case $\delta s \to 0$, equation (I.5) becomes an ordinary differential equation (ODE) of the following form:

$$\frac{\mathrm{d}I}{\mathrm{d}s} = -\mu I, \tag{I.6}$$

or

$$\frac{\left(\dfrac{\mathrm{d}I}{\mathrm{d}s}\right)}{I} = -\mu. \tag{I.7}$$

The above may be rewritten as

$$\frac{\mathrm{d}}{\mathrm{d}s}\left(\ln I\right) = -\mu. \tag{I.8}$$

Hence,

$$I = I_0 \exp\left(-\int_L \mu(s)\mathrm{d}s\right), \tag{I.9}$$

where I_0 represents the initial γ-ray intensity, and L denotes the length of the line traveled by the ray undergoing attenuation. It must be emphasized that the integral in the right-hand side of equation (I.9) is a line integral.

The aim in SPECT imaging is to reconstruct the distribution of the radiation sources. Equation (I.9) provides information for a single source. However, we need to acquire information about the distribution as a whole. Hence, we express the distribution as a function $f(x_1, x_2)$ of point-sources. In this direction, the generalization of equation (I.9) leads to the reducing, or attenuation, factor

$$\exp\left(-\int_{L(\mathbf{x})} \mu(s)\mathrm{d}s\right) f, \tag{I.10}$$

only this time the integration is applied on $L(\mathbf{x})$, i.e. the segment of the ray L from point $\mathbf{x} = (x_1, x_2)$ to the detector, instead of L itself. Summing over all point sources, and taking into account the factor (I.10) yields the following generalization of equation (I.9) for SPECT:

$$I_S = \int_L \exp\left(-\int_{L(\mathbf{x})} \mu(s)\mathrm{d}s\right) f \mathrm{d}\tau, \tag{I.11}$$

under the assumption that the linear attenuation coefficient μ obeys Beer's law (I.9). It is worth mentioning that we must require that the function f decays at infinity sufficiently fast in order to balance for the effect of the exponential weight in the integral (I.11) [42]. For details, see figure 1.2 and the relevant analysis performed on Chapter 1 and Chapter 4. In SPECT applications, the data are given in the form of I_S, as in equation (I.11).

We note that in PET, where instead of a single photon the positron emission is pairwise and in opposite directions, equation (I.11) simplifies to

$$I_P = \exp\left(-\int_L \mu(s)\mathrm{d}s\right) \int_L f \mathrm{d}\tau, \tag{I.12}$$

where the line integration occurs along the whole ray L. In this case, the factor $\exp\left(-\int_L \mu(s)\mathrm{d}s\right)$ is a constant in the overall integration, and all measurements are embedded in I_P. For the mathematical transition from SPECT to PET, see Section 1.4 and Remark 1.4.

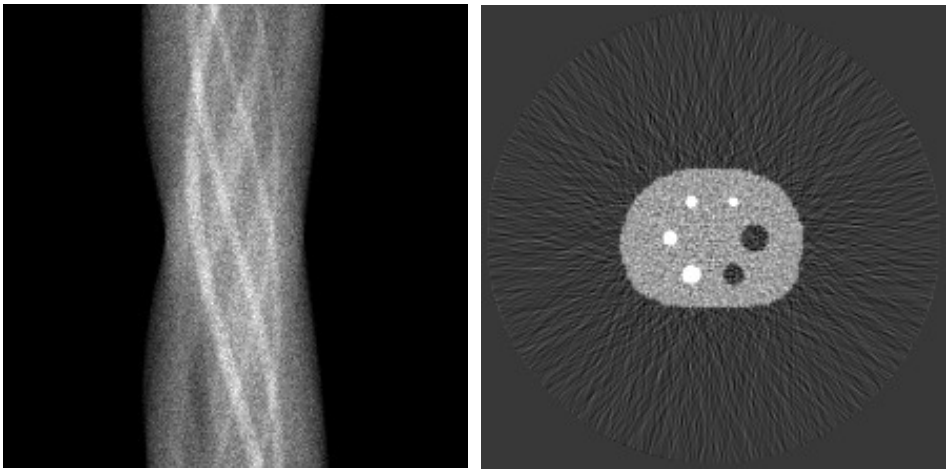

(a) Data: $\widehat{f}_\mu = \int_L e^{-\int_{L(\mathbf{x})} \mu(s)\mathrm{d}s} f \mathrm{d}\tau$. (b) Reconstruction: f, the inverse of $\widehat{f}_\mu$.

Figure I.2: Tomography as an inverse mathematical problem.

I.4 Emission tomography as an inverse problem in mathematics

There exist several integral transforms associated with tomography [37]. Several great mathematicians, including Gelfand [43], have studied these transforms in the context of inverse problems. From a mathematical point of view, emission tomography, which is the branch of medical imaging that includes PET and SPECT [34], is considered within the inverse problem paradigm. In this direction, equation (I.11) implies an inverse problem, namely

$$I_S = \widehat{f}_\mu \tag{I.13}$$

where the right-hand side of equation (I.11) is replaced by $\widehat{f}_\mu$, and the subscript μ emphasizes the dependence on the linear attenuation function μ, see figure I.2.

Equation (I.13) allows us to express the main inverse problem involved in emission tomography, namely to invert the integral transform $\widehat{f}_\mu$ and to retrieve f in the sense that

$$\widehat{f}_\mu = \int_L \exp\left(-\int_{L(\mathbf{x})} \mu(s)\mathrm{d}s\right) f \mathrm{d}\tau. \tag{I.14}$$

Similarly, the corresponding inverse problem in PET arises from

$$I_P = \widehat{f}, \tag{I.15}$$

where the right-hand side of equation (I.12) is replaced by $\widehat{f}$. It is worth noting that there is no μ subscript in the right-hand side of equation (I.15), since, in the case of PET, the linear attenuation function μ and its line integral are considered constants, see Remark 1.4 in Chapter 1.

I.5 Publications originating from this thesis

The research conducted for the purposes of this thesis at the Research Center of Mathematics of the Academy of Athens and at the Department of Mathematics, School of Applied Mathematical and Physical Sciences of the National Technical University of Athens, resulted in the following publications listed below.

Journal papers

1. N.E. Protonotarios, A.S. Fokas, K. Kostarelos, G.A. Kastis, *The attenuated spline reconstruction technique for single photon emission computed tomography*, Journal of the Royal Society Interface 15(148), pp. 20180509 (2018), [44]

2. N.E. Protonotarios, G.M. Spyrou, G.A. Kastis, *Automatic cumulative sums contour detection of FBP-reconstructed multi-object nuclear medicine images*, Computers in Biology and Medicine 85(1), pp. 43–52 (2017), [45],

Conference papers

3. N.E. Protonotarios, A. Charalambopoulos, K. Kacperski, G.A. Kastis, A.S. Fokas, *A spline approach to parallel-hole collimator deblurring for aSRT reconstructed SPECT images*, IEEE BioInformatics and BioEngineering (IEEE BIBE 2019), Athens, IEEE (2019), [46],

4. N.E. Protonotarios, A.S. Fokas, A. Gaitanis, G.A. Kastis, *aSRT: A new analytic reconstruction algorithm for SPECT*, 2016 IEEE Nuclear Science Symposium, Medical Imaging Conference and Room-

Temperature Semiconductor Detector Workshop (2016 IEEE NSS MIC RTSD), Strasbourg, IEEE (2017), [47],

5. N.E. Protonotarios, G.M. Spyrou, G.A. Kastis, *Cumulative sums for edge determination of a single object in PET and SPECT images*, 5$^{\text{th}}$ International Conference on Mathematical Modeling in Physical Sciences (ICM^2), Athens, in Journal of Physics: Conference Series 738(1), pp. 012010, IOP Publishing (2016), [48].

Conference talks and abstracts

6. N.E. Protonotarios, G.M. Spyrou, G.A. Kastis, *Cumulative sums for masking in nuclear medicine image reconstruction*, Bio-Medical Instrumentation and related Engineering and Physical Sciences (BIOMEP), Athens (2017), [49],

7. N.E. Protonotarios, G.A. Kastis, A.S. Fokas, *Attenuated spline reconstruction technique for SPECT/CT*, 9$^{\text{th}}$ Conference of the Eastern Mediterranean Region and the Italian Region of the International Biometric Society (EMR-IBS), Thessaloniki (2017), [50],

8. N.E. Protonotarios, A.S. Fokas, A. Gaitanis, G.A. Kastis, *Inversion of the attenuated Radon transform using cubic splines*, 1$^{\text{st}}$ European Congress of Medical Physics (ECMP), Athens, (2016), [51],

9. N.E. Protonotarios, A.S. Fokas, G.A. Kastis, *Attenuated Radon transform inversion through piecewise polynomial interpolation of SPECT/CT data*, 5$^{\text{th}}$ International Conference on Mathematical Modeling in Physical Sciences (ICM^2), Athens, (2016), [52],

10. A.S. Fokas, G.A. Kastis, N.E. Protonotarios, *Analytic reconstructions for PET, SPECT, MEG and EEG*, Advanced Inverse Problems (AIP), Helsinki, (2015), [53].

Book chapter

11. N.E. Protonotarios, G.A. Kastis, A.S. Fokas, *A new approach for the inversion of the attenuated Radon transform*, Mathematical Analysis and Applications, Springer, 2020, [54].

I.6 Structure of thesis

The thesis consists of six chapters, divided into two parts. In **Part I**, we present the Radon transform in $\mathbb{R}^2$, its attenuated generalization and their inversions. In **Part II**, we present our results regarding the applications of these transforms and their corresponding inversions in emission tomography, and particularly in the field of mathematical medical imaging. More specifically:

- **Part I**: Radon transforms and their inversions.
  - **Chapter 1**: We present the Radon transform in $\mathbb{R}^2$ and its generalization, namely the attenuated Radon transform, appropriately defined in the so-called *local coordinates*.
  - **Chapter 2**: We investigate several aspects of the mathematical inversion of both the unattenuated and attenuated Radon transforms in $\mathbb{R}^2$, especially in the context of non-Fourier analysis.
- **Part II**: Applications in PET and SPECT medical imaging.
  - **Chapter 3**: We deal with the concept of sinogram contour and edge detection in the context of inverse problems, and we present an automated method for determining the contour of either single or multiple objects reconstructed tomographic images of nuclear medicine modalities such as PET and SPECT.
  - **Chapter 4**: We present a novel approach for SPECT image reconstruction, namely the *attenuated spline reconstruction technique* (aSRT), which provides an analytic formula for the inverse attenuated Radon transform, and involves the computation of the Hilbert transforms of the linear attenuation function and of two sinusoidal functions of the attenuated sinogram.
  - **Chapter 5**: We present a spline-based method for deblurring reconstructed images of SPECT/CT imaging systems equipped with parallel-hole collimators, based on the classification of the collimator in terms of its blurring profile.
  - **Chapter 6**: We list all open questions arising from the mathematical problems investigated in the thesis and our plans to further investigate them in the near future.

Part I

The Radon transform in $\mathbb{R}^2$, its generalization and their inversions

Chapter 1

The Radon transform in $\mathbb{R}^2$ and its generalization

1.1 Local coordinates

The Radon transform, $\mathcal{R}$, integrates a function f on $\mathbb{R}^n$ over its corresponding hyperplanes [37]. In the case of $\mathbb{R}^2$, the Radon transform involves line integration along lines, and more precisely along families of parallel lines. The line integral[1] of a continuous function $f : D \subset \mathbb{R}^2 \to \mathbb{R}$ along a differentiable curve $C : [a, b] \to D \subset \mathbb{R}^2$ is defined by:

$$\int_C f \mathrm{d}s = \int_a^b f\left(\mathbf{r}(\tau)\right) \left|\left|\mathbf{r}'(\tau)\right|\right|_2 \mathrm{d}\tau, \tag{1.1}$$

where $\mathbf{r} : [a, b] \to C$ is a bijective map, namely the parameterization of the curve C, and $||\cdot||_2$ denotes the L^2-norm in $\mathbb{R}^2$. We need to employ a convenient and easy-to-manipulate coordinate description for parallel lines, especially when focusing on tomography and medical imaging applications. The following selection of coordinates comes quite naturally, hence the term "line coordinates", or "local coordinates".

A line L on the x_1x_2-plane can be specified by the signed distance from the origin, ρ, $(-\infty < \rho < \infty)$, and the angle with the x_1-axis, θ $(0 \leq \theta < 2\pi)$, see figure 1.1. We denote the corresponding unit vectors parallel and perpendicular to L by $\mathbf{e}^{\parallel}$ and $\mathbf{e}^{\perp}$, respectively. The unit vectors are given

[1] A more appropriate term is "curve integral", however the potentially misleading term "line integral" remained unchanged. In Greek, the only term used is "επικαμπύλιο ολοκλήρωμα", which actually means "integral along a curve".

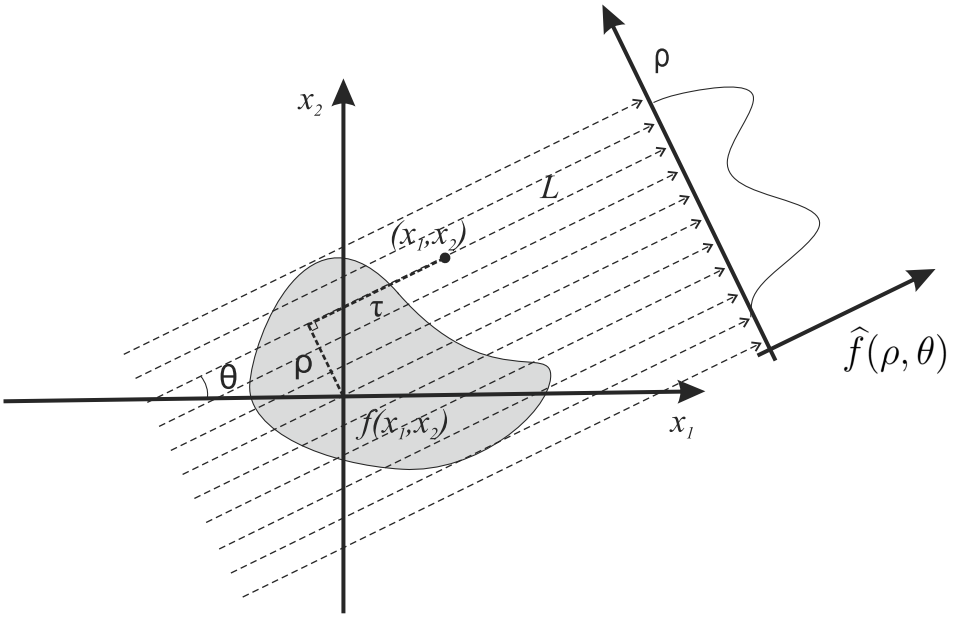

Figure 1.1: A two-dimensional object $f(x_1, x_2)$ and its projections $\widehat{f}(\rho, \theta)$. Both Cartesian (x_1, x_2) and local (ρ, τ) coordinates are indicated.

by

$$\mathbf{e}^{\parallel} = (\cos\theta, \sin\theta)\,,$$
$$\mathbf{e}^{\perp} = (-\sin\theta, \cos\theta)\,.$$

Every point $\mathbf{x} = (x_1, x_2)$ on L in Cartesian coordinates can be expressed in terms of the line coordinates (ρ, τ) via

$$\mathbf{x} = \rho\,\mathbf{e}^{\perp} + \tau\,\mathbf{e}^{\parallel},$$

where τ denotes the arc length. Therefore,

$$x_1 := x_1(\rho, \tau; \theta) = \tau\cos\theta - \rho\sin\theta, \tag{1.2a}$$

$$x_2 := x_1(\rho, \tau; \theta) = \tau\sin\theta + \rho\cos\theta. \tag{1.2b}$$

This way, the family of all parallel lines can be represented by simply fixing the angle θ and by letting ρ vary. Furthermore, for the family of all parallel lines $L_{\rho,\theta}$ on the x_1x_2-plane that form an angle θ with the x_1-axis, we choose

the following parameterization $\mathbf{r}$, by employing equations (1.2):

$$\mathbf{r}(\tau) = \begin{bmatrix} \tau\cos\theta - \rho\sin\theta \\ \tau\sin\theta + \rho\cos\theta \end{bmatrix}. \tag{1.3}$$

The above choice is in agreement with the fact that τ represents the arc length of the line L. It is worth noting that

$$\left|\left|\mathbf{r}'(\tau)\right|\right|_2 = \sqrt{\left(\frac{\mathrm{d}x_1}{\mathrm{d}\tau}\right)^2 + \left(\frac{\mathrm{d}x_2}{\mathrm{d}\tau}\right)^2} = 1, \tag{1.4}$$

hence, equation (1.3) is a natural parameterization of the lines L. It turns out that this specific type of parameterization is very useful, especially when dealing with integrals along families of straight lines. Taking into account the above, if the curve C is a line L naturally parameterized by the arc length τ, the initial line integral (1.1) may be rewritten as follows:

$$\begin{aligned} \int_C f\mathrm{d}s &= \int_L f\left(x_1(\tau,\rho,\theta), x_2(\tau,\rho,\theta)\right)\mathrm{d}\tau \\ &= \int_{-\infty}^{\infty} f\left(\tau\cos\theta - \rho\sin\theta, \tau\sin\theta + \rho\cos\theta\right)\mathrm{d}\tau \end{aligned} \tag{1.5}$$

Equations (1.2) can be inverted and expressed in the local coordinates (ρ,τ) in terms of the Cartesian coordinates (x_1,x_2) and the associated angle θ, as follows:

$$\rho := \rho(x_1,x_2;\theta) = x_2\cos\theta - x_1\sin\theta, \tag{1.6a}$$

$$\tau = \tau(x_1,x_2;\theta) = x_2\sin\theta + x_1\cos\theta. \tag{1.6b}$$

Definition 1.1. *The space of Schwartz functions, or the space of rapidly decreasing functions on $\mathbb{R}^n$ is denoted by $\mathcal{S}(\mathbb{R}^n)$ and is defined as:*

$$\mathcal{S}(\mathbb{R}^n) = \{f \in C^\infty(\mathbb{R}^n) : ||f||_{\alpha,\beta} < \infty\} \subset C^\infty(\mathbb{R}^n), \tag{1.7}$$

where

$$||f||_{\alpha,\beta} = \sup_{x\in\mathbb{R}^n}\left|x^\alpha D^\beta f(x)\right|, \quad \forall \text{ multi-index } \alpha,\beta,$$
$$\left|x^\alpha D^\beta f(x)\right| \to 0, \quad \textit{as } |x|\to\infty. \tag{1.8}$$

1.2 The Radon transform in $\mathbb{R}^2$

The celebrated Radon transform [1, 2] of a two-dimensional function is defined as the set of all its line integrals [3, 55]. It is worth noting that Radon in his seminal paper [2] refers to the concept of line integrals as *straight line integrals*.

Definition 1.2. *The line integral of a two-dimensional Schwartz function $f \in \mathcal{S}(\mathbb{R}^2)$ along straight lines on the plane, see Definition 1.1 and equation 1.5, is referred to as the "Radon transform" $\mathcal{R}$ of $f(x_1, x_2)$ and is denoted by $\widehat{f}(\rho, \theta)$. The Radon transform is usually stored in the form of the so-called sinogram, expressed as follows:*

$$\widehat{f}(\rho,\theta) = (\mathcal{R}f)(\rho,\theta) = \int_{-\infty}^{\infty} f(\tau\cos\theta - \rho\sin\theta, \tau\sin\theta + \rho\cos\theta)\mathrm{d}\tau, \quad 0 \le \theta < 2\pi,\ -\infty < \rho < \infty, \tag{1.9}$$

An alternative representation of the Radon transform involves Dirac's delta function (line impulse) and is expressed as follows [56]:

$$\widehat{f}(\rho,\theta) = \int_{-\infty}^{\infty}\int_{-\infty}^{\infty} f(x_1,x_2)\delta(\rho + x_1\sin\theta - x_2\cos\theta)\mathrm{d}x_1\mathrm{d}x_2. \tag{1.10}$$

We illustrate the importance of the Radon transform in the following examples.

Example 1. $f(x_1, x_2) = e^{-(x_1^2+x_2^2)}$. For the calculation of the Radon transform of the above function, we apply equation (1.9), as follows:

$$\begin{aligned}
\widehat{f}(\rho,\theta) &= \int_{-\infty}^{\infty} f(\tau\cos\theta - \rho\sin\theta, \tau\sin\theta + \rho\cos\theta)\mathrm{d}\tau \\
&= \int_{-\infty}^{\infty} e^{-\left[(\tau\cos\theta-\rho\sin\theta)^2+(\tau\sin\theta+\rho\cos\theta)^2\right]}\mathrm{d}\tau \\
&= \int_{-\infty}^{\infty} e^{-(\tau^2+\rho^2)}\mathrm{d}\tau = e^{-\rho^2}\int_{-\infty}^{\infty} e^{-\tau^2}\mathrm{d}\tau = \\
&= \frac{\sqrt{\pi}}{2}e^{-\rho^2}\left(\lim_{\tau\to\infty}\mathrm{erf}\,(\tau) - \lim_{\tau\to-\infty}\mathrm{erf}\,(\tau)\right) \\
&= \sqrt{\pi}e^{-\rho^2}.
\end{aligned}$$

Example 2. If the function f represents a circle centered at the origin, i.e.

$$f(x_1, x_2) = \begin{cases} 1, & \text{for} \quad x_1^2 + x_2^2 \leq R^2 \\ 0, & \text{otherwise} \end{cases}.$$

Then, for $|\rho| \leq R$, the Radon tranform is

$$\begin{aligned} \widehat{f}(\rho, \theta) &= \int_{-\infty}^{\infty} f(\tau \cos\theta - \rho \sin\theta, \tau \sin\theta + \rho \cos\theta) \mathrm{d}\tau \\ &= \int_{-\sqrt{R^2-\rho^2}}^{\sqrt{R^2-\rho^2}} \mathrm{d}\tau = 2\sqrt{R^2 - \rho^2}, \end{aligned}$$

whereas for $\rho \notin [-R, R]$ the Radon transform vanishes.
The transform pair (1.9) gives rise to the following *inverse problem*: Given the function $\widehat{f}(\rho, \theta)$, $0 \leq \theta < 2\pi$, $-\infty < \rho < \infty$, reconstruct the function $f(x_1, x_2)$. This is the main mathematical problem in PET tomography. In principal, the above problem was solved by Johann Radon himself in 1917 [1, 2]. The inversion of the Radon transform is explained in detail in Chapters 2 and 4.

1.3 Properties of the Radon transform in $\mathbb{R}^2$

We present some of the most important properties of the Radon transform in $\mathbb{R}^2$, as outlined in [3, 35, 37, 57–59].

Weighted sum

The Radon transform of a finite weighted sum of functions is the finite weighted sum of the Radon transforms of the involved functions, namely,

$$\left(\mathcal{R} \left\{ \sum_{i=1}^{N} a_i f_i \right\} \right) (\rho, \theta) = \sum_{i=1}^{N} \left(\mathcal{R} \left\{ a_i f_i \right\} \right) (\rho, \theta). \tag{1.11}$$

Proof. Inserting the left-hand side of equation (1.11) in equation (1.9) yields

$$\left(\mathcal{R} \left\{ \sum_{i=1}^{N} a_i f_i \right\} \right) (\rho, \theta) = \int_{-\infty}^{\infty} \left(\sum_{i=1}^{N} a_i f_i (\tau \cos\theta - \rho \sin\theta, \tau \sin\theta + \rho \cos\theta) \right) \mathrm{d}\tau$$

$$
\begin{aligned}
&= \int_{-\infty}^{\infty} \Big[a_1 f_1(\tau\cos\theta - \rho\sin\theta, \tau\sin\theta + \rho\cos\theta)\mathrm{d}\tau \\
&\quad + \cdots + \int_{-\infty}^{\infty} a_N f_N(\tau\cos\theta - \rho\sin\theta, \tau\sin\theta + \rho\cos\theta)\Big]\mathrm{d}\tau \\
&= \sum_{i=1}^{N} \left(\int_{-\infty}^{\infty} a_i f_i(\tau\cos\theta - \rho\sin\theta, \tau\sin\theta + \rho\cos\theta) \right) \mathrm{d}\tau. \\
&= \sum_{i=1}^{N} \left(\mathcal{R}\left\{a_i f_i\right\}\right)(\rho,\theta).
\end{aligned}
$$

■

Scaling

The Radon transform of a function with scaled variables is itself a scaled Radon transform of the initial function, namely,

$$
\left(\mathcal{R}\left\{f(\lambda x_1, \lambda x_2)\right\}\right)(\rho,\theta) = \frac{1}{\lambda}\left(\mathcal{R}\left\{f\right\}\right)(\lambda\rho,\theta)\,. \tag{1.12}
$$

Proof. In the defining equation (1.9), we insert the left-hand side of equation (1.12), as follows:

$$
\begin{aligned}
\left(\mathcal{R}\left\{f(\lambda x_1, \lambda x_2)\right\}\right)(\rho,\theta) &= \int_{-\infty}^{\infty} f(\lambda(\tau\cos\theta - \rho\sin\theta), \lambda(\tau\sin\theta + \rho\cos\theta))\mathrm{d}\tau \\
&= \int_{-\infty}^{\infty} f(\lambda\tau\cos\theta - \lambda\rho\sin\theta, \lambda\tau\sin\theta + \lambda\rho\cos\theta)\mathrm{d}\tau \\
&= \frac{1}{\lambda}\int_{-\infty}^{\infty} f\left(\tau'\cos\theta - (\lambda\rho)\sin\theta, \tau'\sin\theta + (\lambda\rho)\cos\theta\right)\mathrm{d}\tau' \\
&= \frac{1}{\lambda}\left(\mathcal{R}\left\{f\right\}\right)(\lambda\rho,\theta)\,,
\end{aligned}
$$

where we have used the change of variables

$$
\tau' = \lambda\tau,
$$

hence

$$
\mathrm{d}\tau' = \lambda\mathrm{d}\tau.
$$

■

Shifting

The Radon transform of a function with a variable shift is itself a shifted Radon transform of the initial function, namely,

$$\left(\mathcal{R}\{f(x_1 - x_1', x_2 - x_2')\}\right)(\rho, \theta) = (\mathcal{R}\{f\})(\rho - \rho', \theta). \tag{1.13}$$

Proof. In the Radon transform definition (1.9), we insert the left-hand side of equation (1.13):

$$\begin{aligned}
&(\mathcal{R}\{f(x_1 - x_1', x_2 - x_2')\})(\rho, \theta) \\
&\quad = \int_{-\infty}^{\infty} f(\tau\cos\theta - \rho\sin\theta - x_1', \tau\sin\theta + \rho\cos\theta - x_2')\mathrm{d}\tau \\
&\quad = \int_{-\infty}^{\infty} f(\tau\cos\theta - \rho\sin\theta - \tau'\cos\theta + \rho'\sin\theta, \\
&\qquad\qquad \tau\sin\theta + \rho\cos\theta - \tau'\sin\theta - \rho'\cos\theta)\mathrm{d}\tau \\
&\quad = \int_{-\infty}^{\infty} f((\tau - \tau')\cos\theta - (\rho - \rho')\sin\theta, (\tau - \tau')\sin\theta + (\rho - \rho')\cos\theta)\mathrm{d}\tau \\
&\quad = \int_{-\infty}^{\infty} f(\tau''\cos\theta - (\rho - \rho')\sin\theta, \tau''\sin\theta + (\rho - \rho')\cos\theta)\mathrm{d}\tau'' \\
&\quad = (\mathcal{R}\{f\})(\rho - \rho', \theta),
\end{aligned}$$

where, following equations (1.2), we have used the fact that

$$x_1' = \tau'\cos\theta - \rho'\sin\theta,$$

$$x_2' = \tau'\sin\theta + \rho'\cos\theta,$$

for some

$$(x_1', x_2') \quad \text{corresponding to} \quad (\rho', \tau'),$$

and the appropriate change of variables

$$\tau'' = \tau - \tau',$$

therefore

$$\mathrm{d}\tau'' = \mathrm{d}\tau.$$

■

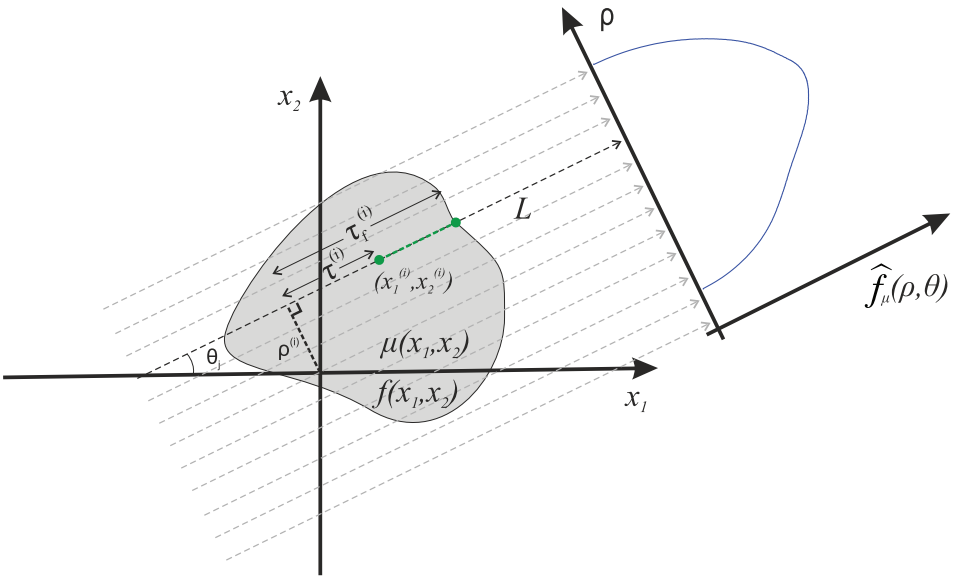

Figure 1.2: Cartesian (x_1, x_2) and local (ρ, θ) coordinates for the attenuated Radon transform.

1.4 A generalization of the Radon transform in $\mathbb{R}^2$: The attenuated Radon transform

The mathematical problem of SPECT medical image reconstruction leads naturally to a generalization of the Radon transform [35], namely the *attenuated Radon transform* or *exponential Radon transform*, denoted by $\mathcal{R}_\mu$. The attenuation concept is represented by the attenuation function $\mu(x_1, x_2)$, and is indicated by the corresponding subscript[2].

Definition 1.3. *We define the line integral of a two-dimensional function $f(x_1, x_2)$ attenuated with respect to the function $\mu(x_1, x_2)$ as the attenuated Radon transform $\mathcal{R}_\mu$ of $f(x_1, x_2)$, denoted by $\widehat{f}_\mu(\rho, \theta)$, see figure 1.2. The attenuated Radon transform is usually stored in the form of the so-called attenuated sinogram, expressed as follows:*

$$\widehat{f}_\mu(\rho,\theta) = (\mathcal{R}_\mu f)(\rho,\theta) = \int_{-\infty}^{\infty} e^{-\int_\tau^\infty \mu(s\cos\theta-\rho\sin\theta, s\sin\theta+\rho\cos\theta)\mathrm{d}s} \times$$
$$f(\tau\cos\theta - \rho\sin\theta, \tau\sin\theta + \rho\cos\theta)\mathrm{d}\tau,\ 0 \le \theta < 2\pi,\ -\infty < \rho < \infty. \quad (1.15)$$

[2]The attenuated Radon transform is sometimes denoted by $\mathcal{A}$, see for example [35].

The above transform (1.15) gives rise to the following *inverse problem*: Given the functions $\widehat{f}_\mu(\rho,\theta)$, $0 \leq \theta < 2\pi$, $-\infty < \rho < \infty$ and $\mu(x_1,x_2)$, $-\infty < x_1, x_2 < \infty$, reconstruct the function $f(x_1,x_2)$. This is the main mathematical problem in SPECT tomography. The inversion of the attenuated Radon transform is explained in detail in Chapters 2 and 4.

Remark 1.4. *In the limit case of no attenuation, i.e.*

$$\mu(x_1,x_2) \to 0,$$

the attenuated Radon transform $\mathcal{R}_\mu$ becomes the non-attenuated Radon transform:

$$\lim_{\mu\to 0} \mathcal{R}_\mu(\cdot) =: \mathcal{R}_0(\cdot) = \mathcal{R}(\cdot).$$

Proof. If $\mu(x_1,x_2) \to 0$, then the integral inside the exponential part of the integral (1.15) becomes 0, hence the exponential tends to 1, therefore equation (1.15) becomes equation (1.9). ■

Remark 1.4 emphasizes the fact that, from a strictly mathematical point of view, the non-attenuated Radon transform is indeed a special, limiting case of the attenuated Radon transform. The attenuated Radon transform has been extensively studied in the literature, especially in [60–62].

Chapter 2

The inversion of the Radon transform in $\mathbb{R}^2$ and of its generalization

2.1 Fourier-based inversion of the Radon transform in $\mathbb{R}^2$

One of the most standard techniques in the mathematics of medical imaging involves the so-called *central slice theorem* (CST). This provides a fundamental tool for the Fourier-based inversion of the Radon transform [63].

Theorem 2.1. *(Central slice theorem). The two-dimensional Fourier transform $\mathcal{F}_2$ of a function $f(x_1, x_2)$ is the one-dimensional Fourier transform $\mathcal{F}_1$ of the Radon transform $\mathcal{R}$ of the same function f. In purely operator notation*

$$\mathcal{F}_2\{f\} = \mathcal{F}_1\{\mathcal{R}\{f\}\}, \tag{2.1}$$

where $\mathcal{F}_2$ is defined by

$$(\mathcal{F}_2\{f\})(\xi_1, \xi_2) = \int_{-\infty}^{\infty}\int_{-\infty}^{\infty} f(x_1, x_2)e^{-2\pi \mathrm{i}(\xi_1 x_1 + \xi_2 x_2)}\mathrm{d}x_1\mathrm{d}x_2, \tag{2.2}$$

$\mathcal{F}_1$ is defined by

$$(\mathcal{F}_1\{g\})(r) = \int_{-\infty}^{\infty} g(\rho)e^{-2\pi \mathrm{i} r\rho}\mathrm{d}\rho, \tag{2.3}$$

and $\mathcal{R}$ is defined in equation (1.9).

Proof. We shall prove the CST by inserting the alternative definition 1.10 of the Radon transform in the right-hand side of equation (2.1). This yields

$$\begin{aligned}
\mathcal{F}_1\left\{\mathcal{R}\left\{f\right\}\right\} &= \int_{-\infty}^{\infty} e^{-2\pi \mathrm{i} r\rho}\left[\int_{-\infty}^{\infty}\int_{-\infty}^{\infty} f(x_1,x_2)\delta(\rho + x_1\sin\theta - x_2\cos\theta)\mathrm{d}x_1\mathrm{d}x_2\right]\mathrm{d}\rho \\
&= \int_{-\infty}^{\infty}\int_{-\infty}^{\infty} f(x_1,x_2)\mathrm{d}x_1\mathrm{d}x_2\left[\int_{-\infty}^{\infty} e^{-2\pi \mathrm{i} r\rho}\delta(\rho + x_1\sin\theta - x_2\cos\theta)\mathrm{d}\rho\right] \\
&= \int_{-\infty}^{\infty}\int_{-\infty}^{\infty} f(x_1,x_2)\mathrm{d}x_1\mathrm{d}x_2\left(e^{-2\pi \mathrm{i} r(-x_1\sin\theta + x_2\cos\theta)}\right) \\
&= \int_{-\infty}^{\infty}\int_{-\infty}^{\infty} f(x_1,x_2)\mathrm{d}x_1\mathrm{d}x_2\left(e^{-2\pi \mathrm{i}(-x_1 r\sin\theta + x_2 r\cos\theta)}\right) \\
&= \int_{-\infty}^{\infty}\int_{-\infty}^{\infty} f(x_1,x_2)e^{-2\pi \mathrm{i}(\xi_1 x_1 + \xi_2 x_2)}\mathrm{d}x_1\mathrm{d}x_2 \\
&= \mathcal{F}_2\left\{f\right\},
\end{aligned}$$

where we introduced the variables ξ_1 and ξ_2 as

$$\xi_1 = -r\sin\theta \quad \text{and} \quad \xi_2 = r\cos\theta, \tag{2.4}$$

and we have treated θ as a constant, in the sense that the above are considered for all θ values involved. ■

Corollary 2.2. *The central slice theorem implies that the Fourier-based inversion of the Radon transform may be written in the following operator form:*

$$\mathcal{R}^{-1} = \mathcal{F}_2^{-1}\mathcal{F}_1. \tag{2.5}$$

The inversion of the Radon tranform may be accomplished without Fourier analysis. One can invert the Radon transform in a slightly more complicated manner, by employing complex analysis. However, the computational benefits of the non-Fourier inversion are significant; these benefits will become very clear in Chapter 4, which illustrates one of the main results of the present thesis, particularly with the introduction of cubic spline functions.

2.2 The inversion of the Radon transform in $\mathbb{R}^2$ without the Fourier transform

2.2.1 Preliminaries

In order to solve the inverse problem defined in equation (1.9) without Fourier analysis and invert the Radon transform, it is essential to introduce appropriate mathematical machinery [64].

Lemma 2.3. *(Generalized Cauchy formula or Pompeiu's formula, [64]). Assume that the function $f(z,\bar{z})$ is continuous and has continuous partial derivatives in a finite region D and on the simple closed boundary ∂D. We denote by ∂D the closed boundary of D with counterclockwise direction. Then, $f(z,\bar{z})$ can be evaluated at any interior point z via the following formula*

$$f(z,\bar{z}) = \frac{1}{2\pi i}\left(\oint_{\partial D} f(\zeta,\bar{\zeta})\frac{\mathrm{d}\zeta}{\zeta - z} + \iint_D \frac{\partial f}{\partial \bar{\zeta}}(\zeta,\bar{\zeta})\frac{\mathrm{d}\zeta\wedge\mathrm{d}\bar{\zeta}}{\zeta - z}\right), \tag{2.6}$$

where the so-called wedge product $\mathrm{d}\zeta\wedge\mathrm{d}\bar{\zeta}$, $\zeta = \xi + i\eta$, $\bar{\zeta} = \xi - i\eta$, is defined as

$$\mathrm{d}\zeta\wedge\mathrm{d}\bar{\zeta} = (\mathrm{d}\xi + \mathrm{i}\mathrm{d}\eta)\wedge(\mathrm{d}\xi - \mathrm{i}\mathrm{d}\eta) = -2\mathrm{i}\mathrm{d}\xi\mathrm{d}\eta. \tag{2.7}$$

Proof. Let the real functions $u(x,y)$ and $v(x,y)$, as well as their partial derivatives $u_x(x,y)$, $u_y(x,y)$, $v_x(x,y)$ and $v_y(x,y)$, be continuous inside a finite region D and on its simple closed boundary ∂D. Green's theorem yields

$$\int_{\partial D}(u\mathrm{d}x + v\mathrm{d}y) = \iint_D (v_x - u_y)\mathrm{d}x\mathrm{d}y. \tag{2.8}$$

Replacing in equation (2.8) (x,y) by (ξ,η) and letting $g = u + \mathrm{i}v$, we find

$$\int_{\partial D} g\mathrm{d}\zeta = -\iint_D \frac{\partial g}{\partial\bar{\zeta}}\mathrm{d}\zeta\wedge\mathrm{d}\bar{\zeta}, \tag{2.9}$$

where $\mathrm{d}\zeta = \mathrm{d}\xi + +\mathrm{i}\mathrm{d}\eta$, $\partial g/\partial\bar{\zeta} = \frac{1}{2}(g_\xi + +\mathrm{i}g_\eta)$ and $\mathrm{d}\zeta\wedge\mathrm{d}\bar{\zeta}$ is defined in equation (2.7). We define the region D_ϵ as follows:

$$D_\epsilon = D\backslash\{|\zeta - z| \le \epsilon\}, \quad \epsilon > 0, \tag{2.10}$$

i.e., D_ϵ is the region D without the circular area centered at $\zeta = z$ with radius ϵ. We denote the boundary of this circular area by ∂D_ϵ. The contour of D_ϵ

comprises of two subcontours, namely ∂D and ∂D_ϵ. Noting that $(\zeta - z)^{-1}$ is analytic in D_ϵ, we may apply Green's theorem in the form (2.9) on the function $g(\zeta) = f(\zeta)(\zeta - z)^{-1}$

$$\oint_{\partial D} \frac{f(\zeta)}{\zeta - z} \mathrm{d}\zeta - \oint_{\partial D_\epsilon} \frac{f(\zeta)}{\zeta - z} \mathrm{d}\zeta = -\iint_D \frac{\partial f/\partial \bar{\zeta}}{\zeta - z} \mathrm{d}\zeta \wedge \mathrm{d}\bar{\zeta}. \tag{2.11}$$

However, we note that the points on the circle ∂D_ϵ can be expressed in the form $\zeta = z + \epsilon e^{\mathrm{i}\theta}$, therefore

$$\oint_{\partial D_\epsilon} \frac{f(\zeta)}{\zeta - z} \mathrm{d}\zeta = \int_0^{2\pi} \frac{f(z + \epsilon e^{\mathrm{i}\theta})}{\epsilon e^{\mathrm{i}\theta}} \mathrm{i}\epsilon e^{\mathrm{i}\theta} \mathrm{d}\theta = \int_0^{2\pi} f(z + \epsilon e^{\mathrm{i}\theta}) \mathrm{i} \mathrm{d}\theta \xrightarrow{\epsilon \to 0} 2\pi \mathrm{i} f(z). \tag{2.12}$$

The above is valid because (a) $f(z)$ is continuous, and (b) the integral of a continuous function inside a bounded region (∂D_ϵ) and the limit ($\epsilon \to 0$) are interchangeable. Similarly, due to the fact that $(\zeta - z)^{-1}$ is integrable inside the region D_ϵ, together with the fact that $f_{\bar{\zeta}}$ is continuous, it follows that the double integral over D_ϵ converges to the double integral over the whole region D. Hence, their difference tends to zero as $\epsilon \to 0$:

$$\left| \iint_{D - D_\epsilon} \frac{\partial f/\partial \bar{\zeta}}{\zeta - z} \mathrm{d}\zeta \wedge \mathrm{d}\bar{\zeta} \right| \leq 2 \int_0^\epsilon \int_0^{2\pi} \frac{\partial f/\partial \bar{\zeta}}{r} r \mathrm{d}r \mathrm{d}\theta \leq 4\pi \Lambda \epsilon, \tag{2.13}$$

where we have used polar coordinates, i.e., $\zeta = z + \epsilon e^{\mathrm{i}\theta}$, and the continuity of $\partial f/\partial \bar{\zeta}$ in a bounded region, namely

$$\left| \frac{\partial f}{\partial \bar{\zeta}} \right| \leq \Lambda. \tag{2.14}$$

As a consequence, we consider equation (2.11) in the limit $\epsilon \to 0$

$$\oint_{\partial D} \frac{f(\zeta)}{\zeta - z} \mathrm{d}\zeta - 2\pi + \mathrm{i} f(z) = -\iint_D \frac{\partial f/\partial \bar{\zeta}}{\zeta - z} \mathrm{d}\zeta \wedge \mathrm{d}\bar{\zeta}, \tag{2.15}$$

therefore, Pompeiu's formula (2.3) follows. ■

Corollary 2.4. *If $f(z)$ is analytic in $\bar{D} = D \cup \partial D$, then Pompeiu's formula* (2.6) *reduces to Cauchy's integral formula*

$$f(z) = \frac{1}{2\pi \mathrm{i}} \oint_{\partial D} \frac{f(\zeta)}{\zeta - z} \mathrm{d}\zeta. \tag{2.16}$$

Proof. The proof is straightforward: if $f(z)$ is analytic in $\bar{D} = D \cup \partial D$, then

$\partial f/\partial\bar{\zeta} = 0$. Hence, Cauchy's integral formula (2.16) follows from Pompeiu's formula (2.6). ■

Lemma 2.5. *(Plemelj formulæ). Let L be a smooth, finite, closed or open contour and let $\varphi(t)$ satisfy a Hölder condition on L. Then, the Cauchy-type integral*

$$\Phi(z) = \frac{1}{2\pi\mathrm{i}} \int_L \frac{\varphi(\tau)}{\tau - z} \mathrm{d}\tau, \tag{2.17}$$

has the limiting values $\Phi^-(t)$ and $\Phi^+(t)$ as z approaches L from the right and the left, respectively, given that t is not an endpoint of L. The limits $\Phi^\pm(t)$ are given by

$$\Phi^\pm(t) = \pm\frac{1}{2}\varphi(t) + \frac{1}{2\pi\mathrm{i}}\ PV \int_L \frac{\varphi(\tau)}{\tau - t} \mathrm{d}\tau, \tag{2.18}$$

where $PV \int$ denotes the Cauchy principal value integral defined by

$$PV \int_L g(\tau)\mathrm{d}\tau = \lim_{\epsilon\to 0} \int_{L-L_\epsilon} g(\tau)\mathrm{d}\tau, \tag{2.19}$$

and L_ε denotes the part of the contour L that is centered around t, with length 2ϵ.

Proof. We shall derive the Plemelj formulæ only in the case that $\varphi(\tau)$ is analytic in the neighborhood of L. The derivation of these formulæ in the more general case of $\varphi(\tau)$ satisfying a Hölder condition on L is far too complicated for the purposes of the present study, see [65]. If $\varphi(\tau)$ is analytic at $\tau = t$, then we use the Cauchy theorem to deform L into two separate contours, namely $L - L_\epsilon$ and C_ϵ, where C_ϵ is the semicircle of radius $r = \epsilon$, centered at $\tau = t$. Taking the limit of equation (2.17) as $\epsilon \to 0$ yields

$$\Phi^+(t) = \lim_{\epsilon\to 0} \frac{1}{2\pi\mathrm{i}} \int_{L-L_\epsilon} \frac{\varphi(\tau)}{\tau - t} \mathrm{d}\tau + \lim_{\epsilon\to 0} \int_{C_\epsilon} \frac{\varphi(\tau)}{\tau - t} \mathrm{d}\tau, \tag{2.20}$$

where we used the deformation $L = (L - L_\epsilon) \cup C_\epsilon$. However, if we use polar coordinates, namely $\tau = t + \epsilon e^{\mathrm{i}\theta}$, then the second integral on he right-hand side of equation (2.20) becomes

$$\lim_{\epsilon\to 0}\frac{1}{2\pi\mathrm{i}}\int_{C_\epsilon}\frac{\varphi(\tau)}{\tau-t}\mathrm{d}\tau=\frac{1}{2\pi\mathrm{i}}\lim_{\epsilon\to 0}\int_{-\pi}^{0}\varphi(t+\epsilon e^{\mathrm{i}\theta})\mathrm{i}\mathrm{d}\theta=\frac{1}{2}\varphi(\tau). \tag{2.21}$$

Hence, equation (2.21) reduces to the equation (2.18) representing $\Phi^+(t)$. Similar considerations apply for the corresponding part of the equation (2.18) representing $\Phi^-(t)$. ■

Lemma 2.6. *The solution of the scalar Riemann-Hilbert problem*

$$\Phi^+(t)-\Phi^-(t)=g(t),\quad t\in L, \tag{2.22a}$$

$$\Phi(z)=O\left(\frac{1}{z}\right),\quad z\to\infty,\quad z\notin L, \tag{2.22b}$$

is given by

$$\Phi(z)=\frac{1}{2\pi\mathrm{i}}\int_L\frac{g(\tau)}{\tau-z}\mathrm{d}\tau. \tag{2.23}$$

Proof. Equation (2.22a), together with Liouville's theorem, implies that the unique solution of the scalar Riemann-Hilbert problem (2.22) is given by (2.23). ■

2.2.2 The Radon transform pair

In 1991, Roman Novikov and Thanasis Fokas rederived the well known inversion of the Radon transform [6] by performing the so-called *spectral analysis* of the following eigenvalue equation:

$$\left[\frac{1}{2}\left(k+\frac{1}{k}\right)\partial_{x_1}+\frac{1}{2\mathrm{i}}\left(k-\frac{1}{k}\right)\partial_{x_2}\right]u(x_1,x_2;k,\bar{k})=f(x_1,x_2),\quad k\in\mathbb{C}. \tag{2.24}$$

As already noted, the Radon transform inversion can be obtained in a more straightforward manner, by employing the two-dimensional Fourier transform. However, the major advantage of the derivation of [6] was established eleven years later (2002) by Novikov [7]. Novikov demonstrated that the inverse attenuated Radon transform can be derived by applying a similar analysis to a slight generalization of equation (2.24), namely the equation

$$\left[\frac{1}{2}\left(k+\frac{1}{k}\right)\partial_{x_1}+\frac{1}{2\mathrm{i}}\left(k-\frac{1}{k}\right)\partial_{x_2}-\mu(x_1,x_2)\right]u(x_1,x_2;k,\bar{k})=f(x_1,x_2),$$
$$k\in\mathbb{C}. \quad (2.25)$$

In the following pages, we present an algorithmic approach for the inversion of the Radon transform. The corresponding analysis, referred to as spectral analysis, consists of two steps:

(a) **The direct problem.** We solve the eigenvalue equation (2.24) in terms of the function f for all complex eigenvalues k. The solution of the eigenvalue equation must be bounded for all complex values of k in $\mathbb{C}$. The direct problem gives rise to a certain problem in complex analysis known as the $\bar{d}$-problem.

(b) **The inverse problem.** Given that the solution u of equation (2.24) is bounded for all complex eigenvalues k, we derive an equivalent representation of u which, instead of depending on f, depends on the Radon transform of f denoted by $\widehat{f}$, as in equation (1.9). The inverse problem gives rise to a certain problem in complex analysis known as the scalar Riemann-Hilbert (RH) problem.

Definition 2.7. *The Hilbert transform of a function $u(t)$, is defined as the following integral:*

$$\mathcal{H}\{u(t)\}=\frac{1}{\pi}\left(PV\int_{-\infty}^{\infty}\frac{u(\tau)}{\tau-t}\mathrm{d}\tau\right). \quad (2.26)$$

Proposition 2.8. *The inversion of the Radon transform $\widehat{f}(\rho,\theta)$ of a function $f(x_1,x_2)\in\mathcal{S}(\mathbb{R}^2)$, defined in equation (1.9) is given by*

$$f(x_1,x_2)=-\frac{1}{4\pi}\int_0^{2\pi}\left[\frac{\partial(\mathcal{H}\widehat{f})(\rho,\theta)}{\partial\rho}\right]_{\rho=x_2\cos\theta-x_1\sin\theta}\mathrm{d}\theta, \quad (2.27)$$

with $-\infty<x_1,x_2<\infty$, $\mathcal{H}$ denoting the Hilbert transform in the variable ρ, as in equation (2.26),

$$(\mathcal{H}\widehat{f})(\rho,\theta)\equiv\frac{1}{\pi}\,PV\int_{-\infty}^{\infty}\frac{\widehat{f}(r,\theta)}{r-\rho}\mathrm{d}r,\quad -\infty<\rho<\infty,\quad 0\le\theta<2\pi, \quad (2.28)$$

and PV $\int$ denotes the Cauchy principal value integral defined in equation (2.19).

Proof. We will invert the Radon transform by performing the spectral analysis of the eigenvalue equation (2.24).

The direct problem: A $\bar{d}$-problem

In order to solve the direct problem, we solve equation (2.24) for all complex k values, assuming that the function f is known. We introduce the following change of variables from (x_1, x_2) to $(z, \bar{z})$:

$$z = \frac{1}{2i}\left(k - \frac{1}{k}\right)x_1 - \frac{1}{2}\left(k + \frac{1}{k}\right)x_2, \tag{2.29a}$$

$$\bar{z} = -\frac{1}{2i}\left(\bar{k} - \frac{1}{\bar{k}}\right)x_1 + \frac{1}{2}\left(\bar{k} + \frac{1}{\bar{k}}\right)x_2. \tag{2.29b}$$

Employing the chain rule we find

$$\partial_{x_1} = \frac{1}{2i}\left(k - \frac{1}{k}\right)\partial_z - \frac{1}{2\mathrm{i}}\left(\bar{k} - \frac{1}{\bar{k}}\right)\partial_{\bar{z}}, \tag{2.30a}$$

$$\partial_{x_2} = -\frac{1}{2}\left(k + \frac{1}{k}\right)\partial_z - \frac{1}{2}\left(\bar{k} + \frac{1}{\bar{k}}\right)\partial_{\bar{z}}. \tag{2.30b}$$

Hence, we are able to rewrite equation (2.24) in the following form:

$$\nu(|k|)\frac{\partial u(x_1, x_2, k)}{\partial \bar{z}} = f(x_1, x_2), \quad k \in \mathbb{C}, \quad |k| \neq 1, \tag{2.31}$$

where

$$\nu(|k|) = \frac{1}{2\mathrm{i}}\left(\frac{1}{|k|^2} - |k|^2\right). \tag{2.32}$$

Equation (2.31) can be further simplified, namely

$$u_{\bar{z}} = \frac{f}{\nu}, \quad |k| \neq 1. \tag{2.33}$$

It is important to note that if μ was analytic, then $\mu_{\bar{z}} = 0$, since the $\bar{z}$ derivative measures the "departure" from analyticity. Furthermore, we supplement equation (2.31) with the following boundary condition at infinity

$$u = O\left(\frac{1}{z}\right), \quad z \to \infty, \quad \text{i.e.} \quad \exists\, B > 0 \quad \text{such that} \quad |u| \leq \frac{B}{|z|}. \tag{2.34}$$

The solution of equation (2.31), equipped with the boundary condition (2.34), via Pompeiu's formula (see Lemma 2.3) is given by

$$u = \frac{1}{2\pi \mathrm{i}} \iint_{\mathbb{R}^2} \frac{f(x_1', x_2')}{\nu(|k|)} \frac{\mathrm{d}z' \wedge \mathrm{d}\bar{z}'}{z' - z}, \quad k \in \mathbb{C}, \quad |k| \neq 1. \tag{2.35}$$

By employing

$$\mathrm{d}z' \wedge \mathrm{d}\bar{z}' = \frac{1}{2\mathrm{i}} \left| \frac{1}{|k|^2} - |k|^2 \right| \mathrm{d}x_1' \mathrm{d}x_2',$$

we rewrite equation (2.35) as follows:

$$u(x_1, x_2, k) = \frac{1}{2\pi \mathrm{i}} \operatorname{sgn}\left(\frac{1}{|k|^2} - |k|^2 \right) \iint_{\mathbb{R}^2} f(x_1', x_2') \frac{\mathrm{d}x_1' \mathrm{d}x_2'}{z' - z}. \tag{2.36}$$

It is evident from equation (2.36) that u depends on k only through $z - z'$, hence $u(x_1, x_2, k)$ constitutes a *sectionally analytic* function with a "jump" across the unit circle $|k| = 1$ of the complex k-plane. Equation (2.36) represents the solution of the direct problem for all complex values of the eigenvalue k, in terms of the function f.

The inverse problem: A Riemann-Hilbert problem

In order to solve the inverse problem, we solve equation (2.24) in terms of $\widehat{f}$, instead of f itself. We note that equation (2.36) implies

$$u = O\left(\frac{1}{k}\right), \quad k \to \infty, \tag{2.37}$$

i.e., the solution u of equation (2.24) is bounded for all complex eigenvalues k.

We note that

$$z - z' = \frac{1}{2\mathrm{i}} \left(k - \frac{1}{k} \right) (x_1 - x_1') - \frac{1}{2} \left(k + \frac{1}{k} \right) (x_2 - x_2'). \tag{2.38}$$

In order to investigate the behavior of u as k approaches the unit circle, let

$$k^{\pm} = (1 \mp \varepsilon) e^{\mathrm{i}\theta}, \quad 0 \leq \theta < 2\pi, \quad \varepsilon > 0. \tag{2.39}$$

Hence,

$$k^+ \mp \frac{1}{k^+} = (1-\varepsilon)e^{\mathrm{i}\theta} \mp (1+\varepsilon)e^{-\mathrm{i}\theta} + O(\varepsilon^2), \tag{2.40a}$$

$$k^- \mp \frac{1}{k^-} = (1+\varepsilon)e^{\mathrm{i}\theta} \mp (1-\varepsilon)e^{-\mathrm{i}\theta} + O(\varepsilon^2). \tag{2.40b}$$

Equation (2.29a) implies

$$\begin{aligned} z - z' = (x_1 - x_1')\sin\theta - (x_2 - x_2')\cos\theta \\ \pm \mathrm{i}\varepsilon\left[(x_1 - x_1')\cos\theta - (x_2 - x_2')\sin\theta\right] + O(\varepsilon^2) \\ = \rho - \rho' \pm \mathrm{i}\varepsilon(\tau - \tau') + O(\varepsilon^2). \end{aligned} \tag{2.41}$$

Let $u^\pm$ denote the limits of the function u as k approaches the unit circle $|k| = 1$ from inside and outside, respectively:

$$u^\pm \equiv \lim_{\varepsilon\to 0} u(x_1, x_2, (1 \mp \varepsilon)e^{\mathrm{i}\theta}) = \lim_{\varepsilon\to 0} u(x_1, x_2, k^\mp). \tag{2.42}$$

Replacing $z - z'$ in equation (2.36) by the corresponding representation (2.41) yields

$$u^\pm = \mp\frac{1}{2\pi\mathrm{i}} \lim_{\varepsilon\to 0} \iint_{\mathbb{R}^2} \frac{\varphi(\rho', \tau', \theta)\mathrm{d}\rho'\mathrm{d}\tau'}{\rho' - [\rho \pm \mathrm{i}\varepsilon(\tau' - \tau)]}, \tag{2.43}$$

where

$$\varphi(\rho, \tau, \theta) = f\left(\tau\cos\theta - \rho\sin\theta, \tau\sin\theta + \rho\cos\theta\right), \tag{2.44}$$

i.e., φ is the function f expressed in the local coordinates. For the evaluation of the limit (2.43), we split the integral over $\mathrm{d}\tau'$, so as to control the sign of $\tau' - \tau$

$$\begin{aligned} u^\pm = \mp\frac{1}{2\pi\mathrm{i}} \lim_{\varepsilon\to 0} \int_{-\infty}^{\infty} \left\{ \int_{-\infty}^{\tau} \frac{\varphi\mathrm{d}\tau'}{\rho' - [\rho \pm \mathrm{i}\varepsilon(\tau' - \tau)]} \right. \\ \left. + \int_{\tau}^{\infty} \frac{\varphi\mathrm{d}\tau'}{\rho' - [\rho \pm \mathrm{i}\varepsilon(\tau' - \tau)]} \right\} \mathrm{d}\rho'. \end{aligned} \tag{2.45}$$

In the first integral of (2.45) $(\tau' - \tau)$ is negative, whereas in the second integral $(\tau' - \tau)$ is positive, thus

$$\begin{aligned} u^\pm = \mp\frac{1}{2\pi\mathrm{i}} \int_{-\infty}^{\tau} \left\{\mp\pi\mathrm{i}\varphi(\rho, \tau', \theta) + (\mathcal{H}\varphi)(\rho, \tau', \theta)\right\} \mathrm{d}\tau' \\ \mp \frac{1}{2\pi\mathrm{i}} \int_{\tau}^{\infty} \left\{\pm\pi\mathrm{i}\varphi(\rho, \tau', \theta) + (\mathcal{H}\varphi)(\rho, \tau', \theta)\right\} \mathrm{d}\tau', \end{aligned} \tag{2.46}$$

where we have employed the Plemelj formulæ, see Lemma 2.5, as well as the definition of the Hilbert transform, see equation (2.28). In the right-hand side of equation (2.46) we add and subtract $\mp\frac{1}{2\pi\mathrm{i}}\int_\tau^\infty \pi\mathrm{i}\varphi(\rho,\tau',\theta)\mathrm{d}\tau'$, to obtain

$$u^\pm = \mp(P^\mp \hat{f})(\rho,\theta) - \int_\tau^\infty \varphi(\rho,\tau',\theta)\mathrm{d}\tau', \tag{2.47}$$

where

$$(P^\mp g)(\rho) = \pm\frac{g(\rho)}{2} + \frac{1}{2\pi\mathrm{i}}\ PV\int_{-\infty}^{\infty}\frac{g(r)}{r-\rho}\mathrm{d}r = \pm\frac{g(\rho)}{2} + \frac{1}{2\mathrm{i}}(\mathcal{H}g)(\rho), \tag{2.48}$$

denote a family of projectors in the variance ρ.

Equations (2.42) and (2.47) imply

$$u^+ - u^- = \mathrm{i}(\mathcal{H}\widehat{f})(\rho,\theta). \tag{2.49}$$

We supplement equation (2.49) with the boundary condition (2.37) and we construct a scalar Riemann-Hilbert problem. The solution to this problem is, according to Lemma 2.6,

$$u = \frac{1}{2\pi\mathrm{i}}\int_{|k'|=1}\frac{(u^+-u^-)(\rho,\theta')\mathrm{d}k'}{k'-k}. \tag{2.50}$$

The equation $|k'|=1$ can be rewritten as $k' = e^{\mathrm{i}\theta'}$, implying that $\mathrm{d}k' = \mathrm{i}e^{i\theta'}\mathrm{d}\theta'$, hence

$$u = \frac{1}{2\pi\mathrm{i}}\int_0^{2\pi}\frac{(u^+-u^-)(\rho,\theta')\mathrm{i}e^{\mathrm{i}\theta'}\mathrm{d}\theta'}{e^{\mathrm{i}\theta'}-k}. \tag{2.51}$$

Replacing in equation (2.51) $u^+ - u^-$ by the right-hand side of equation (2.49), yields:

$$u = -\frac{1}{2\pi\mathrm{i}}\int_0^{2\pi}\frac{e^{\mathrm{i}\theta'}(\mathcal{H}\widehat{f})(\rho,\theta')\mathrm{d}\theta'}{e^{\mathrm{i}\theta'}-k},\ k\in\mathbb{C},\ |k|\neq 1,\ \rho\in\mathbb{R}. \tag{2.52}$$

Equation (2.52) represents the solution to the inverse problem. In order to express f as a function of $\widehat{f}$ we must utilize the equivalence of the solutions of the direct and inverse problems, provided by equations (2.36) and (2.52), respectively. We proceed with the asymptotic analysis of the behavior of u for large k. Equation (2.52) yields

$$u = \left\{ \frac{1}{2\pi \mathrm{i}} \int_0^{2\pi} e^{\mathrm{i}\theta'} (\mathcal{H}\widehat{f})(\rho, \theta') \mathrm{d}\theta' \right\} \frac{1}{k} + O\left(\frac{1}{k^2}\right), \quad k \to \infty. \tag{2.53}$$

Substituting in equation (2.24) the above expression, we find that the $O(1)$ term implies

$$f = \frac{1}{4\pi \mathrm{i}} \left(\partial_{x_1} - \mathrm{i}\partial_{x_2}\right) \int_0^{2\pi} e^{\mathrm{i}\theta} (\mathcal{H}\widehat{f})(\rho, \theta) \Big|_{\rho = x_2 \cos\theta - x_1 \sin\theta} \mathrm{d}\theta. \tag{2.54}$$

Using the identity

$$\left(\partial_{x_1} - \mathrm{i}\partial_{x_2}\right) = e^{-\mathrm{i}\theta} (\partial_\tau - \mathrm{i}\partial_\rho), \tag{2.55}$$

in equation (2.54), we obtain equation (2.27). ■

An immediate consequence of the above, is the following corollary.

Corollary 2.9. *Let $k^\pm$ denote the limits of k, defined in equation* (2.39)*, as k approaches the unit circle from inside and outside the unit circle ($|k| = 1$), and let z and ν be defined in equations* (2.29a) *and* (2.32)*, respectively. Then,*

$$\lim_{k \to k^\pm} \left(\partial_{\bar{z}}^{-1} \left\{ \frac{f(x_1, x_2)}{\nu(|k|)} \right\} \right) = \mp \left(P^\mp \widehat{f} \right)(\rho, \theta) - \int_\tau^\infty \varphi(\rho, s, \theta) \mathrm{d}s, \qquad (\rho, \tau) \in \mathbb{R}^2, \quad \theta \in (0, 2\pi), \tag{2.56}$$

where $\widehat{f}$ denotes the Radon transform of f (defined in equation (1.9)*), and $P^\pm$, (ρ, τ) and φ are defined in equations* (2.48)*,* (1.6) *and* (2.44)*, respectively.*

Proof. Equation (2.33) implies that

$$u(x_1, x_2, k) = \partial_{\bar{z}}^{-1} \left\{ \frac{f(x_1, x_2)}{\nu(|k|)} \right\}. \tag{2.57}$$

Therefore, taking the limit of equation (2.57) as k approaches the unit circle $|k| = 1$ from inside and outside yields

$$u^\pm(x_1, x_2) = \lim_{k \to k^\pm} \left(\partial_{\bar{z}}^{-1} \left\{ \frac{f(x_1, x_2)}{\nu(|k|)} \right\} \right), \tag{2.58}$$

where $u^\pm$ is defined in equation (2.42). Inserting equation (2.47) in equation (2.58) yields equation (2.56). ■

2.3 The inversion of the attenuated Radon transform in $\mathbb{R}^2$

In [7] Novikov demonstrated that the inverse attenuated Radon transform can be derived by performing the spectral analysis of the eigenvalue equation (2.25), which is a slight generalization of the eigenvalue equation (2.24). However, one can derive the inversion of the attenuated Radon transform in a simpler manner, using the results of the inversion of the non-attenuated Radon transform (see Section 2.2) as well as Corollary 2.9.

Proposition 2.10. *The inverse of the attenuated Radon transform $\widehat{f}_\mu(\rho,\theta)$ of a function $f(x_1,x_2)$, attenuated with respect to the function $\mu(x_1,x_2)$ (with $f,\mu\in S(\mathbb{R}^2)$), defined in equation* (1.15) *is given by*

$$f(x_1,x_2)=\frac{1}{4\pi}(\partial_{x_1}-\mathrm{i}\partial_{x_2})\int_0^{2\pi}e^{\mathrm{i}\theta}J(x_1,x_2,\theta)\mathrm{d}\theta,\quad -\infty<x_1,x_2<\infty, \tag{2.59a}$$

where the function J is defined by

$$J(x_1,x_2,\theta)=e^{M(\tau,\rho,\theta)}L_\mu(\rho,\theta)\widehat{f}_\mu(\rho,\theta)\Big|_{\substack{\tau=x_2\sin\theta+x_1\cos\theta\\ \rho=x_2\cos\theta-x_1\sin\theta}}, \tag{2.59b}$$

with M and L_μ defined by

$$M(\tau,\rho,\theta)=\int_\tau^\infty \mu\left(s\cos\theta-\rho\sin\theta,s\sin\theta+\rho\cos\theta\right)\mathrm{d}s, \tag{2.59c}$$

$$L_\mu(\rho,\theta)=e^{P^-\widehat{\mu}(\rho,\theta)}P^-e^{P^-\widehat{\mu}(\rho,\theta)}+e^{-P^+\widehat{\mu}(\rho,\theta)}P^+e^{P^+\widehat{\mu}(\rho,\theta)}; \tag{2.59d}$$

in equation (2.59d)*, $\widehat{\mu}$ represents the Radon transform of the attenuation function μ, i.e.,*

$$\widehat{\mu}(\rho,\theta)=\int_{-\infty}^{\infty}\mu\left(\tau\cos\theta-\rho\sin\theta,\tau\sin\theta+\rho\cos\theta\right)\mathrm{d}\tau,$$
$$0\le\theta<2\pi,\quad -\infty<\rho<\infty, \tag{2.59e}$$

whereas the projection operators $P^\pm$ are defined in equation (2.48).

Proof. Rewriting equation (2.25) in the form

$$u_{\bar{z}} + \frac{\mu}{\nu} u = \frac{f}{\nu}, \tag{2.60}$$

and multiplying both sides of equation (2.60) by $e^{\partial_{\bar{z}}^{-1}\left\{\frac{\mu}{\nu}\right\}}$, yields

$$u_{\bar{z}} e^{\partial_{\bar{z}}^{-1}\left\{\frac{\mu}{\nu}\right\}} + \frac{\mu}{\nu} u e^{\partial_{\bar{z}}^{-1}\left\{\frac{\mu}{\nu}\right\}} = \frac{f}{\nu} e^{\partial_{\bar{z}}^{-1}\left\{\frac{\mu}{\nu}\right\}}. \tag{2.61}$$

Therefore,

$$\frac{\partial}{\partial \bar{z}} \left(u e^{\partial_{\bar{z}}^{-1}\left\{\frac{\mu}{\nu}\right\}} \right) = \frac{f}{\nu} e^{\partial_{\bar{z}}^{-1}\left\{\frac{\mu}{\nu}\right\}}. \tag{2.62}$$

Hence,

$$e^{\partial_{\bar{z}}^{-1}\left\{\frac{\mu}{\nu}\right\}} u = \partial_{\bar{z}}^{-1} \left\{ \frac{f}{\nu} e^{\partial_{\bar{z}}^{-1}\left\{\frac{\mu}{\nu}\right\}} \right\}, \quad (x_1, x_2) \in \mathbb{R}^2, \quad k \in \mathbb{C}. \tag{2.63}$$

Equation (2.63) represents the solution to the direct problem, which, following the same approach as with the inversion of the non-attenuated Radon transform, defines a sectionally analytic function u with a "jump" across the unit circle, $|k| = 1$, of the complex k-plane. Furthermore, u satisfies the estimate (2.37). Therefore, u is given by equation (2.51). However, this time the jump $u^+ - u^-$ will be different than the one given by equation (2.49). The determination of the jump involves the limits of $\partial_{\bar{z}}^{-1}(f/\nu)$ as k approaches $k^{\pm}$, hence can be computed via Corollary 2.9. In the limit $k \to k^{\pm}$, equation (2.63), where f is replaced by μ, implies

$$e^{\left(\mp P^{\mp}\widehat{\mu} - \int_{\tau}^{\infty} \Phi(\rho,s,\theta)\mathrm{d}s\right)} u^{\pm} = \lim_{k \to k^{\pm}} \partial_{\bar{z}}^{-1} \left\{ \frac{f}{\nu} e^{\left(\mp P^{\mp}\widehat{\mu} - \int_{\tau}^{\infty} \Phi(\rho,s,\theta)\mathrm{d}s\right)} \right\}, \tag{2.64}$$

where $\widehat{\mu}$ denotes the Radon transform of μ, defined in equation (1.9), and Φ denotes the function μ expressed in the local coordinates:

$$\Phi(\rho, \tau, \theta) = \mu\left(\tau\cos\theta - \rho\sin\theta, \tau\sin\theta + \rho\cos\theta\right). \tag{2.65}$$

Applying Corollary 2.9 on the right hand side of equation (2.64) and using $\widehat{f}_{\mu}$ defined in equation (1.15) yields

$$\mp P^{\mp} e^{\mp P^{\mp}\widehat{\mu}} \widehat{f}_{\mu} - \int_{\tau}^{\infty} \varphi(\rho, \tau', \theta) e^{\mp P^{\mp}\widehat{\mu} e^{-\int_{\tau}^{\infty} \Phi(\rho,s,\theta)}\mathrm{d}s} \mathrm{d}\tau', \tag{2.66}$$

where in equation (2.56), instead of f we used the function

$$\left(e^{\mp P^{\mp}\widehat{\mu}e^{-\int_{\tau}^{\infty}\Phi(\rho,s,\theta)}\mathrm{d}s}\right)f.$$

We note that inside the integral of the expression (2.66), the term $e^{\mp P^{\mp}\widehat{\mu}}$ is independent of τ', hence it can come outside the integral. This means that this specific term can be canceled throughout equation (2.64). Therefore, the jump is given by

$$u^{+}-u^{-}=-J, \tag{2.67}$$

where J is defined in equation (2.59b). Hence, equation (2.51) implies

$$u=-\frac{1}{2\pi}\int_{0}^{2\pi}\frac{J(\rho,\tau,\theta')e^{\mathrm{i}\theta'}\mathrm{d}\theta'}{e^{\mathrm{i}\theta'}-k}. \tag{2.68}$$

Therefore,

$$u=\left[\frac{1}{2\pi}\int_{0}^{2\pi}e^{\mathrm{i}\theta}J(\rho,\tau,\theta)\mathrm{d}\theta\right]\frac{1}{k}+O\left(\frac{1}{k^2}\right),\quad \text{as}\quad k\to\infty. \tag{2.69}$$

Substituting equation (2.69) in equation (2.25), we find that the $O(1)$ term in equation (2.25) implies equation (2.59a). ■

Part II

Applications in PET and SPECT medical imaging

Chapter 3

Sinogram masking with CUSUM

The present chapter deals with the concept of sinogram contour detection in the context of inverse problems and it is based on [45] and [48]. The problem of determining the contours of objects in nuclear medicine images has been studied extensively in the past, however most of the analysis has focused on a single object as opposed to multiple objects. The aim of this work is to develop an automated method for determining the contour of either single or multiple objects in filtered backprojection (FBP) reconstructed tomographic images of nuclear medicine modalities such as PET and SPECT. These contours can be used for computing body edges for attenuation correction in both PET and SPECT, as well as for eliminating corresponding streak artifacts outside the objects; this could be extremely useful in compressive sensing reconstruction [66]. Contour detection is accomplished by applying a modified cumulative sums (CUSUM) scheme in the sinogram, i.e. the data space (the space of the Radon transform of the images). Our novel approach automatically detects all objects in the image, without requiring *a priori* knowledge of the number of distinct objects in the reconstructed image. This method has been evaluated in simulated phantoms, such as an image-quality (IQ) phantom and two digital multi-object phantoms, as well as a real NEMA phantom and a clinical thoracic study. In this direction, a GE Discovery PET scanner was employed. The detected contours achieved root mean square accuracy of 1.14 pixels, 1.69 pixels and 3.28 pixels and a Hausdorff distance of 3.13, 3.12 and 4.50 pixels, for the simulated

image-quality phantom PET study, the real NEMA phantom and the clinical thoracic study, respectively. These results correspond to a significant improvement over recent results obtained in similar studies. Furthermore, we obtained an optimal sub-pattern assignment (OSPA) localization error of 0.94 and 1.48, for the two-objects and three-objects simulated phantoms, respectively. Our method performs efficiently for sets of convex objects and hence it provides a robust tool for automatic contour determination with precise results. It is also worth noting that sinogram masking results in a significant reduction in calculation time during reconstruction.

3.1 An introduction to edge-detection

In nuclear medicine the two prevailing, noninvasive tomographic imaging modalities are positron emission tomography (PET) and single-photon emission computed tomography (SPECT). These nuclear medicine techniques, which are usually referred to as "emission tomography", have significant preclinical and clinical applications and can be employed to a vast variety of medical fields including neurology, oncology, cardiology and psychiatry [67].

PET uses the unique decay characteristics of radiopharmaceuticals, such as FDG (^{18}F-2-deoxy-2-fluoro-D-glucose). When FDG is intravenously introduced into the patient's body, it is distributed in tissues in a manner determined by its biochemical properties [38]. Then, PET detectors detect the corresponding annihilation photons (coincidence gamma rays) that are produced when positrons interact with electrons [4]. On the other hand, in SPECT the intravenously injected tracers, such as technetium (^{99}Tc) labeled with an appropriate agent, radiate single photons. This time, the detectors count individual photons (γ-ray events) [5].

Image reconstruction is the main goal for almost all inverse problems in imaging, although it is usually adopted in a tomography context, suggesting reconstruction from projection data, i.e. sinograms [68]. There are several reconstruction algorithms which are mainly distinguished as analytic and iterative. The predominant analytic approach for image reconstruction is *filtered backprojection* (FBP). FBP is based on the inversion of the Radon transform via the central slice theorem [63], see theorem 2.1 in page 61. The advantages of FBP amongst other analytic methods are undoubtedly its speed and simplicity. However, its main limitation lies on its mere for-

mulation, which, intrinsically, does not incorporate the statistical nature of light; at the same time, it usually generates “streak artifacts" in the reconstructed images involved. These streak artifacts are due to incomplete data measurement, such as angular undersampling, or poor counting statistics [4]. The dominant iterative approach for image reconstruction is *ordered subset expectation maximization* (OSEM). In this chapter, we will focus on FBP-reconstructed images.

Although OSEM image reconstructions do not exhibit streak artifacts and incorporate the statistical nature of light in the Poisson sense, there are numerous cases where FBP has shown to produce improved quantitative results over OSEM. For example, in several neuroreceptor studies, especially if a low count rate cannot be avoided, FBP reconstruction is sometimes preferable to OSEM, in order to estimate the total volume of the distribution [69]. Another study by Reilhac et al. [70] suggests that the iterative reconstruction methods are biased at low statistics, especially in the lower part of the image dynamic range and for cold regions. Furthermore, according to Boellaard et al. [71], patient data indicated that OSEM and FBP provide equivalent results in the imaging of brain, myocardium, and tumor regions of interest (ROIs).

Since the 1980s, the main mathematical problem of determining the contour of an object for attenuation purposes in nuclear medicine has received reasonable attention in the literature, especially in studies where contour detection is accomplished via the sinogram. In cases where no computed tomography (CT) is present, contour detection is a necessary approach for determining the corresponding attenuation map for attenuation correction purposes. Nevertheless, even in cases with a CT present (such as PET/CT), CT delivers single snapshots of the breathing cycle and, when used for attenuation correction, it may generate edge artifacts in most of the PET respiratory cycle, even though respiratory gating of PET is, in general, possible [72].

There are numerous methods that have been proposed in order to address the problem of contour detection. It is obvious that the simplest possible method is sinogram thresholding, although this relatively subjective method is neither adaptive nor automatic. Other contour detection methods include: (a) the maximum slopes algorithm for head contour determination in PET [73], making use of the first derivative of the projections in order to

specify the abrupt changes through the derivative maxima, (b) the Tomitani method, encompassing differential geometry aspects in contour finding [74], (c) the seminal Canny approach to edge detection, encompassing principles from the calculus of variations [75], (d) the automated body contours finding method in SPECT [76] which incorporates thresholding, smoothing and fourth-order Fourier fitting, (e) the online brain attenuation correction procedure for head contour determination [77], based on the Tomitani method and a sinogram finite differences scheme, (f) the method for determination of concave body outlines from SPECT sinograms before reconstruction making use of a fourth-rank tensor projector operator [78], (g) the mixed detection and validation methods utilizing the sinogram derivatives and cosine fitting in low count emission images [72], (h) the sinogram segmentation technique, achieved by surface deformation fitting between the projected model and the input sinogram [79], (i) the novel truncation correction method, utilizing the idea of sinogram decomposition, where sinogram curves are considered as individual image points [80], (j) the sinogram segmentation technique for direct metal suppression in CT [81], (k) the metal artifact reduction through sinogram segmentation method of lumbar spine CT images [82], (l) the pre-reconstruction sinogram filtering approach based on three-dimensional (3D) mean-median filters in PET reconstructions, aiming to minimize angular blurring artifacts, to smooth flat regions and to preserve the edges [83], as well as (m) the denoising algorithm for cone-beam CT sinograms, encompassing a certain regularization in terms of gradient and Hessian [84].

Most of the aforementioned methods correspond to single-object cases. More specifically, the first two and the fifth one focus mainly on the brain and adjacent skull regions. Furthermore, all the methods mentioned above are based on the concepts of thresholding, image segmentation and sinogram differentiation. The method presented in this chapter takes into account only the values of the sinogram in a straightforward manner, without computing any corresponding threshold or derivative.

The main goal of the current chapter is to develop an automated method for determining the contour of multiple objects in FBP-reconstructed images. This method can be used for obtaining body edges for attenuation correction purposes. In this direction, it is worth mentioning that:

(i) in PET/CT, body edge detection throughout the PET sequence can improve the single CT scan before attenuation correction [72],

(ii) in brain SPECT imaging, contour determination is essential for accurate attenuation correction [72], and

(iii) in PET and SPECT CT-less imaging, it could provide a good starting point for a uniform attenuation map. Furthermore, body edge detection could eliminate streak artifacts outside the body, which could be very useful in the area of compressive sensing reconstruction, where the sinogram and image can be "cleaned" for outside artifacts in every iteration [66].

By applying a simplified cumulative sums (CUSUM) scheme in the sinogram, as originally developed by Page [85], we were able to automatically detect all objects in the image without requiring:

- prior knowledge of the number of distinct objects in the reconstructed image, and
- visually selected threshold values, the calculation of noisy sinogram derivatives, or the use of segmentation techniques.

The image masking process is accomplished via the sinogram mask, taking into account one of the results of Kastis et al. [56]. In particular, that a pixel which is outside the boundary spanned by an object (and hence has zero value) can be singled out from the sinogram by first identifying the detector locations $\rho_k = \rho_k(\theta_l)$ for all angles θ_l that receive contribution from this pixel; then, for every (x, y) if there is even one θ_k such that $\widehat{f}(\rho_k, \theta_l) = 0$ it follows that $f(x, y)$ must be zero. This condition arises from the very nature of the Radon transform itself, which is a sum of positive terms and thus is zero only when *all* terms are zero. Following this result, we are able to reconstruct the sinogram mask in order to produce the image mask. This way image masking is accomplished via sinogram masking, since we reconstruct the masked sinogram.

3.2 Materials and methods used in CUSUM

3.2.1 The CUSUM-based algorithm

The CUSUM algorithm was originally introduced by E.S. Page in his seminal Biometrika article in 1954 [85]. It encapsulates the notions of:

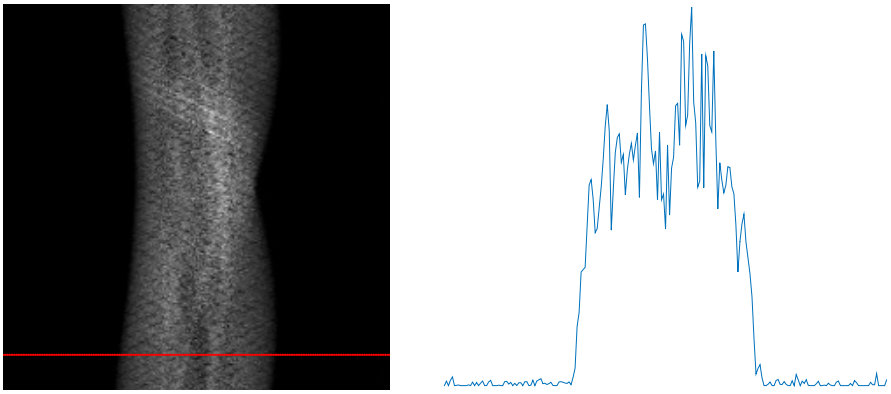

(a) All sinogram rows. (b) Single sinogram row.

Figure 3.1: Sinogram finite support for nuclear imaging: (a) 2D and (b) 3D.

- adaptive thresholding, and
- complete memory of the information embedded in previous observations [86].

Let $\widehat{f}_{ij}$ denote the sinogram, i.e. the tabulated, matrix version of either the Radon transform (PET) or the attenuated Radon transform (SPECT) of the two-dimensional (2D) radioactivity distribution function $f(x, y)$, as in [56]. The sinogram is a matrix with N_θ rows (angular dimension, θ) and N_ρ columns (signed distance dimension, ρ), with elements

$$\widehat{f}_{ij} = \widehat{f}(\rho_i, \theta_j), \quad \text{for} \quad i = 1, \ldots, N_\rho, \quad \text{and} \quad j = 1, \ldots, N_\theta.$$

In medical modalities such as PET and SPECT, we assume that $(\widehat{f}_{ij})$ has finite support, see figure 3.1. Given that $\widehat{f}_{ij}$ has finite support, it is safe to assume that for every row j of the sinogram there are two "almost zero intervals", one on the leftmost and another on the rightmost side. Let the intervals' lengths be ℓ_L and ℓ_R pixels, respectively. For the sake of simplicity, we assume that

$$\ell_L = \ell_R = \ell$$

and we consider this length a user-defined parameter. This length parameter, ℓ, is the only user-defined parameter in our method and depends on the size of the object. The parameter ℓ provides a rather precise estimation of the noise distribution for the two edges (either left or right) of the sinogram.

In order to find the left as well as the right abrupt changes (jumps) of the sinogram in each row, we introduce the following cumulative sums (CUSUM statistics) $L_n^{(j)}$ and $R_n^{(j)}$ for the left and right side respectively and for each row j:

$$L_0^{(j)} = 0, \tag{3.1a}$$

$$L_n^{(j)} = \max\left\{0, L_{n-1}^{(j)} + \widehat{f}_{n,j} - \left(\mu_L^{(j)} + \lambda\sigma_L^{(j)}\right)\right\}, \quad n = 1, \ldots, N_\rho, \tag{3.1b}$$

where $\mu_L^{(j)}$ and $\sigma_L^{(j)}$ are the mean and standard deviation (SD) of the left "almost zero interval" of row j, i.e.:

$$\mu_L^{(j)} = \frac{1}{\ell}\sum_{i=1}^{\ell}\widehat{f}_{ij} \quad \text{and} \quad \sigma_L^{(j)} = \sqrt{\frac{1}{\ell}\sum_{i=1}^{\ell}\left(\widehat{f}_{ij} - \mu_L^{(j)}\right)^2}, \tag{3.2}$$

and λ is a user-defined positive number (namely the multiplier of the SD), conventionally set at $\lambda = 3$, but any λ may be used [87]. The value of λ is related to the size of the persistent shift we are interested to detect and the smaller the size the smaller the value of λ. From the above definition it is clear that, until it detects the first abrupt change from left to right, the left cumulative sum is non-decreasing, i.e.

$$L_m^{(j)} \geq L_n^{(j)} \quad \text{for all} \quad m > n.$$

Similarly,

$$R_{N_\rho}^{(j)} = 0, \tag{3.3a}$$

$$R_{n-1}^{(j)} = \max\left\{0, R_n^{(j)} + \widehat{f}_{n-1,j} - \left(\mu_R^{(j)} + \lambda\sigma_R^{(j)}\right)\right\}, \quad n = N_\rho, N_{\rho-1}, \ldots, 2, 1, \tag{3.3b}$$

where $\mu_R^{(j)}$ and $\sigma_R^{(j)}$ are the mean and standard deviation of the right "almost zero interval", i.e.:

$$\mu_R^{(j)} = \frac{1}{\ell}\sum_{i=N_\rho-\ell+1}^{N_\rho}\widehat{f}_{ij} \quad \text{and} \quad \sigma_R^{(j)} = \sqrt{\frac{1}{\ell}\sum_{i=N_\rho-\ell+1}^{N_\rho}\left(\widehat{f}_{ij} - \mu_R^{(j)}\right)^2}. \tag{3.4}$$

Once again, from the above definition it is clear that, until it detects the first abrupt change from right to left, the right cumulative sum is non-increasing, i.e.

$$R_m^{(j)} \leq R_n^{(j)} \quad \text{for all} \quad m > n.$$

3.2.2 Single-object contour determination

In order to find both the leftmost and the rightmost boundary pixels of the j-th row of the sinogram, denoted by

$$\rho_{L_0}^{(j)} \quad \text{and} \quad \rho_{R_0}^{(j)},$$

respectively, we find both indices by the following:

$$i_{L_0}^{\prime(j)} = \max_{1<n<N_\rho} \ker L_n^{(j)} \quad \text{and} \quad i_{R_0}^{\prime(j)} = \min_{1<n<N_\rho} \ker R_n^{(j)}, \tag{3.5}$$

where $\ker \Lambda$ is the kernel (or zero set) of Λ, defined by

$$\ker \Lambda = \{\text{all } i \text{ such that } \Lambda = 0\}, \quad \Lambda \in \left\{ L_i^{(j)}, R_i^{(j)} \right\}.$$

For every row j, two index “clouds" are created, namely

$$(i_{L_0}^{\prime(j)}, j) \quad \text{and}(i_{R_0}^{\prime(j)}, j).$$

We proceed with polynomial fitting of degree $n \geq 3$ (user defined) and as a result we get two index curves, namely

$$i_{L_0}^{\text{fit}} = i_{L_0}^{\text{fit}}(j) \quad \text{and} \quad i_{R_0}^{\text{fit}} = i_{R_0}^{\text{fit}}(j).$$

The user may add padding of p pixels, where p is a non-negative integer, so that the indices of the left and right exterior boundaries are

$$i_{L_0}^{(j)} = i_{L_0}^{\text{fit}}(j) - p \quad \text{and} \quad i_{R_0}^{(j)} = i_{R_0}^{\text{fit}}(j) + p, \quad p = 0, 1, \ldots, \left\lfloor \frac{N_\rho}{2} \right\rfloor. \tag{3.6}$$

In this manner, two curves are created, namely

$$\rho_{L_0} = \rho_{L_0}(\theta_j) \quad \text{and} \quad \rho_{R_0} = \rho_{R_0}(\theta_j),$$

which correspond to

$$i_{L_0} = i_{L_0}(j) \quad \text{and} \quad i_{R_0} = i_{R_0}(j),$$

respectively. These two curves are the exterior edges (or outer boundary curves) of the sinogram. If the sinogram consists of one solid non-zero region and hence the image depicts a single object with one closed boundary, then the sinogram mask is created rather effortlessly, see Sec. 3.2.4.

3.2.3 Multi-object contour determination

If the image depicts N distinct objects with closed boundaries, then the sinogram consists of many almost-zero regions. In this case, we need to distinguish each row j according to its number of peaks, N_j, i.e. if for a fixed row j^* (and hence fixed angle θ_{j^*}) the number of peaks is $N_{j^*} = 2$, then the function

$$g(\rho_i) = \widehat{f}_{ij^*} = \widehat{f}(\rho_i, \theta_{j^*})$$

is bimodal in ρ_i. The number of distinct objects in the image is ruled by the number of peaks, for each row, in the following manner:

$$N = \max_{1 \le j \le N_\theta} N_j. \tag{3.7}$$

Then, in the case of multimodal sinograms, for each angle θ, we must search, again via cumulative sums, inside the exterior index interval

$$I_0^{(j)} = [i_{L_0}^{(j)}, i_{R_0}^{(j)}], \tag{3.8}$$

for “almost zero" subintervals. Therefore, we are trying to find left and right “inner boundary" pixels, namely

$$i_{L_k}^{(j)} \quad \text{and} \quad i_{R_k}^{(j)}, \quad \text{for} \quad k = 1, \dots N_j - 1,$$

outside of which there are no counts, i.e. the sinogram value is zero. We note that $k = 0$ represents the one-object case, described above. For simplification we introduce the notation

$$I_k^{(j)} = [i_{L_{k-1}}^{(j)}, i_{R_{N_j-k}}^{(j)}], \quad k = 1, \dots, N_j, \quad N_j > 1. \tag{3.9}$$

Another difficulty in the multi-object case arises from the fact that there is no *a priori* knowledge of the number of distinct objects, N. The way to overcome this difficulty is to deploy M CUSUM "agents", A_m, inside $I_0^{(j)}$. It is important to note that M is a user-defined, sufficiently large positive integer; recommended values for this parameter require $M > N_\rho$, for example $M = 1000$. Each of these agents is responsible for pinpointing any abrupt changes both on its left and on its right; it begins its search from random starting pixels,

$$s_m \in I_0^{(j)}, \quad m = 1, \ldots, M,$$

and makes use of the CUSUM algorithm inside $I_0^{(j)}$. The above imply that the exact same method is being used inside the initial interval, only this time there exists an element of randomness, due to the fact that we do not know *a priori* whether an agent will find or not a new subinterval, i.e. we do not know whether $N \geq 2$ or not in advance.

Similarly, we introduce the following cumulative sums $L_n^{(j)}(A_m)$ and $R_n^{(j)}(A_m)$ for the left and right side respectively and for each row j:

$$L_{\rho_{L_0}}^{(j)}(A_m) = 0, \tag{3.10a}$$

$$L_n^{(j)}(A_m) = \max\left\{0, L_{n-1}^{(j)}(A_m) + \widehat{f}_{n,j} - \left(\mu_L^{(j)} + \lambda\sigma_L^{(j)}\right)\right\}, \tag{3.10b}$$

and

$$R_{N_\rho}^{(j)}(A_m) = 0, \tag{3.11a}$$

$$R_{n-1}^{(j)}(A_m) = \max\left\{0, R_n^{(j)}(A_m) + \widehat{f}_{n-1,j} - \left(\mu_R^{(j)} + \lambda\sigma_R^{(j)}\right)\right\}, \tag{3.11b}$$

where the parentheses emphasize the dependence of each (left and right) CUSUM statistic on the m-th agent, starting at pixel s_m, $m = 1, \ldots, M$, $\mu_L^{(j)}$ and $\sigma_L^{(j)}$ are defined in equation (3.2), $\mu_R^{(j)}$ and $\sigma_R^{(j)}$ are defined in equation (3.4), and λ is described above. Then, in order to find $i_{L_1}^{(j)}$, if it exists, i.e. $N_j > 1$, we take the minimum over the agents

$$i_{L_1}^{(j)} = \min_{1 \leq m \leq M}\left\{\max_{1<n<N_\rho} \ker L_n^{(j)}(A_m)\right\} - p, \tag{3.12a}$$

and in order to find $i_{R_1}^{(j)}$, if it exists, we take the maximum over the agents

$$i_{R_1}^{(j)} = \max_{1\leq m\leq M}\left\{\min_{1<n<N_\rho} \ker R_n^{(j)}(A_m)\right\} + p, \tag{3.12b}$$

We follow the same procedure, recursively, to find indices

$$i_{L_2}^{(j)} \quad \text{and} \quad i_{R_2}^{(j)} \quad \text{up to} \quad i_{L_{N_j-1}}^{(j)} \quad \text{and} \quad i_{R_{N_j-1}}^{(j)}, \quad \text{for} \quad N_j > 1,$$

wherever they exist. It is important to note that if the boundary pixel $i_{L_{k^*}}^{(j)}$ (or $i_{R_{k^*}}^{(j)}$) does not exist, for some

$$k^* \leq N_j - 1,$$

then we assign this pixel an index of zero, i.e. if

$$k^* \quad \text{is such that} \quad \nexists \quad i_{L_{k^*}}^{(j)} \quad \text{or} \quad \nexists \quad i_{R_{k^*}}^{(j)},$$

then:

$$i_{L_k}^{(j)} = 0 \quad \text{and} \quad i_{R_k}^{(j)} = 0 \quad \forall \quad k > k^*. \tag{3.12c}$$

Using the above definition, we are able to quantify the inability to further stratify the subintervals $I_k^{(j)}$ without prior knowledge of N_j.

3.2.4 Sinogram masking

Unimodal sinograms

Sinogram masking when $N = 1$ is performed by setting, for each row j, the mask equal to one inside $I_0^{(j)}$ and equal to zero everywhere else. The sinogram mask, $\mathbf{M}_S^1$, is a matrix consisting of zeros and ones and is defined as follows:

$$\mathbf{M}_S^1(\rho_i, \theta_j) = \begin{cases} 1, & \text{if } i \in I_0^{(j)} \\ 0, & \text{otherwise} \end{cases}, \quad \text{for} \quad N = 1. \tag{3.13a}$$

Multimodal sinograms

Sinogram masking in the case of $N > 1$ can be proved to be quite more challenging; it is performed by setting, for each row j, the mask equal to

one inside the intervals $I_k^{(j)}$, $k = 1, \ldots, N$ and equal to zero everywhere else. Once again, the sinogram mask, $\mathbf{M}_S^N$, is a matrix consisting of zeros and ones and is defined as a slight modification of equation (3.13a):

$$\mathbf{M}_S^N(\rho_i, \theta_j) = \begin{cases} 1, & \text{if } i \in \bigcup_{k=1}^{N} I_k^{(j)} \\ 0, & \text{otherwise} \end{cases}, \quad \text{for} \quad N > 1, \tag{3.13b}$$

where $N > 1$ and $I_k^{(j)}$ are defined in equations (3.7) and (3.9) respectively. We note that equations (3.13) provide the sinogram mask for all cases, without prior specification of N.

3.2.5 Image masking

The image mask $\mathbf{M}_I$ is constructed from the sinogram mask taking into account one of the main results of Kastis et al. [56], namely that a pixel which is outside the boundary spanned by an object and hence has zero value, can be singled out from the sinogram by first identifying the detector locations $\rho_k = \rho_k(\theta_l)$ for all angles θ_l that receive contribution from this pixel; then, for every (x, y) if there is even one θ_k such that $\widehat{f}(\rho_k, \theta_l) = 0$ it follows that $f(x, y)$ must be zero. This condition arises from the very nature of the Radon transform (sinogram), which is a sum of positive terms and thus is zero only when *all* terms are zero. Following this result, we reconstruct the sinogram mask in order to produce the image mask.

In this direction, let Q_x and Q_y denote the number of rows (x direction) and columns (y direction) of the reconstructed image matrix. Common practice in nuclear imaging suggests square images, i.e $Q_x = Q_y = Q$, hence the image mask $\mathbf{M}_I = \mathbf{M}_I(x_i, y_j)$, $i, j = 1, \ldots, Q$ is a square $Q \times Q$ matrix. For every $(x_i, y_j)_{i,j=1}^{Q}$, we find $\rho = \rho(\theta_l)$ for all $(\theta_l)_{l=1}^{N_\theta}$, according to equation (3) of [56]. In the general case, this calculated ρ does not necessarily coincide with the $(\rho_k)_{k=1}^{N_\rho}$ partition of the sinogram $\widehat{f}_{kl}$ and hence we need to find the nearest fixed k (and hence ρ_k), since ρ always lies in an interval of the form $[\rho_k, \rho_{k+1}]$ for some appropriate index k. This way, the calculated curve $\rho = \rho(\theta)$ becomes $\rho_k = \rho_k(\theta_l)$ through shifting to the nearest integer index, for all angles θ_l. The value of the sinogram mask is calculated on the curve, $\mathbf{M}_S(\rho_k(\theta_l), \theta_l)$, and if there exists an angle $\theta_l = \tilde{\theta}$ such that $\mathbf{M}_S(\rho_k, \tilde{\theta}) = 0$, then the image mask must be zero; otherwise the mask is one:

Input	$\rho_i,\ \theta_j,\ \widehat{f}_{ij},\ N_\rho,\ N_\theta,\ \lambda,\ \ell,\ n,\ p,\ M,\ s_m$ and Q
Output	$\mathbf{M}_S(\rho_i, \theta_j)$ and $\mathbf{M}_I(x_i, y_j)$
Step 1a:	$\forall\ (\theta_j)_{j=1}^{N_\theta}$ calculate $\mu_L^{(j)}$, $\sigma_L^{(j)}$, $\mu_R^{(j)}$, $\sigma_R^{(j)}$, $(L_n^{(j)})_{n=1}^{N_\rho}$, $(R_n^{(j)})_{n=1}^{N_\rho}$.
Step 1b:	Find initial indices $i'^{(j)}_{L_0}$ and $i'^{(j)}_{R_0}$ via $\ker L_n^{(j)}$ and $\ker R_n^{(j)}$.
Step 1c:	Polynomially fit (degree n) to find $i^{\mathrm{fit}(j)}_{L_0}$ and $i^{\mathrm{fit}(j)}_{R_0}$.
Step 1d:	Add padding p to find $i^{(j)}_{L_0}$ and $i^{(j)}_{R_0}$ and $I_0^{(j)}$.
Step 2a:	Deploy M agents A_m inside $I_0^{(j)}$ (random starting points s_m).
Step 2b:	For $i > 1$ find indices (if any) $i^{(j)}_{L_i}$ and $i^{(j)}_{R_i}$ via $\ker L_n^{(j)}(A_m)$ and $\ker R_n^{(j)}(A_m)$ and padding p, else assign index value of 0.
Step 3:	Find $(N_j)_{j=1}^{N_\theta}$ and, thus, N.
Step 4:	Perform sinogram masking by calculating $\mathbf{M}_S$.
Step 5a:	$\forall\ (x_i, y_j)_{i,j=1}^{Q}$ find $\rho = \rho(\theta_l)$ and then nearest $\rho_k = \rho_k(\theta_l)$.
Step 5b:	Calculate $\mathbf{M}_S(\rho_k(\theta_l), \theta_l)$.
Step 5c:	Perform image masking by calculating $\mathbf{M}_I$: if $\exists\ \theta_l$ such that $\mathbf{M}_S(\rho_k, \theta_l) = 0$, then $\mathbf{M}_I(x_i, y_j) = 0$, else $\mathbf{M}_I(x_i, y_j) = 1$.

Table 3.1: Algorithm for image masking via CUSUM.

$$\mathbf{M}_I(x_i, y_j) = \begin{cases} 0, & \text{if } \exists\ \theta_l \text{ such that } \mathbf{M}_S(\rho_k(\theta_l), \theta_l) = 0 \\ 1, & \text{otherwise} \end{cases}, \tag{3.14}$$

for $k = 1, \ldots, N_\rho$ and $l = 1, \ldots, N_\theta$.

In summary, image masking is performed as follows: a) we specify the length (ℓ, in pixels) of the “almost zero" interval as well as the multiplier (λ) of the standard deviation of counts (σ) within this specific area for a given sinogram, b) we find the left and right initial boundary curves, through left and right cumulative sums and by considering the boundary points for each angle (θ) as points on a curve, c) we obtain the final exterior curves of the sinogram via polynomial fitting and optional padding (p, in pixels), d) we deploy “agents" that search for internal edges (if any) within the exte-

rior boundaries, but with random starting points (s_m) and without *a priori* knowing the total number of non-zero intervals, e) we find the interior boundaries of the sinogram and hence the sinogram mask ($\mathbf{M}_S$) by reapplying left and right cumulative sums and f) we construct an image mask ($\mathbf{M}_I$) from the sinogram mask, under the following condition: if a pixel is outside the boundary of an object, and thus has zero value, then there exists at least one angle such that the Radon transform of this specific pixel has zero value in the image mask there, since a pixel in image space maps to a curve in sinogram space. The sinogram and image masking procedures are outlined in Table 3.1.
Our method was implemented in GNU Octave, a freely redistributable high-level interpreted language and software, primarily intended for numerical computations.

3.2.6 Data acquisition, reconstructions and implementation

Simulation studies

The simulation studies were performed employing simulated sinograms of:

(i) an image-quality (IQ) phantom ($N = 1$),

(ii) a digital phantom simulating two separate bodies (two ellipses emulating a slice of two human legs, $N = 2$),

(iii) a digital phantom simulating three separate bodies (three ellipses emulating a slice of a human torso and two arms, $N = 3$), as well as

(iv) a concave phantom ($N = 1$), all under Poisson noise of 10% of the total counts.

Software for Tomographic Image Reconstruction (STIR) [88] was employed to simulate the GE Discovery ST PET/CT scanner [89]. This specific scanner consists of 24 detector rings with diameter of 88.62 cm. Every detector ring consists of 70 detector blocks, and each block in turn consists of an array of 6×6 crystals (that is a total of 420 crystals per ring). The dimensions of the resulting, simulation-generated sinograms are $N_\rho = 221$ detectors and $N_\theta = 210$ angles, with a detector bin size of 3.195 mm each. For further details of this particular scanner, see [89]. For all phantoms involved in our

simulation studies, the size of the square image grid was 128, i.e. 128×128 pixels.

For the simulation studies performed, we assigned the parameters the following values:

- $\lambda = 3$ for the σ multiplier,
- $n = 7$ for the degree of the polynomial fit, and
- $M = 1000$ for the number of deployed agents.

As far as the length of the "almost zero interval" is concerned, the following values were used:

- $\ell = 60$ pixels for the simulated IQ phantom,
- $\ell = 50$ pixels for the two-object and three-object phantoms, and
- $\ell = 75$ pixels for the concave phantom.

For the simulated IQ and the concave phantoms we did not add padding, however we assigned padding of

- $p = 1$ pixel for the two-object phantom, and
- $p = 2$ pixels for the three-object phantom.

Phantom studies

We also employed our automatic method for an image-quality phantom representing a human torso, namely a NEMA IEC Body Phantom Set^{TM}, Data Spectrum Corp, Hillsborough, NC, USA. The GE Discovery ST PET/CT scanner was used to acquire the corresponding sinograms. This specific phantom incorporates six coaxial isocenter spheres with diameters of 10, 13, 17, 22, 28, and 37 mm, respectively. A cylindrical insert, simulating the lungs, with a diameter of 50 mm was installed in the phantom's center. The cylinder's (cold insert) density is 0.30 g/ml and its attenuation coefficient is approximately equal to the average value of the attenuation coefficient in the lungs [90]. The phantom was loaded with an aqueous solution of ^{18}F with a background activity concentration of 5.3 kBq/cm^3 according to the guidelines of the NEMA Standards Publication NU 2-2001 [91]. In order

to simulate lesions with lesion-to-background ratio of four, the six spheres were filled with a concentration four times larger than the background. The NEMA phantom was transaxially positioned in the center of the GE Discovery ST PET/CT system, whereas axially it was positioned in a way that the center of the spheres was placed at the axial center of the scanner. An emission scan was obtained in two-dimensional (2D) mode, with septa in place, in a single bed position and a CT scan followed in order to obtain the attenuation correction mapping. The emission scan acquired a total of 100×10^6 counts and all sinograms were subsequently corrected for deadtime, normalization, randoms, scatter and attenuation.

The two-dimensional sinograms were then transferred to a computer for reconstruction with STIR. Once again, the dimensions of the acquired sinograms were $N_\rho = 221$ detectors and $N_\theta = 210$ angles and the reconstructed image size was 221×221 pixels ($Q = 221$). For the real NEMA phantom we set the parameters' the values as follows:

- $\ell = 60$ pixels for the"almost zero interval",
- $\lambda = 3$ for the σ multiplier,
- $n = 7$ for the degree of the polynomial fit,
- $M = 1000$ for the number of agents, and
- no padding, i.e. $p = 0$ pixels.

Clinical study

A clinical study of a patient's thorax was performed by employing emission scans from the GE Discovery ST PET/CT scanner. The total counts of the sinogram were 1.6×10^6 counts and the length of the "almost zero interval" was set at

- $\ell = 40$ pixels.

The same parameters were used as in all previous studies performed.

Reconstructions

The reconstructions of all sinograms involved were performed in STIR using two-dimensional FBP with a ramp filter with a cutoff at Nyquist frequency.

The reconstructed images size was $Q = 221$, i.e. 221×221 pixels, resulting in a pixel size of 3.195 mm, equal with the detector bin size.

3.2.7 Comparison metrics

For the comparison of the simulated-phantom results with the actual phantom, we employed three different metrics, namely the root mean square (RMS) error e_{rms}, the Hausdorff distance e_H, and the optimal sub-pattern assignment (OSPA) metric localization error $\bar{e}^{(c)}_{p,\text{loc}}$.

Root mean square error

The root mean square error (e_{rms}, in pixels) between the estimated and actual boundary locations, for all angles of projection θ_j, $j = 1, \ldots, N_\theta$ is given by:

$$e_{\text{rms}} = \sqrt{\frac{\sum_{j=1}^{N_\theta} \left(\tilde{R}_j - R_j\right)^2}{N_\theta}}, \tag{3.15}$$

where

$$\tilde{R}_j = i^{(j)}_{R_0} - i^{(j)}_{L_0}, \tag{3.16}$$

$i^{(j)}_{L_0}$, $i^{(j)}_{R_0}$ are defined in equation (3.6), and $\tilde{R}_j$, R_j correspond to the estimated and actual edge locations, respectively, and thus are represented by the distance from the center of the Radon space (sinogram space) to the projection ray that passes through the object boundary; this is exactly the same metric that Barnden, Dickson and Hutton used in [72] for their evaluation.

The RMS metric is meaningful only for one-object cases, i.e. N=1, since it compares the image and sinogram boundaries as a whole. For this reason, we computed the above metric only for the $N = 1$ cases, i.e. the simulated IQ phantom, the real NEMA phantom and the clinical thoracic study.

Hausdorff distance

The dominant approach in the evaluation of segmentation algorithms is the Hausdorff distance, e_H. The Hausdorff distance between two curves,

$$A = \{a_1, a_2, \ldots, a_m\} \quad \text{and} \quad B = \{b_1, b_2, \ldots, b_m\},$$

is calculated by:

$$e_H(A,B) = \max\left(\max_i \mathrm{d}(a_i,B), \max_j \mathrm{d}(b_j,A)\right), \tag{3.17}$$

where d, i.e. the distance to the closest point, is defined by

$$\mathrm{d}(a_i,B) = \min_j \|b_j - a_i\|, \tag{3.18}$$

as described in [92, 93]. In our case, the curves A and B represent the segmented boundary and the ground-truth boundary. Therefore, the Hausdorff distance reflects the maximum mismatch between the segmentation and the ground truth [94]. Since the Hausdorff distance metric deals with closed boundary curves, it is only valid for one-object cases.

OSPA metric localization error

We employed the OSPA metric (or OSPA distance) in the context of multi-object performance evaluation. More specifically, we computed the p-th order "per object" localization error, $\bar{e}^{(c)}_{p,\mathrm{loc}}$, between the phantom binary map and the calculated mask, as in [95]. The localization error was evaluated via the following expression:

$$\bar{e}^{(c)}_{p,\mathrm{loc}}(X,Y) = \left(\frac{1}{n}\min_{\pi\in\Pi_n}\sum_{i=1}^{m}\mathrm{d}^{(c)}(x_i,y_{\pi(i)})^p\right)^{\frac{1}{p}}, \tag{3.19}$$

where

$$\mathrm{d}^{(c)}(x,y) := \min\left(c, \mathrm{d}(x,y)\right)$$

denotes the distance between x and y cut-off at $c > 0$ (outlier sensitivity), Π_k denotes the set of permutations on $\{1,2,\ldots,k\}$ for any $k \in \mathbb{N}$, $X = \{x_1,\ldots,x_m\}$, $Y = \{y_1,\ldots,y_n\}$ and $p \geq 1$ is the cardinality penalty. A practical choice for our case is

- $p = 2$ (second order error), and
- $c = 1$,

therefore,

$$\mathrm{d}^{(1)}(x,y) = \mathrm{d}(x,y),$$

given that the values of d are always less or equal to 1 (since we are comparing binary maps in a pixel-by-pixel manner). Furthermore, all matrices involved are square matrices, hence

$$m = n = Q.$$

As a result, we are interested in determining $\bar{e}^{(1)}_{2,\mathrm{loc}}$:

$$\bar{e}^{(1)}_{2,\mathrm{loc}}(X,Y) = \left(\frac{1}{Q} \min_{\pi \in \Pi_n} \sum_{i=1}^{Q} \mathrm{d}(x_i, y_{\pi(i)})^2 \right)^{\frac{1}{2}}, \tag{3.20}$$

where d is treated in the context of square, $Q \times Q$ matrices hence, is naturally computed as follows

$$\mathrm{d} := \mathrm{d}_2(A,B) = \sqrt{\sum_{i=1}^{Q} \sum_{i=1}^{Q} (a_{ij} - b_{ij})^2}, \tag{3.21}$$

i.e. d is chosen to be the Euclidean matrix distance, where $A = (a_{ij})$ and $B = (B_{ij})$ are $Q \times Q$ matrices. The OSPA localization error is meaningful in multi-object cases, i.e. $N > 1$. For this reason we computed it for all corresponding cases, namely the simulated two and three-object digital phantoms. In these cases the OSPA error is a measure of the "distance", in the generalized sense, between the binary version of the phantom and its calculated binary mask. The above are valid under the assumption that no cardinality error occurs, i.e. the number of reconstructed objects remains the same with the original number of objects depicted in each phantom.

3.3 CUSUM results

The execution time for contour determination depends on the number of total distinct objects (N) and is clearly less in cases were $N = 1$. More specifically, in all $N = 1$ cases (the simulated IQ phantom, the simulated concave phantom, the real NEMA phantom as well as the clinical thoracic phantom) the execution time was less than 4.3 s (4.21 s, 4.12 s, 4.29 s and 4.02 s, respectively) and in the simulated two-ellipses phantom and three-ellipses phantom cases the execution time was significantly larger, namely more than 22 s (22.27s and 22.76 s, respectively). All studies were executed on a Dell Precision T1700 workstation with an Intel® Xeon® CPU E3-1241 v3 processor, running on a 64-bit Windows® 10 environment.

	Single-object			Multi-object	
	Simulated	Real		Simulated	
	IQ	NEMA	Thoracic	2-obj.	3-obj.
RMS error	1.14	1.69	3.28	-	-
Hausdorff distance	3.13	3.12	4.50	-	-
OSPA error	-	-	-	0.94	1.48

Table 3.2: CUSUM error measurements, in pixels.

In Table 3.2 we present the results obtained from the computation of all comparison metrics investigated, both from the simulated and real studies. It is important to note that the RMS error and the Hausdorff distance can only be determined in single-object cases, whereas the OSPA localization error is only defined for multi-object cases.

3.3.1 Simulation studies

Simulated IQ phantom

For the IQ phantom study, the sinogram edge-detection, sinogram mask, reconstructed image and masked reconstructed image are shown in figure 3.2. The corresponding surface plots are presented in figure 3.3. This specific digital phantom simulates the human torso, hence the number of distinct objects with a clearly defined boundary in the image is 1. The cross-section of the sinogram is unimodal for all angles θ_j. The agents confirm the fact that for all angles θ_j of the sinogram $N_j = 1$, hence $N = 1$. By visual inspection, both the sinogram mask and the image mask are correctly identified. Figure 3.2 indicates that all FBP artifacts outside the object have been substantially removed and the object is preserved intact. For the simulated IQ phantom,

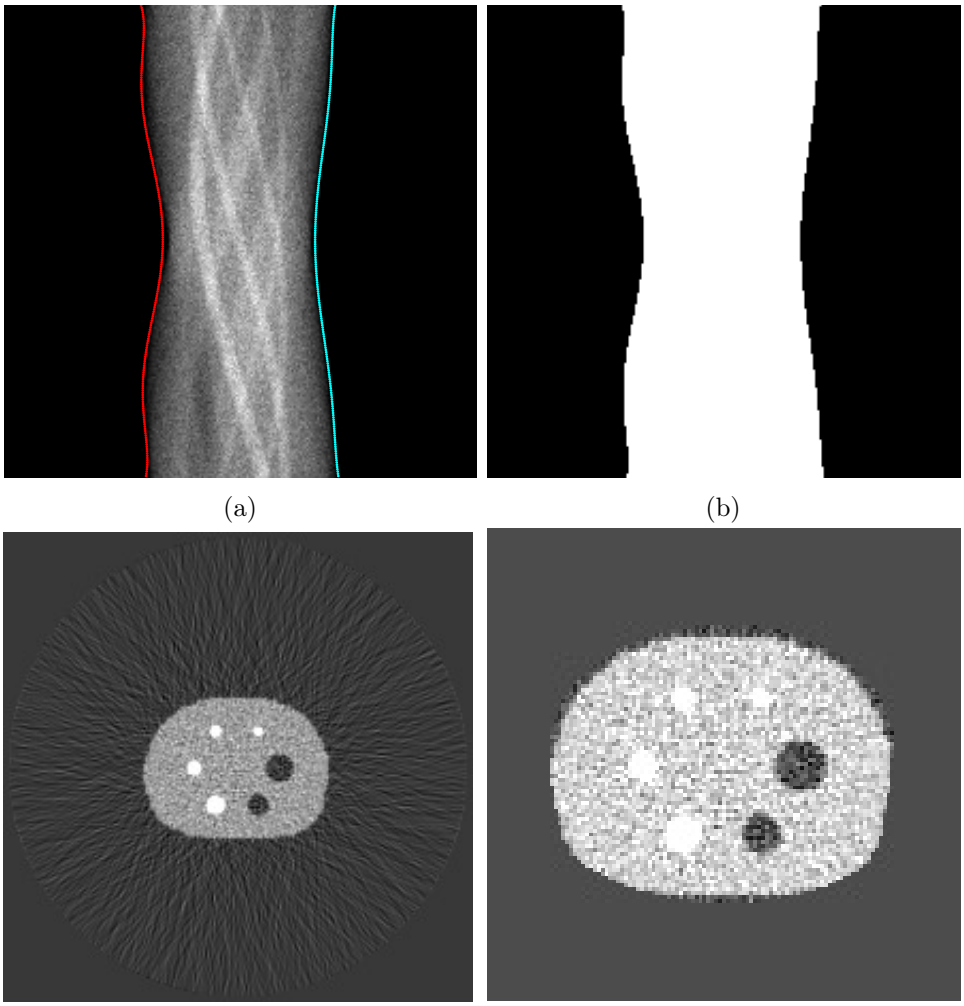

(a) (b)

(c) (d)

Figure 3.2: Sinogram and image edge detection and masking for the simulated IQ phantom ($N = 1$): (a) Sinogram edge detection with polynomial fitting and padding ($n = 7$, $p = 0$, $\lambda = 3$, $\ell = 60$, $M = 1000$), (b) Sinogram mask, (c) FBP reconstructed image, (d) Enlarged masked image to enhance visual inspection.

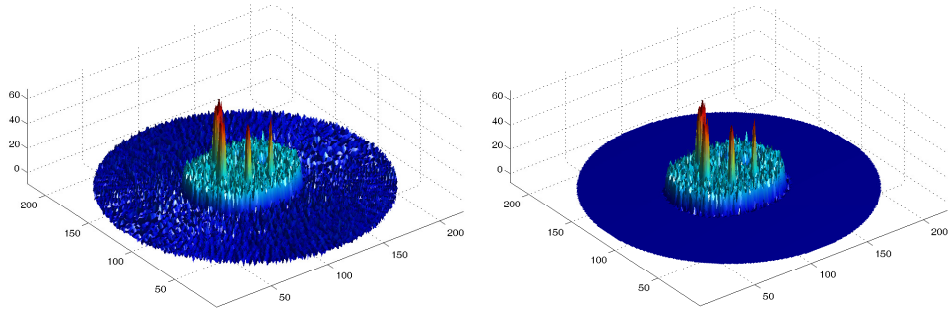

Figure 3.3: IQ phantom surface plots of reconstructions: initial (left) and masked (right).

the root mean square error was

$$e_{\text{rms}} = 1.14 \text{ pixels},$$

hence, the deviation between actual and estimated value was 3.64 mm. Furthermore, the Hausdorff distance was measured to be

$$e_H = 3.13 \text{ pixels}, \quad \text{i.e.} \quad 10.00 \text{ mm}.$$

Two-object phantom: simulation of human legs

For the digital two-object phantom the sinogram edge-detection, sinogram mask, reconstructed image and masked reconstructed image are shown in figure 3.4. The corresponding surface plots are presented in figure 3.5. This particular digital phantom emulates a slice of two human legs, hence the number of distinct objects in the image is 2. Again, this is confirmed by the agents, which detected 2 distinct objects. It is clear by visual inspection that both the sinogram and image masks are correctly identified. Only a few image pixels still remain uncorrected, after applying the image mask (see figure 3.4d). Figure 3.4 indicates that all FBP artifacts outside the objects have been removed and the objects are preserved intact. For the simulated two-object phantom, the OSPA localization error was

$$\bar{e}^{(1)}_{2,\text{loc}} = 0.94 \text{ pixels},$$

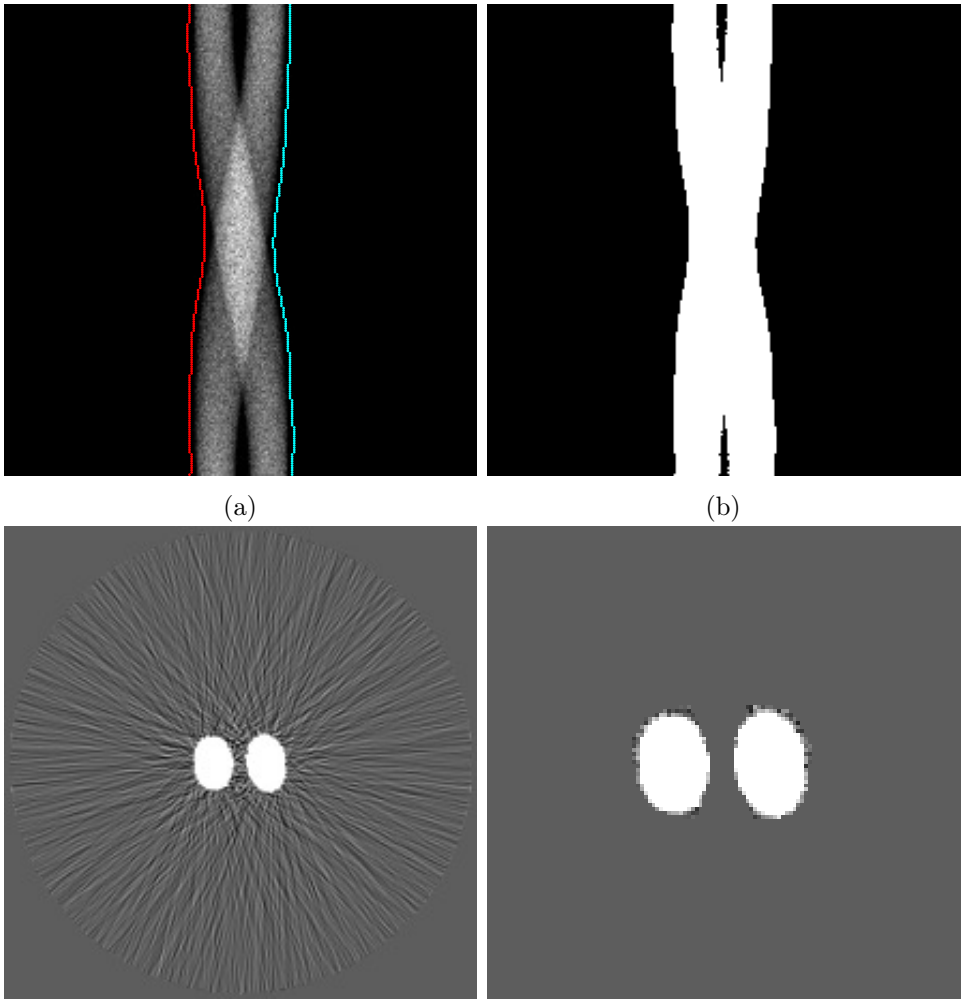

(a) (b)

(c) (d)

Figure 3.4: Sinogram and image edge detection and masking for the simulated two-object digital phantom ($N = 2$): (a) Sinogram edge detection with polynomial fitting and padding ($n = 7$, $p = 1$, $\lambda = 3$, $\ell = 50$, $M = 1000$), (b) Sinogram mask, (c) FBP reconstructed image, (d) Enlarged masked image to enhance visual inspection.

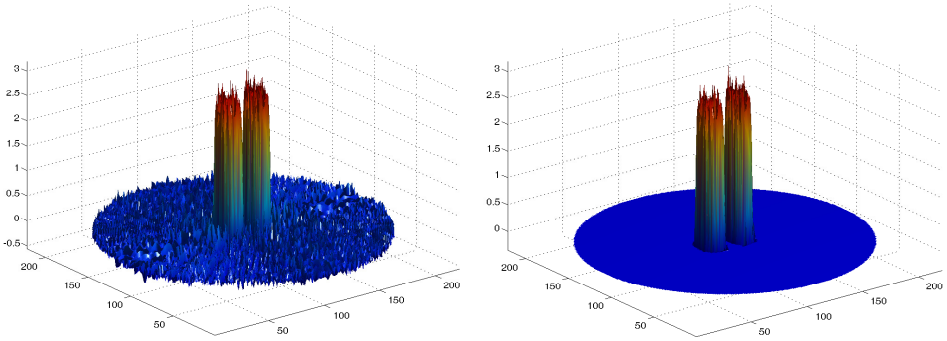

Figure 3.5: Two-object phantom surface plots of reconstructions: initial (left) and masked (right).

corresponding to a second-order deviation between actual and estimated mask of 3.00 mm.

Three-object phantom: simulation of human torso and arms

For the digital three-object phantom study, the sinogram edge-detection, sinogram mask, reconstructed image and masked reconstructed image are shown in figure 3.6. The corresponding surface plots are presented in figure 3.7. This digital phantom emulates a slice of a human torso and two human arms, hence the number of distinct objects with a clearly defined boundary in the image is 3. The agents confirm that $N = 3$. By visual inspection, the masking process identifies all three objects correctly. After masking, there remain only a few uncorrected pixels (see figure 3.6d). Furthermore, the inside zero area of the central object (torso) remain intact, as expected. Figure 3.6 indicates that all FBP artifacts outside the objects have been removed and the objects are preserved intact. For the simulated three-object phantom, the OSPA localization error was

$$\bar{e}^{(1)}_{2,\mathrm{loc}} = 1.48 \text{ pixels, or } 4.73 \text{ mm.}$$

Concave phantom

For the digital concave phantom study, the sinogram edge-detection, sinogram mask, reconstructed image and masked reconstructed image are shown

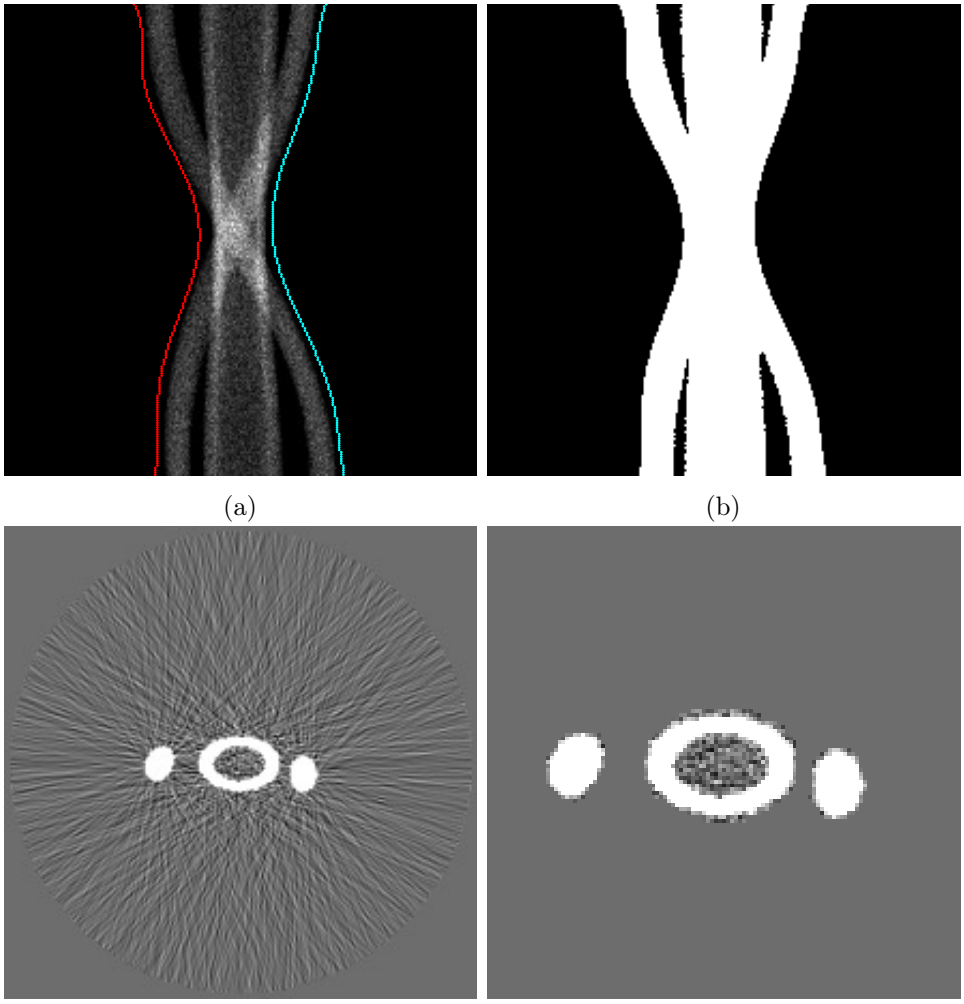

(a) (b)

(c) (d)

Figure 3.6: Sinogram and image edge detection and masking for the simulated three-object digital phantom ($N = 3$): (a) Sinogram edge detection with polynomial fitting and padding ($n = 7$, $p = 2$, $\lambda = 3$, $\ell = 50$, $M = 1000$), (b) Sinogram mask, (c) FBP reconstructed image, (d) Enlarged masked image to enhance visual inspection.

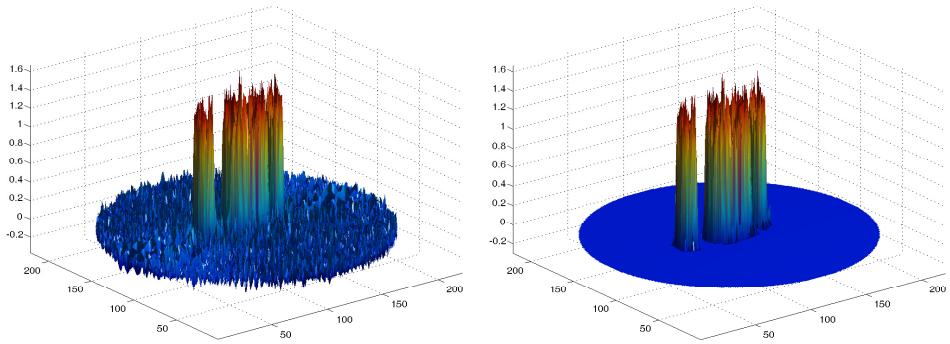

Figure 3.7: Three-object phantom surface plots of reconstructions: initial (left) and masked (right).

in figure 3.8. The corresponding surface plots are presented in figure 3.9. This is a single-object phantom, a fact that is confirmed by the agents. Figure 3.8 indicates that not all FBP artifacts outside the object have been removed; there are several nonzero pixels inside what appears to be the convex hull of the boundary of the object, i.e. the smallest convex set that contains the boundary of the object and the object itself. The object is preserved intact, only this time its size is overestimated: the mask is now much larger than the object, since it encapsulates the convex hull of the object and its boundaries.

3.3.2 Real studies

The main challenge of determining the boundaries in a real sinogram, in comparison to a simulated one, is the fact that a real sinogram may contain non-zero, and even negative, values. This specific fact raises concern regarding the accuracy of any edge detection method applied. However, in our case the inexistence of the positivity constraint did not affect the accuracy of neither the edge detection nor the sinogram masking, especially in the case of the clinical thoracic study.

Phantom study

For the NEMA phantom study, the sinogram, sinogram edge-detection, sinogram mask, reconstructed image and masked reconstructed image are shown

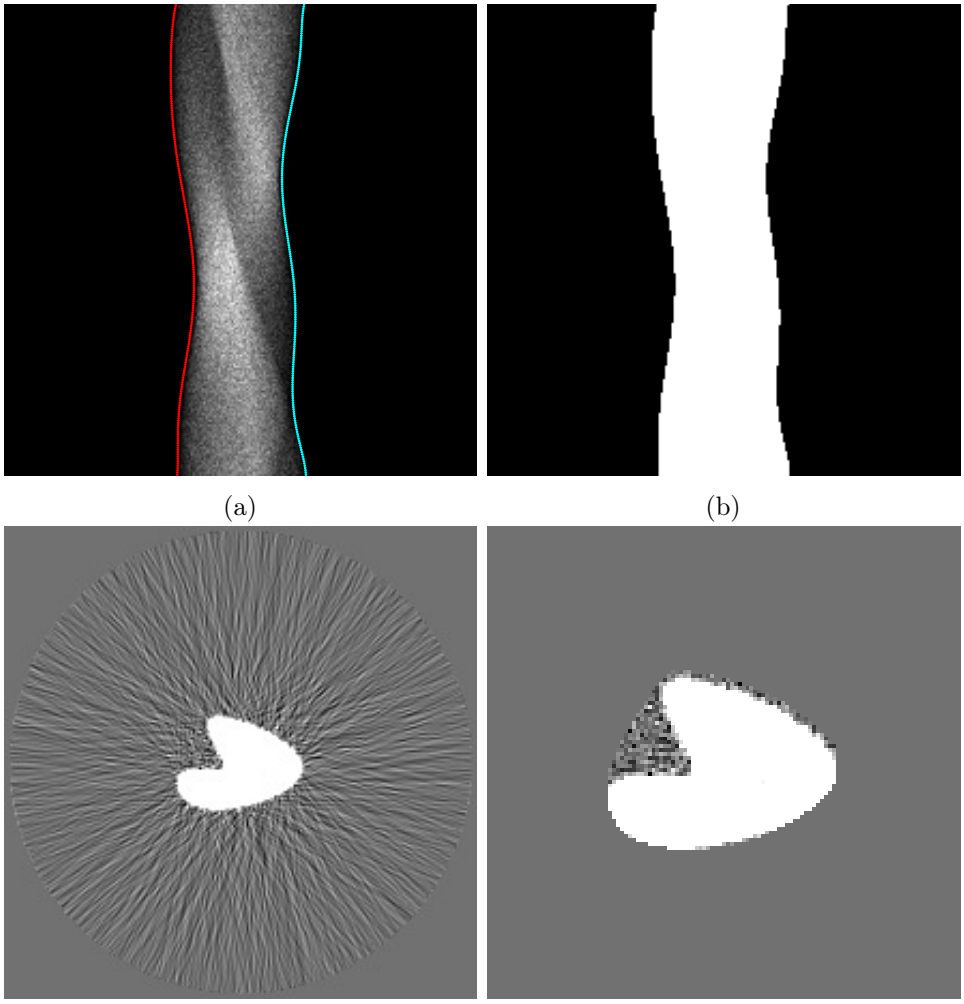

(a) (b)

(c) (d)

Figure 3.8: Sinogram and image edge detection and masking for the simulated concave phantom ($N = 1$): (a) Sinogram edge detection with polynomial fitting and padding ($n = 7$, $p = 0$, $\lambda = 3$, $\ell = 75$, $M = 1000$), (b) Sinogram mask, (c) FBP reconstructed image, (d) Enlarged masked image to enhance visual inspection.

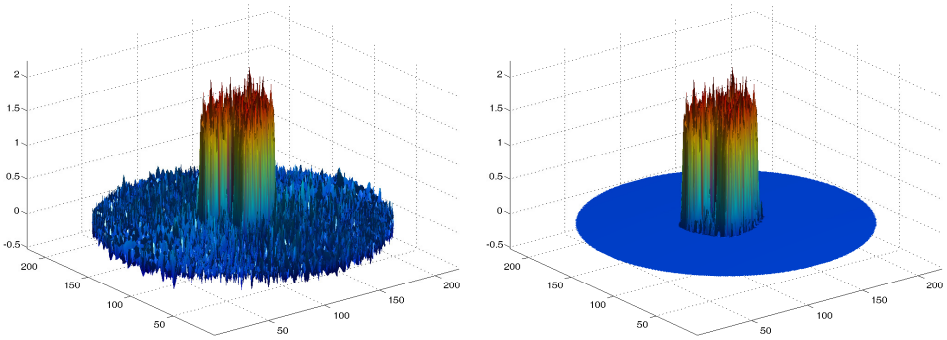

Figure 3.9: Concave phantom surface plots of reconstructions: initial (left) and masked (right).

in figure 3.10. The corresponding surface plots are presented in figure 3.11. This real phantom simulates the human torso. The cross-section of the sinogram, acquired by the GE Discovery ST PET/CT scanner, is unimodal for all angles. The agents confirm the fact that $N_j = 1$ for all angles θ_j, and hence $N = 1$. Figure 3.10 indicates that not only does the image mask identifies the phantom, it also ensures that all FBP artifacts outside the object have been removed. The value of the RMS error for the real NEMA phantom was

$$e_{\text{rms}} = 1.69 \text{ pixels},$$

which corresponds to a length of 5.40 mm. Furthermore, the Hausdorff distance was measured at

$$e_H = 3.12 \text{ pixels},$$

corresponding to a distance of 9.97 mm.

Clinical study

For the real clinical study the sinogram, sinogram edge-detection, sinogram mask, reconstructed image and masked reconstructed image are shown in figures 3.12 and 3.13. This clinical study was performed in the thoracic region of the patient, hence the number of distinct objects with a clearly defined boundary in the image is 1. This is confirmed by the fact that for

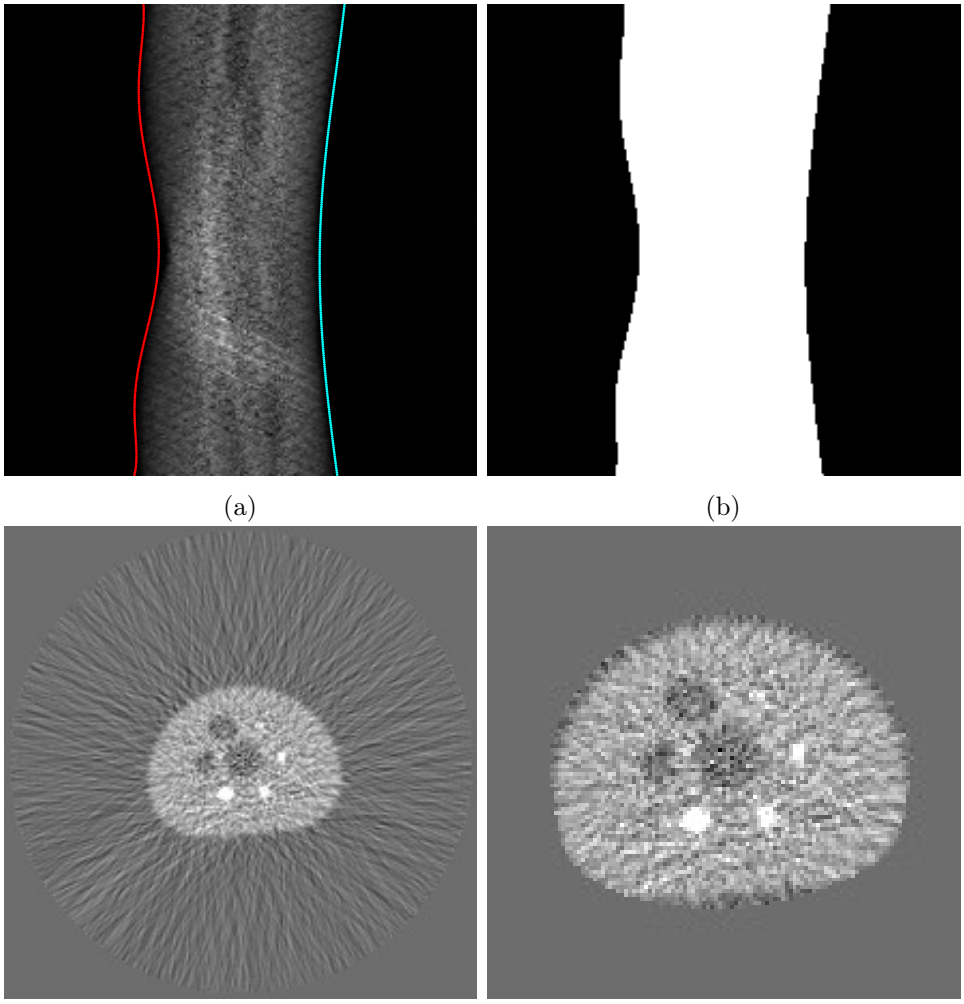

(a) (b)

(c) (d)

Figure 3.10: Sinogram, acquired by the GE Discovery ST PET/CT scanner, and image edge detection and masking for the real NEMA phantom ($N = 1$): (a) Sinogram edge detection with polynomial fitting and padding ($n = 7$, $p = 0$, $\lambda = 3$, $\ell = 60$, $M = 1000$), (b) Sinogram mask, (c) FBP reconstructed image, (d) Enlarged masked image to enhance visual inspection.

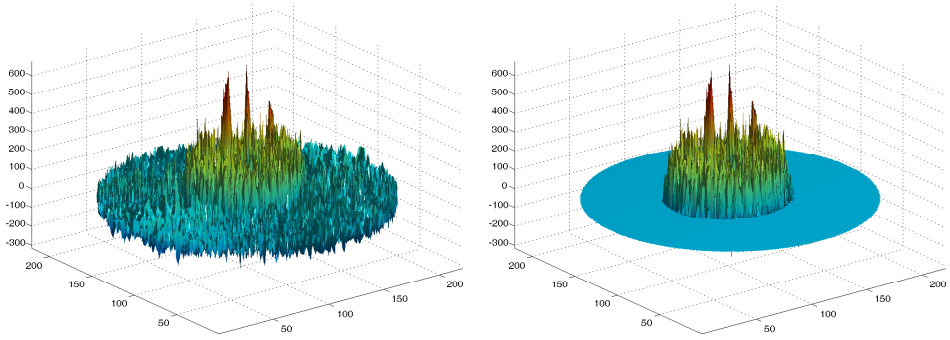

Figure 3.11: NEMA phantom surface plots of reconstructions: initial (left) and masked (right).

all angles θ_j of the sinogram $N_j = 1$, hence $N = 1$. Figures 3.12 and 3.13 indicate that all FBP artifacts outside the object have been removed. The value of the root mean square error for the real NEMA phantom was

$$e_{\text{rms}} = 3.28 \text{ pixels},$$

which corresponds to a length of 10.48 mm.
Furthermore, the relevant Hausdorff distance in the real clinical study was measured

$$e_H = 4.50 \text{ pixels},$$

which corresponds to a total distance of 14.38 mm.

3.4 Analysis and discussion of CUSUM results

In this chapter, we presented a method to automatically determine the contour of multi-object FBP-reconstructed nuclear medicine images, without prior knowledge of the total number of objects involved. In order to accomplish the goal of our study, a CUSUM-based algorithm has been implemented and tested in simulated and real phantoms. Given a sinogram, we perform sinogram edge detection and thus create a sinogram mask. By mapping the masked sinogram into the image space, we create an image mask, and subsequently determine the contour of all objects depicted on the corresponding image.

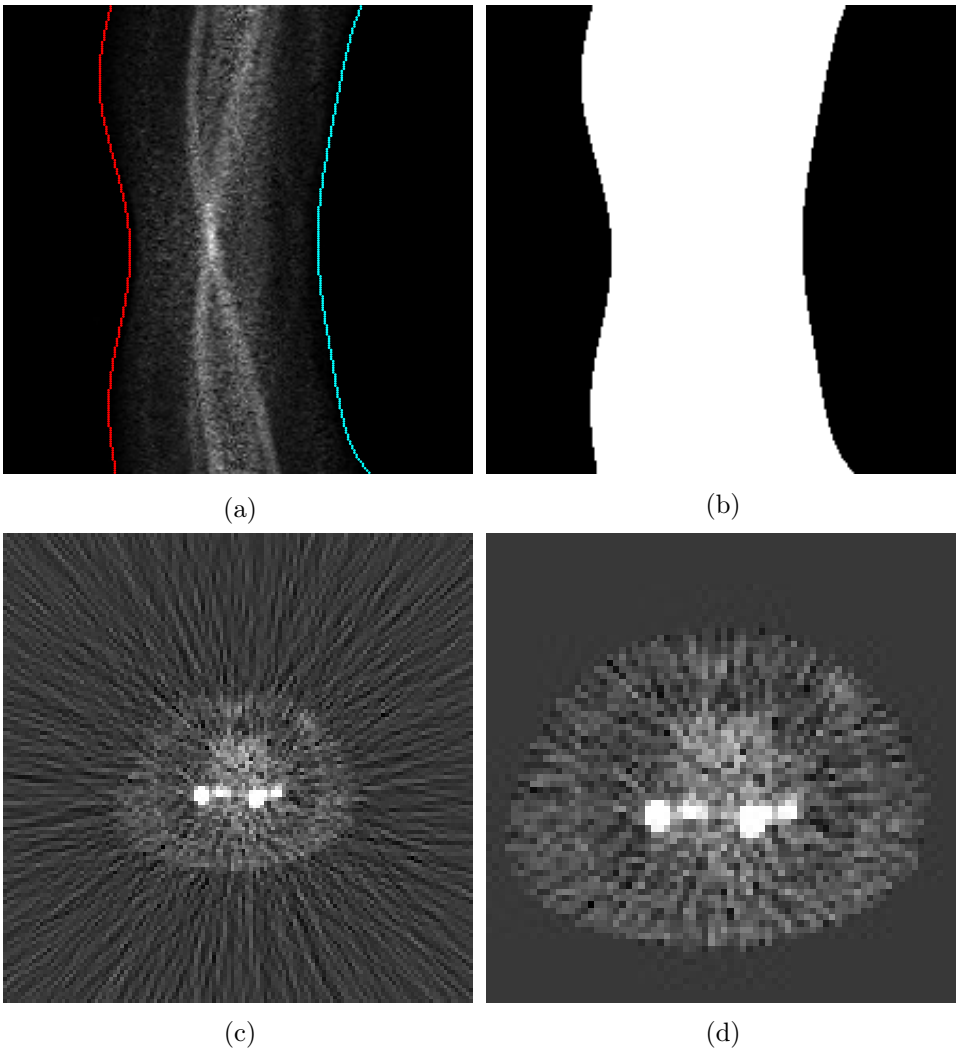

(a) (b)

(c) (d)

Figure 3.12: Sinogram, acquired by the GE Discovery ST PET/CT scanner, and image edge detection and masking for a slice of the clinical thoracic study ($N = 1$): (a) Sinogram edge detection with polynomial fitting and padding ($n = 7$, $p = 0$, $\lambda = 3$, $\ell = 40$, $M = 1000$), (b) Sinogram mask, (c) FBP reconstructed image, (d) Enlarged masked image to enhance visual inspection. The bright spots correspond to tumor locations.

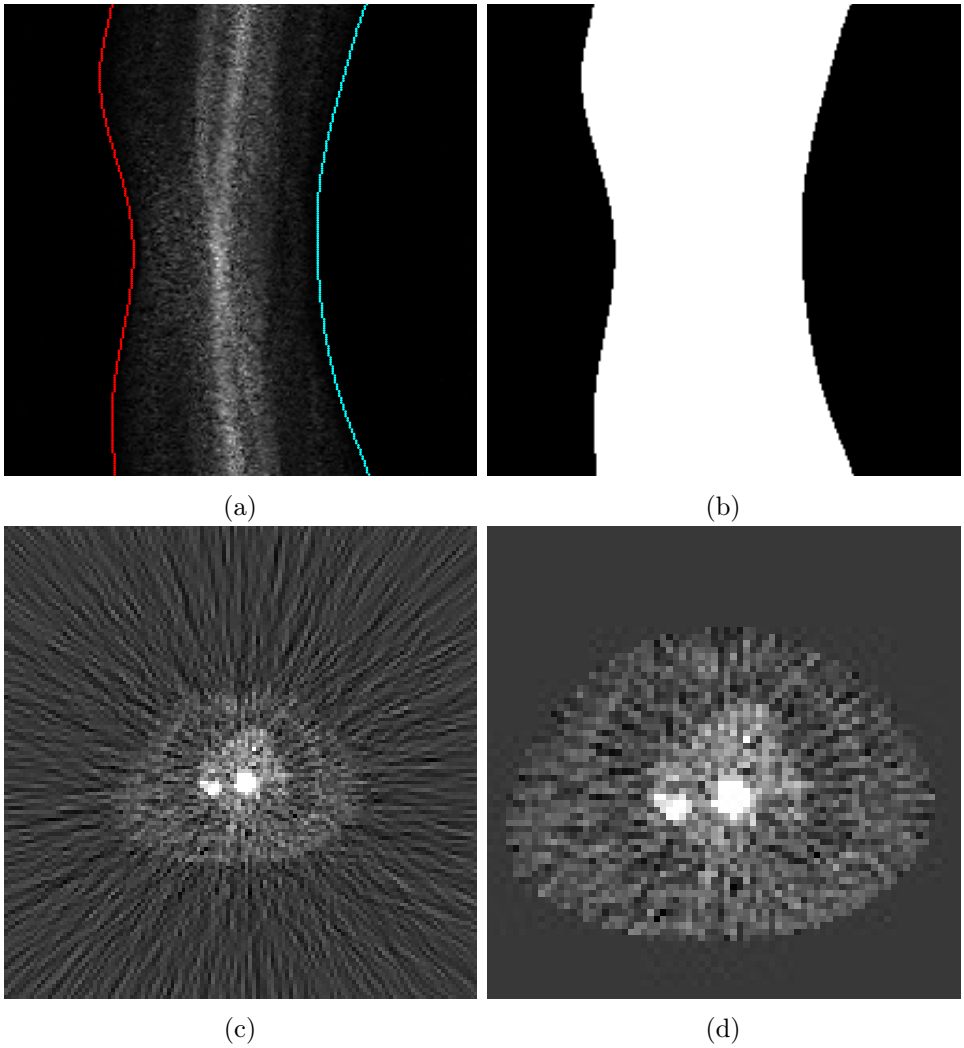

(a) (b)

(c) (d)

Figure 3.13: Sinogram, acquired by the GE Discovery ST PET/CT scanner, and image edge detection and masking for another slice of the clinical thoracic study ($N = 1$): (a) Sinogram edge detection with polynomial fitting and padding ($n = 7$, $p = 0$, $\lambda = 3$, $\ell = 40$, $M = 1000$), (b) Sinogram mask, (c) FBP reconstructed image, (d) Enlarged masked image to enhance visual inspection. The bright spots correspond to tumor locations.

For the simulated studies, our results clearly indicate that our method is fully capable of identifying single as well as multiple objects in the reconstructed image, within a small error. In order to quantify this statement and to evaluate the usability of our method, we have employed three comparison metrics, namely the root mean square error and the Hausdorff distance for one-object images, and the OSPA localization error for multi-object images, respectively. More specifically, for the single-object case, the measured RMS error was in the order of a pixel, whereas the Hausdorff distance (which signifies the maximum deviation from the actual value) was 3 pixels. For the multi-object cases, the measured OSPA second order localization error (which signifies the miss-distance in the field of multi-object performance evaluation) was less than two pixels in both 2-object and 3-object images.

For the real studies, our results suggest that our method is fully efficient in identifying the objects, once again within a small error. For the real single-object cases, the RMS errors were less than two pixels and in the order of three pixels for the real NEMA phantom and the clinical thoracic study, respectively. Furthermore, the Hausdorff distance was in the order of 3 pixels for the real NEMA phantom and less than 5 pixels for the clinical thoracic study. Since the evaluation of any segmentation method is known to be a very hard problem, the criteria for a good segmentation algorithm are usually application-dependent, subjective and hard to define explicitly. It is worth noting that relatively little research has been performed on the segmentation evaluation process [96].

We think it is essential to compare our results with the results of [72] in a meaningful manner. In this direction, we tested the method proposed by Barnden, Dickson and Hutton [72], which is based on "real" images, on one-object phantom images used in this paper. This way we were able to compare these results more consistently. In particular, we employed the threshold crossing method with second derivative at 12% threshold without any outlier rejection (D2T12), as described in [72]. For all one-object cases, the root mean square error (e_{rms}) of our method was smaller than the corresponding root mean square error of D2T12 edge detection method. Detailed comparisons between the RMS error measurements of these two methods are shown in Table 3.3.

Relatively recent studies suggest that the edge detection process in nuclear tomography is closely related to thresholding and sinogram derivative

Edge detection method	**IQ**	**NEMA**	**Thoracic**
CUSUM	1.14	1.69	3.28
D2T12	1.42	2.72	3.99

Table 3.3: Measured RMS error comparison between CUSUM method and D2T12 of [72] for one-object studies, in pixels.

calculations. For example, Hosoba et al. [76] recommended thresholding for contour detection in SPECT, whereas Barnden et al. [72] proposed a mixed methodology scheme for edge detection, that includes sinogram thresholding, calculation of sinogram derivatives up to second degree and, ultimately, preliminary selection of the appropriate method by visual inspection. Furthermore, in the latest sinogram-based approaches in CT, such as the studies by Elangovan and Whitaker [79], Kaewlek et al. [82], and Veldkamp et al. [81], the sinogram undergoes segmentation either through deformation or completion-replacement via interpolation. With our suggested method, no thresholding or sinogram derivatives calculations are necessary. Our method performs automated edge detection for multiple objects through the back-projection of the sinogram mask. Most of the works mentioned above limit their studies in one-object cases only. Our proposed approach is automated and the only required parameter is the zero interval ℓ (number of pixels) which the user can obtain by visual inspection of the sinogram. However, one can use our algorithm in a fully automated fashion by finding the optimal ℓ value for each imaging protocol/scanner. The minimum recommended value of the zero interval for all scanners is

$$\ell = 10 \text{ pixels},$$

which represents the default fully-automatic setup for all scanners.

We also note that our proposed contour detection method is robust and all the parameters involved are optimized. In particular, the standard deviation multiplier, λ, is optimized at

$$\lambda = 3,$$

since the persistent shift in all cases investigated was accurately detected at

this level. The polynomial fitting degree was optimal at

$$n = 7,$$

and for the number of agents deployed, the value

$$M = 1000$$

suffices for all studies performed. Our tests suggest that even the padding parameter was optimized at

$$p = 0,$$

i.e. no padding, for all single-object cases. Furthermore, the optimal values of

$$p = 1 \quad \text{and} \quad p = 2,$$

for two and three objects cases were used, respectively.

The method proposed in this chapter is able to perform accurately and efficiently for convex objects, such as the IQ, two-object, three-object and NEMA phantoms. Overall, it provides a very useful tool for automatic contour determination. However, there appears a certain limitation in applying our algorithm holistically for concave objects, due to the fact that, in concave cases, there is always a certain “shadow" of the Radon transform. As a result, the masked image in concave cases encompasses the convex hull of the boundary of the object and hence it overestimates the size of the object. Furthermore, the padding parameter p, is always provided in order to avoid discretization errors. These errors appear, since from a known sinogram, and hence from known detector locations, we need to engage the nearest detector (ρ_i) for every distinct pixel (x_i, y_j). Furthermore, there are certain limitations in applying our method, such as

(a) low count imaging, and

(b) SPECT scans during which there are parts of the patient's body that are outside the field of view (FOV).

The mechanism described in the present chapter can be proven to be useful for computing body edges for attenuation correction in PET or SPECT systems that do not include a CT. As we will discuss extensively in chapter 4, attenuation correction is one of the numerous applications of all contouring

techniques in general, and not exclusively of our method. The usefulness of creating attenuation maps arises especially in developing countries where, even nowadays, there are PET and SPECT systems without a coupled CT scanner. Even in cases where a CT is indeed available, i.e. PET/CT or even SPECT/CT, the CT delivers single snapshots of the breathing cycle and when used for attenuation correction it may possibly generate edge artifacts in most of the respiratory cycle, with or without respiratory gating [72]. Our method can determine the boundaries of the object and thus create an attenuation map. Furthermore, our technique is expected to be very useful in eliminating noise outside the objects being imaged in compressive sensing reconstructions. More specifically, it can be proven helpful in the desired image decomposition as a background separation tool, see [66].

Our CUSUM method will be particularly useful for iterative reconstruction methods, such as compressive sensing, that aim to use FBP operators. Such methods would use the forward back projectors per iteration, hence the streak artifacts, when present in the back projected image, will keep getting worse per iteration dominating the signal. Compressive sensing utilizes non-linear iterative reconstruction methods and if it employs an FBP operator, then the sinogram masking will be necessary. In compressive sensing tomographic reconstruction, as in most iterative reconstruction methods, the sinogram must be "cleaned" of external artifacts in every iteration.

In this chapter, we have focused on FBP reconstructions. However, in reconstruction cases and techniques other than FBP where the reconstruction is performed pixel-by-pixel (i.e. techniques that utilize pixel-driven approaches and thus reconstruct the sinogram on a pixel-by-pixel basis), the presented method can dramatically reduce reconstruction time; these techniques include:

- the so-called "spline reconstruction technique" for PET (SRT) evaluated in [56] and extended for SPECT (aSRT for SPECT) in Chapter 4 and in [44], or
- the two-step Hilbert transform method, with utilization of a differentiated backprojection (DBP) step, see [97].

3.5 Conclusion and future work

For the purposes of this chapter, an automatic method for the contour detection of FBP-reconstructed, multi-object nuclear medicine images has been developed and tested in simulated and real phantoms. Our proposed method, based on cumulative sums, automatically detects all objects in the reconstructed image without the requirement of prior knowledge of the total number of distinct objects being imaged. Through contour determination, we were able to efficiently compute body edges. In future studies, we intend to implement our method in STIR as well as to design and implement a stand-alone application for contour detection, image masking and the elimination of streak artifacts.

3.6 Chapter acknowledgments

The work presented in the present chapter was partially supported by the research programme “Inverse Problems and Medical Imaging" (200/842) of the Research Committee of the Academy of Athens. I would like to thank Associate Professor of Statistics Panagiotis Tsiamyrtzis (Athens University of Economics and Business) for his valuable suggestions and comments. I would also like to thank Alexandros Samartzis from the Nuclear Medicine Department of Evangelismos General Hospital for providing real PET data.

Chapter 4

A novel method for inverting the attenuated Radon transform

In this chapter we present the attenuated spline reconstruction technique (aSRT), which provides an innovative approach for SPECT image reconstruction [44,47]. aSRT is based on an analytic formula for the inverse attenuated Radon transform (IART). It involves the computation of the Hilbert transforms of the linear attenuation function and of two sinusoidal functions of the attenuated sinogram, see equation (1.15). These computations are performed by employing the corresponding attenuation data provided by computed tomography (CT) scans, and by utilizing custom-made cubic spline interpolation. Our purpose in the present chapter is:

(a) to present the mathematical setting of aSRT, as part of a substantial extension of [8],

(b) to reconstruct both simulated and real attenuated SPECT data using aSRT, and

(c) to evaluate aSRT by comparing it with two of the main inversion modalities, namely filtered back-projection (FBP), and ordered subsets expectation minimization (OSEM) reconstruction algorithms.

In this direction, we performed simulation studies by employing an image quality (IQ) phantom and an appropriate attenuation map. Reconstructed

images were generated for 45, 90 and 180 views over 360 degrees with 20 realizations and involved Poisson noise of three different levels (NL), namely 100% (NL1), 50% (NL2) and 10% (NL3) of the total counts, respectively. Furthermore, real attenuated SPECT sinograms were reconstructed from a real study of a Jaszczak phantom, as well as from a clinical myocardial SPECT/CT study. Comparisons between aSRT, FBP and OSEM reconstructions were performed using several image metrics such as contrast, bias and image roughness. The results suggest that aSRT can efficiently produce accurate attenuation-corrected reconstructions for both simulated and real phantoms, as well as for clinical data. In particular, in the case of the clinical myocardial study, aSRT produced image reconstructions with higher cold contrast than both FBP and OSEM. By incorporating the attenuation correction within itself, aSRT may provide an improved alternative to FBP. This is particularly promising especially for "cold" regions, as the ones occurring in myocardial ischemia, as a result of partial or complete blockage of the coronary arteries.

4.1 An introduction to SPECT and attenuation

SPECT is an important nuclear medicine modality with vast clinical and preclinical applications, especially in the medical fields of cardiology (myocardial perfusion imaging) and neurology (neuroimaging). This imaging technique provides information regarding functional aspects of patients' organs, particularly the heart and the brain. SPECT nuclear imaging may detect a denervated myocardium, and even ischaemic heart failure [98].

This specific nuclear medicine tomographic imaging technique utilizes the unique chemical characteristics of decaying radiopharmaceuticals, that consist of a targeting agent labeled with a radioisotope, such as technetium-99 (^{99}Tc) [40,99], iodine-123 (^{123}I) [100], xenon-133 (^{133}Xe) [101], and thallium-201 (^{201}Tl) [102]. The radiopharmaceutical is introduced into the patient intravenously and it is distributed in the body in a manner governed by its biochemical properties [38]. The injected radiotracers radiate single photons and the detectors count these individual photons, as *γ-ray events* [5].

As in all inverse problems related with tomography, nuclear medicine image reconstruction is performed by reconstructing projection data, usually stored in the form of sinograms [68]. There exist several image reconstruction

algorithms, characterized either as *analytic* or *iterative*. The predominant analytic image reconstruction technique is *filtered backprojection* (FBP) [103], whereas the predominant iterative image reconstruction approach is *ordered subset expectation maximization* (OSEM) [104]. In this work we shall focus on analytic reconstruction techniques, assuming parallel-beam geometry [105].

Attenuation correction is an important part of the SPECT reconstruction process, especially in the context of cardiac perfusion imaging [106]. It is often considered as the potential "holy grail" of the SPECT nuclear imaging field [107]. The main aim of attenuation correction is to minimize false-positive defects, so that attenuation-corrected reconstructions may allow for better quantification of potential abnormalities [108]. However, until quite recently (the early 2000s), only less than 10% of SPECT cameras worldwide were equipped with attenuation correction capabilities [109], even though since the early 1980s substantial efforts were made to allow image fusion, especially in brain studies [30]. Nowadays, hybrid SPECT/CT [110] is becoming a standard dual medical imaging modality, with various SPECT/CT systems being currently commercially available. There exists a variety of studies that demonstrate the superiority of SPECT/CT over stand-alone SPECT in terms of diagnostic accuracy [111]. This specific dual imaging approach is now suitable for a wide variety of diagnostic applications with clinical impact [112], essentially addressing the ultimate objective in nuclear medicine of shortening the acquisition time and of providing accurate, high-quality attenuation-corrected fusion imaging [31].

SPECT reconstruction algorithms aim to invert the attenuated Radon transform, see equation (1.15) in Section 1.4, which provides a certain generalization of the two-dimensional Radon transform. The attenuated Radon transform, defined in Definition 1.3 in page 58, is the line integral of the distribution of the radioactive material inside the patient's body, attenuated with respect to the associated linear attenuation coefficient. The corresponding attenuated SPECT data are usually stored as camera projections, which can be expressed as attenuated sinograms, similar to the sinograms of positron emission tomography (PET). The analytical approach to SPECT reconstruction always involves the *inverse attenuated Radon transform* (IART), i.e. the inversion of the attenuated sinogram. Following the pioneering work of Novikov [7] in 2002, an explicit mathematical formulation of IART was given in 2006 by Fokas, Iserles and Marinakis [8]. For the inversion of the

attenuated Radon transform, other analytical SPECT reconstruction techniques based on Novikov's work [7] include:

(i) Natterer's exact inversion formulæ [60], which is closely related to Novikov's inversion formula [7],

(ii) Tretiak-Metz seminal algorithm [61],

(iii) Metz and Pan technique [113], considered as a further improvement of the work of Tretiak and Metz [61],

(iv) Kunyansky's elegant reconstruction algorithm [62], which may be viewed as a generalization of the Tretiak-Metz algorithm [61],

(v) Bal and Moireau's method [114], and

(vi) the work of Ammari et al. [115], which provide a closely related asymptotic imaging technique in photoacoustics, in the presence of wave attenuation.

The numerical implementation of the above analytic algorithms is based on the concept of filtered back-projection. Furthermore, the numerical techniques listed above employ the convolution property of the Fourier transform. Fourier convolution is applied, in order to compute the Hilbert transform involved in the attenuated Radon transform inversion. In this direction, and for the cancelation of high frequencies involved, the application of appropriate filters is often necessary.

In this chapter we present an alternative numerical technique for the numerical evaluation of the inverse attenuated Radon transform occurring in SPECT, namely the attenuated spline reconstruction technique (aSRT). aSRT is a novel two-dimensional analytic image reconstruction algorithm and is based on a new and improved mathematical derivation of an earlier implementation introduced by Fokas, Iserles and Marinakis [8]. For the computation of the Hilbert transforms of the linear attenuation function and of two sinusoidal functions of the attenuated Radon transform, we employ custom-made, third-degree splines, instead of the traditional Fourier-based approach. It is important to note that the method used in [8] and in the present chapter both employ cubic splines. Indeed, in our case, we applied splines for the computation of the Hilbert transform of $\hat{\mu}$ (see equation (4.5)),

the two sinusoidal functions of the attenuated sinogram, namely G_c and G_s (see equations (4.8)) and the function G (defined in equation (4.7)). The corresponding analysis is presented on Section 4.3. These specific functions are different from the functions encountered in [8]; it will be shown that these functions simplify the numerical implementation of the inversion of the attenuated Radon transform. The differences mentioned above become quite clear if we compare equation (3.6) of [8] with the corresponding equation (4.6) of Theorem 4.1 of the present chapter. Therefore, our new derivation improves substantially the earlier formulation, leading to simplified expressions which have the important advantage that they can be implemented numerically in a significantly more efficient manner. aSRT, in comparison to the industry standard FBP and OSEM, has the advantage of incorporating attenuation correction within itself. Furthermore, it is worth noting that all necessary calculations involved are performed in the image (physical) space, as opposed to the Fourier space.

It is important to emphasize the fact that aSRT differs from SRT for PET, developed by Kastis et al. [116, 117]. aSRT constitutes a substantial generalization of SRT: SRT aims to invert the non-attenuated Radon transform, i.e. the line integrals of the radioactive distribution, while our algorithm aSRT inverts the corresponding line integrals attenuated with respect to the linear attenuation function, μ. Although in both PET and SPECT the transmitted gamma rays suffer a relative intensity loss, as outlined by the well-known Beer's law (see Section I.3), from a mathematical aspect, the inversion occurring in PET (non-attenuated Radon) is a special case of the corresponding inversion in SPECT (attenuated Radon). In the former case, the attenuation factor is the integral of the linear attenuation function (μ) along a single line, whereas in the latter the attenuation factor is the integral of μ along a single line segment.

The aim of the present work is (a) to present the mathematical setting of aSRT and all equations involved, (b) to reconstruct simulated and real attenuated sinograms, i.e. SPECT/CT data, using aSRT in order to evaluate its performance, and (c) to compare aSRT with filtered backprojection and ordered subsets expectation maximization. It is worth noting that this is the first work involving the analytic inversion of the attenuated Radon transform, where reconstructions of real clinical data are performed, and improved bias and contrast with respect to FBP are demonstrated.

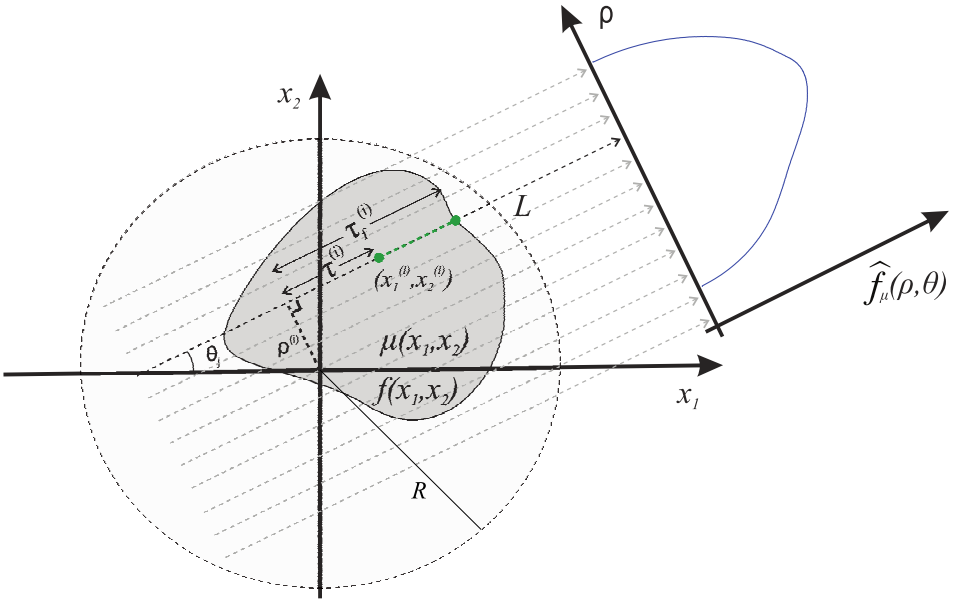

Figure 4.1: A two-dimensional object, with attenuation coefficient $\mu(x_1, x_2)$, being imaged with parallel-beam projection geometry. Cartesian (x_1, x_2) and local (ρ, τ) coordinates are indicated.

4.2 A novel inversion formula for the attenuated Radon transform

We shall follow the ideas and notation introduced in Chapter 1. We consider a line L on the plane, specified by two real numbers, namely the signed distance from the origin ρ, $-\infty < \rho < \infty$, and the angle with the x_1-axis θ, $0 \leq \theta < 2\pi$, see figure 4.1. The unit vectors parallel ($\mathbf{e}^{\parallel}$) and perpendicular ($\mathbf{e}^{\perp}$) to L are given by

$$\mathbf{e}^{\parallel} = (\cos\theta, \sin\theta) \quad \text{and} \quad \mathbf{e}^{\perp} = (-\sin\theta, \cos\theta)\,.$$

Therefore, every point on L in cartesian coordinates $\mathbf{x} = (x_1, x_2)$ can be expressed in terms of the so-called *local* coordinates (ρ, τ) via

$$\mathbf{x} = \rho\,\mathbf{e}^{\perp} + \tau\,\mathbf{e}^{\parallel},$$

where τ denotes the arc length along the line L. Hence,

$$x_1 = \tau\cos\theta - \rho\sin\theta \quad \text{and} \quad x_2 = \tau\sin\theta + \rho\cos\theta. \tag{4.1}$$

We can invert equations (4.1) and express the local coordinates (ρ, τ) in terms of the cartesian coordinates (x_1, x_2) and their corresponding angle θ via the following equations:

$$\rho = x_2\cos\theta - x_1\sin\theta \quad \text{and} \quad \tau = x_2\sin\theta + x_1\cos\theta. \tag{4.2}$$

As indicated in Definition 1.3, the line integral of a function $f : \mathbb{R}^2 \to \mathbb{R}$ attenuated with respect to an attenuation function $\mu : \mathbb{R}^2 \to \mathbb{R}$ is called the attenuated Radon transform of $f(x_1, x_2)$. It is usually stored in the form of the so-called *attenuated sinogram* and will be denoted by $\widehat{f}_\mu(\rho, \theta)$:

$$\widehat{f}_\mu(\rho,\theta) = \int_{-\infty}^{\infty} e^{-\int_\tau^\infty \mu(s\cos\theta-\rho\sin\theta, s\sin\theta+\rho\cos\theta)\mathrm{d}s} \times$$
$$f(\tau\cos\theta - \rho\sin\theta, \tau\sin\theta + \rho\cos\theta)\mathrm{d}\tau,\ 0 \le \theta < 2\pi,\ -\infty < \rho < \infty, \tag{4.3}$$

where the subscript μ emphasizes the dependence on the linear attenuation function.

Associated with equation (4.3) there exists the following **inverse problem**: Given the functions $\mu(x_1, x_2)$, $-\infty < x_1, x_2 < \infty$, and $\widehat{f}_\mu(\rho, \theta)$, $0 \le \theta < 2\pi$, $-\infty < \rho < \infty$, determine the function $f(x_1, x_2)$. The relevant inversion formula, called the inverse attenuated Radon transform (IART) was first derived by Novikov [7] in 2002, extending the derivation of the analogous result for the inverse Radon transform presented by Fokas and Novikov in 1991 [6]. It was several years later (2006) shown by Fokas, Iserles and Marinakis in [8] that the inversion formula can actually be obtained via a slight modification of a certain formula initially contained in [6]. This inversion formula for the attenuated Radon transform was given by:

$$f(x_1, x_2) = \frac{1}{4\pi}(\partial_{x_1} - \mathrm{i}\partial_{x_2}) \int_0^{2\pi} e^{\mathrm{i}\theta} J(x_1, x_2, \theta)\mathrm{d}\theta,\ -\infty < x_1, x_2 < \infty, \tag{4.4a}$$

where the function J is defined by

$$J(x_1, x_2, \theta) = e^{M(\tau,\rho,\theta)} L_\mu(\rho, \theta)\widehat{f}_\mu(\rho, \theta)\Big|_{\substack{\tau = x_2\sin\theta + x_1\cos\theta \\ \rho = x_2\cos\theta - x_1\sin\theta}}, \tag{4.4b}$$

with M and L_μ defined by

$$M(\tau,\rho,\theta) = \int_\tau^\infty \mu\left(s\cos\theta - \rho\sin\theta, s\sin\theta + \rho\cos\theta\right) \mathrm{d}s, \tag{4.4c}$$

$$L_\mu(\rho,\theta) = e^{P^-\widehat{\mu}(\rho,\theta)} P^- e^{P^-\widehat{\mu}(\rho,\theta)} + e^{-P^+\widehat{\mu}(\rho,\theta)} P^+ e^{P^+\widehat{\mu}(\rho,\theta)}. \tag{4.4d}$$

In equation (4.4d), $\widehat{\mu}$ represents the Radon transform of the attenuation function μ, i.e.,

$$\widehat{\mu}(\rho,\theta) = \int_{-\infty}^\infty \mu\left(\tau\cos\theta - \rho\sin\theta, \tau\sin\theta + \rho\cos\theta\right) \mathrm{d}\tau, \qquad 0 \le \theta < 2\pi,\ -\infty < \rho < \infty, \tag{4.4e}$$

whereas $P^\pm$ denotes the following projection operators in the signed distance variable ρ:

$$(P^\pm g)(\rho) = \pm\frac{g(\rho)}{2} + \frac{1}{2\pi\mathrm{i}}\left(PV\int_{-\infty}^\infty \frac{g(r)}{r-\rho}\mathrm{d}r\right), \quad -\infty < \rho < \infty, \tag{4.4f}$$

where $PV\int$ denotes the principal value integral, as in equation (2.19).

In what follows, it is useful to define F as half the Hilbert transform, defined in equation (2.26), of $\widehat{\mu}$, which is in turn defined in equation (4.4e)

$$F(\rho,\theta) \equiv \frac{1}{2}\mathcal{H}\left\{\widehat{\mu}(\rho,\theta)\right\} = \frac{1}{2\pi}\left(PV\int_{-\infty}^\infty \frac{\widehat{\mu}(r,\theta)}{r-\rho}\mathrm{d}r\right), \tag{4.5}$$

where $\mathcal{H}$ denotes the Hilbert transform in the variable ρ, as in Definition 2.26.

Theorem 4.1. *The inversion formula for the attenuated Radon transform, defined in equation* (4.4a)*, of a function $f(x_1,x_2)$ attenuated with respect to a function $\mu(x_1,x_2)$ is equivalent to the representation*

$$f(x_1,x_2) = -\frac{1}{2\pi}\int_0^{2\pi} e^{M(\tau,\rho,\theta)}\left[M_\rho(\tau,\rho,\theta)G(\rho,\theta) + G_\rho(\rho,\theta)\right]\Big|_{\substack{\rho=x_2\cos\theta - x_1\sin\theta \\ \tau=x_2\sin\theta + x_1\cos\theta}} \mathrm{d}\theta, \tag{4.6}$$

subscripts denote differentiation with respect to ρ, M is defined in equation (4.4c) *and G is defined by*

$$G(\rho,\theta) = e^{-\frac{1}{2}\widehat{\mu}(\rho,\theta)}\left[\cos(F(\rho,\theta))G^C(\rho,\theta) + \sin(F(\rho,\theta))G^S(\rho,\theta)\right], \tag{4.7}$$

with the functions G^C and G^S defined by

$$G^C(\rho,\theta) = \frac{1}{2\pi} PV \int_{-\infty}^{\infty} e^{\frac{1}{2}\widehat{\mu}(r,\theta)} \cos F(r,\theta) \frac{\widehat{f}_\mu(r,\theta)\mathrm{d}r}{r-\rho}, \tag{4.8a}$$

$$G^S(\rho,\theta) = \frac{1}{2\pi} PV \int_{-\infty}^{\infty} e^{\frac{1}{2}\widehat{\mu}(r,\theta)} \sin F(r,\theta) \frac{\widehat{f}_\mu(r,\theta)\mathrm{d}r}{r-\rho}. \tag{4.8b}$$

Proof. We apply the operator L_μ, defined in equation (4.4d), on the attenuated Radon transform $\widehat{f}_\mu$, defined in equation (1.15), as follows:

$$\begin{aligned}\left(L_\mu \widehat{f}_\mu\right)(\rho,\theta) = \Big\{ & e^{P^-\widehat{\mu}(\rho,\theta)} P^- e^{P^-\widehat{\mu}(\rho,\theta)} \\ & + e^{-P^+\widehat{\mu}(\rho,\theta)} P^+ e^{P^+\widehat{\mu}(\rho,\theta)} \Big\} \widehat{f}_\mu(\rho,\theta).\end{aligned} \tag{4.9}$$

Equations (4.4f) and (4.5) imply

$$e^{P^\pm\widehat{\mu}} = e^{\pm\frac{\widehat{\mu}}{2} - \mathrm{i}F}. \tag{4.10}$$

Hence,

$$e^{P^-\widehat{\mu}} P^- \left\{ e^{-P^-\widehat{\mu}} \widehat{f}_\mu \right\} = e^{-\frac{\widehat{\mu}}{2} - \mathrm{i}F} \left[-\frac{1}{2} e^{\frac{\widehat{\mu}}{2} + \mathrm{i}F} \widehat{f}_\mu + \frac{1}{2\mathrm{i}} \mathcal{H} \left\{ e^{\frac{\widehat{\mu}}{2} + \mathrm{i}F} \widehat{f}_\mu \right\} \right], \tag{4.11a}$$

and

$$e^{-P^+\widehat{\mu}} P^+ \left\{ e^{P^+\widehat{\mu}} \widehat{f}_\mu \right\} = e^{-\frac{\widehat{\mu}}{2} + \mathrm{i}F} \left[\frac{1}{2} e^{\frac{\widehat{\mu}}{2} - \mathrm{i}F} \widehat{f}_\mu + \frac{1}{2\mathrm{i}} \mathcal{H} \left\{ e^{\frac{\widehat{\mu}}{2} - \mathrm{i}F} \widehat{f}_\mu \right\} \right]. \tag{4.11b}$$

By further analyzing equations (4.11), we can decipher equation (4.9). More specifically, for the simplification of equation (4.9), we first take into account equation (4.5) and then combine equations (4.10) and (4.11) and rewrite the operator L_μ in the form

$$\left(L_\mu \widehat{f}_\mu\right)(\rho,\theta) = \frac{1}{2\mathrm{i}} e^{-\frac{\widehat{\mu}}{2}} \left[e^{-\mathrm{i}F} \mathcal{H} \left\{ e^{\frac{\widehat{\mu}}{2} + \mathrm{i}F} \widehat{f}_\mu \right\} + e^{\mathrm{i}F} \mathcal{H} \left\{ e^{\frac{\widehat{\mu}}{2}\mathrm{i}F} \widehat{f}_\mu \right\} \right]. \tag{4.12}$$

Using Euler's formula

$$e^{\mathrm{i}F} = \cos F + \mathrm{i} \sin F,$$

equation (4.12) simplifies as follows:

$$\left(L_\mu \widehat{f}_\mu\right)(\rho,\theta) = \frac{1}{2\mathrm{i}} e^{-\frac{\widehat{\mu}}{2}} \left[(\cos F - \mathrm{i}\sin F)\mathcal{H}\left\{e^{\frac{\widehat{\mu}}{2}+\mathrm{i}F}\widehat{f}_\mu\right\} + (\cos F + \mathrm{i}\sin F)\mathcal{H}\left\{e^{\frac{\widehat{\mu}}{2}-\mathrm{i}F}\widehat{f}_\mu\right\}\right]. \quad (4.13a)$$

Further expansion of (4.13a) yields

$$\left(L_\mu \widehat{f}_\mu\right)(\rho,\theta) = \frac{1}{2\mathrm{i}} e^{-\frac{\widehat{\mu}}{2}} \left[\cos F\left(\mathcal{H}\left\{e^{\frac{\widehat{\mu}}{2}+\mathrm{i}F}\widehat{f}_\mu\right\} + \mathcal{H}\left\{e^{\frac{\widehat{\mu}}{2}-\mathrm{i}F}\widehat{f}_\mu\right\}\right) - \mathrm{i}\sin F\left(\mathcal{H}\left\{e^{\frac{\widehat{\mu}}{2}+\mathrm{i}F}\widehat{f}_\mu\right\} - \mathcal{H}\left\{e^{\frac{\widehat{\mu}}{2}-\mathrm{i}F}\widehat{f}_\mu\right\}\right)\right], \quad (4.13b)$$

which in turn implies

$$\left(L_\mu \widehat{f}_\mu\right)(\rho,\theta) = \frac{1}{2\pi\mathrm{i}} e^{-\frac{\widehat{\mu}}{2}} \left[\cos F\left(PV\int_{-\infty}^{\infty} \frac{e^{\frac{\widehat{\mu}}{2}+\mathrm{i}F} + e^{\frac{\widehat{\mu}}{2}-\mathrm{i}F}}{r-\rho}\widehat{f}_\mu \mathrm{d}r\right) - \mathrm{i}\sin F\left(PV\int_{-\infty}^{\infty} \frac{e^{\frac{\widehat{\mu}}{2}+\mathrm{i}F} - e^{\frac{\widehat{\mu}}{2}-\mathrm{i}F}}{r-\rho}\widehat{f}_\mu \mathrm{d}r\right)\right]. \quad (4.13c)$$

This way, we are able to rewrite the above expression as

$$\left(L_\mu \widehat{f}_\mu\right)(\rho,\theta) = \frac{1}{2\pi\mathrm{i}} e^{-\frac{\widehat{\mu}}{2}} \left[\cos F\left(PV\int_{-\infty}^{\infty} \frac{e^{\frac{\widehat{\mu}}{2}}(e^{\mathrm{i}F} + e^{-\mathrm{i}F})}{r-\rho}\widehat{f}_\mu \mathrm{d}r\right) - \mathrm{i}\sin F\left(PV\int_{-\infty}^{\infty} \frac{e^{\frac{\widehat{\mu}}{2}}(e^{\mathrm{i}F} - e^{-\mathrm{i}F})}{r-\rho}\widehat{f}_\mu \mathrm{d}r\right)\right], \quad (4.13d)$$

or even

$$\left(L_\mu \widehat{f}_\mu\right)(\rho,\theta) = \frac{1}{2\pi\mathrm{i}} e^{-\frac{\widehat{\mu}}{2}} \left[\cos F\left(PV\int_{-\infty}^{\infty} \frac{e^{\frac{\widehat{\mu}}{2}}(2\cos F)}{r-\rho}\widehat{f}_\mu \mathrm{d}r\right) - \mathrm{i}\sin F\left(PV\int_{-\infty}^{\infty} \frac{e^{\frac{\widehat{\mu}}{2}}(2\mathrm{i}\sin F)}{r-\rho}\widehat{f}_\mu \mathrm{d}r\right)\right]. \quad (4.13e)$$

The final step involves the following manipulation,

$$\left(L_\mu \widehat{f}_\mu\right)(\rho,\theta) = \frac{2}{\mathrm{i}} e^{-\frac{\widehat{\mu}}{2}} \left[\cos F \left(\frac{1}{2\pi}\left\{PV \int_{-\infty}^{\infty} \frac{e^{\frac{\widehat{\mu}}{2}} \cos F}{r-\rho} \widehat{f}_\mu \mathrm{d}r\right\}\right) + \sin F \left(\frac{1}{2\pi}\left\{PV \int_{-\infty}^{\infty} \frac{e^{\frac{\widehat{\mu}}{2}} \sin F}{r-\rho} \widehat{f}_\mu \mathrm{d}r\right\}\right)\right], \quad (4.13f)$$

which leads to the final simplification of equation (4.12), as follows:

$$\left(L_\mu \widehat{f}_\mu\right)(\rho,\theta) = -2\mathrm{i} e^{-\frac{\widehat{\mu}}{2}} \left[\cos(F) G^C + \sin(F) G^S\right], \quad (4.14)$$

with $G^C(\rho,\theta)$ and $G^S(\rho,\theta)$ defined in equations (4.8a) and (4.8b), respectively. In equation (4.14), if we take into account the definition (4.7) of the function $G(\rho,\theta)$ we find

$$\left(L_\mu \widehat{f}_\mu\right)(\rho,\theta) = -2\mathrm{i} G(\rho,\theta). \quad (4.15)$$

Hence, equation (4.9) becomes equation (4.15). It is important to note that equation (4.15) implies that the function

$$\left(L_\mu \widehat{f_\mu}\right)(\rho,\theta)$$

is purely imaginary, i.e.

$$\mathrm{Re}\left\{\left(L_\mu \widehat{f_\mu}\right)(\rho,\theta)\right\} = 0.$$

Thus, equations (4.4b) and (4.15) imply that

$$J(x_1,x_2,\theta) = -2\mathrm{i}\left[e^{M(\tau,\rho,\theta)} G(\rho,\theta)\right]_{\substack{\tau = x_2\sin\theta + x_1\cos\theta \\ \rho = x_2\cos\theta - x_1\sin\theta}}. \quad (4.16)$$

Therefore, using the differential operator

$$(\partial_{x_1} - \mathrm{i}\partial_{x_2}) = e^{-\mathrm{i}\theta}(\partial_\tau - \mathrm{i}\partial_\rho), \quad (4.17)$$

which arises from the application of the chain rule to the local coordinates, defined in equations (4.1), we can calculate the action of the operator (4.17)

on J:

$$\begin{aligned}(\partial_{x_1} - \mathrm{i}\partial_{x_2})J &= -2\mathrm{i}e^{-\mathrm{i}\theta}(\partial_\tau - \mathrm{i}\partial_\rho)\left\{e^M G\right\}_{\substack{\rho=x_2\cos\theta - x_1\sin\theta \\ \tau=x_2\sin\theta + x_1\cos\theta}} \\ &= -2\mathrm{i}e^{-i\theta}\left[e^M(M_\tau - \mathrm{i}M_\rho)G + e^M(G_\tau - \mathrm{i}G_\rho)\right]_{\substack{\rho=x_2\cos\theta - x_1\sin\theta \\ \tau=x_2\sin\theta + x_1\cos\theta}} \\ &= -2e^{-\mathrm{i}\theta}e^M\left[-\mathrm{i}\mu G + M_\rho G + G_\rho\right]_{\substack{\rho=x_2\cos\theta - x_1\sin\theta \\ \tau=x_2\sin\theta + x_1\cos\theta}}, \qquad (4.18)\end{aligned}$$

where we have used the identities

$$M_\tau(\tau,\rho,\theta)\Big|_{\substack{\rho=x_2\cos\theta - x_1\sin\theta \\ \tau=x_2\sin\theta + x_1\cos\theta}} = \mu(x_1,x_2) \quad \text{and} \quad G_\tau(\rho,\theta) = 0.$$

Inserting the operator $(\partial_{x_1} - \mathrm{i}\partial_{x_2})$ inside the integral in the right-hand side of equation (4.4a) and combining equations (4.16) and (4.18), yields

$$f(x_1,x_2) = -\frac{1}{2\pi}\int_0^{2\pi} e^M\left[-\mathrm{i}\mu G + M_\rho G + G_\rho\right]\Bigg|_{\substack{\rho=x_2\cos\theta - x_1\sin\theta \\ \tau=x_2\sin\theta + x_1\cos\theta}} \mathrm{d}\theta. \qquad (4.19)$$

The first term of the integral on the right-hand side of equation (4.19) can be simplified as follows:

$$\begin{aligned}-\mathrm{i}\int_0^{2\pi}\mu(x_1,x_2)\left[e^{M(\tau,\rho,\theta)}G(\rho,\theta)\right]_{\substack{\tau=x_2\sin\theta + x_1\cos\theta \\ \rho=x_2\cos\theta - x_1\sin\theta}}\mathrm{d}\theta \\ = \frac{1}{2}\mu(x_1,x_2)\int_0^{2\pi} J(x_1,x_2,\theta)\mathrm{d}\theta. \qquad (4.20)\end{aligned}$$

Equation (2.9) of [8], with μ replaced by u, evaluated at $\lambda = 0$ yields

$$u(x_1,x_2,0) = \frac{1}{2\pi}\int_0^{2\pi} J(x_1,x_2,\theta)\mathrm{d}\theta.$$

Furthermore, the limit $\lambda \to 0$ of equation (2.2) of [8] yields

$$\frac{\partial u(x_1,x_2,0)}{\partial \bar{z}} = 0,$$

Hence, u is analytic everywhere, including infinity. Recalling the assumption of Proposition 2.1 of [8] that u satisfies the boundary condition

$$u = O\left(\frac{1}{z}\right), \quad z \to \infty,$$

it follows that the entire function u vanishes (Liouville's theorem), thus

$$\int_0^{2\pi} J(x_1, x_2, \theta)\mathrm{d}\theta = 0. \tag{4.21}$$

Hence, taking into account equation (4.21), equation (4.20) implies that

$$\int_0^{2\pi} \mu(x_1, x_2) \left[e^{M(\tau,\rho,\theta)} G(\rho, \theta) \right]_{\substack{\tau = x_2 \sin\theta + x_1 \cos\theta \\ \rho = x_2 \cos\theta - x_1 \sin\theta}} \mathrm{d}\theta = 0.$$

The above implies that (4.19) simplifies to

$$f(x_1, x_2) = -\frac{1}{2\pi} \int_0^{2\pi} e^M \left(M_\rho G + G_\rho \right) \Big|_{\substack{\rho = x_2 \cos\theta - x_1 \sin\theta \\ \tau = x_2 \sin\theta + x_1 \cos\theta}} \mathrm{d}\theta. \tag{4.22}$$

Therefore, equation (4.4a) becomes equation (4.6). ■

4.3 Numerical implementation using splines

In order to numerically evaluate all quantities involved in equation (4.6), we employ the Gauss-Legendre quadrature for the computation of the function $M(\tau, \rho, \theta)$, as well as custom-made splines [118] for the computation of the functions $G(\rho, \theta)$ and $F(\rho, \theta)$. For all the functions appearing in the inversion formula of the attenuated Radon transform, we assume that the evaluation of the solution to the inverse problem (4.4) is performed at the points

$$\left(x_1^{(i)}, x_2^{(j)} \right)_{i,j=1}^{n},$$

i.e. in a given square reconstruction grid, as common medical imaging practise suggests.

4.3.1 The evaluation of $M(\tau, \rho, \theta)$ and its ∂_ρ derivative

The integral for the function $M(\tau, \rho, \theta)$ (4.4c) involves the computation of the integral of the given attenuation function $\mu(x_1, x_2)$ from

$$s = \tau^{(i)} \quad \text{to} \quad s = \tau_f^{(i)},$$

see figure 4.1. However,

$$\left(\rho^{(i)}\right)^2 + \left(\tau_f^{(i)}\right)^2 \leq R^2,$$

where R denotes the radius of the circular path centered at the origin, which includes the supports of both $f(x_1, x_2)$ and $\mu(x_1, x_2)$. Therefore,

$$M(\tau^{(i)}, \rho^{(i)}, \theta_j) = \int_{\tau^{(i)}}^{\sqrt{R^2-\left(\rho^{(i)}\right)^2}} \mu\left(s\cos\theta_j - \rho^{(i)}\sin\theta_j, \right. \\ \left. s\sin\theta_j + \rho^{(i)}\cos\theta_j\right) \mathrm{d}s. \quad (4.23)$$

The above integral can be computed using the Gauss-Legendre quadrature with two functional evaluations at every step,

$$\int_{s_1}^{s_2} f(s)\mathrm{d}s \sim \frac{1}{2}(s_2 - s_1)\left[f(\tau_1) + f(\tau_2)\right],$$

where

$$\tau_1 = s_1 + \frac{1}{2}\left(1 - \frac{\sqrt{3}}{3}\right)(s_2 - s_1), \quad \tau_2 = s_1 + \frac{1}{2}\left(1 + \frac{\sqrt{3}}{3}\right)(s_2 - s_1).$$

For the evaluation of the partial derivative of M with respect to ρ, $M_\rho(\tau, \rho, \theta)$, we employ an appropriate finite difference scheme, as in [119].

4.3.2 The evaluation of $F(\rho, \theta)$

For the evaluation of $F(\rho, \theta)$, i.e. the half of the Hilbert transform of $\widehat{\mu}(\rho, \theta)$ in the variable ρ, we proceed in a similar way as in [116]. However, this time, instead of evaluating the partial derivative of the Hilbert transform of $\widehat{\mu}(\rho, \theta)$ with respect to ρ, we evaluate the Hilbert transform of $\widehat{\mu}(\rho, \theta)$, itself.

We assume that a function

$$f : [-1, 1] \times [0, 2\pi] \to \mathbb{R},$$

with arguments indicated by (ρ, θ), is given for every θ at the n points $\{\rho_i\}_1^n$. We denote the value of f at ρ_i by f_i:

$$f_i := f_i(\theta) = f(\rho_i, \theta), \quad \rho_i \in [-1, 1], \quad 0 \leq \theta < 2\pi, \quad i = 1, \ldots, n. \quad (4.24)$$

Furthermore, we assume that both $f(\rho,\theta)$ and its derivative with respect to ρ vanish at the endpoints $\rho_1=-1$ and $\rho_n=1$:

$$f(-1,\theta)=f(1,\theta)=0,\quad 0\le\theta<2\pi, \tag{4.25a}$$

$$\frac{\partial f}{\partial\rho}(-1,\theta)=\frac{\partial f}{\partial\rho}(1,\theta)=0,\quad 0\le\theta<2\pi. \tag{4.25b}$$

In each subinterval P_i, with

$$P_i=[\rho_i,\rho_{i+1}]\subseteq[\rho_1,\rho_n]=[-1,1],\quad i=1,\dots,n-1,$$

we approximate $f(\rho,\theta)$ by third-degree cubic splines in the variable ρ, denoted by $S_i^{(3)}(\rho,\theta)$:

$$f(\rho,\theta)\sim S_i^{(3)}(\rho,\theta),\quad \rho\in P_i,\quad 0\le\theta<2\pi,\quad i=1,\dots,n-1.$$

This specific cubic spline interpolates the function $f(\rho,\theta)$ at the knots $\{\rho_i\}_{i=1}^n$ in the sense that

$$S_i^{(3)}(\rho_i,\theta)=f_i(\theta),\quad i=1,\dots,n-1. \tag{4.26}$$

More specifically,

$$S_i^{(3)}(\rho,\theta)=\sum_{j=0}^{3}c_i^{(j)}\rho^j,\quad \rho\in P_i,\quad 0\le\theta<2\pi,\quad i=1,\dots,n-1, \tag{4.27}$$

where the constants $\left\{c_i^{(j)}\right\}_{i=1}^n$ for $j=0,\dots,3$, are given by the following expressions, see [116, 119]:

$$c_i^{(0)}=\frac{\rho_{i+1}f_i-\rho_i f_{i+1}}{\Delta_i}+\frac{f_i''}{6}\left(-\rho_{i+1}\Delta_i+\frac{\rho_{i+1}^3}{\Delta_i}\right)+\frac{f_{i+1}''}{6}\left(\rho_i\Delta_i-\frac{\rho_i^3}{\Delta_i}\right), \tag{4.28a}$$

$$c_i^{(1)}=\frac{f_{i+1}-f_i}{\Delta_i}-\frac{f_i''}{6}\left(-\Delta_i+\frac{3\rho_{i+1}^2}{\Delta_i}\right)+\frac{f_{i+1}''}{6}\left(-\Delta_i+\frac{3\rho_i^2}{\Delta_i}\right), \tag{4.28b}$$

$$c_i^{(2)}=\frac{1}{2\Delta_i}(\rho_{i+1}f_i''-\rho_i f_{i+1}''), \tag{4.28c}$$

$$c_i^{(3)}=\frac{f_{i+1}''-f_i''}{6\Delta_i}, \tag{4.28d}$$

$$\Delta_i=\rho_{i+1}-\rho_i, \tag{4.28e}$$

with f_i'' denoting the second derivative of $f(\rho,\theta)$ with respect to ρ evaluated at ρ_i, i.e.,

$$f_i'' = \left.\frac{\partial^2 f(\rho,\theta)}{\partial\rho^2}\right|_{\rho=\rho_i}, \quad i=1,\ldots,n. \tag{4.29}$$

It is important to note that equation (4.29) involves the "second derivative" of the data. However, the assumption that the data are smooth enough to even possess a second derivative is an oversimplification. To resolve this issue, we simply replace the second derivative of the data with the second derivative of its interpolating spline. In this direction, and following the notation introduced in equation (4.27), we denote the second derivative in question by $S_i^{(1)}(\rho,\theta)$

$$S_i^{(1)}(\rho,\theta) = 2c_i^{(2)}(\theta) + 6c_i^{(3)}(\theta)\rho, \quad \rho\in P_i, \quad 0\le\theta<2\pi, \tag{4.30}$$

for every $i=1,\ldots,n-1$. Following the principle of equation (4.29), we denote the second derivative of the interpolating spline, evaluated at ρ_i with

$$S_i'' = \left.\frac{\partial^2 S_i^{(1)}(\rho,\theta)}{\partial\rho^2}\right|_{\rho=\rho_i}. \tag{4.31}$$

This way, equations (4.28) may be rewritten as follows

$$c_i^{(0)} = \frac{\rho_{i+1}f_i - \rho_i f_{i+1}}{\Delta_i} + \frac{S_i''}{6}\left(-\rho_{i+1}\Delta_i + \frac{\rho_{i+1}^3}{\Delta_i}\right) + \frac{S_{i+1}''}{6}\left(\rho_i\Delta_i - \frac{\rho_i^3}{\Delta_i}\right), \tag{4.32a}$$

$$c_i^{(1)} = \frac{f_{i+1}-f_i}{\Delta_i} - \frac{S_i''}{6}\left(-\Delta_i + \frac{3\rho_{i+1}^2}{\Delta_i}\right) + \frac{S_{i+1}''}{6}\left(-\Delta_i + \frac{3\rho_i^2}{\Delta_i}\right), \tag{4.32b}$$

$$c_i^{(2)} = \frac{1}{2\Delta_i}(\rho_{i+1}S_i'' - \rho_i S_{i+1}''), \tag{4.32c}$$

$$c_i^{(3)} = \frac{S_{i+1}''-S_i''}{6\Delta_i}, \tag{4.32d}$$

where S_i'' denotes the second derivative of $S_i^{(3)}(\rho,\theta)$ with respect to ρ evaluated at ρ_i, and Δ_i is defined in equation (4.28e).

Equation (4.27) implies

$$PV\int_{\rho_i}^{\rho_{i+1}} \frac{f(r,\theta)}{r-\rho}\mathrm{d}r \;\sim\; \sum_{j=0}^{3} c_i^{(j)} I_i^{(j)}(\rho), \tag{4.33}$$

where

$$I_i^{(j)}(\rho) = PV \int_{\rho_i}^{\rho_{i+1}} \frac{r^j}{r-\rho} \mathrm{d}r, \quad j = 0, \ldots, 3. \tag{4.34}$$

Straightforward calculations yield the following identities for the integrals defined in (4.34):

$$I_i^{(0)}(\rho) = \ln \left| \frac{\rho_{i+1} - \rho}{\rho_i - \rho} \right|, \tag{4.35a}$$

$$I_i^{(1)}(\rho) = \Delta_i + \rho I_i^{(0)}(\rho), \tag{4.35b}$$

$$I_i^{(2)}(\rho) = \frac{1}{2}\left(\rho_{i+1}^2 - \rho_i^2\right) + \Delta_i \rho + \rho^2 I_i^{(0)}(\rho), \tag{4.35c}$$

$$I_i^{(3)}(\rho) = \frac{1}{3}\left(\rho_{i+1}^3 - \rho_i^3\right) + \frac{1}{2}\left(\rho_{i+1}^2 - \rho_i^2\right)\rho + \Delta_i \rho^2 + I_i^{(0)}(\rho)\rho^3. \tag{4.35d}$$

Substituting equations (4.34) and (4.35) in equation (4.33) we find

$$\oint_{\rho_i}^{\rho_{i+1}} \frac{f(r,\theta)}{r-\rho} \mathrm{d}r \;\sim\; \alpha_i(\theta) + \beta_i(\theta)\rho + \gamma_i(\theta)\rho^2 + \left(\sum_{j=0}^{3} c_i^{(j)} \rho^j \right) I_i^{(0)}(\rho), \tag{4.36}$$

where

$$\alpha_i(\theta) = c_i^{(1)}(\theta)\Delta_i + \frac{1}{2} c_i^{(2)} \left(\rho_{i+1}^2 - \rho_i^2\right) + \frac{1}{3} c_i^{(3)} \left(\rho_{i+1}^3 - \rho_i^3\right), \tag{4.37}$$

$$\beta_i(\theta) = \left(c_i^{(2)}(\theta)\Delta_i + \frac{1}{2} c_i^{(3)}(\theta) \left(\rho_{i+1}^2 - \rho_i^2\right) \right), \tag{4.38}$$

$$\gamma_i(\theta) = c_i^{(3)}(\theta)\Delta_i. \tag{4.39}$$

Taking into account equations (4.28), the above expressions simplify as follows:

$$\alpha_i(\theta) = (f_{i+1} - f_i) - \frac{1}{36}[17\rho_{i+1}^2 - 19\rho_{i+1}\rho_i + 8\rho_i^2]S_i'' - \frac{1}{36}[4\rho_{i+1}^2 - 5\rho_{i+1}\rho_i - 5\rho_i^2]S_{i+1}'', \tag{4.40}$$

$$\beta_i(\theta) = \frac{1}{12}\left[(5\rho_{i+1} - \rho_i)\, S_i'' - (5\rho_i - \rho_{i+1})\, S_{i+1}'' \right], \tag{4.41}$$

$$\gamma_i(\theta) = \frac{S_{i+1}'' - S_i''}{6}. \tag{4.42}$$

Hence, using the identity

$$PV\int_{-1}^{1}\frac{f(r,\theta)}{r-\rho}\mathrm{d}r=\sum_{i=1}^{n-1}\left(PV\int_{\rho_i}^{\rho_{i+1}}\frac{f(r,\theta)}{r-\rho}\mathrm{d}r\right), \tag{4.43}$$

equation (4.36) implies

$$\begin{aligned}PV\int_{-1}^{1}\frac{f(r,\theta)}{r-\rho}\mathrm{d}r \;\sim\; & A(\theta)+B(\theta)\rho+\frac{1}{6}(S_n''-S_1'')\rho^2\\ &+\sum_{i=1}^{n-2}\left[S_i^{(3)}(\rho,\theta)-S_{i+1}^{(3)}(\rho,\theta)\right]\ln|\rho_{i+1}-\rho|\\ &+S_{n-1}^{(3)}(\rho,\theta)\ln|\rho_n-\rho|-S_1^{(3)}(\rho,\theta)\ln|\rho_1-\rho|,\end{aligned} \tag{4.44}$$

where

$$A(\theta)=\sum_{i=1}^{n-1}\alpha_i(\theta)\quad\text{and}\quad B(\theta)=\sum_{i=1}^{n-1}\beta_i(\theta). \tag{4.45}$$

The right-hand-side of equation (4.44) involves the functions $\{f_i\}_1^n$, which are known, and the functions $\{S_i''\}_1^n$, which are unknown, see equation (4.31). If we denote the first derivative of the cubic spline ($S_i^{(3)}$) with respect to the variable ρ by $S_i^{(2)}$, where the superscript denotes that $S_i^{(2)}$ is quadratic, then we find

$$S_i^{(2)}(\rho,\theta)=\frac{\partial S_i^{(3)}(\rho,\theta)}{\partial\rho}=c_i^{(1)}(\theta)+2c_i^{(2)}(\theta)\rho+3c_i^{(3)}(\theta)\rho^2. \tag{4.46}$$

In order to compute $\{S_i''\}_1^n$ we follow the procedure of [116], namely we solve the system of the following n equations, taking into account the continuity of the first derivative of the cubic spline:

$$S_i^{(2)}(\rho_{i+1},\theta)=S_{i+1}^{(2)}(\rho_{i+1},\theta),\quad i=1,\ldots,n-2,\quad 0\le\theta<2\pi \tag{4.47a}$$

$$S_1^{(2)}(\rho_1,\theta)=S_{n-1}^{(2)}(\rho_n,\theta)=0. \tag{4.47b}$$

The continuity of the spline, namely

$$S_i^{(3)}(\rho_{i+1},\theta)=S_{i+1}^{(3)}(\rho_{i+1},\theta)\quad i=1,\ldots,n-2,$$

and

$$S_1^{(3)}(\rho_1,\theta)=S_{n-1}^{(3)}(\rho_n,\theta)=0,$$

see equations (4.25a), implies that the points $\{\rho_i\}_1^n$ are *removable logarithmic singularities*. If we apply equation (4.44) with

$$f(\rho,\theta) = \widehat{\mu}(\rho,\theta),$$

we are able to compute $F(\rho,\theta)$.

4.3.3 The evaluation of $G(\rho,\theta)$ and its ∂_ρ derivative

Let f^C and f^S denote the following trigonometric functions:

$$f^C(\rho,\theta) = e^{\frac{1}{2}\widehat{\mu}(\rho,\theta)}\cos(F(\rho,\theta))\widehat{f}_\mu(\rho,\theta), \quad -1 \le \rho \le 1, \quad 0 \le \theta < 2\pi, \tag{4.48a}$$

$$f^S(\rho,\theta) = e^{\frac{1}{2}\widehat{\mu}(\rho,\theta)}\sin\left(F(\rho,\theta)\right)\widehat{f}_\mu(\rho,\theta), \quad -1 \le \rho \le 1 \quad 0 \le \theta \le 2\pi, \tag{4.48b}$$

where $\widehat{\mu}$, $\widehat{f}_\mu$ and F are given in equations (4.4e), (4.3) and (4.5), respectively.

We suppose that the attenuated sinogram, $\widehat{f}_\mu(\rho,\theta)$, is given at the points $\{\rho_i\}_1^n$. Then, by computing $\widehat{\mu}(\rho,\theta)$ and $F(\rho,\theta)$ at these points, we can compute the functions $f^C(\rho,\theta)$ and $f^S(\rho,\theta)$ at the same points. Hence, using equation (4.44) and replacing $f(\rho,\theta)$ by $f^C(\rho,\theta)$ and $f^S(\rho,\theta)$, we can compute $G^C(\rho,\theta)$ and $G^S(\rho,\theta)$, respectively. For the elimination of the removable logarithmic singularities of $G^C(\rho,\theta)$ and $G^S(\rho,\theta)$ we require that both f^C and f^S vanish at the endpoints:

$$f^C(\rho_1,\theta) = f^C(-1,\theta) = 0 \quad \text{and} \quad f^C(\rho_n,\theta) = f^C(1,\theta) = 0, \tag{4.49a}$$

$$f^S(\rho_1,\theta) = f^S(-1,\theta) = 0 \quad \text{and} \quad f^S(\rho_n,\theta) = f^S(1,\theta) = 0. \tag{4.49b}$$

The above equations are valid provided that

$$\widehat{f}_\mu(\rho_1,\theta) = \widehat{f}_\mu(-1,\theta) = 0 \quad \text{and} \quad \widehat{f}_\mu(\rho_n,\theta) = \widehat{f}_\mu(1,\theta) = 0, \tag{4.50}$$

which is always the case in nuclear medicine, due to the assumption that the attenuated sinogram must always have a finite support. By combining $G^C(\rho,\theta)$ and $G^S(\rho,\theta)$, we are able to calculate $G(\rho,\theta)$ as in equation (4.7). For the numerical evaluation of the derivative of G with respect to ρ, $G_\rho(\rho,\theta)$, we employ a suitable finite difference scheme [119], in the same manner as we did for the evaluation of $M_\rho(\rho,\theta)$.

Sphere	Diameter (mm)	Activity
S_1	12.7	hot
S_2	15.9	hot
S_3	19.1	hot
S_4	25.4	hot
S_5	31.8	cold
S_6	38.0	cold
S_b	216.0	warm

Table 4.1: Simulated IQ phantom details.

4.4 Materials and methods used in aSRT

4.4.1 Simulated data

Simulated phantom

For the purposes of our simulations, we have modeled a rotating, single-head gamma camera comprising 129 scintillation crystals. The corresponding square image grid size used was 129×129 pixels. The image and detector pixel size was in all simulation studies 4 mm. We have performed an assessment of aSRT by employing simulated data of an image quality (IQ) phantom. This specific phantom has been employed in order to quantitate the ability of each reconstruction technique to detect both hot and cold lesions of variable size inside a radioactive background. The IQ phantom consists of four circular hot regions (with diameters of 12.7, 15.9, 19.1 and 25.4 mm, denoted with S_1 to S_4, respectively) and two circular cold regions (with diameters of 31.8 and 38 mm, denoted with S_5 and S_6, respectively), inside a larger warm region that simulates the background, see table 4.1 for details. The diameter of the larger background circle (denoted by S_0) is 21.6 cm. The ratio of radioactive concentration (α) between hot regions (α_h) and the warm background (α_b) is

$$\frac{\alpha_h}{\alpha_b} = 4,$$

for the four hot regions. The so-called "cold regions" have zero radioactive concentration.

The simulations of the attenuated sinograms of the IQ phantom were generated in the STIR framework [88], each time using appropriate attenuation maps. The sinograms were acquired for 45, 90 and 180 views over 360 degrees. Three different noise levels (NL) were investigated:

1. 100% (NL1),
2. 50% (NL2),
3. 10% (NL3)

of the total counts. Using the initial noiseless sinogram (NL0) as the starting point, we generated 20 Poisson noise realizations at the three different levels (NL1, NL2 and NL3). For 180 views, the sinograms contained, for each noise level,

- 6×10^6 events for NL0,
- 6×10^6 events for NL1,
- 3×10^6 events for NL2,
- 0.6×10^6 events for NL3,

respectively. Similarly, in the cases of 90 and 45 views, the corresponding numbers of events were

- 3×10^6 events for NL0,
- 3×10^6 events for NL1,
- 1.5×10^6 events for NL2,
- 0.3×10^6 events for NL3,

for 90 views, and

- 1.5×10^6 events for NL0,
- 1.5×10^6 events for NL1,
- 0.75×10^6 events for NL2,
- 0.15×10^6 events for NL3,

for 45 views, respectively.

Implementation of aSRT, of FBP and of OSEM

aSRT Reconstructions All aSRT reconstructions were performed in Matlab. There was no post-reconstruction filtering applied in any aSRT reconstructions employed.

FBP Reconstructions The non-corrected FBP reconstructions of the simulated date were generated in the open-source software library STIR [88]. At a later stage, a ramp filter was applied to these reconstructions with cut-off frequency equal to the Nyquist frequency. It is worth mentioning that the STIR library does not provide a built-in, dedicated function for attenuation correction for FBP in SPECT/CT. Hence, all FBP reconstructions were corrected for attenuation purposes in Matlab, according to Chang's 1^{st} order attenuation correction methodology. For this purpose, CT attenuation maps were employed as in [120]. Furthermore, it is important to note that Chang's method is an intrinsically approximate attenuation correction method, by design.

OSEM Reconstructions Attenuation-corrected OSEM reconstructions were generated with:

- 5 subsets,
- 5 iteration updates (OSEM5),
- 10 iteration updates (OSEM10),
- 20 iteration updates (OSEM20),
- 30 iteration updates (OSEM30),
- 40 iteration updates (OSEM40),
- 50 iteration updates (OSEM50).

The above OSEM reconstructions were generated in STIR with attenuation correction taken into account; however neither detector/collimator response nor scatter correction were simulated.

Sphere	Diameter (mm)	Activity
S_1	12.7	cold
S_2	15.9	cold
S_3	19.1	cold
S_4	25.4	cold
S_5	31.8	cold
S_6	38.0	cold

Table 4.2: Clinical Jaszczak phantom details.

4.4.2 Real data

For the purposes of real data reconstructions, we utilized data from a real Jaszczak phantom study, and from a clinical myocardial study.

Real Jaszczak phantom

We have performed reconstructions of a real Jaszczak phantom, with data provided by a Mediso AnyScan® SC SPECT/CT scanner, equipped with the Nucline™ all-modality acquisition software. For this specific Technetium (^{99}Tc) SPECT/CT study, low energy high resolution (LEHR) parallel collimators were used. The attenuated sinograms were provided by Mediso Medical Imaging Systems, Budapest. The phantom is the standard Jaszczak phantom™ and consists of six cold solid spheres with diameters of 12.7, 15.9, 19.1, 25.4, 31.8 and 38 mm, denoted by S_1 to S_6, respectively, see table 4.2. We used 128 number of views, with a corresponding reconstruction grid size of 256×256 pixels. The image and detector pixel size was 2.13 mm, as common practise suggests. The number of events per slice was approximately 1.2×10^6, whereas the total amount of radioactivity in the phantom was 8 mCi (296 MBq) of Technetium-99m isotope. The total scan duration was 64 minutes, corresponding to 30 seconds acquisition, for each of the 128 projections collected. Three realizations ($R = 3$) were employed during this real phantom SPECT/CT study. It is important to emphasize the fact that the standard Jaszczak phantom involves cold regions only.

Clinical data

We acquired real clinical SPECT data from a GE Millennium VG Hawkeye™ SPECT/CT system. The Millennium VG camera of this specific GE scanner includes two extra large rectangular Digital XP detectors, which can image isotopes of energies within the range of 59 keV to 511 keV. For the purposes of this study, a patient was injected with 3 mCi (111 MBq) of Thallium-201 isotope. Attenuated sinograms of this myocardial perfusion ^{201}Tl stress study were acquired for 60 views, and were reconstructed using aSRT, FBP and OSEM, within a 64×64 reconstruction grid. All necessary corrections, including attenuation, detector/collimator response and scatter, were performed according to the manufacturer's clinical protocol. The image and detector pixel size used was 7.81 mm. The number of events per slice was approximately 1.4×10^6. Furthermore, the total scan duration was 17 minutes, corresponding to 17 seconds acquisition for each of the 60 projections collected.

4.4.3 Image metrics

For the determination of the quality of the reconstructed images for all phantoms investigated, a region of interest (ROI) analysis was performed. Comparisons of aSRT with FBP and OSEM were performed evaluating contrast, bias and image roughness, as described below and in [117, 121]. More specifically, the following image quality metrics were calculated:

(a) hot region contrast, C_h,

(b) cold region contrast, C_c,

(c) % bias for hot regions, b_h,

(d) bias % of background for cold regions, b_c, and

(e) background image roughness, IR.

In order to determine the ROI statistics at each solid phantom sphere, circular ROIs were employed. The diameters of all ROIs were the same as the diameters of the lesions being measured. We calculated several image metrics for all noise levels and we averaged the corresponding results over all realizations, R.

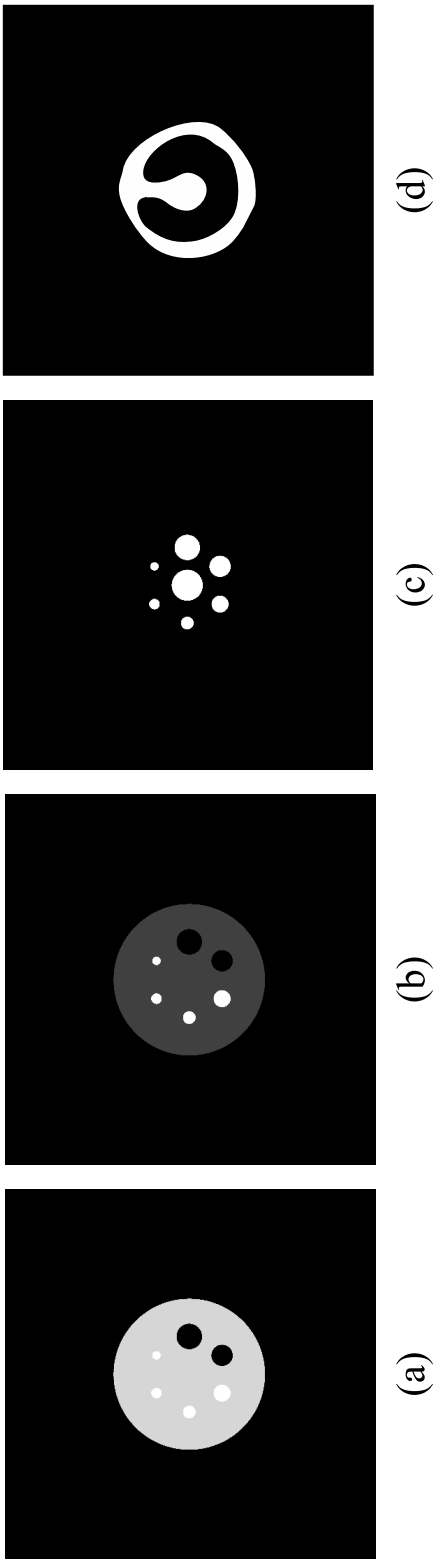

Figure 4.2: (a) IQ phantom, indicating four hot (white) and two cold regions (black) inside a warm background (light gray), (b) Attenuation map for the IQ phantom simulations, indicating four hot (white) and two cold regions (black) inside a warm background (dark gray), corresponding to linear attenuation coefficient values μ (cm^{-1}) of 0.176, 0 and 0.154, respectively, (c) and (d) Circular ROIs employed for the calculation of image metrics.

Hot region contrast (C_h). The hot region contrast (C_h) was calculated for each hot circular region using the following equation [116]:

$$C_h = \frac{1}{R}\sum_{r=1}^{R}\frac{1-\dfrac{m_{h,r}}{m_{b,r}}}{1-\dfrac{a_h}{a_b}}, \tag{4.51}$$

where $m_{h,r}$ and $m_{b,r}$ are the average counts (mean pixel value) measured in each hot sphere and in the background ROI, respectively, for each realization, r, and a_h and a_b are the actual radioactivity of each hot region and the background, respectively. In the case of the simulated IQ phantom used, the ratio (a_h/a_b) is four. We note that C_h is also referred to in the literature as contrast recovery coefficient (CRC).

Cold region contrast (C_c). In a similar manner, the cold region contrast (C_c) was calculated for each cold circular region using the equation

$$C_c = 1 - \frac{1}{R}\sum_{r=1}^{R}\frac{m_{c,r}}{m_{b,r}}, \tag{4.52}$$

where $m_{c,r}$ are the average counts (mean pixel value) measured in each cold circular region and in the background ROI.

% Bias for hot regions (b_h). The %bias for hot spheres (b_h) for each hot circular region was calculated using the equation

$$b_h = \frac{100}{a_h}\times\left[\frac{1}{R}\sum_{r=1}^{R}(m_{h,r}-a_h)\right]. \tag{4.53}$$

Bias % of background for cold regions (b_c). The bias % of background for cold regions (b_c) for each cold circular region was calculated via the formula

$$b_c = \frac{100}{a_b}\times\left(\frac{1}{R}\sum_{r=1}^{R}m_{c,r}\right). \tag{4.54}$$

Image roughness (IR). The image roughness (IR) of the background was calculated as in [117]. This metric measures the pixel-to-pixel variability of the reconstructed image [116] and the perceived image noise [122].

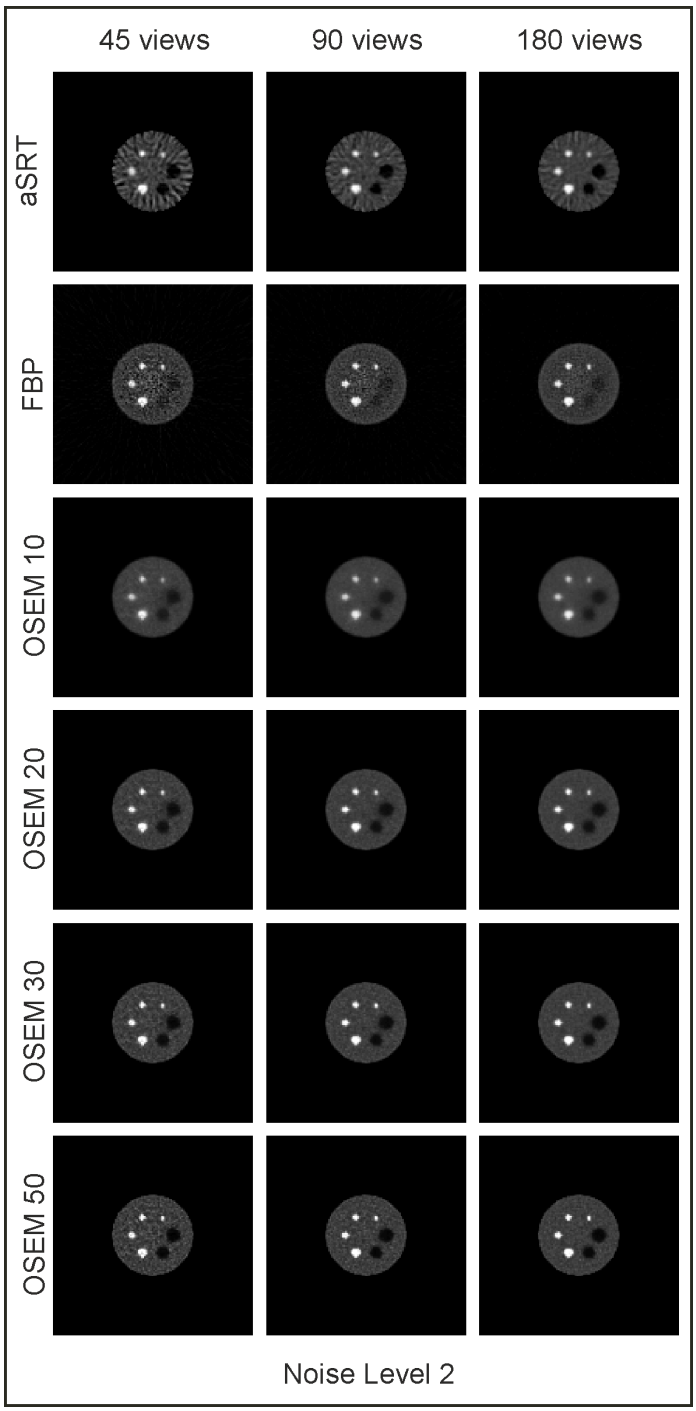

Figure 4.3: IQ phantom reconstructions at noise level 2 (NL2, 50% of counts) with various reconstruction methods (aSRT, FBP and OSEM with 10, 20, 30 and 50 iterations) at 45, 90 and 180 views.

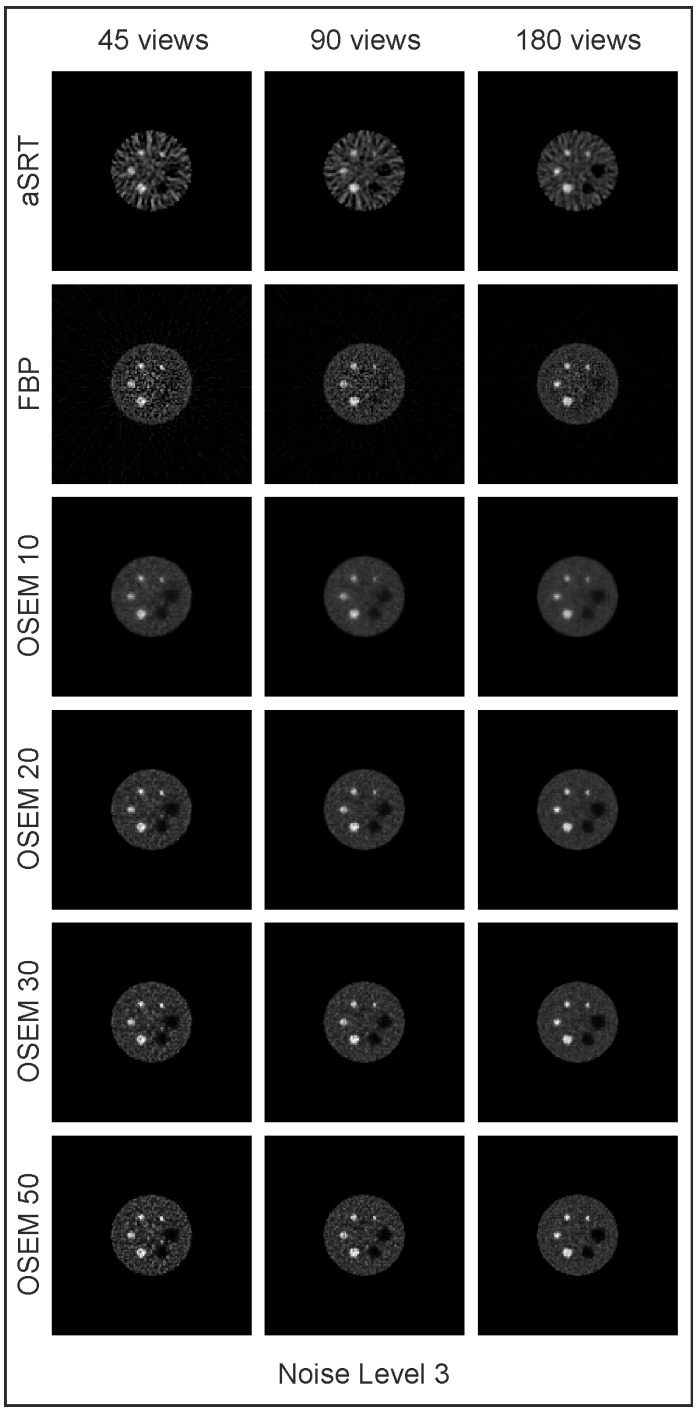

Figure 4.4: IQ phantom reconstructions at noise level 3 (NL3, 10% of counts) with various reconstruction methods (aSRT, FBP and OSEM with 10, 20, 30 and 50 iterations) at 45, 90 and 180 views.

Similar considerations were applied for the cold contrast calculations of all real studies investigated. For the real Jaszczak phantom, we employed ROIs similar to the ones of the IQ phantom simulations. For the clinical myocardial, study we performed an ROI analysis outlined as follows: in the center of the area of the left ventricle of the patient, we selected a circular region, which corresponds to the cold region uptake. Subsequently, we manually drew an ROI in the myocardial area over the annulus, corresponding to the warm background area of the myocardium. Furthermore, we drew similar ROIs for three consecutive slices and, as in the cases of the simulated IQ phantom and the real Jaszczak phantom, averaged the cold contrast measurements over all realizations, as in equation (4.52).

4.5 aSRT results

4.5.1 Simulations

The reconstruction time per slice, for a 45-projections sinogram was

- 2.3 sec for aSRT,
- 3.7 sec for OSEM20,
- 5.2 sec for OSEM30, and
- 13.7 sec for attenuation-corrected FBP,

using an Intel® Xeon® CPU E3-1241 processor, 16GB RAM. The longer time in FBP reconstructions is due to the fact that the attenuation correction was performed in Matlab. Therefore, in this case aSRT was faster than both OSEM and FBP.

The simulated IQ phantom is presented in figure 4.2a, whereas the corresponding attenuation map is presented in figure 4.2b. The ROIs employed for the determination of the image metrics are shown in figure 4.2c. Reconstructed images using aSRT, FBP, and OSEM with 10, 20, 30 and 50 iterations for the IQ phantom, for all numbers of views (45, 90 and 180) are presented in figure 4.3 for noise level 2 (NL2), and in figure 4.4 for noise level 3 (NL3). The reconstructions presented in figures 4.3 and 4.4 are, at each noise level, characteristic reconstructions of one (out of twenty) Poisson-noise realizations. In all reconstructed images presented, the all-black color

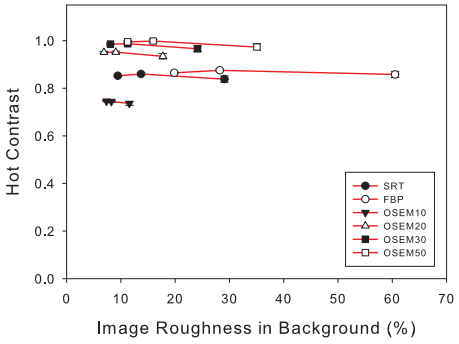

(a) Hot sphere 4 (S_4) hot contrast.

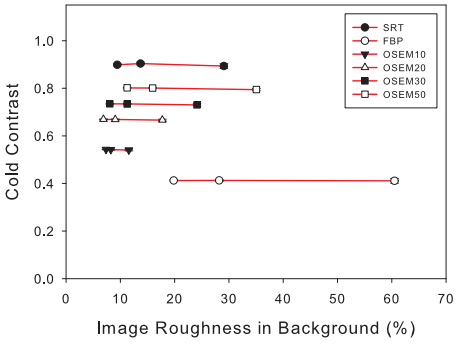

(b) Cold sphere 6 (S_6) cold contrast.

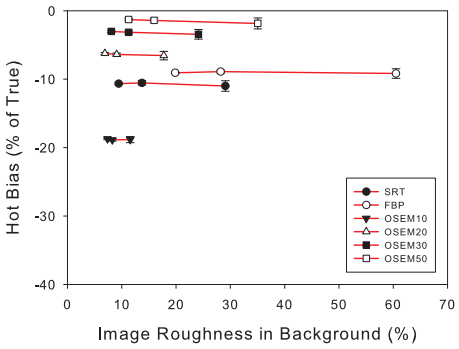

(c) Hot sphere 4 (S_4) hot bias.

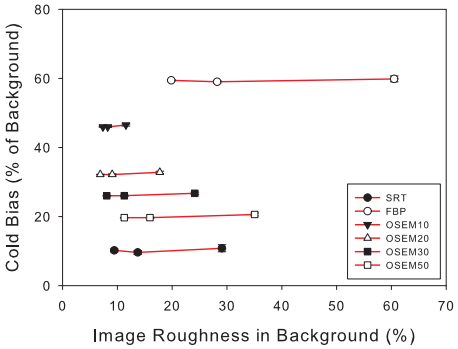

(d) Cold sphere 6 (S_6) cold bias.

Figure 4.5: Contrast (C) and bias (b) measurements vs. image roughness (IR) at 90 views for the hot sphere S_4 and for the cold sphere S_6. The leftmost datum point in each curve corresponds to NL1, the midpoint to NL2 and the rightmost to NL3.

represents zero values, whereas the value of the all-white color represents the maximum value of the IQ phantom reconstruction. Therefore, the scale employed in figures 4.3 and 4.4 is the same for all images, and realizations, involved.

The contrast and bias for the hot S_4 sphere (25.4-mm) and the cold S_6 (38-mm) sphere as functions of the image roughness for 90 and 180 views are presented in figures 4.5 and 4.6 respectively, for the various reconstruction techniques used. In each subplot, the leftmost datum point in each curve corresponds to NL1, the midpoint to NL2, and the rightmost to NL3.

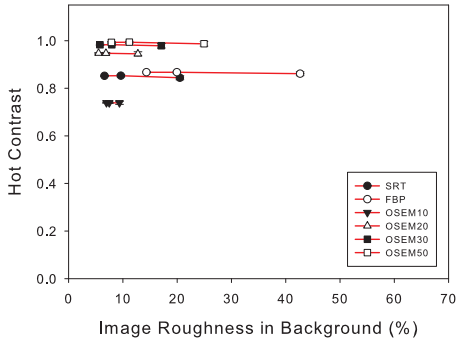

(a) Hot sphere 4 (S_4) hot contrast.

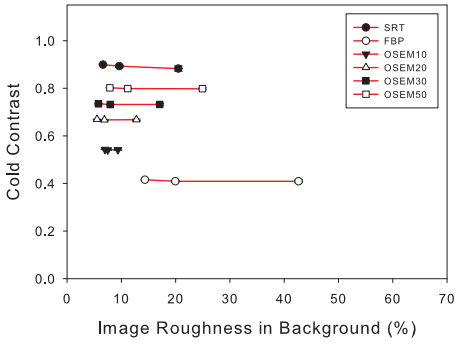

(b) Cold sphere 6 (S_6) cold contrast.

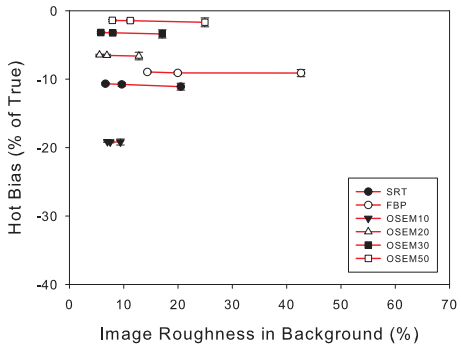

(c) Hot sphere 4 (S_4) hot bias.

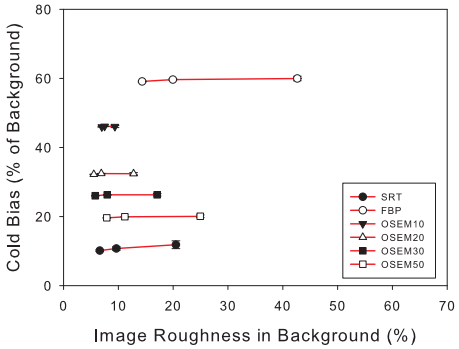

(d) Cold sphere 6 (S_6) cold bias.

Figure 4.6: Contrast (C) and bias (b) measurements vs. image roughness (IR) at 180 views for the hot sphere S_4 and for the cold sphere S_6. The leftmost datum point in each curve corresponds to NL1, the midpoint to NL2 and the rightmost to NL3.

4.5.2 Real data

Real Jaszczak phantom

aSRT and FBP reconstructions of the real Jaszczak phantom, as well as the corresponding attenuation map (CT) and ROIs, are presented in figure 4.7. It is important to note that OSEM reconstructions for the real Jaszczak phantom were unavailable at the time of the analysis. This Jaszczak phantom study is a typical cold study, therefore only cold contrast (C_c) was calculated. Cold contrast (C_c) and bias measurements for the 6 cold spheres of the real Jaszczak phantom for the reconstruction techniques used, are presented in figure 4.8a and figure 4.8b, respectively.

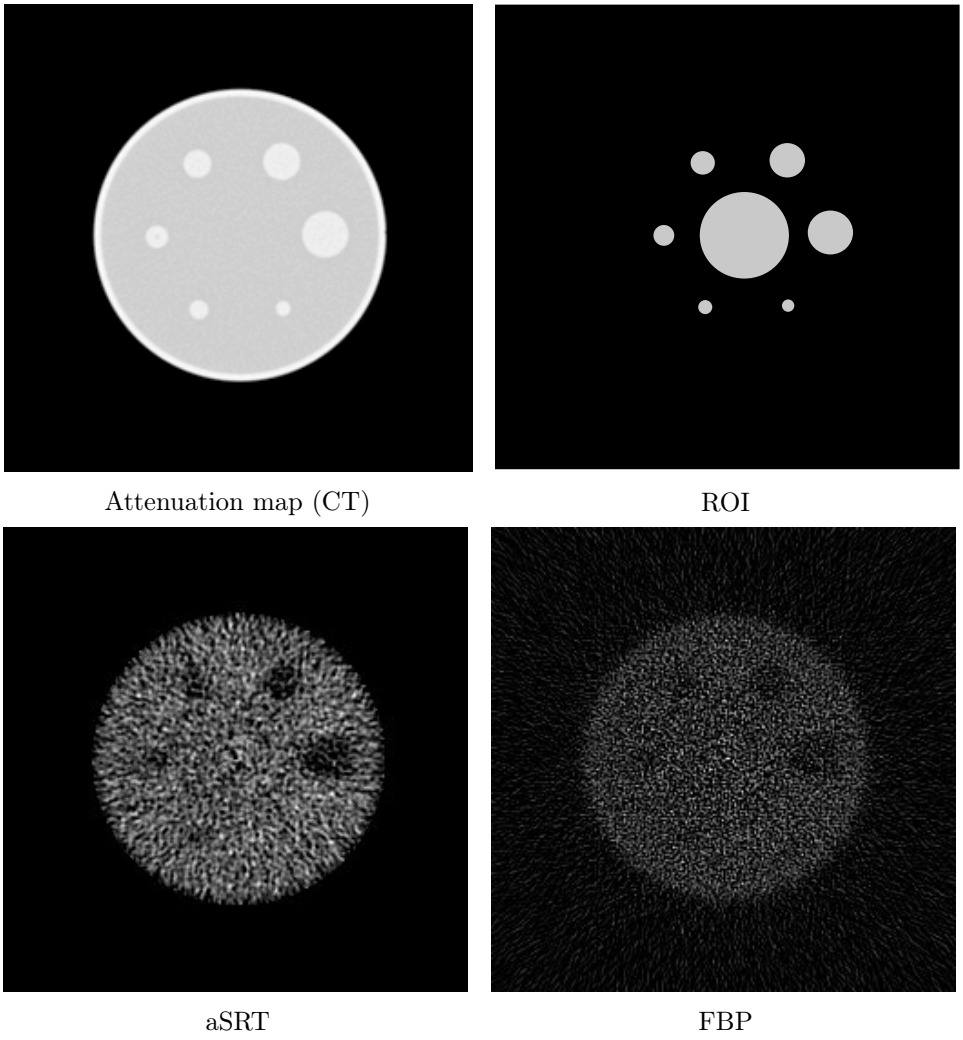

Figure 4.7: Attenuation map, ROI and reconstructions of a real Jaszczak phantom, cold spheres' region.

Clinical data

Reconstructions via aSRT, FBP, OSEM (10 iterations), as well as the corresponding attenuation map (CT) and ROIs of the real clinical myocardial study, are presented in figure 4.9. All relevant clinical data and attenuated sinograms were acquired from a GE Millennium VG Hawkeye^{TM} SPECT/CT system. Furthermore, in order to quantify the effect of each reconstruction technique presented, we have performed cold contrast analysis and calculations in this cardiac study. The corresponding results are shown in figure 4.10.

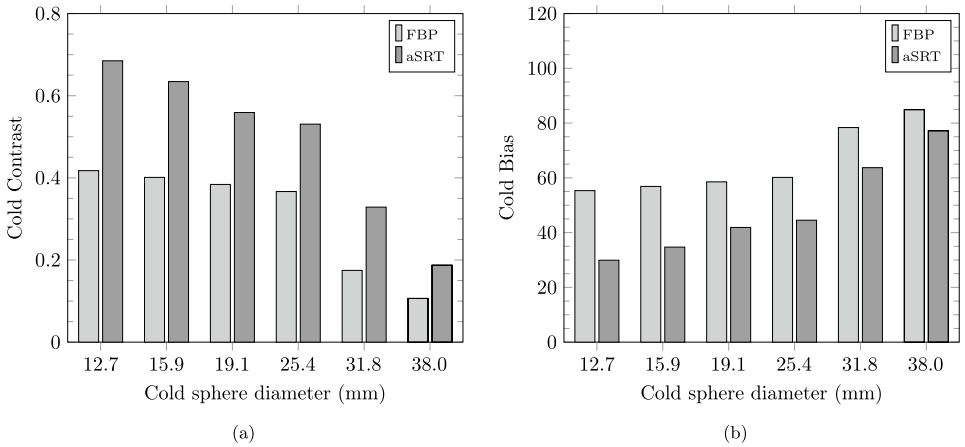

Figure 4.8: Cold contrast (a) and cold bias (b) measurements for the six cold spheres of the real Jaszczak phantom.

4.6 Analysis and discussion of the aSRT inversion

Simulation studies. For the simulation studies, in all images presented in the present chapter, it is evident that all hot circular regions can be clearly identified, at all noise levels, and by all reconstruction algorithms. However, the cold regions reconstructed with FBP are not shown very clearly, especially in the relatively extreme case of NL3 at 45 views. Some streak artefacts at the edge of the phantom appear in the aSRT reconstructions, especially at low number of projection angles. These streak artefacts are the result of incomplete data measurement, also referred to as "angular undersampling" [4], and are closely related to the back-projection operator (integral over theta). Similar streak artefacts are present at low number of projections in all analytic reconstructions that utilize a back-projection operator, such as FBP and Natterer's inversion formula [60]. It is important to note that the cases of NL3 are quite unrealistic, especially the case of 45 views, corresponding to an extremely low number of 3.333 counts per projection.

Overall, FBP reconstructions exhibited higher image roughness in all noise levels and all numbers of projections. Furthermore, the image roughness of aSRT reconstructions is similar to the image roughness of OSEM50 reconstructions, for all noise levels. As expected, in the variations of OSEM reconstructions, the noise level increases as the number of iterations increases. Furthermore, the contrast increases as the number of OSEM iterations increases, whereas the bias decreases, in both hot and cold regions. For all

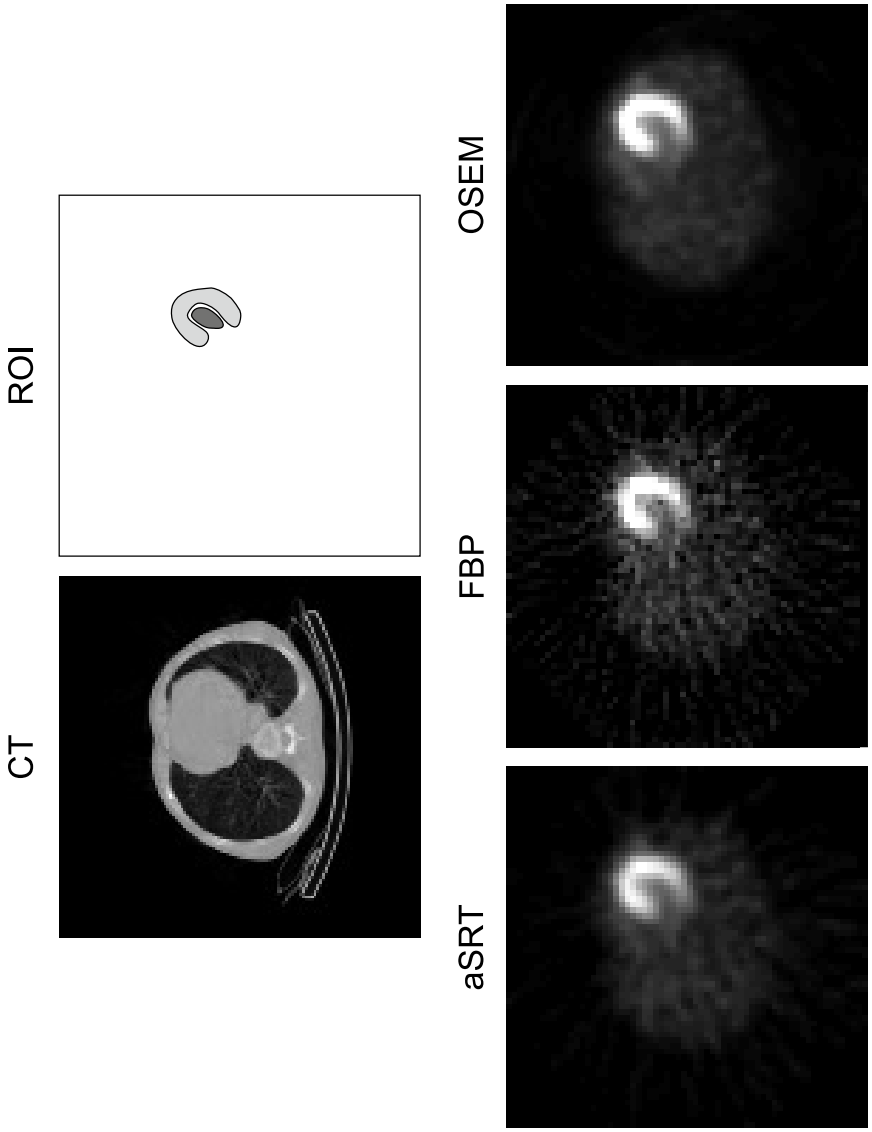

Figure 4.9: Attenuation map (CT scan), ROI and reconstructions of real clinical cardiac data, acquired from a GE Millennium VG Hawkeye^{TM} SPECT/CT system.

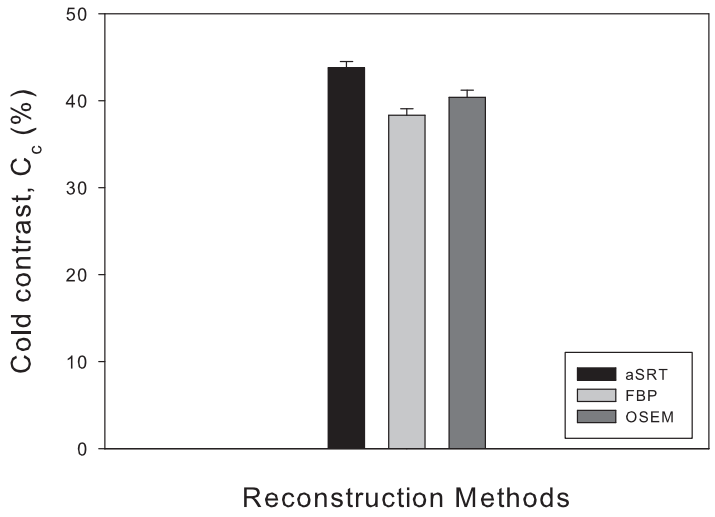

Figure 4.10: Cold contrast measurements for the real clinical myocardial study.

reconstruction techniques used and for all noise levels investigated, the image roughness, represented in the x-axis in figures 4.5 and 4.6, respectively, increases as the number of views decreases. This is expected, as mentioned above, due to lower angular sampling.

For the cold regions of the IQ phantom, aSRT provided images with lower bias and higher contrast than FBP and OSEM for all iteration updates investigated. The cold region contrast, as well as the cold bias exhibited, as expected, small variations as a function of the initial noise level of the sinograms, see table 4.3. For the 38-mm cold circular region (S_6), the aSRT-reconstructed images exhibited a cold contrast (C_c) of 0.89, which was higher than the contrast of all other reconstruction techniques. For the reconstructed images via FBP, the contrast was substantially low (0.41) for S_6. The OSEM contrast varied from 0.54 for OSEM10 to 0.79 for OSEM50. Similarly, the cold bias % of background (b_c) value for aSRT was the lowest of all other techniques studied (10.80%), whereas for FBP was the highest (59.85%). The cold bias % of background values for OSEM reconstructions varied from 46.49% for OSEM10 to 20.59% for OSEM50. Therefore, aSRT provides better quality images for the cold regions, in terms of both contrast and bias.

Method	**Cold contrast (C_c)**	**Cold bias (b_c)**
aSRT	0.84	-10.98%
FBP	0.86	-9.17%
OSEM10	0.74	-18.83%
OSEM50	0.97	-1.84%

Table 4.3: Cold contrast (C_c) and bias (b_c) measurements for the S_6 cold sphere.

For the hot regions of the IQ phantom, aSRT provided images with bias and contrast similar to FBP. However, those values for FBP are achieved at the expense of considerably increasing the image roughness. Both the hot %bias (b_h) and the hot contrast (C_h) for aSRT were between OSEM10 and OSEM20, in all cases. All hot lesions investigated demonstrated negative hot bias, i.e. $b_h < 0$. The contrast, as well as the bias, demonstrated negligible variations as functions of the sinogram noise level, see table 4.4. For the 25.48-mm hot circular lesion (S_4), the hot contrast value was 0.84 for aSRT, 0.86 for FBP, and from 0.74 for OSEM10 to 0.97 for OSEM50. In addition, the hot %bias value was –10.98% for aSRT, –9.17% for FBP, and from –18.83% for OSEM10 to –1.84% for OSEM50. FBP exhibited similar contrast with aSRT, although at the expense of higher levels of image roughness. It is important to note that the ROI placement for the background affects the image roughness of aSRT. Selecting a background ROI which includes the central region of the phantom, as well as areas at the edge of the object (streaking artefacts) results in an increase in image roughness for aSRT, see figure 4.2d. More specifically, the new image roughness values for NL1 to NL3 were: (i) for 90 views, 13,53%, 18.74% and 40.54%, respectively, and (ii) for 180 views, 9.43%, 13.31% and 28.87%, respectively. These specific values for aSRT image roughness (IR) are still lower that the corresponding ones of FBP reconstructions. As expected, in the cases of FBP and OSEM, the corresponding values of IR remained unchanged. It is important to note that contrast and bias measurements are not affected by the choice of the background ROI.

Method	**Hot contrast (C_h)**	**Hot bias (b_h)**
aSRT	0.89	10.80%
FBP	0.41	59.85%
OSEM10	0.54	46.49%
OSEM50	0.79	20.59%

Table 4.4: Hot contrast (C_h) and bias (b_h) measurements for the S_4 hot sphere.

Real phantom studies. For the real Jaszczak phantom studies, the image reconstructed via FBP exhibited significantly higher image roughness (0.96) than the one reconstructed with aSRT (0.51). It is evident that for the cold Jaszczak phantom study, the contrast and bias measurements in aSRT reconstructions are superior to the ones in FBP reconstructions in all cold spheres investigated, see figures 4.8a and 4.8b, respectively.

Clinical studies. For the clinical myocardial ^{201}Tl stress test perfusion SPECT/CT study, aSRT exhibited a cold contrast (C_c) of approximately 44%, FBP of approximately 38% and OSEM of approximately 40%, see figure 4.10. Hence, aSRT reconstructions exhibited cold contrast improvement of approximately 14% over FBP reconstructions and 8% improvement over OSEM reconstructions. Therefore, it is evident that in cold cardiac regions, aSRT produces images with higher cold contrast than both OSEM and FBP. It should be noted that, among the relevant literature of analytic inversion of the attenuated Radon transform, aSRT was the only method to be tested with reconstructions of clinical data. The improvement of our algorithm over FBP and OSEM is a clear indication that aSRT may be valuable in the imaging of structures such as the nucleus and annulus of spines, mitral valves etc. Furthermore, we must emphasize that for the clinical studies no artefacts were present, indicating that some of the simulated cases studied suffered from quite "unrealistic" high noise and small number of projections. These were cases, chosen in order to investigate the limitations of our method. Overall, the improvement in bias and contrast of the cold regions of aSRT over OSEM can be explained by recalling that OSEM usually exhibits slow convergence in regions of low counts, as a result of the intrinsic positivity constraint imposed by the statistical algorithm itself.

4.7 Outcome and further investigation

aSRT is a novel, effective analytic method capable of reconstructing SPECT data and producing attenuation-corrected images. In the present chapter we have compared aSRT with FBP and OSEM using simulated and real phantoms, as well as real clinical data. We have presented an improved version of the analytic formula for the inversion of the attenuated Radon transform and have implemented aSRT numerically. Furthermore, we have evaluated the aSRT reconstruction capability in comparison with the corresponding FBP and OSEM ones using contrast, bias, and image roughness.

Our tests suggest that aSRT can efficiently produce accurate attenuation-corrected reconstructions for simulated phantoms as well as real data. In particular, it appears that aSRT has a rather noticeable advantage in cold regions in comparison with both FBP and our implementation of OSEM. More specifically, the aSRT results of the clinical myocardial study are encouraging, indicating that aSRT could provide useful reconstructions in a real clinical setting. Further investigation is needed to better quantify with the help of physicians, the improvement of aSRT in myocardial imaging. Clinical studies involving myocardial ischemia are in progress. Overall, aSRT may provide an improved alternative to FBP for SPECT/CT reconstruction.

4.8 Chapter acknowledgments

The work presented in the current chapter was partially supported by the research program “Inverse Problems and Medical Imaging" (200/855) of the Research Committee of the Academy of Athens. I would like to thank Dr. Theodore Skouras of the Medical Physics Department of the University Hospital of Patras for providing the real SPECT/CT data, Dr. Anastasios Gaitanis, of the Biomedical Research Foundation of the Academy of Athens for his assistance in real data acquisition. In addition, I would like to thank Miklos Kovacs, Gabor Nemeth and Andras Wirth of Mediso Medical Imaging Systems, Budapest, for providing the real phantom data. Furthermore, I am grateful to Dr. Vangelis Marinakis of the Technological Educational Institute of Western Greece, whose earlier code provided the starting point for the numerical part of the present chapter.

Chapter 5

Radon data deblurring

In the present chapter, we present a spline-based method for deblurring aSRT-reconstructed images of SPECT/CT imaging systems equipped with parallel-hole collimators, based on [46]. aSRT, or the attenuated spline reconstruction technique, is a recently developed analytic algorithm capable of reconstructing attenuation-corrected SPECT/CT images [44]. Our method is based on the classification of the collimator in terms of its blurring profile, rather than the use of the so-called *point response function*. By deblurring the initial attenuated sinogram, we are able to reconstruct images with less blurring, via aSRT.

Simulation studies were performed by employing an image quality (IQ) phantom and the corresponding attenuation map. Reconstructed images were generated for 180 projections over 360 degrees. Furthermore, 20 realizations of Poisson noise were created at a noise level of 50% of the total counts. For the purposes of the IQ phantom simulations, we employed a typical low-energy, high-resolution (LEHR) collimator, and subsequently blurred the relevant data using a Gaussian blur profile with a corresponding standard deviation, σ, value of 0.019. Comparisons between blurred and deblurred sinogram reconstructions were performed using 2 appropriate metrics, namely hot contrast (local metric) and the no-reference perceptual blur metric (global metric).

Our preliminary results indicate that the algorithm presented in this chapter is capable of efficiently compensating for the collimator blur effect, especially in the context of aSRT-reconstructed SPECT images. The metrics employed indicate that our algorithm can be proven to be useful in clinical

SPECT imaging as well as in biomedical image processing and analysis in general. Therefore, this blurring-compensating technique for parallel-hole collimation could provide efficient deblurring in SPECT imaging and may be helpful in improving image quality of SPECT reconstructions.

5.1 An introduction to deblurring

SPECT utilizes a rotating gamma camera to acquire the projections required for image reconstruction [4]. It is a nuclear medicine modality of crucial importance with preclinical and clinical applications, especially in myocardial perfusion imaging and neuroimaging. SPECT scans provide information regarding functional characteristics of the internal organs being imaged; relevant examples include functional brain imaging and functional cardiac imaging, even the diagnosis of coronary heart disease [123]. In SPECT imaging, the patient is injected with a radiopharmaceutical, such as technetium (^{99}Tc) or thallium (^{201}Tl), labeled with an appropriate radioactive tracer agent. The short-lived radioisotope undergoes nuclear decay and radiates single photons (γ-rays): the camera detects these individual photons [5].

All SPECT scanners combine photon detectors along with collimators. The collimator limits the photons reaching the detector to a small range of allowable directions [124], operating as a γ-ray focusing mechanism. Only the photons that are able to travel unobstructed through the collimator holes are detected. The aim in imaging is to reconstruct the original location of the source. For this purpose, the incidence angle of the detected photons on the detector needs to be determined. The collimator provides a mapping of the lines of response to particular detector positions [125]. Collimation is an important aspect of SPECT imaging, since it affects the image quality (contrast, resolution, sensitivity) of the resulting reconstructed images.

The two predominant categories of collimators are

- parallel-hole collimators, and
- pinhole collimators,

depending on the type of their focusing mechanism. Pinhole collimators have a single hole, conical shape and are mainly used in the imaging of small organs in order to provide magnification [120], and to achieve superior resolution [126]. Parallel-hole collimation is the most commonly used image

formation aperture in nuclear medicine [125]. Parallel-hole collimators consist of parallel holes, or channels, perpendicular to the detector faces [127]. In this chapter we shall focus on parallel-hole collimator apertures.

A point source being imaged corresponds to a blurred dot, as a result of collimation. The severity of blurring depends on the characteristics of the collimator, and on the distance between the source and the camera [128]. SPECT images are usually degraded by collimator blurring, normally reducing the resolution [129]. The further away the collimator is from the object being imaged, the more blurring occurs [130]. Compensating for the collimator-detector response in SPECT is of crucial importance for accurate quantification and, ultimately, deblurring [131].

The problem of efficiently correcting SPECT collimator blurring has been studied extensively in the past, especially in the context of inverting the so-called *blurred Radon transform* [132]. Specifically, in [133], a filtering method is presented, which compensates for the distance-dependent detector response, based on the *frequency-distance principle*. Furthermore, there exists the well-known frequency-distance method (and the corresponding relation) utilizing Fourier analysis [124, 134, 135]. The concept of the ideal projection is usually described by the corresponding point spread function and dealt with as the projection of a point source placed at a certain distance from the detector, as described in [132]. Other approaches include the mixed method of simultaneous attenuation correction and distance-dependent deblurring [136], the frequency-distance relation with Gaussian diffusion [137], and the analogous study for spinning-slat collimators [138] based on [124]. However, most of the analysis has focused on Fourier analysis.

In the present chapter we present a simple and efficient method for the deblurring of SPECT images with parallel-hole collimators, extending the spline context of aSRT, introduced recently [44]. We note that we focus on aSRT-reconstructed SPECT images. The deblurring process is based on the spline interpolation of the blurred sinogram, and the corresponding inversion of the "blurred" version of the attenuated Radon transform. By reconstructing the deblurred sinogram, we were able to deblur the reconstructed images and improve their hot contrast, as defined in equation (5.29).

5.2 Mathematical formulation

5.2.1 Attenuated Radon inversion via aSRT without blur

SPECT measurements are usually stored in the form of an attenuated sinogram, denoted, for the purposes of the present chapter, by $\widetilde{g}_\mu(\rho,\theta)$, and expressed in the so-called *local coordinates* (ρ,θ), see [44]:

$$\widetilde{g}_\mu(\rho,\theta) = \int_{-\infty}^{\infty} e^{-\int_\tau^\infty \mu(s\cos\theta-\rho\sin\theta, s\sin\theta+\rho\cos\theta)\mathrm{d}s} \times g(\tau\cos\theta-\rho\sin\theta, \tau\sin\theta+\rho\cos\theta)\ \mathrm{d}\tau, \quad (5.1)$$

for $0 \leq \theta < 2\pi$ and $-\infty < \rho < \infty$. The above expression represents the attenuated Radon transform of the two dimensional radioactivity distribution function $g(x_1,x_2)$, namely its line integrals, attenuated with respect to the attenuation function $\mu(x_1,x_2)$, as in Definition 1.3. The inverse problem arising in SPECT image reconstruction, associated with equation (5.1), is to determine the function $g(x_1,x_2)$, given the functions $\mu(x_1,x_2)$, $-\infty < x_1,x_2 < \infty$, and $\widetilde{g}_\mu(\rho,\theta)$, $0 \leq \theta < 2\pi$, $-\infty < \rho < \infty$. The analytic inversion formula for the attenuated Radon transform pair was first derived in [7], as a result of the extension of the analogous inversion presented in [6], and rederived in [8]. This analytic formula was later simplified in [44] via aSRT.

5.2.2 Blurred data

SPECT measurements are usually blurred due to collimation. Equation (5.1) neglects the fact that the collimator of a gamma camera has a finite, distance-dependent spatial resolution. This resolution is usually described by an impulse response function usually referred to as the "point response function" [124], $p(\rho,r)$, which is the projection of a point source at a distance r onto the detector plane. The photons that create the image propagate in straight lines, therefore the collimator blurred projections $g_\mu(\rho,\theta)$ can be described as weighted integrals of the ideal parallel projections $\widetilde{g}_\mu(\rho,\theta)$, see figure 5.1:

$$g_\mu(\rho,\theta) = \int_{-\pi/2}^{\pi/2} w(\delta)\widetilde{g}_\mu(\rho'(\rho,\delta),\theta+\delta)\mathrm{d}\delta, \quad (5.2)$$

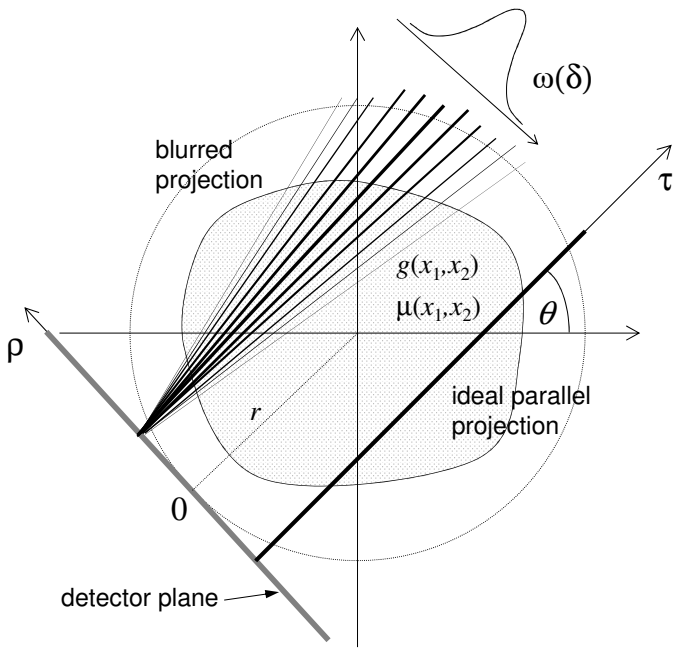

Figure 5.1: SPECT projections ideal parallel projections, corresponding to the attenuated Radon transform, and real projections, blurred due to collimation.

where $w(\delta)$ and $\rho'(\rho, \delta)$ denote the weight function of the collimator and the rotated projection variable, respectively. We assume that:

(i) each bin, sometimes referred to as "partition", of the collimator receives information from an angular span of 2Δ, $0 < \Delta \leq \frac{\pi}{2}$, and

(ii) the angular variable δ lies in the corresponding symmetrical interval, i.e. $\delta \in [-\Delta, \Delta]$.

The weight function $w(\delta)$ encompasses the properties of the collimator and depends on the angle δ between the given direction and the normal to the detector surface. This function may also be referred to as the *blur profile*. The conventional point spread function can be obtained from the weight function $w(\delta)$ via the simple relation

$$p(\rho, \delta) = w\left(\arctan\left(\frac{\rho}{\delta}\right)\right).$$

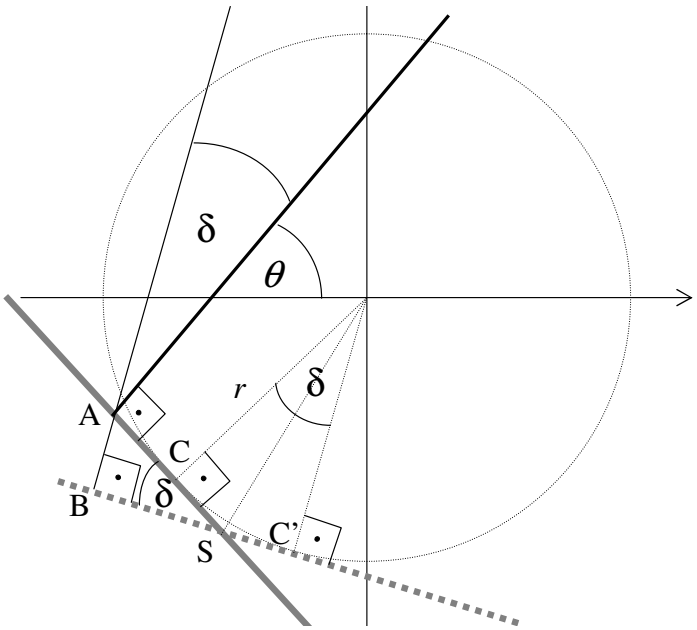

Figure 5.2: Rotated geometry.

For the computation of the rotated projection variable $\rho'(\rho, \delta)$ involved in the integral (5.2), let us consider the rotated geometry, as in figure 5.2:

$$\rho'(\rho,\delta) = BC' = C'S + SB = r\tan\left(\frac{\delta}{2}\right)(1+\cos\delta) + \rho\cos\delta$$
$$= r\sin\delta + \rho\cos\delta, \quad (5.3)$$

where we assumed that the detector rotates around the object being imaged, along a circular path of radius r. In the limit case $\delta \sim 0$, equation (5.3) simplifies to

$$\rho'(\rho,\delta) = r\delta + \rho, \quad (5.4)$$

where R is treated as a constant of the scanning system. Therefore, equation (5.2) becomes

$$g_\mu(\rho,\theta) = \int_{-\frac{\pi}{2}}^{\frac{\pi}{2}} w(\delta)\ \widetilde{g}_\mu(r\delta+\rho, \theta+\delta)\ \mathrm{d}\delta. \quad (5.5)$$

It is worth mentioning that two of the most commonly used collimator blur profiles include the following:

1. **triangular blur**

$$w(\delta) = \begin{cases} \frac{1}{\Delta^2}(\delta + \Delta), & \delta \in [-\Delta, 0], \\ \frac{1}{\Delta^2}(\Delta - \delta), & \delta \in (0, \Delta], \\ 0, & \text{otherwise}, \end{cases} \quad \text{and} \tag{5.6}$$

2. **Gaussian blur**

$$w(\delta) = \frac{1}{\sqrt{2\pi}\sigma} e^{-\frac{\delta^2}{2\sigma^2}}, \quad \sigma = \sigma(\Delta). \tag{5.7}$$

In both blurring cases it is evident that the weight function w is normalized, i.e.,

$$\int_{-\infty}^{\infty} w(\delta)\mathrm{d}\delta = \int_{-\frac{\pi}{2}}^{\frac{\pi}{2}} w(\delta)\mathrm{d}\delta = 1. \tag{5.8}$$

In the present chapter we shall focus on Gaussian blurring.

5.2.3 Numerical implementation

We aim to solve equation (5.5) for the ideal data $\widetilde{g}_\mu$ in terms of the blurred data g_μ, given the weight function w and the radius r. For the numerical implementation we employ custom-made cubic splines, as in Section 4.3.2. In each subinterval $[\rho_i, \rho_{i+1}]$, for all $i = 1, \ldots, n-1$, we expand both $g_\mu(\rho, \theta)$ and $\widetilde{g}_\mu(\rho, \theta)$ via cubic splines (denoted by $S_i^{(3)}(\rho, \theta)$ and $\widetilde{S}_i^{(3)}(\rho, \theta)$, respectively) in the variable ρ, i.e.:

$$g_\mu(\rho, \theta) = S_i^{(3)}(\rho, \theta) = \sum_{j=0}^{3} c_i^{(j)}(\theta)\rho^j, \tag{5.9a}$$

and

$$\widetilde{g}_\mu(\rho, \theta) = \widetilde{S}_i^{(3)}(\rho, \theta) = \sum_{j=0}^{3} \widetilde{c}_i^{\,(j)}(\theta)\rho^j. \tag{5.9b}$$

In this connection, we take into account the fact that the function $g_\mu(\rho, \theta)$, $-1 \leq \rho \leq 1$, $0 \leq \theta \leq 2\pi$, is given for every θ at the n points $\{\rho_i\}_1^n$. We

denote the value of g_μ at ρ_i by g_i, i.e.,

$$g_i := g_i(\theta) = g_\mu(\rho_i, \theta), \quad \rho_i \in [-1, 1], \quad \theta \in [0, 2\pi). \tag{5.10}$$

The cubic spline $S_i^{(3)}(\rho, \theta)$ defined in equations (5.9) interpolates the function $g_\mu(\rho, \theta)$ at the knots $\{\rho_i\}_{i=1}^n$ in the sense that

$$S_i^{(3)}(\rho_i, \theta) = g_i, \quad i = 1, \ldots, n-1. \tag{5.11}$$

Furthermore, we assume that both $g_\mu(\rho, \theta)$ and its derivative with respect to ρ vanish at the endpoints $\rho_1 = -1$ and $\rho_n = 1$:

$$g_\mu(-1, \theta) = g_\mu(1, \theta) = 0, \quad 0 \le \theta < 2\pi, \tag{5.12a}$$

$$\frac{\partial g_\mu}{\partial \rho}(-1, \theta) = \frac{\partial g_\mu}{\partial \rho}(1, \theta) = 0, \quad 0 \le \theta < 2\pi. \tag{5.12b}$$

The constants $\{c_i^{(j)}\}_1^n$ of the spline expansions (5.9) of the blurred sinogram $g_\mu(\rho, \theta)$ can be derived following the spline setting of [44, 119] and of Section 4.3.2 of this thesis, and are given by the following equations:

$$c_i^{(0)}(\theta) = \frac{\rho_{i+1} g_i - \rho_i g_{i+1}}{\Delta_i} + \frac{g_i''}{6}\left(-\rho_{i+1}\Delta_i + \frac{\rho_{i+1}^3}{\Delta_i}\right) + \frac{g_{i+1}''}{6}\left(\rho_i \Delta_i - \frac{\rho_i^3}{\Delta_i}\right), \tag{5.13a}$$

$$c_i^{(1)}(\theta) = \frac{g_{i+1} - g_i}{\Delta_i} - \frac{g_i''}{6}\left(-\Delta_i + \frac{3\rho_{i+1}^2}{\Delta_i}\right) + \frac{g_{i+1}''}{6}\left(-\Delta_i + \frac{3\rho_i^2}{\Delta_i}\right), \tag{5.13b}$$

$$c_i^{(2)}(\theta) = \frac{1}{2\Delta_i}(\rho_{i+1} g_i'' - \rho_i g_{i+1}''), \tag{5.13c}$$

$$c_i^{(3)}(\theta) = \frac{g_{i+1}'' - g_i''}{6\Delta_i}, \tag{5.13d}$$

and

$$\Delta_i = \rho_{i+1} - \rho_i, \tag{5.13e}$$

with g_i'' denoting the second derivative of $g_\mu(\rho, \theta)$ with respect to ρ evaluated at ρ_i, i.e.,

$$g_i'' = \left.\frac{\partial^2 g_\mu(\rho, \theta)}{\partial \rho^2}\right|_{\rho=\rho_i}, \quad i = 1, \ldots, n. \tag{5.14}$$

Equations (5.13) involve the functions $\{g_i\}_1^n$, which are known, and the functions $\{g_i''\}_1^n$, which are unknown. If we denote the derivative of the cubic spline, $S_i^{(3)}$, by $S_i^{(2)}$, where the superscript denotes that $S_i^{(2)}$ is quadratic, we find

$$S_i^{(2)}(\rho,\theta) = \frac{\partial S_i^{(3)}(\rho,\theta)}{\partial \rho} = c_i^{(1)}(\theta) + 2c_i^{(2)}(\theta)\rho + 3c_i^{(3)}(\theta)\rho^2. \tag{5.15}$$

In order to compute $\{g_i''\}_1^n$ we follow the procedure of [116], namely we solve the system of the following n equations (continuity of the first derivative of the cubic spline):

$$S_i^{(2)}(\rho_{i+1},\theta) = S_{i+1}^{(2)}(\rho_{i+1},\theta), \tag{5.16a}$$

$$S_1^{(2)}(\rho_1,\theta) = S_{n-1}^{(2)}(\rho_n,\theta) = 0, \tag{5.16b}$$

for every $i = 1,\dots,n-2$, and $\theta \in [0,2\pi)$. The continuity of the spline, namely $S_i^{(3)}(\rho_{i+1},\theta) = S_{i+1}^{(3)}(\rho_{i+1},\theta)$ for $i = 1,\dots,n-2$, and $S_1^{(3)}(\rho_1,\theta) = S_{n-1}^{(3)}(\rho_n,\theta) = 0$ (see equations (5.12)), implies that the points $\{\rho_i\}_1^n$ are removable logarithmic singularities.

For the inversion of the integral in equation (5.5), we proceed by assuming that for small angles $\delta \in [-\Delta,\Delta]$, see equation (5.4), the coefficients $\widetilde{c}_i^{\,(j)}(\theta)$ remain unchanged, i.e. $\widetilde{c}_i^{\,(j)}(\theta+\delta) = \widetilde{c}_i^{\,(j)}(\theta)$ (sensitivity). This yields

$$\sum_{j=0}^{3} c_i^{(j)}(\theta)\rho^j = \int_{-\Delta}^{\Delta} w(\delta) \left(\sum_{j=0}^{3} \widetilde{c}_i^{\,(j)}(\theta)(r\delta+\rho)^j \right) \mathrm{d}\delta. \tag{5.17}$$

We denote the integral on the right-hand side of equation (5.17) by I and we expand it, to find

$$\begin{aligned} I = \left(\sum_{j=0}^{3} \widetilde{c}_i^{\,(j)}(\theta)\rho^j \right) I_0 + \left[\widetilde{c}_i^{\,(1)}(\theta) + 2\widetilde{c}_i^{\,(2)}(\theta)\rho + 3\widetilde{c}_i^{\,(3)}(\theta)\rho^2 \right] r I_1 \\ + \left[\widetilde{c}_i^{\,(2)}(\theta) + 3\widetilde{c}_i^{\,(3)}(\theta)\rho \right] r^2 I_2 + \widetilde{c}_i^{\,(3)}(\theta) r^3 I_3, \end{aligned} \tag{5.18}$$

where

$$I_j = \int_{-\Delta}^{\Delta} w(\delta)\delta^j \mathrm{d}\delta \quad j = 0,1,2,3. \tag{5.19}$$

For each $j = 0,1,2,3$, the integral I_j represents the j-th moment of the collimator distribution function w. Given that w is normalized, see equation

(5.8), equation (5.19) implies

$$I_0 = 1, \quad I_1 = 0, \quad I_2 = \beta, \quad \text{and} \quad I_3 = 0, \tag{5.20}$$

where β is the variance of the distribution, therefore

$$\beta = \frac{\Delta^2}{6} \quad \text{and} \quad \beta = \sigma^2,$$

in the particular cases of triangular (see equation (5.6)) and Gaussian (see equation (5.7)) blurring, respectively. Substituting equations (5.20) in equation (5.18) implies that equation (5.17) may be rewritten in the form

$$\begin{aligned} c_i^{(0)}(\theta) + c_i^{(1)}(\theta)\rho + c_i^{(2)}(\theta)\rho^2 + c_i^{(0)}(\theta)\rho^3 = \left[\widetilde{c}_i^{\,(0)}(\theta) + r^2\beta\widetilde{c}_i^{(2)}(\theta)\right] \\ + \left[\widetilde{c}_i^{(1)}(\theta) + 3r^2\beta\widetilde{c}_i^{(3)}(\theta)\right]\rho + \widetilde{c}_i^{(2)}(\theta)\rho^2 + \widetilde{c}_i^{(3)}(\theta)\rho^3. \end{aligned} \tag{5.21}$$

Therefore,

$$\widetilde{c}_i^{\,(0)}(\theta) = c_i^{(0)}(\theta) + r^2\beta c_i^{(2)}(\theta), \tag{5.22a}$$

$$\widetilde{c}_i^{\,(1)}(\theta) = c_i^{(1)}(\theta) + 3r^2\beta c_i^{(3)}(\theta), \tag{5.22b}$$

$$\widetilde{c}_i^{\,(2)}(\theta) = c_i^{(2)}(\theta), \tag{5.22c}$$

$$\widetilde{c}_i^{\,(3)}(\theta) = c_i^{(3)}(\theta). \tag{5.22d}$$

The above coefficients correspond to the new, custom-made cubic spline, namely

$$\widetilde{S}_i^{(3)}(\rho,\theta) = \sum_{j=0}^{3} \widetilde{c}_i^{\,(j)}(\theta)\rho^j, \quad \rho_i \in [-1,1], \quad \theta \in [0,2\pi). \tag{5.23}$$

Matlab implementation. It is worth noting that in Matlab, cubic splines ($S_i^{(3)}$) are treated as

$$S_i^{(3)}(\rho,\theta) = \sum_{j=0}^{3} m_i^{(4-j)}(\theta)(\rho-\rho_i)^j, \quad \rho \in [\rho_i,\rho_{i+1}], \quad \theta \in [0,2\pi), \tag{5.24}$$

as opposed to the more standard cubic spline definition (5.9). Expressing equation (5.24) in the form of equations (5.9) yields

$$c_i^{(0)}(\theta) = -\rho_i^3 m_i^{(1)}(\theta) + \rho_i^2 m_i^{(2)}(\theta) - \rho_i m_i^{(3)}(\theta) + m_i^{(4)}(\theta), \tag{5.25a}$$

$$c_i^{(1)}(\theta) = 3\rho_i^2 m_i^{(1)}(\theta) - 2\rho_i m_i^{(2)}(\theta) + m_i^{(3)}(\theta), \tag{5.25b}$$

$$c_i^{(2)}(\theta) = -3\rho_i m_i^{(1)}(\theta) + m_i^{(2)}(\theta), \tag{5.25c}$$

$$c_i^{(3)}(\theta) = m_i^{(1)}(\theta). \tag{5.25d}$$

Taking into account equations (5.22), we represent $\left\{\widetilde{c}_i^{(\ell)}\right\}_{\ell=1}^4$ as a function of $\left\{c_i^{(\ell)}\right\}_{\ell=1}^4$, i.e.

$$\widetilde{c}_i^{(\ell)} = \mathcal{G}\left\{c_i^{(\ell)}\right\}, \quad \ell = 0, 1, 2, 3, 4.$$

In particular,

$$\widetilde{c}_i{}^{(0)}(\theta) = -\rho_i(\rho_i^2 + 3r^2\beta)m_i^{(1)}(\theta) + (\rho_i^2 + r^2\beta)m_i^{(2)}(\theta) - \rho_i m_i^{(3)}(\theta) + m_i^{(4)}(\theta), \tag{5.26a}$$

$$\widetilde{c}_i{}^{(1)}(\theta) = 3(\rho_i^2 + r^2\beta)m_i^{(1)}(\theta) - 2\rho_i m_i^{(2)}(\theta) + m_i^{(3)}(\theta), \tag{5.26b}$$

$$\widetilde{c}_i{}^{(2)}(\theta) = -3\rho_i m_i^{(1)}(\theta) + m_i^{(2)}(\theta), \tag{5.26c}$$

$$\widetilde{c}_i{}^{(3)}(\theta) = m_i^{(1)}(\theta). \tag{5.26d}$$

As in equation (5.23), the resulting spline is of the following form

$$\widetilde{S}_i^{(3)}(\rho, \theta) = \sum_{j=0}^{3} \widetilde{m}_i^{(4-j)}(\theta)(\rho - \rho_i)^j, \rho \in [\rho_i, \rho_{i+1}], \quad \theta \in [0, 2\pi). \tag{5.27}$$

By combining equations (5.26) with equations (5.22) and (5.27), we express the new coefficients, $\left\{\widetilde{m}_i^{(\ell)}\right\}_{\ell=1}^4$, as functions of the initial ones $\left\{m_i^{(\ell)}\right\}_{\ell=1}^4$,

$$\widetilde{m}_i^{(1)}(\theta) = m_i^{(1)}(\theta), \tag{5.28a}$$

$$\widetilde{m}_i^{(2)}(\theta) = m_i^{(2)}(\theta), \tag{5.28b}$$

$$\widetilde{m}_i^{(3)}(\theta) = 3r^2\beta m_i^{(1)}(\theta) + m_i^{(3)}(\theta), \tag{5.28c}$$

$$\widetilde{m}_i^{(4)}(\theta) = r^2 \beta m_i^{(2)}(\theta) + m_i^{(4)}(\theta). \tag{5.28d}$$

5.3 Materials and methods used in deblurring

5.3.1 Simulations

For the purposes of the simulations, we have modelled a rotating, single-head gamma camera consisting of 129 scintillation crystals, with a corresponding image grid size of 129×129 pixels. The image size, as well as the detector pixel size was 4 mm. Following the same motivation as with the previous two chapters, we employed simulated data of an image quality (IQ) phantom, which simulates the human thorax. This specific phantom was employed in order to quantitate the efficiency of the reconstruction technique to detect hot and cold lesions of variable size inside a radioactive background. This specific phantom consists of four hot circular regions (with diameters of 12.7, 15.9, 19.1 and 25.4 mm, denoted with S_1, S_2, S_3 and S_4, respectively) and two cold circular regions (with diameters of 31.8 and 38 mm, denoted with S_5 and S_6, respectively), inside a larger warm circular region of diameter 216 mm that simulates the background, see table 4.1. Simulated sinograms of the IQ phantom were generated in STIR [88] using appropriate attenuation maps. The attenuated sinograms were acquired for 180 views over 360 degrees, and contained

- 6×10^6 events for the noiseless case.

Using the initial noiseless sinogram as the starting point, we generated 20 Poisson-noise realizations at a noise level of 50% of the total counts, i.e.

- 3×10^6 events for the Poisson-noise case.

In order to determine the quality of the reconstructed images of the IQ phantoms investigated, we performed a region of interest (ROI) analysis. For the calculation of the ROI statistics at each sphere, circular ROIs were employed in Matlab. The diameters of all ROIs were equal to the ones of the lesions being investigated. Several image metrics were calculated for all noise levels and averaged over all realizations, R, see Section 5.3.2, below. For the simulation of the blurring of the attenuated sinograms involved, we applied Gaussian blurring and we employed a typical low-energy, high-resolution

(LEHR) collimator, with a Gaussian standard deviation

$$\sigma = 0.019.$$

5.3.2 Metrics

For the evaluation of our deblurring method, we employed two image metrics, one global and one local, namely

a) **global metric**: the no-reference perceptual blur metric, b_F, and

b) **local metric**: hot contrast, C_h.

No-reference perceptual blur metric

The no-reference perceptual blur metric (b_F) was presented in [139], in order to control and quantify the blur effect in images. It is independent of

- edge spreading,
- choice of threshold, and
- the presence of noise.

In this direction, by comparing between different intensity variations, this image metric is capable of quantifying the blur annoyance of an image (blurring neighboring pixels before and after low-pass filtering). For the evaluation of b_F, we employed the algorithm proposed by Crete et al. in [139]. It is worth noting that the no-reference perceptual blur metric is normalized, i.e.

$$0 \leq b_F \leq 1,$$

and that the lower the metric, the less the blurring effect measured.

Hot contrast

The contrast recovery coefficient (CRC), also referred to as hot region contrast (C_h), see Section 4.4.3, was calculated for each hot circular region using the following expression, as in [116]:

$$C_h = \frac{1}{R} \sum_{r=1}^{R} \frac{\frac{m_{h,r}}{m_{b,r}} - 1}{\frac{a_h}{a_b} - 1}, \tag{5.29}$$

where $m_{h,r}$ and $m_{b,r}$ denote the mean pixel value measured in each hot region and in the background ROI, respectively, for each realization, r, and a_h and a_b are the actual radioactivity of each hot region and of the background, respectively. In our simulations, the ratio (a_h/a_b) is 4.

5.4 Deblurring results

All simulations were executed on a Dell Precision T1700 workstation with an Intel® Xeon® CPU E3-1241 processor, running on a 64-bit Windows® 10 environment with 16 GB RAM. For the IQ phantom, the initial blurred sinogram and the corresponding deblurred sinogram are shown in figures 5.3a and 5.3b, respectively. Similarly, aSRT reconstructions of the blurred sinogram and the corresponding ones of the deblurred sinogram are shown in figures 5.4a and 5.4b, respectively. The sinograms and reconstructed images presented in these figures are characteristic reconstructions of 1, out of 20 Poisson noise realizations at each noise level. In all the reconstructed images presented in the figures, the value of the all-white color represents the maximum value in the IQ phantom, and the all-black color represents zero values. The aSRT reconstructions of the IQ phantom were generated for 180 views over 360 degrees and 20 realizations of Poisson noise. This noise level corresponds to the 50% of the total counts.

For the simulated IQ phantom, the no-reference blur metric was 0.773 for the aSRT-reconstruction of the blurred sinogram, whereas the corresponding metric in the case of the aSRT-reconstruction of the deblurred sinogram was 0.744, see table 5.1. The no-reference blur metric measurement comparisons are presented in figure 5.5. Furthermore, before deblurring the hot contrast (C_h) in the four hot spheres, S_1 to S_4, of the IQ phantom was measured C_h^1=49.9%, C_h^2=64.1%, C_h^3=63.2% and C_h^4=76.1%, respectively. Similarly, in the deblurred case, the corresponding values were C_h^1=51.8%, C_h^2=66.7%, C_h^3=66.1% and C_h^4=79.9%, respectively. The hot contrast measurement comparisons are presented in figure 5.6. For details, see table 5.2.

5.5 Analysis of deblurring results

In this chapter we have developed a technique to compensate for the blur effect in SPECT imaging. In order to accomplish this goal, a spline-based

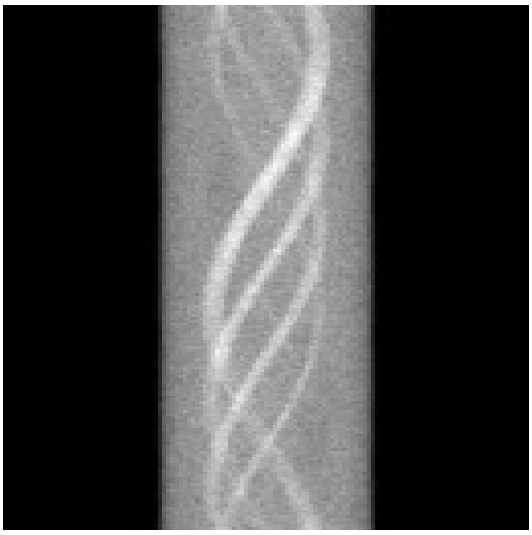

(a) Blurred attenuated sinogram of the IQ phantom.

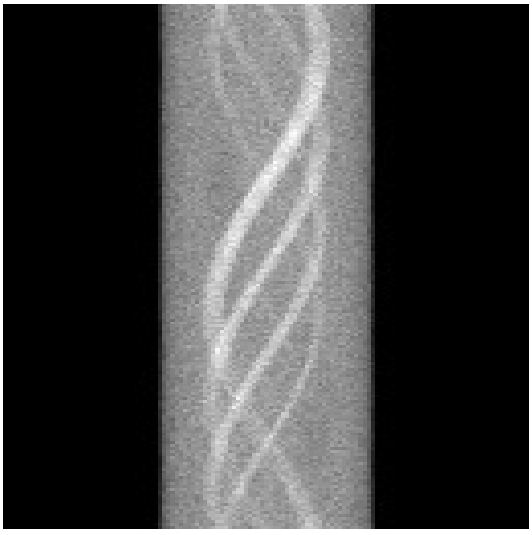

(b) Delurred attenuated sinogram of the IQ phantom.

Figure 5.3: Attenuated sinograms of the IQ phantom.

Method	**No-reference blur metric (b_F)**
Blurred	0.773
Deblurred	0.744

Table 5.1: No-reference blur metric (b_F) measurements for the IQ phantom.

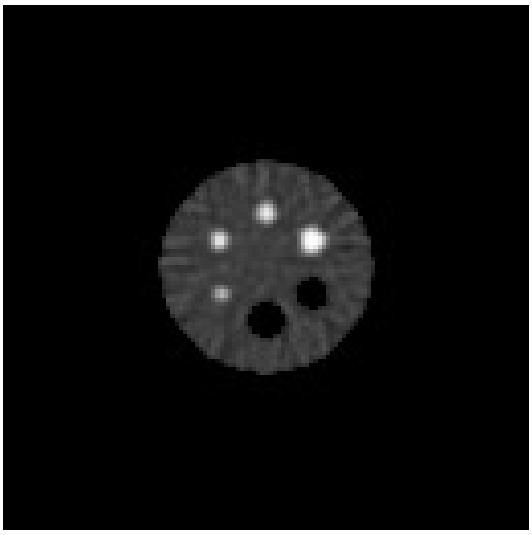

(a) aSRT reconstruction of the blurred sinogram of the IQ phantom.

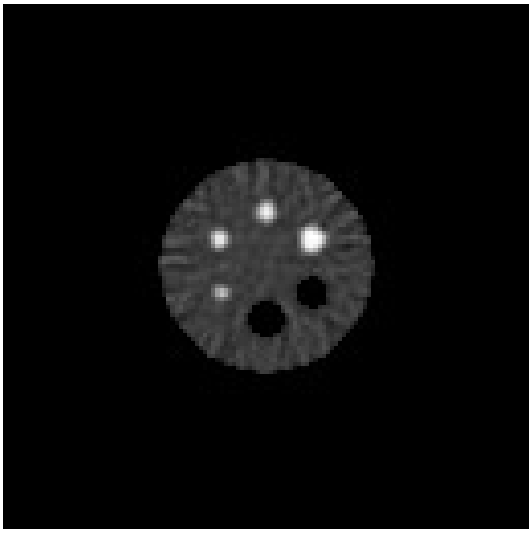

(b) aSRT reconstruction of the deblurred sinogram of the IQ phantom.

Figure 5.4: Reconstructions of the IQ phantom via aSRT.

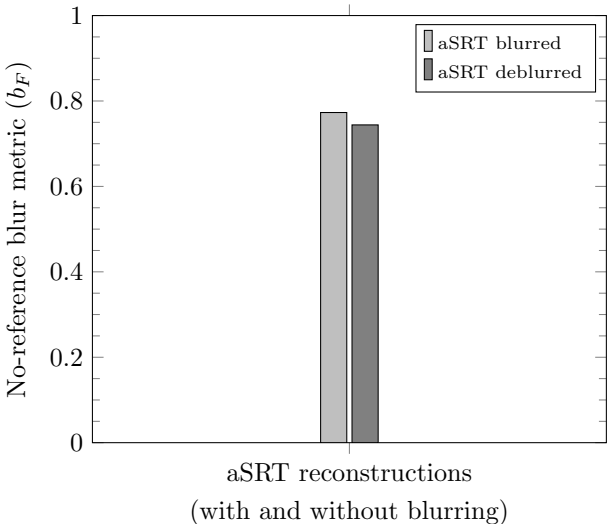

Figure 5.5: No-reference blur metric (b_F) measurement comparisons for the aSRT reconstructions of the IQ phantom.

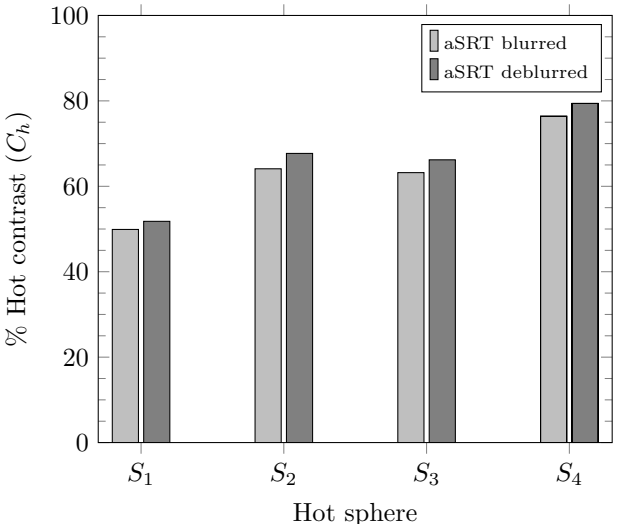

Figure 5.6: Hot contrast (C_h) measurement comparisons for the aSRT reconstructions of the IQ phantom.

Sphere	**Hot contrast (C_h), blur**	**Hot contrast (C_h), deblur**
S_1	49.9%	51.8%
S_2	64.1%	66.7%
S_3	63.2%	66.1%
S_4	76.1%	79.9%

Table 5.2: Hot contrast (C_h) measurements for the IQ phantom.

deblurring algorithm has been implemented and tested in simulated phantom data. For our simulations, in the images presented in figures 5.4a and 5.4b, it is evident that deblurring has been achieved. In order to quantify the deblurring and to evaluate the usability of our method, we have employed two comparison metrics, namely the no-reference perceptual blur metric (b_F) and the hot contrast (C_h). Our results suggest that our method performed deblurring efficiently, since the deblurred sinograms provided reconstructions with lower no-reference perceptual blur metric and higher hot contrast than the ones originating from blurred sinograms, for all 4 hot regions investigated.

Our deblurring algorithm provided better quality images in terms of both hot contrast and no-reference blur metric. More specifically: (a) the overall no-reference blur metric decreased by 3.75%, and (b) in all four hot regions of the IQ phantom, the hot contrast increased 3.8%, 4.1%, 4.6% and 5,00%, respectively (average increase of 4.4%). We note that for the purposes of our simulations, we employed a typical LEHR collimator, with a Gaussian σ value of 0.019.

The effects of any deblurring method are expected to be more distinct in cases of collimators with higher σ values. Hence, in the future, we plan to evaluate our deblurring method by employing parallel-hole collimators with higher σ. In this direction, we aim to simulate phantoms with high sensitivity collimators with σ values in the vicinity of 0.05. Furthermore, we plan to test the usability of our method in real clinical data and to implement it in STIR [88], probably including time-of-flight considerations [140].

5.6 Conclusion

We have developed a novel method for the deblurring of reconstructed SPECT images via aSRT, and have tested the proposed algorithm in simulated phantoms. Our algorithm is based on the specification of the collimator in terms of its blur profile, rather than its point response function. Preliminary results indicate that our method is capable of compensating for the collimator blur effect, which is intrinsic in SPECT imaging. By deblurring the blurred sinograms, we were able to reconstruct images with less blurring, via aSRT. The metrics employed indicate that our algorithm can be proven to be useful for clinical SPECT applications.

5.7 Chapter acknowledgments

The work presented in the current chapter was partially supported by the research program “Inverse Problems and Medical Imaging" (200/920) of the Research Committee of the Academy of Athens. I would like to thank Prof. Konstantina Nikita of the School of Electrical and Computer Engineering of the National Technical University of Athens for her valuable suggestions and comments.

Chapter 6

Future work

This thesis deals with several different mathematical problems with direct applications in PET and SPECT imaging, namely:

- the edge detection of both the non-attenuated (PET) and the attenuated (SPECT) versions of the Radon transform in two dimensions, referred to as *sinogram masking*, and the subsequent "cleaner" image reconstruction of the masked sinograms,
- the introduction of a new mathematical method for the efficient inversion of the attenuated Radon transform and its numerical implementation, and
- the compensation for the blur effect in two-dimensional attenuated Radon transform, which is inherent in all cases of SPECT attenuated sinograms.

In the near future, we plan to further investigate all open aspects of the above mathematical problems. More specifically:

- **Regarding sinogram masking**: we intend to implement our masking method in STIR, as well as to design and implement a stand-alone application for contour detection, image masking and the elimination of streak artifacts.
- **Regarding aSRT**: since the aSRT results of the clinical myocardial study are quite encouraging, it is evident that aSRT could provide useful medical image reconstructions in a clinical setting. Further investigations are essential, especially with the help of clinical physicians,

in order to better quantify the improvement of aSRT in myocardial perfusion imaging. Clinical studies focusing on myocardial ischemia are currently in progress. If further scrutinized, aSRT may provide an alternative to the industry-standard FBP for SPECT/CT reconstruction.

- **Regarding sinogram deblurring**: we plan to further examine our deblurring method by employing parallel-hole collimators with higher σ values. In this direction, we aim to simulate phantoms with high sensitivity collimators with σ values in the vicinity of 0.05. Furthermore, we plan to test the usability of our algorithm in real clinical data, and to implement our technique in the framework of STIR, or relevant software.

Bibliography

[1] J. Radon, Über die Bestimmung von Funktionen durch ihre Integralwerte längs gewisser Mannigfaltigkeiten, Akad. Wiss. 69 (1917) 262–277.

[2] J. Radon, On the determination of functions from their integral values along certain manifolds, IEEE transactions on medical imaging 5 (4) (1986) 170–176. doi:10.1109/TMI.1986.4307775.

[3] P. Kuchment, The Radon Transform and Medical Imaging, CBMS-NSF Regional Conference Series in Applied Mathematics, Society for Industrial and Applied Mathematics, 2014.

[4] S. Cherry, J. Sorenson, M. Phelps, Physics in Nuclear Medicine, 3rd Edition, Elsevier Health Sciences, 2003.

[5] K. Iniewski, Medical Imaging: Principles, Detectors, and Electronics, Wiley-Interscience, New York, NY, USA, 2009.

[6] A. Fokas, R. Novikov, Discrete analogues of $\bar{d}$-equation and of Radon transform, Comptes Rendus Acad. Sci. Série 1, Mathématique 313 (2) (1991) 75–80.

[7] R. Novikov, An inversion formula for the attenuated X-ray transformation, Ark. Mat. 40 (1) (2002) 145–167. doi:10.1007/BF02384507.

[8] A. Fokas, A. Iserles, V. Marinakis, Reconstruction algorithm for single photon emission computed tomography and its numerical implementation, J. R. Soc. Interface 3 (6) (2006) 45–54. doi:10.1098/rsif.2005.0061.

[9] A. S. Fokas, A Unified Approach to Boundary Value Problems, Vol. 78, Society for Industrial and Applied Mathematics, 2008. doi:10.1137/1.9780898717068.

[10] Nobel Media AB, The Nobel Prize in Physics 1902, https://www.nobelprize.org/prizes/physics/1902/summary/, Accessed: 6 Nov 2019 (2019).

[11] A. M. Cormack, Computed tomography: Some history and recent developments, in: Proc. Symposia Appl. Math, Vol. 27, 1982, pp. 35–42.

[12] H. Bockwinkel, On the propagation of light in a biaxial crystal about a midpoint of oscillation, Verh. Konink Acad. V. Wet. Wissen. Natur. 14 (1906) 636–651.

[13] K. L. Wininger, History of mathematics special interest group of the Mathematical Association of America, HOMSIGMAA (2011).

[14] K. Denecker, J. Van Overloop, F. Sommen, The general quadratic Radon transform, Inverse problems 14 (3) (1998) 615.

[15] A. M. Cormack, Representation of a function by its line integrals, with some radiological applications, Journal of Applied Physics 34 (9) (1963) 2722–2727. doi:10.1063/1.1729798.

[16] A. M. Cormack, Representation of a function by its line integrals, with some radiological applications II, Journal of Applied Physics 35 (10) (1964) 2908–2913. doi:10.1063/1.1713127.

[17] Nobel Media AB, Allan M. Cormack – Facts, https://www.nobelprize.org/prizes/medicine/1979/cormack/facts/, Accessed: 5 Nov 2019 (2019).

[18] C. Richmond, Sir Godfrey Hounsfield's Obituary (2004).

[19] Nobel Media AB, With a Little Help from my Friends, https://www.nobelprize.org/prizes/medicine/1979/perspectives/, Accessed: 5 Nov 2019 (2019).

[20] M. E. Phelps, E. J. Hoffman, N. A. Mullani, M. M. Ter-Pogossian, Application of annihilation coincidence detection to transaxial reconstruction tomography, Journal of Nuclear Medicine 16 (3) (1975) 210–224.

[21] M. M. Ter-Pogossian, M. E. Phelps, E. J. Hoffman, N. A. Mullani, A positron-emission transaxial tomograph for nuclear imaging (PETT), Radiology 114 (1) (1975) 89–98. doi:10.1148/114.1.89.

[22] D. A. Rich, A brief history of positron emission tomography, Journal of Nuclear Medicine Technology 25 (1) (1997) 4–11.

[23] L. Jaroff, A winning combination, Time 156 (23) (2000) Inventions.

[24] G. Mariani, H. W. Strauss, Positron emission and single-photon emission imaging: synergy rather than competition, European Journal of Nuclear Medicine and Molecular Imaging 38 (7) (2011) 1189–1190. doi:10.1007/s00259-011-1767-3.

[25] R. J. Jaszczak, The early years of single photon emission computed tomography (SPECT): an anthology of selected reminiscences, Physics in Medicine & Biology 51 (13) (2006) R99. doi:10.1088/0031-9155/51/13/R07.

[26] D. E. Kuhl, R. Q. Edwards, Image separation radioisotope scanning, Radiology 80 (4) (1963) 653–662. doi:10.1148/80.4.653.

[27] D. E. Kuhl, R. Q. Edwards, Reorganizing data from transverse section scans of the brain using digital processing, Radiology 91 (5) (1968) 975–983. doi:10.1148/91.5.975.

[28] D. E. Kuhl, R. Q. Edwards, A. R. Ricci, R. J. Yacob, T. J. Mich, A. Alavi, The Mark IV system for radionuclide computed tomography of the brain, Radiology 121 (2) (1976) 405–413. doi:10.1148/121.2.405.

[29] T. Beyer, D. W. Townsend, T. Brun, P. E. Kinahan, M. Charron, R. Roddy, J. Jerin, J. Young, L. Byars, R. Nutt, et al., A combined PET/CT scanner for clinical oncology, Journal of Nuclear Medicine 41 (8) (2000) 1369–1379.

[30] A. K. Buck, S. Nekolla, S. Ziegler, A. Beer, B. J. Krause, K. Herrmann, K. Scheidhauer, H.-J. Wester, E. J. Rummeny, M. Schwaiger, et al., SPECT/CT, Journal of Nuclear Medicine 49 (8) (2008) 1305–1319. doi:10.2967/jnumed.107.050195.

[31] G. Mariani, L. Bruselli, T. Kuwert, E. E. Kim, A. Flotats, O. Israel, M. Dondi, N. Watanabe, A review on the clinical uses of SPECT/CT, European Journal of Nuclear Medicine and Molecular Imaging 37 (10) (2010) 1959–1985. doi:10.1007/s00259-010-1390-8.

[32] O. Israel, O. Pellet, L. Biassoni, D. De Palma, E. Estrada-Lobato, G. Gnanasegaran, T. Kuwert, C. la Fougère, G. Mariani, S. Massalha, D. Paez, F. Giammarile, Two decades of SPECT/CT – the coming of age of a technology: An updated review of literature evidence, European Journal of Nuclear Medicine and Molecular Imaging 46 (10) (2019) 1990–2012. doi:10.1007/s00259-019-04404-6.

[33] M. M. Khalil, Elements of gamma camera and SPECT systems, in: Basic Sciences of Nuclear Medicine, Springer, 2010, pp. 155–178. doi:10.1007/978-3-540-85962-8_10.

[34] M. N. Wernick, J. N. Aarsvold, Emission tomography: the fundamentals of PET and SPECT, Elsevier, 2004.

[35] S. R. Deans, The Radon Transform and Some of its Applications, Courier Corporation, 2007.

[36] R. Brinks, T. M. Buzug, Image reconstruction in positron emission tomography (PET): the 90th anniversary of Radon's solution/bildrekonstruktion in der Positronen-Emissions-Tomographie (PET): zum 90. Jahrestag von Radons Lösung, Biomedizinische Technik 52 (6) (2007) 361–364.

[37] F. Natterer, F. Wuebbeling, Mathematical Methods in Image Reconstruction, Monographs on Mathematical Modeling and Computation, Society for Industrial and Applied Mathematics, 2001.

[38] M. E. Phelps, PET: Physics, Instrumentation, and Scanners, Springer-Verlag New York, 2006.

[39] N. R. Zürcher, A. Bhanot, C. J. McDougle, J. M. Hooker, A systematic review of molecular imaging (PET and SPECT) in autism spectrum disorder: current state and future research opportunities, Neuroscience & Biobehavioral Reviews 52 (2015) 56–73. doi:10.1016/j.neubiorev.2015.02.002.

[40] R. D. Neirinckx, L. R. Canning, I. M. Piper, D. P. Nowotnik, R. D. Pickett, R. A. Holmes, W. A. Volkert, A. M. Forster, P. S. Weisner, J. A. Marriott, et al., Technetium-99m d, l-HM-PAO: A new radiopharmaceutical for SPECT imaging of regional cerebral blood perfusion, Journal of Nuclear Medicine 28 (2) (1987) 191–202.

[41] J. C. Masdeu, Single-photon emission computed tomography, in: Neurobiology of Disease, Elsevier, 2007, pp. 829–837. doi:10.1016/B978-012088592-3/50078-5.

[42] L. Ehrenpreis, The universality of the Radon transform, Oxford mathematical monographs, Oxford University Press, 2003.

[43] I. Gelfand, M. Graev, N. Vilenkin, Generalized Functions, Academic Press, New York, 1965.

[44] N. E. Protonotarios, A. S. Fokas, K. Kostarelos, G. A. Kastis, The attenuated spline reconstruction technique for single photon emission computed tomography, J. R. Soc. Interface 15 (148) (2018) 20180509. doi:10.1098/rsif.2018.0509.

[45] N. E. Protonotarios, G. M. Spyrou, G. A. Kastis, Automatic cumulative sums contour detection of FBP-reconstructed multi-object nuclear medicine images, Computers in biology and medicine 85 (1) (2017) 43–52. doi:10.1016/j.compbiomed.2017.04.010.

[46] N. E. Protonotarios, A. Charalambopoulos, K. Kacperski, G. A. Kastis, A. S. Fokas, A spline approach to parallel-hole collimator deblurring for aSRT-reconstructed SPECT images, in: 2019 IEEE BioInformatics and BioEngineering (BIBE), IEEE, 2019, pp. 1–6 (to appear).

[47] N. E. Protonotarios, A. S. Fokas, A. Gaitanis, G. A. Kastis, aSRT: A new analytic reconstruction algorithm for SPECT, in: 2016 IEEE Nuclear Science Symposium, Medical Imaging Conference and Room-Temperature Semiconductor Detector Workshop (NSS/MIC/RTSD), IEEE, 2016, pp. 1–6. doi:10.1109/NSSMIC.2016.8069451.

[48] N. E. Protonotarios, G. M. Spyrou, G. A. Kastis, Cumulative sums for edge determination of a single object in PET and SPECT images, in:

Journal of Physics: Conference Series, Vol. 738, IOP Publishing, 2016, p. 012010. doi:10.1088/1742-6596/738/1/012010.

[49] N. E. Protonotarios, G. M. Spyrou, G. A. Kastis, Cumulative sums for masking in nuclear medicine image reconstruction, in: Bio-Medical Instrumentation and related Engineering and Physical Sciences (BIOMEP, Athens), 2017.
URL http://biomep.teiath.gr/2017/proceedings.html

[50] N. E. Protonotarios, G. A. Kastis, A. S. Fokas, Attenuated spline reconstruction technique for SPECT/CT, in: 9th Conference of the Eastern Mediterranean Region and the Italian Region of the International Biometric Society (EMR-IBS), Thessaloniki, 2017.
URL http://www2.stat-athens.aueb.gr/~emribs/page/EMR2017/EMR_PROGRAM_29APR17.pdf

[51] N. E. Protonotarios, A. S. Fokas, A. Gaitanis, G. A. Kastis, Inversion of the attenuated Radon transform using cubic splines, Physica Medica 32 (2016) 242–243. doi:10.1016/j.ejmp.2016.07.510.

[52] N. E. Protonotarios, A. S. Fokas, G. A. Kastis, Attenuated Radon transform inversion through piecewise polynomial interpolation of SPECT/CT data, in: 5th International Conference on Mathematical Modeling in Physical Sciences (ICM^2), Athens, 2016.

[53] A. S. Fokas, G. A. Kastis, N. E. Protonotarios, Analytic reconstructions for PET, SPECT, MEG and EEG, in: Advanced Inverse Problems (AIP), Helsinki, 2015.
URL https://www.aip2015.fips.fi/mainAipBookOfAbstracts.pdf

[54] N. E. Protonotarios, G. A. Kastis, A. S. Fokas, A new approach for the inversion of the attenuated Radon transform, in: T. M. Rassias, P. M. Pardalos (Eds.), Mathematical Analysis and Applications, Springer, 2020.

[55] A. C. Kak, M. Slaney, Principles of Computerized Tomographic Imaging, Society for Industrial and Applied Mathematics, 1987.

[56] G. A. Kastis, D. Kyriakopoulou, A. Gaitanis, Y. Fernández, B. F. Hutton, A. S. Fokas, Evaluation of the spline reconstruction technique for PET, Medical physics 41 (4) (2014) 042501.

[57] S. Helgason, Integral Geometry and Radon Transforms, Springer, 2011.

[58] T. Durrani, D. Bisset, The Radon transform and its properties, Geophysics 49 (8) (1984) 1180–1187. doi:10.1190/1.1441747.

[59] P. A. Toft, J. A. Sørensen, The Radon transform - Theory and implementation, PhD thesis (1996).

[60] F. Natterer, Inversion of the attenuated Radon transform, Inverse Probl. 17 (1) (2001) 113–119. doi:10.1088/0266-5611/17/1/309.

[61] O. Tretiak, C. Metz, The exponential Radon transform, SIAM J. Appl. Math. 39 (2) (1980) 341–354. doi:10.1137/0139029.

[62] L. A. Kunyansky, A new SPECT reconstruction algorithm based on the Novikov explicit inversion formula, Inverse Probl. 17 (2) (2001) 293–306. doi:10.1088/0266-5611/17/2/309.

[63] H. H. Barrett, The Radon transform and its applications, Progress in Optics 21 (1984) 217–286. doi:10.1016/S0079-6638(08)70123-9.

[64] M. J. Ablowitz, A. S. Fokas, A. Fokas, Complex Variables: Introduction and Applications, Cambridge University Press, 2003.

[65] N. I. Muskhelishvili, Singular integral equations, P. Nordhoff, Groningen, 1953.

[66] B. Trémoulhéac, N. Dikaios, D. Atkinson, S. R. Arridge, Dynamic MR image reconstruction–separation from undersampled (k, t)-space via low-rank plus sparse prior, IEEE transactions on medical imaging 33 (8) (2014) 1689–1701.

[67] D. C. Costa, L. Spilowsky, P. J. Ell, Nuclear medicine in neurology and psychiatry, The Lancet 354 (9184) (1999) 1107–1111. doi:10.1016/S0140-6736(99)06095-X.

[68] H. H. Barrett, K. J. Myers, Foundations of Image Science, Wiley, 2004.

[69] M.-J. Bélanger, J. Mann, R. V. Parsey, OSEM and FBP reconstructions at low count rates: Effect on 3D PET studies of [11C] WAY-100635, NeuroImage 21 (1) (2004) 244 – 250. doi:http://dx.doi.org/10.1016/j.neuroimage.2003.08.035.

[70] A. Reilhac, S. Tomeï, I. Buvat, C. Michel, F. Keheren, N. Costes, Simulation-based evaluation of OSEM iterative reconstruction methods in dynamic brain PET studies, Neuroimage 39 (1) (2008) 359–368.

[71] R. Boellaard, A. Van Lingen, A. A. Lammertsma, Experimental and clinical evaluation of iterative reconstruction (OSEM) in dynamic PET: Quantitative characteristics and effects on kinetic modeling, Journal of Nuclear Medicine 42 (5) (2001) 808–817.

[72] L. R. Barnden, J. Dickson, B. F. Hutton, Detection and validation of the body edge in low count emission tomography images, Computer Methods and Programs in Biomedicine 84 (2–3) (2006) 153 – 161, Medical Image Segmentation Special Issue. doi:http://dx.doi.org/10.1016/j.cmpb.2006.08.001.

[73] M. Bergström, J. Litton, L. Eriksson, C. Bohm, G. Blomqvist, Determination of object contour from projections for attenuation correction in cranial positron emission tomography, Journal of Computer Assisted Tomography 6 (2) (1982) 365–372.

[74] T. Tomitani, An edge detection algorithm for attenuation correction in emission CT, IEEE Transactions on Nuclear Science 34 (1) (1987) 309–312.

[75] J. Canny, A computational approach to edge detection, IEEE Transactions on pattern analysis and machine intelligence (6) (1986) 679–698.

[76] M. Hosoba, H. Wani, H. Toyama, H. Murata, E. Tanaka, Automated body contour detection in SPECT: effects on quantitative studies, Journal of Nuclear Medicine 27 (7) (1986) 1184–1191.

[77] C. Michel, A. Bol, A. de Volder, A. Goffinet, Online brain attenuation correction in PET: Towards a fully automated data handling in a clinical environment, European Journal of Nuclear Medicine 15 (11) (1989) 712–718. doi:10.1007/BF00631762.

[78] J. Case, M. King, D.-S. Luo, E. J. Soares, M. S. Rabin, et al., Determination of concave body outlines from SPECT projection data, in: IEEE Nuclear Science Symposium and Medical Imaging Conference Record, Vol. 2, 1, 1995, pp. 944–948.

[79] V. Elangovan, R. T. Whitaker, From sinograms to surfaces: A direct approach to the segmentation of tomographic data, in: International Conference on Medical Image Computing and Computer-Assisted Intervention, Springer, 2001, pp. 213–223.

[80] A. A. Zamyatin, S. Nakanishi, Extension of the reconstruction field of view and truncation correction using sinogram decomposition, Medical physics 34 (5) (2007) 1593–1604.

[81] W. J. Veldkamp, R. M. Joemai, A. J. van der Molen, J. Geleijns, Development and validation of segmentation and interpolation techniques in sinograms for metal artifact suppression in CT, Medical physics 37 (2) (2010) 620–628.

[82] T. Kaewlek, D. Koolpiruck, S. Thongvigitmanee, M. Mongkolsuk, S. Thammakittiphan, S.-o. Tritrakarn, P. Chiewvit, Metal artifact reduction and image quality evaluation of lumbar spine CT images using metal sinogram segmentation, Journal of X-ray science and technology 23 (6) (2015) 649–666.

[83] S. S. Mokri, M. I. Saripan, A. A. Rahni, A. Nordin, S. Hashim, M. Marhaban, PET image reconstruction incorporating 3D mean-median sinogram filtering, IEEE Transactions on Nuclear Science 63 (1) (2016) 157–169.

[84] D. Karimi, R. Ward, A denoising algorithm for projection measurements in cone-beam computed tomography, Computers in biology and medicine 69 (2016) 71–82.

[85] E. S. Page, Continuous inspection schemes, Biometrika 41 (1/2) (1954) 100–115.

[86] M. Basseville, I. V. Nikiforov, Detection of Abrupt Changes: Theory and Application, Prentice-Hall, Inc., Upper Saddle River, NJ, USA, 1993.

[87] A. Knight, E. Williams, An evaluation of cusum analysis and control charts applied to quantitative gamma-camera uniformity parameters for automated quality control, European Journal of Nuclear Medicine 19 (2) (1992) 125–130. doi:10.1007/BF00184128.

[88] K. Thielemans, C. Tsoumpas, S. Mustafovic, T. Beisel, P. Aguiar, N. Dikaios, M. W. Jacobson, STIR: Software for Tomographic Image Reconstruction release 2, Phys. Med. Biol. 57 (4) (2012) 867–883. doi:10.1088/0031-9155/57/4/867.

[89] V. Bettinardi, M. Danna, A. Savi, M. Lecchi, I. Castiglioni, M. Gilardi, H. Bammer, G. Lucignani, F. Fazio, Performance evaluation of the new whole-body PET/CT scanner: Discovery ST, European Journal of Nuclear Medicine and Molecular Imaging 31 (6) (2004) 867–881. doi:10.1007/s00259-003-1444-2.

[90] M. Daube-Witherspoon, J. Karp, M. Casey, F. DiFilippo, H. Hines, G. Muehllehner, V. Simcic, C. Stearns, L. Adam, S. Kohlmyer, V. Sossi, PET performance measurements using the NEMA NU 2-2001 standard, Journal of Nuclear Medicine 43 (2002) 1398–1409.

[91] NEMA, NEMA NU 2-2001: Performance measurements of positron emission tomographs, Rosslyn, VA, Tech. rep., National Electrical Manufacturers Association (2001).

[92] D. P. Huttenlocher, G. A. Klanderman, W. J. Rucklidge, Comparing images using the Hausdorff distance, IEEE Transactions on pattern analysis and machine intelligence 15 (9) (1993) 850–863.

[93] V. Chalana, Y. Kim, A methodology for evaluation of boundary detection algorithms on medical images, IEEE transactions on medical imaging 16 (5) (1997) 642–652.

[94] K. W. Bowyer, Validation of medical image analysis techniques, in: M. Sonka, J. M. Fitzpatrick (Eds.), Handbook of Medical Imaging, Vol. 2, SPIE, 2006, Ch. 10, pp. 567–607.

[95] D. Schuhmacher, B.-T. Vo, B.-N. Vo, A consistent metric for performance evaluation of multi-object filters, IEEE Transactions on Signal Processing 56 (8) (2008) 3447–3457.

[96] H. Zhang, J. E. Fritts, S. A. Goldman, Image segmentation evaluation: A survey of unsupervised methods, Computer Vision and Image Understanding 110 (2) (2008) 260–280.

[97] F. Noo, R. Clackdoyle, J. D. Pack, A two-step Hilbert transform method for 2D image reconstruction, Physics in Medicine and Biology 49 (17) (2004) 3903–3923.

[98] J. J. Bax, M. Di Carli, J. Narula, V. Delgado, Multimodality imaging in ischaemic heart failure, The Lancet 393 (10175) (2019) 1056–1070. doi:10.1016/S0140-6736(18)33207-0.

[99] D. S. Berman, R. Hachamovitch, H. Kiat, I. Cohen, J. A. Cabico, F. P. Wang, J. D. Friedman, G. Germano, K. Van Train, G. A. Diamond, Incremental value of prognostic testing in patients with known or suspected ischemic heart disease: A basis for optimal utilization of exercise technetium-99m sestamibi myocardial perfusion single-photon emission computed tomography, Journal of the American College of Cardiology 26 (3) (1995) 639–647.

[100] K. Marek, J. Seibyl, S. Zoghbi, Y. Zea-Ponce, R. Baldwin, B. Fussell, D. Charney, C. Van Dyck, P. Hoffer, R. Innis, [^{123}I]β-CIT/SPECT imaging demonstrates bilateral loss of dopamine transporters in hemi-Parkinson's disease, Neurology 46 (1) (1996) 231–237. doi:10.1212/WNL.46.1.231.

[101] K. Ogasawara, A. Ogawa, T. Yoshimoto, Cerebrovascular reactivity to acetazolamide and outcome in patients with symptomatic internal carotid or middle cerebral artery occlusion: A Xenon-133 single-photon emission computed tomography study, Stroke 33 (7) (2002) 1857–1862. doi:10.1161/01.STR.0000019511.81583.A8.

[102] A. S. Iskandrian, S. C. Chae, J. Heo, C. D. Stanberry, V. Wasserleben, V. Cave, Independent and incremental prognostic value of exercise single-photon emission computed tomographic (SPECT) Thallium imaging in coronary artery disease, Journal of the American College of Cardiology 22 (3) (1993) 665–670. doi:10.1016/0735-1097(93)90174-Y.

[103] P. P. Bruyant, Analytic and iterative reconstruction algorithms in SPECT, Journal of Nuclear Medicine 43 (10) (2002) 1343–1358.

[104] T. Yokei, H. Shinohara, H. Onishi, Performance evaluation of OSEM reconstruction algorithm incorporating three-dimensional distance-

dependent resolution compensation for brain SPECT: A simulation study, Annals of Nuclear Medicine 16 (1) (2002) 11–18.

[105] R. J. Jaszczak, J. Li, J. Wang, R. E. Coleman, Three-dimensional SPECT reconstruction of combined cone beam and parallel beam data, Physics in Medicine & Biology 37 (3) (1992) 535.

[106] A. Cuocolo, Attenuation correction for myocardial perfusion SPECT imaging: Still a controversial issue, Eur. J. Nucl. Med. Mol. Imaging 38 (10) (2011) 1887–1889. doi:10.1007/s00259-011-1898-6.

[107] G. Germano, P. J. Slomka, D. S. Bermana, Attenuation correction in cardiac SPECT: The boy who cried wolf?, J. Nucl. Cardiol. 14 (1) (2007) 25–35. doi:10.1016/j.nuclcard.2006.12.317.

[108] F. Wacker, Attenuation correction, or the emperor's new clothes? [editorial], J. Nucl. Med. 40 (1999) 1310–1312.

[109] R. C. Hendel, Attenuation correction: Eternal dilemma or real improvement?, Q. J. Nucl. Med. Mol. Imaging 49 (1) (2005) 30–42.

[110] M. K. O'Connor, B. J. Kemp, Single-photon emission computed tomography/computed tomography: Basic instrumentation and innovations, in: Seminars in nuclear medicine, Vol. 36, Elsevier, 2006, pp. 258–266. doi:10.1053/j.semnuclmed.2006.05.005.

[111] A. Bockisch, L. S. Freudenberg, D. Schmidt, T. Kuwert, Hybrid imaging by SPECT/CT and PET/CT: Proven outcomes in cancer imaging, in: Seminars in nuclear medicine, Vol. 39, Elsevier, 2009, pp. 276–289. doi:10.1053/j.semnuclmed.2009.03.003.

[112] F. Chowdhury, A. Scarsbrook, The role of hybrid SPECT-CT in oncology: Current and emerging clinical applications, Clinical radiology 63 (3) (2008) 241–251. doi:10.1016/j.crad.2007.11.008.

[113] C. E. Metz, X. Pan, A unified analysis of exact methods of inverting the 2-D exponential Radon transform, with implications for noise control in SPECT, IEEE Trans. Med. Imag. 14 (4) (1995) 643–658.

[114] G. Bal, P. Moireau, Fast numerical inversion of the attenuated Radon transform with full and partial measurements, Inverse Probl. 20 (4) (2004) 1137–1164. doi:10.1088/0266-5611/20/4/009.

[115] H. Ammari, E. Bretin, V. Jugnon, A. Wahab, Photoacoustic imaging for attenuating acoustic media, in: H. Ammari (Ed.), Mathematical Modeling in Biomedical Imaging II: Optical, Ultrasound, and Opto-Acoustic Tomographies, Springer Berlin Heidelberg, Berlin, Heidelberg, 2012, Ch. 3, pp. 57–84. doi:10.1007/978-3-642-22990-9_3.

[116] G. A. Kastis, D. Kyriakopoulou, A. Gaitanis, Y. Fernández, B. F. Hutton, A. S. Fokas, Evaluation of the spline reconstruction technique for PET, Med. Phys. 41 (4) (2014) 042501. doi:10.1118/1.4867862.

[117] G. A. Kastis, A. Gaitanis, A. P. Samartzis, A. S. Fokas, The SRT reconstruction algorithm for semiquantification in PET imaging, Med. Phys. 42 (10) (2015) 5970–5982. doi:10.1118/1.4931409.

[118] M. Unser, J. Fageot, J. P. Ward, Splines are universal solutions of linear inverse problems with generalized TV regularization, SIAM Review 59 (4) (2017) 769–793. doi:10.1137/16M1061199.

[119] W. H. Press, S. A. Teukolsky, W. T. Vetterling, B. P. Flannery, Numerical Recipes 3rd Edition: The Art of Scientific Computing, 3rd Edition, Cambridge University Press, New York, NY, USA, 2007.

[120] K. Saha, S. C. Hoyt, B. M. Murray, Application of Chang's attenuation correction technique for single-photon emission computed tomography partial angle acquisition of Jaszczak phantom, J. Med. Phys. 41 (1) (2016) 29–33. doi:10.4103/0971-6203.177278.

[121] H. Zaidi (Ed.), Quantitative Analysis in Nuclear Medicine Imaging, Springer, 2006.

[122] S. Tong, A. M. Alessio, P. E. Kinahan, Noise and signal properties in PSF-based fully 3D PET image reconstruction: An experimental evaluation, Physics in Medicine and Biology 55 (5) (2010) 1453–1473. doi:10.1088/0031-9155/55/5/013.

[123] J. P. Greenwood, N. Maredia, J. F. Younger, J. M. Brown, J. Nixon, C. C. Everett, P. Bijsterveld, J. P. Ridgway, A. Radjenovic, C. J. Dickinson, et al., Cardiovascular magnetic resonance and single-photon emission computed tomography for diagnosis of coronary heart disease

(CE-MARC): A prospective trial, The Lancet 379 (9814) (2012) 453–460. doi:10.1016/S0140-6736(12)60936-2.

[124] W. Xia, R. M. Lewitt, P. R. Edholm, Fourier correction for spatially variant collimator blurring in SPECT, IEEE Trans. Med. Imag. 14 (1) (1995) 100–115. doi:10.1109/42.370406.

[125] K. van Audenhaege, R. van Holen, S. Vandenberghe, C. Vanhove, S. D. Metzler, S. C. Moore, Review of SPECT collimator selection, optimization, and fabrication for clinical and preclinical imaging, Med. Phys. 42 (8) (2015) 4796–4813. doi:10.1118/1.4927061.

[126] B. F. Hutton, M. Occhipinti, A. Kuehne, D. Máthé, N. Kovács, et al., Development of clinical simultaneous SPECT/MRI, Br. J. Radiol. 91 (1081) (2017) 20160690. doi:10.1259/bjr.20160690.

[127] N. H. Clinthorne, L.-G. Meng, Small animal SPECT, SPECT/CT, and SPECT/MRI, in: R. Weissleder, B. D. Ross, A. Rehemtulla, S. S. Gambhir (Eds.), Molecular Imaging: Principles and Practice, PMPH-USA, Shelton, 2010, Ch. 6, pp. 76–98.

[128] T. G. Turkington, D. R. Gilland, Basics of SPECT Scanning: Emission and Transmission, in: G. K. von Schulthess, D. T. Schmid (Eds.), Molecular Anatomic Imaging: PET-CT and SPECT-CT Integrated Modality Imaging, 2nd Edition, Lippincott Williams & Wilkins, 2007, Ch. 4.

[129] C. Kamphuis, F. J. Beekman, P. P. van Rijk, M. A. Viergever, Dual matrix ordered subsets reconstruction for accelerated 3D scatter compensation in single-photon emission tomography, Eur. J. Nucl. Med. 25 (1) (1998) 8–18. doi:10.1007/s002590050.

[130] G. Zeng, G. Gullberg, B. Tsui, J. Terry, Three-dimensional iterative reconstruction algorithms with attenuation and geometric point response correction, IEEE Trans. Nucl. Sci. 38 (2) (1991) 693–702.

[131] S. Y. Chun, J. A. Fessler, Y. K. Dewaraja, Correction for collimator-detector response in SPECT using point spread function template, IEEE transactions on medical imaging 32 (2) (2013) 295–305.

[132] P. Boccacci, P. Bonetto, P. Calvini, A. R. Formiconi, A simple model for the efficient correction of collimator blur in 3D SPECT imaging, Inverse Probl. 15 (4) (1999) 907–930. doi:10.1088/0266-5611/15/4/306.

[133] S. J. Glick, B. Penney, M. A. King, C. L. Byrne, Noniterative compensation for the distance-dependent detector response and photon attenuation in SPECT imaging, IEEE Trans. Med. Imag. 13 (2) (1994) 363–374.

[134] P. R. Edholm, R. M. Lewitt, B. Lindholm, Novel properties of the Fourier decomposition of the sinogram, in: Physics and Engineering of Computerized Multidimensional Imaging and Processing, Vol. 671, International Society for Optics and Photonics, 1986, pp. 8–19.

[135] R. M. Lewitt, P. R. Edholm, W. Xia, Fourier method for correction of depth-dependent collimator blurring, in: Medical Imaging III: Image Processing, Vol. 1092, International Society for Optics and Photonics, 1989, pp. 232–244.

[136] L. van Elmbt, S. Walrand, Simultaneous correction of attenuation and distance-dependent resolution in SPECT: An analytical approach, Phys. Med. Biol. 38 (9) (1993) 1207–1217. doi:10.1088/0031-9155/38/9/003.

[137] V. Kohli, M. A. King, S. J. Glick, T.-S. Pan, Comparison of frequency-distance relationship and Gaussian-diffusion-based methods of compensation for distance-dependent spatial resolution in SPECT imaging, Phys. Med. Biol. 43 (4) (1998) 1025–1037. doi:10.1088/0031-9155/43/4/029.

[138] G. L. Zeng, Detector blurring and detector sensitivity compensation for a spinning slat collimator, IEEE Trans. Nucl. Sci. 53 (5) (2006) 2628–2634. doi:10.1109/TNS.2006.882574.

[139] F. Crete, T. Dolmiere, P. Ladret, M. Nicolas, The blur effect: perception and estimation with a new no-reference perceptual blur metric, in: Human vision and electronic imaging XII, Vol. 6492, International Society for Optics and Photonics, 2007, p. 64920I.

[140] N. Efthimiou, E. Emond, P. Wadhwa, C. Cawthorne, C. Tsoumpas, K. Thielemans, Implementation and validation of time-of-flight PET image reconstruction module for listmode and sinogram projection data in the STIR library, Physics in medicine and biologydoi:10.1088/1361-6560/aaf9b9.